Using Colour-Magnitude-Diagrams to Study the Evolution of Young Stellar Populations

Nathan J. Mayne

Submitted by Nathan James Mayne to the University of Exeter as a thesis for the degree of Doctor of Philosophy in Physics, February, 2008.

This thesis is available for Library use on the understanding that it is copyright material and that no quotation from the thesis may be published without proper acknowledgement.

I certify that all material in this thesis which is not my own work has been identified and that no material has previously been submitted and approved for the award of a degree by this or any other University.

Signed: .....
Nathan J. Mayne

Date: .....

Abstract

Timescales for stellar evolution and star and planet formation are critical to provide constraints on theories. The accuracy of these timescales, and therefore our ability to confidently reject a given model, rely on the accuracy of the derived ages for star-forming-regions (SFRs). In this study I have developed the new techniques and adopted or updated the existing techniques necessary to derive precise age orders for a range of SFRs.

Deriving precise ages for SFRs requires precise distances and extinctions. I have applied a new technique, τ^2 fitting (Naylor & Jeffries, 2006), to derive a set of self-consistent and statistically robust distances (and mean extinctions), with associated uncertainties for 12 SFRs. I have also revised and formalised a widely used method of deriving individual extinctions, the Q-method (Johnson & Morgan, 1953). These new data show that the largest remaining uncertainty in deriving distances to SFRs is composition.

Deriving ages or age orders for pre-main-sequence (pre-MS) populations using pre-MS theoretical isochrones has been shown to be unreliable at present (Naylor et al., 2002; Bonatto et al., 2004; Pinsonneault et al., 2004), largely due to model dependencies and spreads within a colour-magnitude diagram (CMD). Therefore, I have developed a technique to model the pre-MS, generating **empirical isochrones**, which effectively removes spreads in pre-MS populations in a CMD.

The derived distances and extinctions have been applied to the empirical isochrones, enabling the creation of an age ordered ladder in intrinsic colour and absolute magnitude. This has been calibrated using ages for fiducial sequences and nominal ages assigned to the separable groups, which are as follows:

- 1 Myr, NGC2244 and IC5146.
- 2 Myrs, NGC6530 and the ONC.
- 3 Myrs, λ Ori, Cep OB3b, NGC2264 and σ Ori.
- 4 – 5 Myrs, NGC2362 and IC348.
- 10 Myrs, NGC7160.
- 13 Myrs, h and χ Per.
- 20 Myrs, NGC1960.
- 40 Myrs, NGC2547.

Once assigned the nominal ages and age orders were combined with ancillary data to investigate rotation rate and disc evolution. The general trends of rotation rate distribution evolution and disc fraction changes with age confirmed existing estimates for the disc survival, and therefore star-disc interaction through disc-locking, with a timescale of ≈ 5 Myrs. However, this study also revealed some of the first evidence of local environment effects. IC348 appears 'out of sequence' in both the rotation rate distribution and disc fraction. Specifically, IC348 has a larger disc fraction than expected at its nominal age and exhibits a rotation rate distribution expected from a much younger SFR (i.e. the ONC). This could be a consequence of the lower number density of O stars (none exist in IC348) and therefore a lower density of *UV* flux, which acts to hasten disc dissipation.

Finally, a potentially important feature of stellar populations in a CMD, the R-C gap was identified. This separation in a CMD of the fully convective pre-MS and main-sequence (MS) stars with radiative cores was found to vary as a function of age. As the R-C gap is also measurable in colour it provides a distance independent age indicator. I have explained the underlying physics of the R-C gap and discussed possible applications of this phase change of the stellar interior. In addition, an overlap between the pre-MS and MS sections of the R-C gap was apparent in all SFRs where the R-C gap could be unambiguously identified. This R-C gap overlap shows that the studied SFRs must contain a **spread** in **isochronal** ages. However, the interpretation of this spread is dependent on the underlying assumptions. If one assumes stars form by a robust slow-star-formation (SSF) mechanism and isochronal ages represent the true age of a star, then these spreads can be construed as true age spreads. Alternatively, if one adopts a rapid-star-formation model (RSF), this spread can be explained as a variation in accretion histories of the constituent stars. As found by Siess et al. (1999) and Tout et al. (1999) accretion can act to accelerate pre-MS star evolution, meaning the isochronal age does not represent the true age of the star. This increases the advantages of empirical isochrones and age ordering over the derivation of individual ages for SFRs. Indeed, this R-C gap overlap could be used to 'normalise out' any spread in age or accretion history and therefore increase the power of derived age orders.

Contents

List of Figures

List of Tables

Declaration

This thesis contains work published or pending publication as papers. The results of Chapter 4 have been accepted for publication in the Monthly Notices of the Royal Astronomical Society (MNRAS). The results and techniques of Chapter 5 have been published in MNRAS, Volume 375, Issue 4, pp. 1220-1240. The results of Chapter 6 are contained in both of the papers so far mentioned. The preliminary results of Chapter 7 are nearing completion and pending submission for publication (March-April 2008).

Acknowledgments

The data used in Chapter 5 were obtained using the Isaac Newton Telescope (INT), by Stuart Littlefair and Eric Saunders. The INT is operated by the Isaac Newton Group in the Spanish Observatorio del Roque de los Muchachos of the Instituto de Astrofisica de Canarias. Various literature data have been used in this thesis. In particular, the astrometry in Chapter 5 utilised the Two Micron All Sky Survey, a joint project of the University of Massachusetts and the Infrared Processing and Analysis Center/California Institute of Technology, funded by the National Aeronautics and Space Administration and the National Science Foundation.

The τ^2 fitting technique used in Chapter 4 was developed by Tim Naylor and Rob Jeffries. Much of the work in this thesis has been improved or was instigated by the perspicacious and well thought out comments of Rob Jeffries. I am particularly thankful to Rob for his hard work and support throughout my PhD. Stuart Littlefair has also proved an invaluable resource and has provided much insight, especially with regards to the periodic variability of stars. The often irritating but always precise insight of my supervisor Tim Naylor, who is particularly adept at uncovering ignorance, obviously provided the most significant source of scientific motivation for the work in this thesis. However, I also owe a debt to Rob King for his cynicism and great knowledge of astrophysics. Eric Saunders has also provided an incredibly measured and thoughtful response to all of my scientific questions. Eric, Rob and Tim are also responsible for translating my over-enthusiastic and often inexact use of the English language. The computing skills required for the work involved in this thesis are due to the input of Alasdair Allan, Chris Reeves, John Rowe and Eric Saunders. In particular Eric has provided an exceedingly patient (and free of charge) computing consultancy service, for which I am very grateful. Almost all of my knowledge of astrophysics has been learned from the staff and students at the astrophysics department of Exeter University, in addition to the people already named of particular note are Matthew Bate, Mark McCaughrean, Daniel Price and Tim Harries. Whilst these people are certainly partly responsible for any success I have in the field they are most certainly not liable for any failures.

On a more personal note I owe thanks to a range of people. Firstly, to the enthusiasm, support (particularly through difficult times, thanks Tim), patience and tremendously inspiring work ethic of the man with the jumpers! Tim has been a consistently excellent PhD supervisor. The companionship and broad ranging discussions I have had with Rob King, Eric Saunders and Paul Keatley have taught me much and I am grateful for their sympathetic ears, interesting perspectives and of course for the laughs. My thanks also go to all of the staff and students at the Astrophysics department of Exeter University for their friendship and tolerance. I also thank my mother and family for showing me that life does not solely consist of what can be thought or read. The support,

guidance and experience of my mother has been an inspiration from an alternative angle and has often forced me to view things from a different perspective.

Finally, and most importantly I thank my partner Lizzie Mason. Without her support (both emotionally and financially), patience, love, encouragement and refreshingly different viewpoint I would not have completed this thesis. I am exceedingly lucky to have met such a kind and giving person and can only hope that I will make her as happy as she makes me.

Thank you all.

NJM
Exeter, Devon, U.K.
February^{6th} 2008

Chapter 1

Introduction

'Let no one expect anything certain from astronomy, which cannot supply it, lest he accept ideas as true that were concieved for another purpose, and so leave this study a greater fool than when he entered it'

Andreas Osiander in an anonymous preface to Copernicus' De revolutionibus, May 1542 (source. John North, 'the fontana history of Astronomy and Cosmology').

Stars are perhaps the single most important objects in astrophysics. On the large scale they are the basic building blocks of galaxies. They are also responsible for the generation of the metal elements (those with a proton number $Z > 3$), in particular the earliest population of stars termed population III creating, via nucleosynthesis, the first metal elements. The creation of these metals from the basic hydrogen (H) and helium (He) left over from the big bang allowed for the formation of the subsequent population I and II stars we see in our Galaxy and others today which have continued the production of the metal elements. These heavy elements provide the material from which planets, dwarf-planets and other sub-stellar objects are formed within the orbits of existing stars. Finally our star, the Sun, provides the required energy for almost all life on Earth.

The fundamental importance of stars has resulted in much scientific research being directed towards understanding their formation and subsequent evolution. There are also clear practical benefits arising from such work. The study of stellar evolution allows us to discover the possible origins of our solar system and begin to predict its possible futures. It also the provides us with an insight into both the fundamental physics of basic environments (e.g. the formation of stars from a cold gaseous inter-stellar medium (ISM)) and the behaviour of physical laws in extreme environments not available for study on Earth (e.g. the extreme temperatures and densities found within stellar cores).

The rest of this thesis is organised as follows. Chapter 2 contains a description of some general principles, and a discussion of the current theoretical models of stellar formation and evolution. Chapter 3 describes methods of comparing observations to theoretical models and thereby deriving constraints for these models. In Chapter 4 a method of deriving distances and extinctions to stellar populations is discussed and some results from this method are presented. Chapter 5 details a technique of modeling populations of young stars. Chapter 6 details the process

of age ordering young stellar populations using the results from the previous Chapters. Chapter 6 also compares the results of age ordering with the predictions of some of the theoretical models. Finally Chapter 7 contains concluding remarks and comments on future work.

Chapter 2

Star formation and evolution

The main material within our galaxy (and others) is the ISM. This medium is made up of several components. The more complex constituents are dust and coronal gas, the former being small micrometre size particles and the latter the remnants of supernovae. The coronal gas is a mix of complex elements formed both during a star's life (via nuclear processes) and during its death (supernovae). By far the most ubiquitous components are the three forms of hydrogen. The simplest form is atomic hydrogen (H) ($T \approx 100K$ and $n_\rho \approx 10^6 - 10^9$ particles m^{-3}), followed by molecular hydrogen (H_2) ($T \approx 5 - 30K$ and $n_\rho > 10^9$ particles m^{-3}) and finally ionised hydrogen (H^+). Ionised hydrogen is very hard to detect and under the correct conditions will combine to form molecular hydrogen. The resulting molecular hydrogen is the component of the ISM from which stars form. Ionised hydrogen is generally found around existing stars where high levels of UV flux have dissociated and ionised the molecular hydrogen.

Large collections of molecular hydrogen are found in irregular conglomerations within our galaxy, and are called giant-molecular-clouds (GMCs). The GMCs often appear turbulent due to their irregular shapes and random internal motions and have masses of up to $10^6 M_\odot$. In spiral galaxies, such as our own (Georgelin & Georgelin, 1976) GMCs are found along the spiral arms with associated massive stars. As massive stars have total lifetimes of less than 10 Myrs these areas must also be associated with recent star formation, and the practical use of this in finding young stars is discussed in Section 3.1.

For stars to form from the molecular hydrogen within a GMC some fraction of the cloud must collapse to become a centrally condensed 'clump'. This 'clump' must be both massive and condensed enough for its own gravity to prevent the thermal energy generated in the contraction from reducing the density enhancement. Many 'clumps' in GMCs are observed to be in this state (Ward-Thompson, 2002). Subsequently these clumps must contract further with their interior densities and temperatures increasing to form pre-stellar and then stellar cores.

What follows in this section is a brief overview of star formation and evolution. Firstly in Section 2.1 the general principles behind ISM collapse are introduced. Then Sections 2.1.1 and 2.1.2 describe simple estimates for a formation and lifetime of a star. Two, more realistic models of star formation are then discussed in Sections 2.2.1 and 2.2.2, with a summary of their major differences in Section 2.7. The impact and consequences of rotation on star formation are explored in Section 2.4.1. The evolution of stars is subsequently discussed in Section 2.4. In particular the

evolution of rotation and its link to material orbiting the star are discussed in Section 2.5.1. Finally a summary of this chapter is provided in Section 2.7.

2.1 General principles

2.1.1 Timescale of collapse

The basic idea that stars are formed from the collapse of a cold ISM (Hartmann, 1998, ISM typically T = 10–100K), is not a new one. The first theoretical treatment of star formation was provided by Jeans (1902), termed *gravitational instability*, and showed that density perturbations in an initially uniform medium can lead to runaway gravitational collapse. The modeled medium is infinite, has a finite pressure but contains no angular momentum/rotation, magnetic flux or turbulence. From this basic treatment a critical mass, called the *Jeans mass* ($M_{\rm J}$), can be derived for which gravity dominates thermal pressure and a local runaway collapse under gravity proceeds (see Larson, 2003, for a further discussion). The Jeans mass can be derived in the following way, assuming a circular (symetric) cloud of Mass M_c and Radius R_c. Starting from the virial theorem

$$2U + \Omega = 0 \tag{2.1}$$

where U is the internal energy and is given by

$$U = \frac{3}{2}\frac{M_c}{\mu m_{\rm H}} kT. \tag{2.2}$$

Here M_c is the mass of the bound ISM, μ the mean molecular weight, $m_{\rm H}$ the weight of the hydrogen atom, k the Boltzmann constant and T the temperature of the ISM. Ω, the gravitational potential energy is given by

$$\Omega = -\frac{3}{5}\frac{GM_c^2}{R_c}, \tag{2.3}$$

where G is the gravitational constant and R_c the radius of the ISM fragment. If the ISM is uniform it will have a constant density, ρ_0. If gravity is to dominate over the internal thermal pressure then

$$2U < \mid \Omega \mid \tag{2.4}$$

This provides the *Jeans mass* or the minimum mass (M_c) where gravitational collapse proceeds as

$$M_{\rm J} = \left(\frac{5KT}{G\mu m_{\rm H}}\right)^{\frac{3}{2}} \left(\frac{3}{4\pi\rho_0}\right)^{\frac{1}{2}}. \tag{2.5}$$

There is a scaling error in this Equation as this treatment neglects the collapse of the background medium which could wipe out the effect of individual density fluctuations (Binney & Tremaine, 1987). More complex treatments for the collapse of cylindrical sections of ISM, which are favoured due to the observation of filaments of the ISM in GMCs or star-forming-regions (SFRs) simply change the scaling of the Jeans Mass (Hartmann, 2002).

Equation 2.5 shows that the mass at which a given fragment in a GMC will collapse is

proportional to the temperature of the ISM and inversely proportional to the density. If for masses greater than M_J collapse under gravity occurs, how long does this take? If only the effects of gravity are considered then the collapse proceeds over the free-fall timescale. This is derived by considering the effect of the gravity of all the mass interior to a point. The timescale for the point mass to fall to the centre of a sphere is then given by

$$t_{ff} = \frac{1}{4}\sqrt{\frac{3\pi}{2G\rho}}. \tag{2.6}$$

This timescale is short for typical densities of the pre-stellar cores (Benson & Myers, 1989, n_H, number density of hydrogen $\approx 2\times10^3$–$2\times10^5 cm^{-3}$) (Ward-Thompson et al., 1999, $\approx 10^4 < n < 10^6 cm^{-3}$), with $t_{ff} \approx 0.1$ Myrs. This gives us a basic estimate for the timescale of collapse from a Jeans mass to a pre-stellar core.

2.1.2 Simple stellar lifetimes

Now a basic timescale for the formation of the Sun has been estimated a basic minimum lifetime or age can also be calculated. Using a simple well known calculation one can prove that the existing age of the Sun prohibits it from being powered by energy of gravitational contraction alone. If the density of a star (here the Sun) is uniform ($\overline{\rho}$) we have

$$M(r) = \frac{4}{3}\pi r^3 \overline{\rho}, \tag{2.7}$$

where M(r) is the mass of the Sun within a given radius. Now dividing the star into concentric shells each shell has a gravitational potential energy of

$$du = -\frac{GM(r)dm}{r}. \tag{2.8}$$

Using Equation 2.7 to substitute for the incremental mass (dm) in Equation 2.8, and then integrating over all radii (R) gives a total gravitational potential energy (U) of

$$U = -\frac{16G\pi^2\overline{\rho}^2}{3}\frac{R^5}{5}, \tag{2.9}$$

Then using Equation 2.7 once more, we arrive at the gravitational energy of a *uniform* sphere:

$$U = -\frac{3}{5}\frac{GM^2}{R}. \tag{2.10}$$

So the energy of collapse of the Sun from infinity to its current radius $R_\odot$ is

$$\Delta U = \frac{3}{5}\frac{GM_\odot^2}{R_\odot} \tag{2.11}$$

Using the virial theorem half of the gravitational potential energy goes into increasing the internal energy of the Sun (i.e. heating it up) and the rest therefore must be radiated away. Therefore equation 2.11 halved and evaluated yields a value for the energy which can be liberated from the Sun's gravitational collapse of E 10^{41} **Joules**. Dividing the total energy available by the Sun's

current luminosity ($L_\odot$) provides an estimated lifetime for which the Sun could be powered by the energy of its collapse. Therefore using $L_\odot = 4\times10^{26}$ Js^{-1} gives an estimated lifetime of 8×10^6 yrs or **8 Myrs**. This value can be evaluated for any star and is is called the *Kelvin-Helmholz* timescale ($t_{\rm KH}$).

As it is known that the Sun is also powered by fusion processes it is useful to calculate an approximate nuclear lifetime. If all the Sun's energy is generated from nuclear processes, using the energy to mass relation provides a total possible energy the Sun could generate. If all mass is converted directly to energy with efficiency ϵ and the fraction of nuclear fuel available is f then

$$E_\odot = f\epsilon M_\odot c^2. \tag{2.12}$$

Evaluated for typical values within the Sun of $\epsilon = 0.7\%$ for fusion of hydrogen to helium, $f \approx 10\%$ and $E_\odot \approx 10^{44} J$, which divided by $L_\odot$ yields a lifetime of $\approx$ **10 Gyrs**. This is called the nuclear timescale.

As the current estimate of the Earth's age from densities of lead isotopes in meteorites is 4,550 Myrs, we can see that the Sun cannot be powered by dynamical collapse alone. Another important aspect of the Kelvin-Helmholz and Nuclear timescales is that they give us an approximate rate for evolution during different parts of a stars life. This is discussed further in Section 3.2.

From these basic principles it is clear that a given mass of an ISM cloud can collapse under gravity with a very simplistic model giving a very short (dynamical) collapse timescale. It is also clear that a simple treatment of the energy available to a star can lead to lifetimes of order 10^6–10^9 years. Now to explore timescales for real star formation we must move to a more sophisticated treatment of a collapsing core.

2.2 Core collapse models

The first model of collapse to a pre-stellar core is the model of Hayashi (1966), where gravity overcomes the internal thermal pressure and the collapse proceeds on the free-fall timescale $t_{\rm ff}$. However as this model neglects the effects of turbulence or magnetic pressure which would act to slow the collapse, the timescale is probably too short.

2.2.1 Slow star formation

GMCs appear to be dynamic turbulent environments having random internal motions (McCray & Snow, 1979) and appear highly irregular, often with filamentary structures. This turbulence appears to scale with the size of the region, which is apparent as the velocity dispersion (from line-width measurements) scales with region size (Falgarone et al., 1992). This turbulence is probably due to gravitation on the large scale and ionising winds from massive stars or supernovae on smaller scales. Regions like the ONC where massive star formation has occurred are in general more turbulent than regions of only low mass star formation such as Taurus (Larson, 1981).

GMCs also have interior magnetic fields (Crutcher, 1999) of strengths from a few to hundreds of μgauss. This magnetic field can act via both a static magnetic field and magneto-

hydrodynamic waves (MHD) to arrest or slow any collapse of charged material. Whether this can provide a meaningful retardation is currently being explored in both simulations (Mac Low & Klessen, 2004) and observations (Bourke et al., 2001). A keenly debated aspect of modern astrophysics is whether turbulent and magnetic pressures significantly slow the formation of stellar cores.

The model adopted as the standard model is that of Shu (1977) and Shu et al. (1987). In this model the magnetic field dominates and the collapse can only occur for neutral particles which diffuse through the ions or charged particles. This process is called ambipolar diffusion and is slow with a timescale of **10 Myrs**. This process will eventually form a centrally condensed core where gravity can then dominate the internal pressures and collapse can continue on the free-fall timescale. This model cannot form binary or multiple systems and the detailed calculations are unreliable (Basu & Mouschovias, 1994). In addition the infall velocities suggested from observations are much larger than those predicted by ambipolar diffusion (Lee et al., 2001). Nakano (1998) finds that the magnetic pressure is not enough to halt or slow a stellar collapse. However, the recent work of Adams & Shu (2007) suggests that the rate of collapse and infall velocities can be increased to match observations as a consequence of internal turbulence. For the purposes of continuing discussion I term this model the slow-star-formation SSF model, with the timescale of 10 Myrs.

2.2.2 Rapid star formation

In recent literature, dominated by observational evidence, a new picture of star formation is being developed. Here the timescale is somewhere between that of a turbulence and magnetic-pressure free dynamical collapse and the slow magnetically-dominated ambipolar diffusion. This model demands a new more dynamic definition of GMCs. I term this rapid-star-formation (RSF) for subsequent discussion.

2.2.2.1 Problems with the standard model

In the standard model (Section 2.2.1) GMCs are thought to be long-lived structures supported by magnetic pressure, with stars forming by slow ambipolar diffusion and subsequent collapse ($t_{\rm form}$ = 5–10 Myrs). The age spread within a given SFR should be of order $t_{\rm form}$. For SSF the long timescale should lead to many older objects associated with areas of active star formation (called PTTS see Section 2.4). In this case if the mass of the cloud is above some critical value the development of large cores and therefore massive stars is possible, leading to OB associations such as Orion. Clouds of a lower mass will only facilitate low mass star formation creating so called T associations such as Taurus. Both of these scenarios are discussed in detail in Section 3.1.

However recent observational evidence suggests that some of these conditions are inaccurate. As discussed in Section 2.2.1, GMCs are clearly turbulent and dynamic entities. There is also evidence that they are transient (Ballesteros-Paredes, 2006) and simply denser regions in a continuum of atomic Hydrogen rather than long-lived isolated entities. There is also a distinct lack of PTTS and most regions of recent star formation lack high densities of molecular hydrogen

(although this is refuted by Palla & Galli, 1997, who argue that this can be accounted for by varying the star formation rate). Age spreads within a given SFR however are very difficult to quantify and this is studied and discussed as part of this thesis in Sections 6.2.3 and 6.1.1.

2.2.2.2 Forming GMCs

The new model of star formation is based on a more dynamic situation. Here GMCs are formed from large scale turbulent flows of atomic hydrogen such as can be provided by gravity waves in spiral arms (Dobbs & Bonnell, 2007; Dobbs et al., 2007). These MHD simulations result in dense filamentary structure within the resulting molecular hydrogen clouds, as discussed in Ballesteros-Paredes et al. (1999) and seen in GMCs. Ballesteros-Paredes et al. (1999) used mapping of atomic hydrogen and CO to deduce that the flow of atomic hydrogen is dominant over the effects of the static molecular hydrogen medium. From MHD simulations Ballesteros-Paredes et al. (1999) found that local collapse can occur quickly, with $t_{\rm form} < 3$ Myrs resulting in stellar feedback which acts to disperse the remaining material. This stellar feedback swiftly lowers the density of the cloud and it quickly becomes 'invisible'. In addition Pringle et al. (2001) showed from the results of Allen et al. (1986)[1] that stars in the galaxy M83 are formed in dense molecular hydrogen regions with the resulting stars disassociating and ionizing the gas 'downstream'. Additional support is found in the discovery and continued studies of 'cirrus' or high galactic latitude atomic hydrogen clouds in the galactic halo (Savage & de Boer, 1981; Magnani et al., 1985; Heithausen et al., 2001). Pringle et al. (2001) states "GMCs appear as the tip of the iceberg..", suggesting that the GMCs we observe are merely the denser visible regions of a background continuum of atomic Hydrogen.

This model is also supported by the studies of Elmegreen (2000). He found that the formation time was comparable to the crossing time (defined as the size of the region over the typical velocity dispersion) of many SFRs, although as discussed in Chapter 5 and Section 3.6.2.2 age determinations of young stellar populations are far from certain. The structure of the embedded clusters of stars within GMCs appears to mirror the structure within the GMCs, suggesting that the structure was frozen in (perhaps by large scale magnetic fields) and the subsequent formation was swift with respect to changes in this structure. Hartmann et al. (2001) argue that GMCs are transient regions, citing the lack of SFR regions embedded in dense molecular clouds. In this picture, once the stars are formed the stellar feedback swiftly lowers the density of the surrounding medium. A recent study of M51 has also confirmed the rapid formation and evolution of GMCs (Elmegreen, 2007).

So we now have evidence for GMCs being formed from dynamic shocks caused by gravity waves in a continuous atomic hydrogen background and being rapidly dispersed by stellar feedback. However, if GMCs form rapidly and are transient, short-lived structures, this demands that stars are formed swiftly after formation of a GMC, and that atomic hydrogen can be converted to molecular hydrogen on an similar timescale. Hartmann et al. (2001) argues, using the formula of Hollenbach et al. (1971) and Elmegreen (1991) (for the column density required for conversion of atomic to molecular hydrogen and that required for self gravity respectively) that formation of

[1] Although this study initially concludes that atomic hydrogen plays a negligible role in GMC formation.

molecular hydrogen from hydrogen via the surfaces of dust grains occurs at a similar density to that required for local collapse (a detailed calculation can be found in Bergin et al., 2001). This implies that local collapse is likely to occur soon after the formation of a molecular cloud.

2.3 Summary

We now have a model of GMC and subsequent star formation with the following properties. Much of the accumulation and dispersion of gas is done during the atomic phase. Once the density of gas is high enough to form molecular hydrogen this matches the density required for local collapse. Magnetic fields do not support the GMCs which are supported only by turbulent motions and finally rapid dispersion or lowering of the density of the surrounding material occurs quickly after star formation.

If one could calculate the age spreads within a given SFR (assumed to be coeval) this would be of the order of the formation time. Studies of apparent age spreads in SFRs such as Hartmann et al. (2001) and Ballesteros-Paredes & Hartmann (2007) argue in favour of RSF. On the other hand, the converse argument is formed using age spreads in SFRs in Burningham et al. (2005a) and Palla et al. (2005) and Jeffries (2007b). However, these apparent age spreads do not necessarily correspond to real age spreads (see Section 6.2.3). Therefore to distinguish between the timescales available for collapse and to provide observational constraints for theoretical models, accurate ages and age spreads for young stars within SFRs are required (see discussion in Sections 3.6 and 6.1.1).

2.4 Evolution of young stellar objects

In the previous section I discussed the timescales for the formation of proto-stars. Here I move on to the timescales involved in subsequent evolution. An important part of this evolution is dominated by the angular momentum of the star and pre-stellar core. In the discussion of the models of star formation presented so far, rotation has been neglected.

2.4.1 Rotation during collapse

GMCs are known to be turbulent and rotating objects (Goodman et al., 1993). As the material contracts to form a pre-stellar core angular momentum must be conserved. Clumps in GMCs are often observed to have a specific angular momentum several orders of magnitude above that found for stars, implying that angular momentum must be lost during collapse, perhaps through interaction with a magnetic field.

A more important consequence of rotation however is the formation of a disc. If one assumes the system is spherically symmetric and exhibits axisymmetric rotation. Then the infall velocities of material above and below the equatorial plane are equal in magnitude and opposite in direction. This results in a shock occuring in the equatorial plane removing momentum from material along the axis normal to this plane. The velocity vector in the equatorial plane remains unchanged, if any heating from the shock is cooled quickly. Further collissions with material in

or entering the equatorial plane can remove velocity components inconsistent with circular motion and an orbiting disc results. The resulting disc transfers momentum away from the star and mass towards it, through viscous interactions. The balance of the lifetime of the disc and the infalling envelope is important as stars can emerge from a pre-natal envelope with or without a dense accretion disc.

Low mass (LM, defined as approximately $M_\star < 2M_\odot$) young stellar objects (YSOs) (a term introduced by Strom, 1972) observed in SFRs within GMCs have been classified by the spectral energy distribution (SED) intro four main classes. These classes are separated on the basis of the presence of an envelope (its density) and a disc. Class I, II and III were first identified by Lada (1987) (and later in Andre & Montmerle, 1994) and are based on the spectral index, a, which is defined as

$$a = \frac{dlogF_\lambda\lambda}{dlog\lambda}, \tag{2.13}$$

Where λ is the wavelength of the radiation and F_λ the flux at this wavelength. A further class, class 0 was defined by Andre et al. (2000). The classes have the following observational properties (Feigelson & Montmerle, 1999).

- **Class 0** These objects have strong, centrally-condensed dust continuum emission at submillimeter wavelengths, very little emission shortward of 10 microns, and powerful jet-like outflows. They have a typical age of $\approx 10^4$ years. .
- **Class I** Here the spectral index of Lada (1987) is $0 < a \leq +3$, meaning an SED with stronger emission at long wavelengths associated with a dusty infalling envelope and show signs of some outflow. They have a typical age of $\approx 10^5$ years.
- **Class II** Following Lada (1987) these sources have $-2 \leq a \leq 0$, indicative of a dusty disc. They have a typical age of $\approx 10^6 - 10^7$ years.
- **Class III** These objects have a spectral index $-3 < a \leq -2$, suggesting these objects have very weak or absent disc structures. They have typical ages from $\approx 10^6 - 10^7$ years upwards.

These classifications led to the postulation of an evolutionary sequence for LM stars moving from class 0-III. However, further examination of their properties suggest a slightly different, more complicated picture.

2.4.2 Pre-main-sequence stars

From Section 2.4.1 I have classifications of several classes of LM YSOs with a tentatively proposed evolutionary sequence. Class 0 and I objects are still deeply embedded in their pre-natal clouds and are observable in the IR and longer wavelengths. However, for class II and class III a central star is visible.

As a star contracts out of the ISM the central density and temperature increases (at a rate dependent on the mass of the object), and the interior of the star can reach the deuterium fusion

limit, entering a quasi-equilibrium state where the energy from this fusion acts to resist the collapse. Further along the contraction the interior density and temperature is sufficient to sustain hydrogen fusion (via $p-p$ chains). At this point the stars is in hydrostatic equilibrium and is defined as being on the zero-age-main sequence (ZAMS). Stars contracting onto the ZAMS are termed pre-main sequence (pre-MS) stars. I will return in more detail to the evolution of stars from pre-MS to ZAMS in Section 3.2.

2.4.2.1 High-mass pre-MS

High-mass stars (HM stars, with approximately $M_\star > 10M_\odot$) evolve very quickly with total lifetimes of order 10^6 yrs and formation times of 10^5 yrs (Garay & Lizano, 1999). These stars (spectral types O and B) are thought to form with massive primordial discs that evolve very quickly on the Kelvin-Helmholz, with $t_{\rm KH} \approx 10^4$yrs (Garay & Lizano, 1999). As these stars form so quickly it is difficult to find them in their early evolutionary pre-MS phase.

Intermediate mass stars (IM stars, with $2M_\odot < M_\star < 10M_\odot$) evolve more swiftly than their LM counterparts but not as fast as the HM stars. IM pre-MS stars in early evolution are called Herbig Be/Ae stars (Herbig, 1960).

2.4.2.2 Low-mass pre-MS

LM pre-MS stars are identified with a class of objects called T Tauri stars (TTS) (First discovered by Joy, 1945, from the spectra of variable stars, the brightest of which is called T Tauri). TTS are characterised by some hydrogen Balmer emission lines probably due to radiation passing through envelope material or from atmospheric activity (this is discussed in detail in Section 3.4.1.3). These objects were classified in terms of their spectroscopic characteristics (see Herbig, 1962, for a review). TTS are very young (from 10^5 to < 10 Myrs old Rydgren et al., 1976; Covino et al., 1997) and are of spectral type K0–M6. They often show strong X-ray and $H\alpha$ emission. These objects are also optically variable, with some showing high levels of veiling (Joy, 1949). Veiling is caused by continuum emission combining with the emission from the central star. Veiling is defined as the ratio of the additional flux at a given wavelength to to that expected from the spectrum of the central star. Finally, these objects can also show IR or NIR excesses.

TTS can be further subdivided based on the characteristics of their spectral emissions.

- **CTTS** Classical TTS correspond to Class II YSOs. They have strong $H\alpha$ emission ($EW >$ 10Å) caused by material accreting on to the central star. IR excess are also found from the re-radiation, by dust grains, of photons emitted by the central stars. NIR excesses can also be present, caused by heating of the inner region of an accretion disc.

- **WTTS**. WTTS correspond to Class I YSOs. These classes of object are chiefly characterised by their weak $H\alpha$ lines ($EW <$ 10Å), with WTTS known as Weak TTS. $H\alpha$ emission in this case is associated with chromospheric activity or photons from the central star interacting with the envelope. WTTS have a reduced IR excess indicative of a smaller or depleted disc and envelope. WTTS show strong X-ray emission from chromospheric surface magnetic activity which is not subsequently weakened by envelope or disc material.

- **PTTS** Post-TTS are the stage of LMS evolution prior to arrival at the ZAMS (between 5 and 10 Myr). They show no features associated with an infalling envelope or accretion disc i.e. no IR excess or UV continuum emission. Like WTTS these objects retain weak $H\alpha$ profiles due to chromospheric surface magnetic activity. These objects are usually separated from WTTS merely by their age or location in a HR diagram. However, a phenomenological difference has been applied by Martin (1997) using spectroscopic information. Martin (1997) identify PTTS stars with spectral types A, F and G for $M_\star > 1M_\odot$, or those stars developing radiative cores on their way towards the MS, and for $M_\star < 1M_\odot$ stars showing significant Li depletion (discussed in Section 3.4.1.6) are classed as PTTS. However, the distinction between WTTS and PTTS is still based primarily on derived ages which as will be shown in this work are unreliable for pre-MS stars.

TTS can have a variety of $H\alpha$ line profiles and have been classified by Reipurth et al. (1996). Type I usually show, symmetric $H\alpha$ emission with little or no absorption. Type II are double peaked (in $H\alpha$ emission) with the secondary peak more than half the primary, or for type III less than half the amplitude of the primary. Types II and III can also be subdivided into classes R and B where the secondary peak is red or blue shifted from the primary, implying the source of the $H\alpha$ emission is moving away or towards the observer respectively. P Cygni or inverse P Cygni profiles are classed as type IV. I return to a more detailed look at the identifying characteristics of pre-MS or TTS stars in Section 3.4.1, but for now I turn to a consideration of their evolutionary states.

2.5 Evolution of the pre-main-sequence

The assumed evolutionary sequence presented in Section 2.4.1 of Class 0-I-II-II shows a star emerging from a pre-natal cloud forming a disc and the disc dissipating with time. For a single star the size of the disc, and the time spent at each stage of the evolutionary sequence, is most likely to be dominated solely by the mass of the star.

It is not clear from any study of an assumed coeval population of stars that the WTTS are definitely older than CTTS. In addition as described in Section 2.2.2 we do not observe many PTTS. However, age derivations for single stars are currently poorly understood (See Chapter 6 for discussion). Therefore, they cannot currently be used to confirm or rule out any evolutionary sequence. It is clear however that almost all of the defining characteristics of the CTTS or WTTS can be assigned to a disc-star (or disc envelope) interaction or lack thereof. The disc-star interaction must be a function of the amount of disc or envelope material at a given age which might be affected by the local environment (see Section 2.6.1 for a further discussion of this). So the early evolution of pre-MS stars can be dominated or at least heavily affected by the presence of a disc.

One important aspect of the evolution of stars at a given mass is that of angular momentum. I have already shown that some of the angular momentum accumulated from the collapse of a rotating GMC is lost, most probably due to torque locking to the ambient magnetic field (see Section 2.4.1). If this process is able to control angular momentum loss in the early collapse it is conceivable that the rotation of a star can be damped further by the same mechanism at later stages

of its evolution.

As the timescale for star formation is much larger than human history we cannot simply observe this process over its entire course in a single example. Instead we must observe snapshots in time using stellar populations. Further detail can be added and differences from region to region due to local environment can only be studied effectively once a basic picture of stellar evolution has been constructed.

As is discussed in Section 2.4 the presence of discs or significant envelope material is observable, as stars with circumstellar material will show IR or NIR excesses (IR excess for envelope material and NIR for inner disc regions). The cause of the excesses is discussed in more detail in Section 3.4.1. For now it is sufficient to state that it is possible to determine whether or not a star has a significant accretion disc. If indeed continuing rotational braking is caused by a disc-star magnetic interaction then rotation rates for young pre-MS stars must also be derived and analysed in conjunction with disc presence indicators.

The determination of rotation rates for pre-MS stars is easily achievable and becoming widely available through photometric variability surveys. As a star rotates its luminosity will vary due to activity on the stellar surface (discussed in more detail in Section 3.4.1). Therefore studies of this luminosity at a given wavelength can yield estimates of the stellar rotation rate and then how it evolves from SFR to SFR or more importantly with age. Rotation rates can also be derived from the broadening of spectral lines due to the differential motion over the stellar surface away from or towards the observer. Disc signatures and rotation rates are two variables which can be studied to allow an estimation of stellar evolutionary timescales. Then once enough detail is established, the effects of local environment on stellar evolution can be investigated.

Circumstellar discs and the study of their evolution is extremely important for another reason. It is this material which will go to form planets around stars. Therefore an understanding of their survival timescales is vitally important to apply constraints to models of planet formation. Inferences on disc survival timescales have recently been made. These have been derived both directly through the comparison with age of the disc fractions in several SFRs (discussed in Section 2.6) and through a possible rotational star disc interaction (discussed in Section 2.5.1.2). In the following sections I discuss how stellar rotation may vary with age, before moving on to the possible link to circumstellar discs.

2.5.1 Angular momentum evolution

As pre-MS stars evolve they contract (see discussion in Section 3.2) and collect angular momentum from the accreting material. Some angular momentum can be lost due to jets and outflows, as seen in the ONC (Bacciotti et al., 2002; Woitas et al., 2005), with these jets being observed to rotate. However such jets only appear for very young objects. So one would expect stars to spin up as they age towards the ZAMS. In fact molecular cloud cores rotate at 5-6 orders of magnitude above solar-type stars on the ZAMS (Bodenheimer, 1995), and during the first ≈ 1 Gyr of life stars appear to lose another 1–2 orders of magnitude in specific angular momentum. Many mechanisms can possibly remove this angular momentum; these possibilities are discussed in Bodenheimer (1995).

As rotation rates can be measured through photometric variability studies they are known with great precision (Barnes, 2003, 1 part in 10,000). However, differential rotation as a function of latitude, as is found in the Sun, is not accounted for and selecting the correct period is an important and difficult area in itself (particularly the problem of removing or avoiding the diurnal period due to the Earths' rotation). In spite of these hindrances the precision with which this measurement can be made has the potential to apply tight constraints to models of stellar physics.

Rotational period distributions are now available for several SFRs from photometric monitoring (e.g Rebull, 2001; Lamm et al., 2004, 2005; Littlefair et al., 2005; Cohen et al., 2004), and the number of studies is set to increase with projects like MONITOR (Aigrain et al., 2007) and VYSOS (Reipurth et al., 2004). Several comparisons of rotational period distributions have been made across SFRs of different ages.

Two simple pictures of rotational evolution have been developed adopting differing assumptions about the mechanisms and timescales of angular momentum transport, both in the stellar interior, and in the removal of angular momentum from the stellar surface. The transport of angular momentum within the stellar interior is not well understood even in the Sun, therefore the assumptions made in any model about this aspect of the rotational evolution are somewhat arbitrary. Thus, for the subsequent discussion of angular momentum evolution I highlight two competing models adopting different models of angular momentum transport in the stellar interior and the role of the star-disc interaction. Whilst, both these models can be shown to agree well with observations, the observations can not yet decide between them.

2.5.1.1 Main-sequence stars

The first model is that of Bouvier et al. (1997), here the stellar interior is modeled as a solid-body rotator, implying efficient angular momentum transport throughout the star. Adopting this assumption essentially sets several parameters which are left free in competing models therefore apparently simplifies the problem greatly. This model relies on three main assumptions (for example core-envelope decoupling). i) The star rotates as a nearly solid-body, ii) During the pre-MS a star can be locked to its accretion disc, removing angular momentum from the star and iii) Magnetised winds can also remove angular momentum from the star. To chart the subsequent evolution requires an initial distribution of disc lifetimes (all stars are assumed to start with accretion discs) and rotation rates (taken from a sample of CTTS stars, which Bouvier et al., 1997, assume retain their initial distribution of rotation rates due to being locked to a disc), and an angular velocity of saturation, where the angular momentum loss mechanism is saturated (dependent on the stellar mass). The study of Bouvier et al. (1997) uses rotational data from IC2391 (Stauffer et al., 1989), IC2602 (Stauffer et al., 1997), α Per (Prosser, 1992, 1994; Stauffer et al., 1989, 1993), the Pleiades (Jones et al., 1996; Soderblom & Mayor, 1993; Stauffer & Hartmann, 1987; Stauffer et al., 1984), M7 (Prosser et al., 1995), M34 (Jones et al., 1996), the Hyades (Radick et al., 1987; Stauffer et al., 1997) and an old field star sample (Wichmann et al., 1997; Covino et al., 1997).

Another simple interpretation, Barnes (2003), is based on the evolution of rotation periods of solar- and late-type stars. Barnes (2003) builds on the work of Stauffer et al. (1984) developed further by Soderblom et al. (1993). These works propose that the core-envelope decoupling, which

is a natural consequence of the rotating stellar models of Endal & Sofia (1981), is related to the rotation rate of the star. This decoupling is a consequence of the fast and slow angular momentum transfers in convective and radiative stellar zones respectively. However for older or more massive stars where a radiative core has formed once the core and envelope have decoupled, re-coupling cannot occur if the process is purely hydrodynamic. Barnes (2003) proposes that the coupling and decoupling processes are actually hydromagnetic, where the zones can re-couple. This theory of 'gyrochronology' is based on studies of IC2391 (Patten & Simon, 1996), IC2602 (Barnes et al., 1999), IC4665 (Allain et al., 1996), α Per (Prosser et al., 1993), Pleiades (van Leeuwen et al., 1987; Krishnamurthi et al., 1998), Hyades (Radick et al., 1987), Coma (Radick et al., 1990), and new observations of M34 and NGC3532 (Barnes, 1998).

Angular momentum loss rates through 'Skumanich' style magnetised winds are well understood (Kawaler, 1988) and are a function of rotation rate and stellar mass (Collier Cameron & Jianke, 1994). Barnes (2003) notes that stellar winds can only remove angular momentum if deep convection zones are present (Schatzman, 1962) and this rate saturates if rotation becomes too fast (MacGregor & Brenner, 1991). Whereas the apparent saturation of angular momentum loss in the models of Bouvier et al. (1997) are ascribed to a possible saturation of the dynamo mechanisms, or a change in the magnetic field topology as suggested by Giampapa et al. (1996). Here, the angular velocity of saturated angular momentum loss is set for different mass ranges.

Therefore, in the models of Barnes (2003), the angular momentum loss from winds relies on the presence and or depth of convective zones. Barnes (2003) splits the stars into three main categories based on the assumption of angular momentum loss through winds. The older field stars in this sample were observed to lie on loci very well described by the surface-field-driven spin down of $\omega \propto t^{-1/2}$, where ω is the angular velocity (Skumanich, 1972). These stars are associated with the 'I' or 'interface' sequence. These show a slow spin down over a timescale of ≈ 1 Gyr. A radiative sequence is identified with very HM stars which do not have convective zones and cannot lose momentum through magnetically driven winds. Finally, a convective sequence is identified with the ultra-fast rotators (UFRs) of younger stars. The interface sequence appears to lose angular momentum at a faster rate with a separation between the interface and convective sequences a possible inverse function of age. The convective sequence of Barnes (2003) has a saturated angular momentum loss rate (Barnes & Sofia, 1996) which cannot remove angular momentum at the rate of the I sequence. The angular momentum removal in this case depends on outer convective zones, as the core is decoupled from the outer convective envelope. The resulting 'isochrones' produced to chart the rotational evolution fit the studied data well.

In the models of Bouvier et al. (1997) where the star is modeled as a solid-body the observations of the rotation rates of older or MS stars can be reproduced reasonably well for $1M_{\odot}$ stars. This is achieved by setting the angular velocity of angular momentum loss saturation optimally for each chosen mass range and adjusting the overall distribution of disc lifetimes. For a $0.8M_{\odot}$ star, the models cannot reproduce the tail of very slow rotators seen in the Pleiades. Bouvier et al. (1997) note this could be caused by the slow re-acceleration of the convective core by the radiative core as is possible in the core-envelope decoupling and re-coupling hydromagnetic models. However, as discussed in Bouvier et al. (1997), if the core and envelope do indeed go

through a decoupling and re-coupling process, then for slower rotators, where the core is rotating rapidly beneath a slower envelope, any dynamo mechanism acting across the boundary layer will be enhanced. This increased magnetic activity should correspond to an increase in X-ray emission, leading to a population of X-ray active slowly rotating stars, which is not observed.

2.5.1.2 Pre-MS stars and disc locking

The theories of Barnes (2003) or Bouvier et al. (1997) fit the observations well for the older or MS stars, with both matching observations reasonable after the adjustment of their respective parameters. Indeed, the difference between their treatments of the stellar interior are somewhat negligible, given that rotation rates of only the stellar surface can be observed, and both treatments give similar results for a fiducial rotation rate of a solar-type star (Bouvier et al., 1997). However, for pre-MS stars a major difference between these two approaches is the role of the star-disc interaction.

The model for angular momentum loss in the pre-MS phase of stellar evolution has been under recent debate (Mathieu, 2004; Herbst et al., 2007; Lamm et al., 2005). Barnes (2003) simply extends the sequences established for older stars to the pre-MS phase, arguing against any requirement for interaction of the star and the disc, citing the lack of evidence for a correlation of slow rotators with disc presence from Stassun et al. (1999) and Rebull (2001). However these studies appear not to be a useful constraint on the extent of star-disc interaction due to a highly non-coeval sample and the use of different mass ranges. The simulations of Bouvier et al. (1997) on the other hand implicitly assume a star-disc interaction, with a characteristic lifetime which can be adjusted in their models. In fact the extra flexibility in this parameter weighed against the more simplistic modeling of the stellar interior, compared to Barnes (2003), probably leads to the reasonable agreement of both these models to the observations of MS stars. In addition, several uncertainties in the data make comparisons to these theoretical simulations unreliable, for instance, the effects of binarity and the adoption of unreliable pre-MS or contraction ages (see Sections 3.6.2.2 and Chapter 5) for most of the clusters.

Further work by Herbst & Mundt (2005) and Herbst et al. (2007) develop the possibility of star-disc interaction consequences from an empirical standpoint. With more recent studies showing strong evidence for stellar rotation and a disc presence connection (Herbst et al., 2002; Lamm et al., 2005; Dahm & Simon, 2005). In particular the recent compelling evidence of a correlation between slowly rotating stars and disc presence in Cieza & Baliber (2007).

2.5.1.2.1 pre-MS stars Herbst & Mundt (2005) use studies of the ONC, NGC2264, Pleiades, IC2602 and α Per, for the mass range $0.4M_{\odot} < M_{\star} < 1.2M_{\odot}$. The initial distributions of the rotation periods of these clusters are assumed to be identical (which at this is point unavoidable, c.f. Section 2.6.1). It is useful to note that rotation rates of individual stars do not appear to change strongly with observational time (see the 5 year study of Cohen et al., 2004) (and the good statistical correlation of rotation rates from multiple studies of one SFR, Lamm et al., 2005). Herbst & Mundt (2005) state that as pre-MS stars are fully convective they are likely to rotate as solid bodies and there is therefore no envelope-core decoupling. The evolution of specific angular momentum

is compared, derived simply from rotation periods, radius and mass (the two latter depending crucially on age, see Section 3.2 for more discussion). This reveals a bi-modal distribution for the younger SFRs (NGC2264 and the ONC), developing over time into an approximately unimodal distribution for the older clusters. This evolution of rotational period distribution and specific angular momentum is shown to evolve most swiftly at young ages. This is shown using the proportion of stars in the slow and fast rotating groups for the ONC and NGC2264. Herbst & Mundt (2005) argues that any 'Skumanich' type wind-driven angular momentum loss would not be a decreasing function of age. This description of the data yield two groups of stars, the rapid and slow rotators. The rapid rotators merely continue to contract to the MS and lose angular momentum via winds at a constant rate to become the UFRs at ZAMS. The slow rotators however must lose more angular momentum during the first few Myrs of the pre-MS phase. Using the relations of radius to age in the Hayashi plane (see Section 3.2) an estimate for the timescale of this interaction is 5–6 Myrs. This timescale is similar to the disc dissipation timescale found by Haisch et al. (2001).

A magnetised braking of a star through interaction with a disc or disc locking was first put forward to explain the slow rotation of some CTTS (Edwards et al., 1993; Camenzind, 1990; Koenigl, 1991). Although, this idea lacks a first principles theoretical model. Herbst & Mundt (2005) proposes that the slow rotators are locked magnetically to an accretion disc. The lack of bi-modal distribution in Rebull (2001) and Stassun et al. (1999) is observed to be due to a highly non-coeval sample and a limited mass range. Support is initially found for a disc locking model in Herbst et al. (2002), Lamm et al. (2005) and Dahm & Simon (2005), where disc indicators have been correlated with slow rotation rates. However, Lamm et al. (2005) found no intra-cluster age effects, but ages derived for single stars could be unreliable (see discussion in Section 6.2.3). A further problem can be found with the rotational distribution for IC348 found in Littlefair et al. (2005). Here, IC348 is assumed to be at a similar age to NGC2264 but exhibits a bi-modal distribution in rotation rates similar to that found in the ONC. The comparison of Littlefair et al. (2005) between IC348, the ONC and NGC2264 does not show a clear evolutionary sequence with age. One explanation for this is that the ages of these clusters are incorrect, this is discussed further in Chapter 6.

2.5.1.2.2 Very LM stars For stars of $M_\star < 0.4 M_\odot$, or very low-mass stars (VLMS) a similar empirical treatment and discussion of the data yields slightly different results. It must be said however that the assignation of masses for pre-MS stars is not a completely robust science (see Chapter 5). Notwithstanding difficulties in mass derivation, period distributions of VLM stars appear to have fewer slowly rotating or disc-locked stars than seen in the distributions of solar-type stars. A model of angular momentum evolution in this mass regime is described in Terndrup et al. (1999) and Sills et al. (2000), between the ages of 30-700 Myrs. For these ages stellar winds appear to remove angular momentum as an exponential function of time, not following a 'Skumanich' law ($\omega \propto t^{-1/2}$) as found in solar mass stars. Scholz & Eislöffel (2004) show that evolution of VLM angular momentum from the young cluster σ Ori to the Pleiades cannot follow simple angular momentum conservation during the pre-MS contraction. This is because many of the rapid rotators would spin up when ageing from σ Orionis (assumed to be ≈ 3 Myrs), resulting

in rotation speeds much faster than the break up velocity (the point at which the star's surface is rotating at the gravitational escape velocity and so the material is no longer bound and is flung out from the star). Therefore, as for solar mass stars, in the VLM case some kind of magnetic breaking during the pre-MS contraction phase is still required. For the faster rotating VLMS this extra angular momentum breaking ($\omega \propto e^t$) could be due to a differing magnetic field structure (Barnes, 2003; Scholz & Eislöffel, 2004). These objects are unlikely to ever develop a radiative core and remain fully convective. This means magnetic fields cannot be generated in an interface or tachocline layer as is the case for the Sun. Instead field generation based on turbulent or α^2 dynamos have been suggested (Durney et al., 1993; Chabrier & Küker, 2006). Thus it is clear that some additional braking mechanism is required (as for solar mass stars) in the early stages of pre-MS contraction (Herbst et al., 2007, $\approx$ 1–3 Myrs). Lamm et al. (2005) suggest an imperfect disc-disc locking regime, where the interaction is similar to the more massive stars but less angular momentum is lost into the disc. This suggests that the efficiency of angular momentum via disc-locking is a function of mass.

2.5.1.3 Recent evidence for disc locking

So it is apparent that a possible mechanism for removing large amounts of angular momentum from rapidly contracting pre-MS stars could be a magnetically driven star-disc interaction, disc-locking. Shu et al. (1994) provide a detailed treatment of this, with Long et al. (2005) providing the most recent such study. However there remains no first principle model for this mechanism, due in no small part to the general difficulty in incorporating magneto-hydrodynamic (MHD) phenomena in simulations or theories. Alternatives to disc-locking have been suggested, primarily magnetically driven winds emanating directly from the stellar surface (Matt & Pudritz, 2005b,a). One advantage these models may have is that within a theory of disc-locking Class I and II objects should both exhibit similar star-disc interaction levels and consequently rotate at similar rates. Covey et al. (2005) find this not to be the case finding that Class I objects rotate faster than Class II Covey et al. (2005) (one possibility is that the locking has not yet been established with an accretion disc). In addition, the broad and deep P Cygni profiles of some CTTS (Mundt, 1984) are indicative of highly blue-shifted line which could only emanate from close to the stellar surface.

Despite its problems disc-locking is beginning to become an accepted mechanism. It is apparent that young pre-MS stars require some angular momentum braking and recent studies are beginning to show increasing evidence for a correlation between rotation rate and disc presence. A recent example is the study of Cieza & Baliber (2007), who consider disc indicators from the *Spitzer* space telescope along with literature rotation periods. Once any mass effects and observational biases are removed they find a clear increase of disc fraction with rotation period.

If disc-locking is an accepted mechanism, an important feature of this model is its possible timescale. As suggested in Herbst & Mundt (2005) and Herbst et al. (2007) disc locking only appears to remove significant angular momentum during the first 5–6 Myrs of a pre-MS stars evolution. This was confirmed recently by Scholz et al. (2007), where significant angular momentum loss was found to stop after $\approx$ 5 Myrs. If this timescale is indicative of disc presence this should mean that disc survival lifetimes are of a similar order. This consequence is discussed in the next

Section.

Given that age estimations for stellar populations are so uncertain (see Chapter 5), the empirical method employed by Herbst & Mundt (2005) and Herbst et al. (2007) of comparing datasets at different ages is our best tool for deriving timescales of disc dissipation.

2.6 Disc dissipation

Discs have important effects on the rotational evolution of the parent star and of course are a pre-requisite for planet building. The key question of their evolution is, how do we get from a pre-MS star with an accretion disc to a solar system with orbiting planets or a lone star? Since the observation of 'proplyds', stellar discs apparently being eroded by stellar winds from massive stars in the ONC (McCaughrean & O'Dell, 1996) it has been accepted that circumstellar discs can be eroded by massive neighbours (Adams et al., 2004) and their parent star (Hollenbach & Gorti, 2005). This is caused by UV flux (and X-rays), which is particularly strong from massive stars, photodisociating material in the disc and creating disc winds (Richling et al., 2006; Hollenbach & Adams, 2004)

Haisch et al. (2001) use an L-band survey and JHKL colours within a colour-magnitude diagram (CMD see Section 3.6) to identify stars with discs. Stars with significant circumstellar disc material have indicative excesses in the IR and sometimes NIR (see Sections 2.4 and 3.4.1). Using literature ages for several SFRs the regions are then compared (with the assumption that the initial disc frequency and dissipation timescales are identical) to derive a disc dissipation timescale. Haisch et al. (2001) find an estimated disc half-life of ≈ 6 Myrs. This figure appears to accord with the timescale expected from the studies of Herbst & Mundt (2005) for disc-locking (see Section 2.5.1.2). Some age estimates in this work however are based on often unreliable pre-MS isochrone fitting (see Sections 3.6.2.2 and Chapter 5). With more precise relative age orders finer detail could be extracted from these data. Particularly the effects of the differences between the local environments for these SFRs.

Recent studies have attempted to derive disc dissipation timescales for single SFRs (Hernández et al., 2006, see for example) using disc indicators and individual ages of stars. Ages derived for single pre-MS stars are highly model dependent (*see* Sctions 3.6.2.2 and Chapter 5). In addition the accuracy of these ages is not clear as they provide age spreads within SFRs of around ≈ 10 Myrs (Palla & Stahler, 1999; Palla et al., 2005, 2007) which is inconsistent with rapid-star formation. This means that these ages can only be valid if we accept SSF over RSF and furthermore are imprecise. Therefore, at this moment one must look sceptically at studies which quote absolute ages for a statistically small populations or individual stars (see Section 6.2.3).

2.6.1 Local environment effects

If discs can be eroded by nearby massive neighbours (McCaughrean & O'Dell, 1996; Adams et al., 2004; Richling et al., 2006) then the density of flux from these neighbours, or equivalently their number density must have an effect on the dispersal timescale of circumstellar accretion discs. With areas containing more (or more densely packed) HM stars and therefore higher UV flux

levels, discs erode much faster than other more quiescent regions. Recent evidence from single cluster disc fraction surveys has in some case suggested that the effects of massive neighbours on disc lifetime, is relatively insignificant (Balog et al., 2007; Hernández et al., 2007). However, this has not be established for a large range of SFRs. In some cases the effect of massive neighbours has been found to be significant (Stolte et al., 2004).

2.7 Summary

It is apparent that current models of star formation and evolution hinge critically on timescales. Broadly speaking two star formation models exist, they conflict on the formation timescale. RSF predicting $t_{\rm form} < 3$ Myrs and for SSF, $t_{form} \approx 5-10$ Myrs. Age spreads within assumed coeval populations (particularly in pre-MS stars) are often used to support both of these models. In the case of subsequent evolution, rotational period distributions in conjunction with ages for several stellar populations have been used to derive an evolutionary sequence involving star-disc interactions. In this sequence it is clear that the age ordering does not support the simple suggested model. In particular the rotational distributions of the ONC, IC348 and NGC2264 do not appear to evolve in the assumed age order. Whether this is evidence of more complicated evolution or wholly due to inaccuracies in age estimates is unclear. As absolute age derivations for pre-MS populations are currently uncertain to a factor two more precise age ordering is perhaps more useful. With more precise age sequencing empirical studies could provide more robust constraints for evolutionary models and perhaps provide evidence of local environment effects. Only after subsequent calibration could ages be used to derive timescales for stellar evolution such as disc survival times.

Comparing observations with observations could yield very precise relative age orders as one is free from many of the assumptions made when comparing data with theory. Populations of pre-MS stars can be compared to find relative age orders. We need to first find several coeval populations of pre-MS stars for a range of SFRs with different median ages and then employ some theory to compare these observations in an equal plane. Age orders can be then be derived.

Chapter 3

Theory to observation

To extract ages for pre-MS stars we must first identify where populations of coeval pre-MS stars can be found. Then we must be able to select the pre-MS stars from a given sample and subsequently fit the sample using theory to derive ages.

3.1 Where do stars form?

Stars form in relatively dense areas of the ISM (see Chapter 2). As HM stars evolve very quickly (lifetimes of ≈ 10 Myrs), areas containing high-mass stars must necessarily be young. So-called OB associations contain huge populations of pre-MS stars with HM stars tending to form in clusters with many LM counterparts (Tan, 2007), most stars are born in OB associations. There is evidence to suggest our Sun was born an OB association (Harper, 1996, see the discussion in). Blaauw (1991) defined OB associations as sparse collections of young early-type stars (spectral type O-B6) whose characteristics imply a common origin. Sites of low mass star formation without massive stars are called T associations. As these associations are sparse they are not gravitationally bound and so will disperse with age. This thesis concentrates on studies of OB associations and their subdivisions. A list of OB associations within 1.5 kpc of the sun was compiled in Ruprecht (1966), with de Zeeuw et al. (1999) providing a list of distances from *HIPPARCOS* data (for associations less than 1 kpc distant from the Sun). For an excellent and more detailed discussion on OB associations see Pozzo (2001).

Within these structures stars can be found in clusters, groups and sub-groups. Within these structures, to first order (notwithstanding formation time), the constituent stars can be assumed coeval. These large populations of coeval stars can then be used to explore various age-dependent parameters. As these areas are often sites of recent star formation they contain Class I, II and III sources. These sites of recent star formation are found along what is inferred to be the spiral arms of our Galaxy, as indeed they appear to be in other galaxies (Cepa & Beckman, 1990). This is probably due to gravitationally driven pressure waves moving through the ISM creating shocks (see discussion in Section 2.2.2).

Wide-field photometric surveys are an excellent tool to study these large regions. However, data must be compared to theoretical models and samples of stars which are associated with a given coeval group identified, i.e. not containing foreground or background stars at very different

ages.

3.2 The HR diagram

Once populations of MS and pre-MS stars can be located a way to derive their characteristics, such as age and distance, is required. To this day the main weapon in an astrophysicists arsenal for comparison of observations to theory remains the Hertzsprung-Russell diagram (HR diagram). Developed from the (independent) work of Enjar Hertzsprung and Henry Russell this plots a stars luminosity against an effective or surface temperature. The effective temperature $T_{\rm eff}$ is defined by the relationship

$$L = 4\pi R_{\star}^2 \sigma T_{\rm eff}^4, \tag{3.1}$$

where L is the total or bolometric luminosity, $R_{\star}$ is the radius of the star and σ is the Stefan-Boltzmann constant.

Stellar evolution on a HR diagram can be determined from the basic principles of star formation and evolution. From observations of spectral type sequences within the HR diagram it was found that differences in spectral types of stars corresponded to differences in colour and therefore surface temperature. This is because the radiation from a star is approximately a black-body emission governed by *Planck's law* for radiation from a black body. *Planck's law* shows that with a change in effective temperature the peak intensity wavelength of black body emission will also shift. This shift in the peak intensity wavelength will then cause a shift in colour. In addition, from Equation 3.1, as a star's radius reduces so does its bolometric luminosity. Using these general rules and theoretical models of the stellar interior it is possible to determine expected luminosities and colours for a range of ages.

Constructing evolutionary sequences from data of spectral types had been attempted before the HR diagram (see for example Monck, 1892). Further work on luminosities and spectral types using new parallaxes was done by Russell (1910) with the first diagram of the peak intensity wavelength against absolute luminosity (or brightness) being published by Hertzsprung (1911). Previous theoretical models where stars were born as distended gaseous nebulae which gradually contract, dimming in the process, could now be compared to data. In Eddington (1924) a relationship between derived masses and absolute luminosity modelling the star as a perfect gas where found to agree well with observations. However, these theoretical considerations could not be formalised into a quantitative theory of stellar evolution until their compositions were known. Stars were found to be composed predominantely of hydrogen by Payne (1925) and later Russell (1929). This allowed Strömgren (1932, 1933) to relate the positions on a HR diagram quantitatively with time and in particular showed that stars appeared to 'sink' with age. From this work Strömgren developed what were perhaps the first **isochrones** or lines of equal age in an HR diagram.

The idea that a star evolves in a HR diagram with time with variations in effective temperature (colour) and luminosity (or brightness) governed also by the mass of the star became generally accepted. So too, was the idea that stars created energy not just from gravitational collapse but also a process which changed their composition (or hydrogen and helium abundances). With fur-

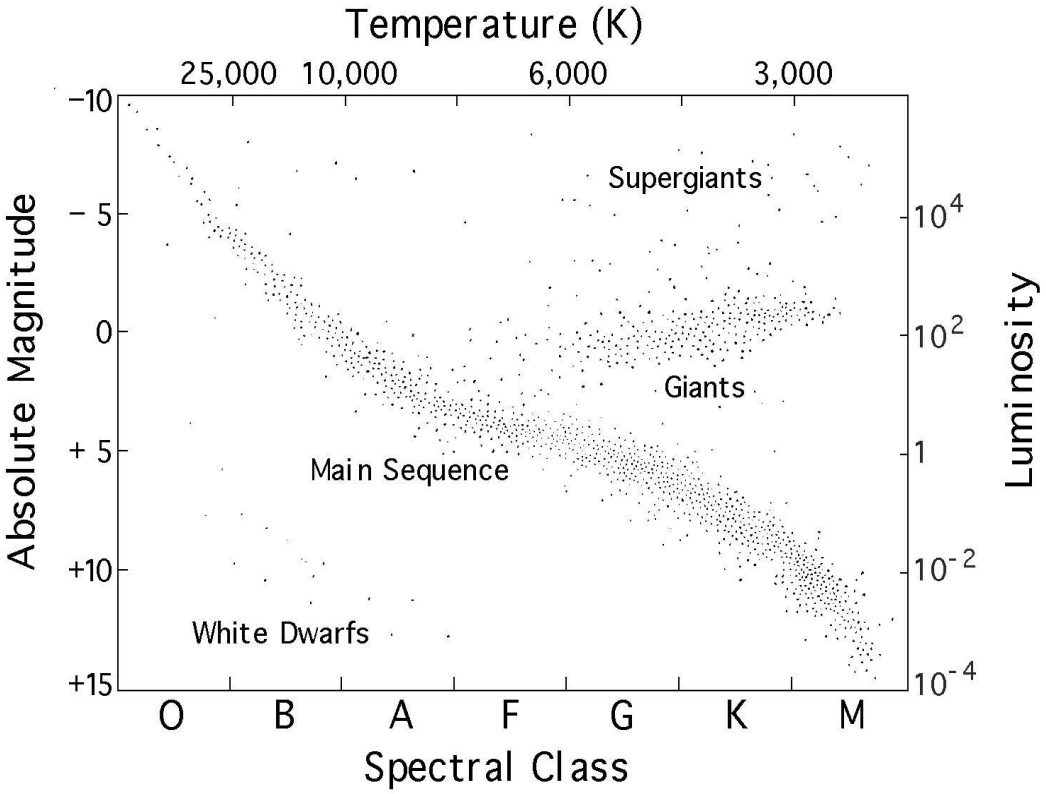

Figure 3.1: Figure of HR diagram showing the MS and post-MS phases. From URL: http://www.math.lsa.umich.edu/mmss/coursesONLINE/Astro/Ex1.2/HR.htm14.gif. The pre-MS stars will appear above and to the right of the main sequence.

ther comparison of data to an empirical version of the HR diagram, (the CMD see Section 3.6) constraints could begin to be applied to theories of evolution within the HR diagram.

Modern formulations of isochrones are based on sophisticated numerical simulations (D'Antona & Mazzitelli, 1997; Siess et al., 2000; Baraffe et al., 2001b; Girardi et al., 2002; Lejeune & Schaerer, 2001, e.g) (discussed in more detail in Section 4.4). Figure 3.2 shows a modern HR diagram with the isochrones of Baraffe et al. (2001b). Figure 3.2 and some simple physics allow us to separate the stars found in each section of the HR diagram into different classes. These classes of object are distinguishable in mass and age and are shown in the schematic Figure 3.1.

- **Pre-main-sequence (pre-MS)** stars, these objects are the fully convective, gravitationally collapsing stars (Hayashi et al., 1962; Hayashi, 1966). As these objects are fully convective their $T_{\rm eff}$ is assumed to be constant as they contract. This is due to convection being the most efficient way of transporting radiation throughout the stellar interior. From equation 3.1 it is clear that the luminosity of these objects will decrease as they contract. This contraction will be governed by the Kelvin-Helmholz or dynamical timescale (Hayashi, 1966), the relation of this contraction to mass was found through the work of Chandrasekhar (1967). This is called the mass-radius relation, and in conjunction with the expected timescales, enabled the modelling of luminosities, effective temperatures and ages for these objects. Within a HR

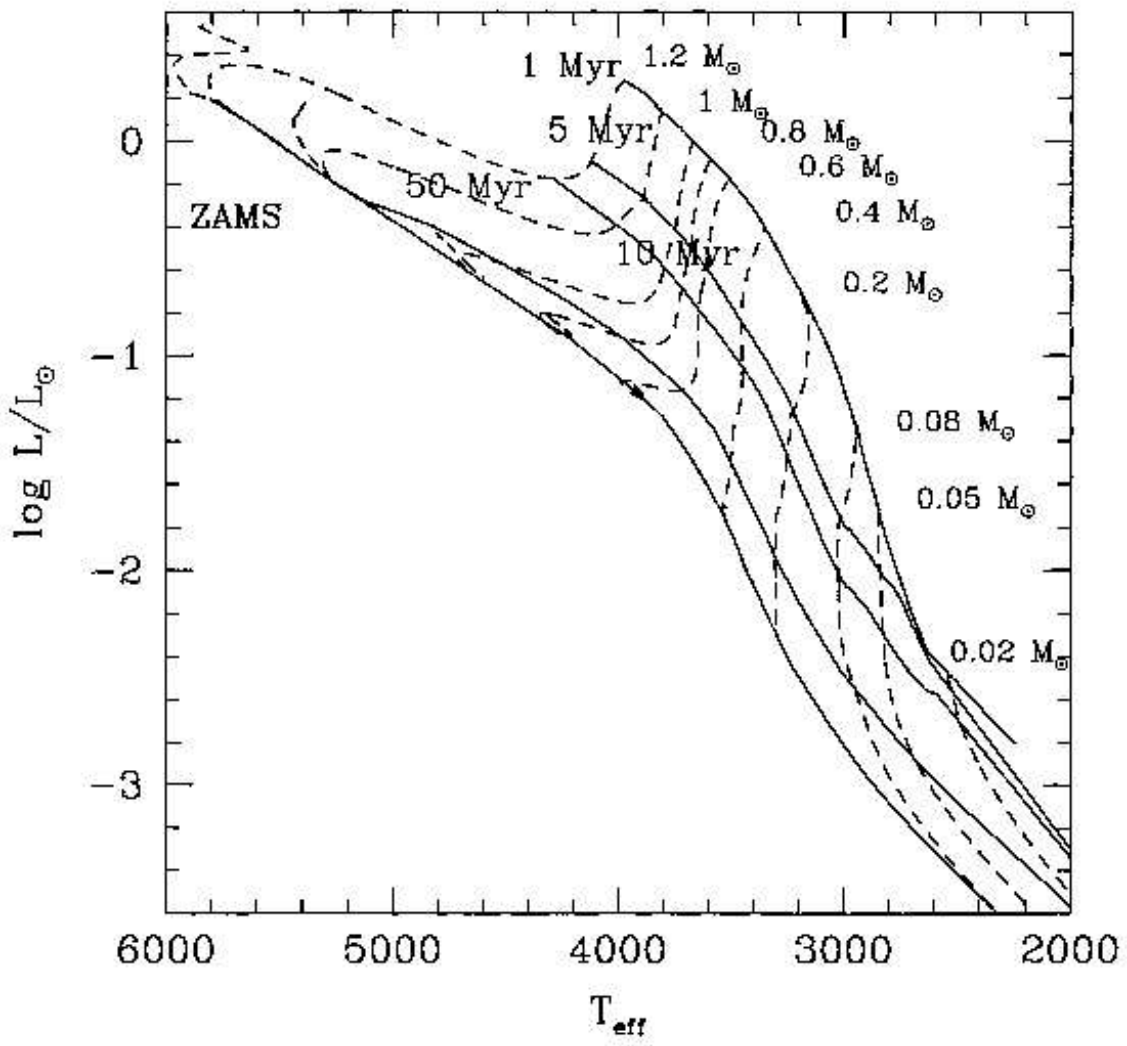

Figure 3.2: Figure of HR diagram of the pre-MS models of Baraffe et al. (2001a). For masses $0.2 - 1.2 M_{\odot}$. Isochrones are the solid lines showing ages of 1, 5, 10 and 50 Myrs. A ZAMS down to $M = 0.075 M_{\odot}$ is also shown as the lowest solid line. The dashed lines are the evolutionary tracks.

diagram (as seen in Figure 3.2) fully convective stars will move approximately vertically downwards on so-called Hayashi tracks in convective equilibrium.

As the stellar interior becomes more dense and therefore optically thick, which happens more swiftly with increasing mass (Hartmann, 2001, as $t_{\rm KH} \propto M_\star^2$), eventually convective cells within the star are no longer buoyant and cannot transport energy away from the star efficiently. An increase in opacity of the core forces energy to be radiated from the stellar core towards the surface. Radiating through the stellar interior involves many absorption and emission events and the energy cannot escape the star as efficiently. For more massive stars (Henyey et al., 1955, $M_\star > 0.5 M_\odot$) this radiative core can be formed before the necessary environmental conditions are met for hydrogen fusion in the core. Here the energy cannot be liberated as efficiently and therefore the temperature increases, the increase in temperature provides a stabilising outward pressure slowing the radial contraction. This slowing in the contraction, combined with the sharp increase in temperature, result in an approximately constant luminosity which only rises slowly compared to the temperature. This means the stars motion is rapid in the effective temperature axis and slow in the luminosity axis within the HR diagram. Henyey et al. (1955) calculated timescales for stars in this stage of radiative equilibrium so-called Henyey tracks (This separation of Hayashi and Henyey tracks could be a crucial tool with which to analyse stellar populations see Chapter 6).

In either case the stellar interiors increase in density and temperature with age. Until nuclear fusion stars.

- **Zero-age-main-sequence (ZAMS)** and **main-sequence (MS)** stars. Once the stellar interior temperature and density is sufficient a star begins fusion of, first Deuterium (Grossman et al., 1974), then hydrogen into helium. Once the point of initiation of hydrogen fusion is reached the thermonuclear energy halts any collapse and the star enters a phase of hydrostatic equilibrium. Once stars enter this equilibrium state they are defined as being on the ZAMS, MS evolution then proceeds through nuclear reactions in the core and hydrostatic balance between the core and outer envelope. The time spent in this phase is a function of mass, however for most LM stars it is a reasonably long-lived and static phase in the HR diagram (see Chapter 4). As the timescales for pre-MS evolution are dependent on mass, as a given SFR ages the mass at which ZAMS is reached will reduce. Therefore a point can be defined where a stellar sequence moves from MS to pre-MS, this is called the turn-on.

- **Post-MS** stars. At the end of their MS lifetime high-mass (HM) stars will exhaust their supplies of hydrogen relatively rapidly, moving on to a less efficient thermonuclear process called the CNO cycle. Depending on the mass of the star it will then evolve into a red-giant a super-giant star. For these stars their radii (and therefore luminosities) are much larger than their MS counterparts but their $T_{\rm eff}$ is lower. As a given SFR ages lower masses will exhaust their core hydrogen and move away from the MS. This age dependent point in the HR diagram is called the turn-off. Subsequent evolution into white dwarfs, supernovae, neutron stars and black holes is beyond the scope of this thesis.

Therefore observations of stellar populations converted into the theoretical plane of the HR

diagram can yield ages derived from turn-offs, turn-ons or essentially the vertical position of pre-MS stars. However, absolute luminosities and effective temperatures cannot be observed directly. This requires data to be shifted to the theoretical plane using physical assumptions. For instance, corrections to luminosity for distance, calculating bolometric luminosities from observations in a specific waveband and calibrating colours to effective temperatures (see further discussion in Sections 4.4). Practically however, it is more desirable to retain the integrity of observed data and adjust the theoretical model to the natural plane of the data.

3.3 The colour-magnitude diagram

The observational equivalent of the HR diagram which was indeed instrumental in its development is the CMD, which plots stellar colours against magnitudes. Practical detectors used in telescopes from older photo-multiplier tubes to modern charge-couple devices (CCDs) can only detect photons within a specific wavelength range (photometry). Filters with known responses can be used to isolate specific areas of the electromagnetic spectrum. Using known filter responses several photometric systems can be defined (for a review of these systems see Bessell, 2005). Photometry over broad bands most commonly uses the photometric system of Johnson (1966) and Glass (1973) (the latter for revision of the JHKL bands), called the *Johson-Cousins-Glass* photometric system. This system defines the passbands of UBVRIJHKLMN. In this work I use the pass bands of *2MASS JHK* (Kleinmann et al., 1994). The modern filter responses used in this work are shown in Figure 3.3, taken from Bessell (2005). The logarithmic scale of brightness or magnitude in this system are calculated by calibrating instrumental magnitudes from the observed fluxes to a standard. Instrumental magnitude is derived from $I = -2.5 log f_\lambda$ where I is instrumental magnitude and f_λ is the integrated flux over the filter response. The Johnson (1966) system can then be calibrated using the Sun or the star Vega. Most often the star Vega is defined as having a magnitude and colours of zero to calibrate a photometric system. Theoretical corrections and calibrations can then be applied to derive luminosities. Bolometric corrections are factors to correct the flux or magnitude in a given band to the bolometric flux or magnitude. Of course these magnitudes will be affected by distance and are therefore called apparent magnitudes. Subtraction of magnitudes result in a measure of the relative flux in each band. Calibrating colours into $T_{\rm eff}$ then requires a conversion applied for the specific colour. Apparent colours can be shifted by interstellar reddening as absorption and emission by the ISM reddens the flux. Therefore to convert fully to an absolute theoretical plane one must account for distances and extinctions caused by intervening material, a process discussed in more detail in Section 3.6.1. For now we assume we can derive absolute colours and magnitudes and convert them into luminosities and $T_{\rm eff}$ values. The reverse operation is also possible i.e. to convert theoretical bolometric luminosities and effective temperatures to expected colours and magnitudes in given bands. This allows the derivation of ages directly from observational data.

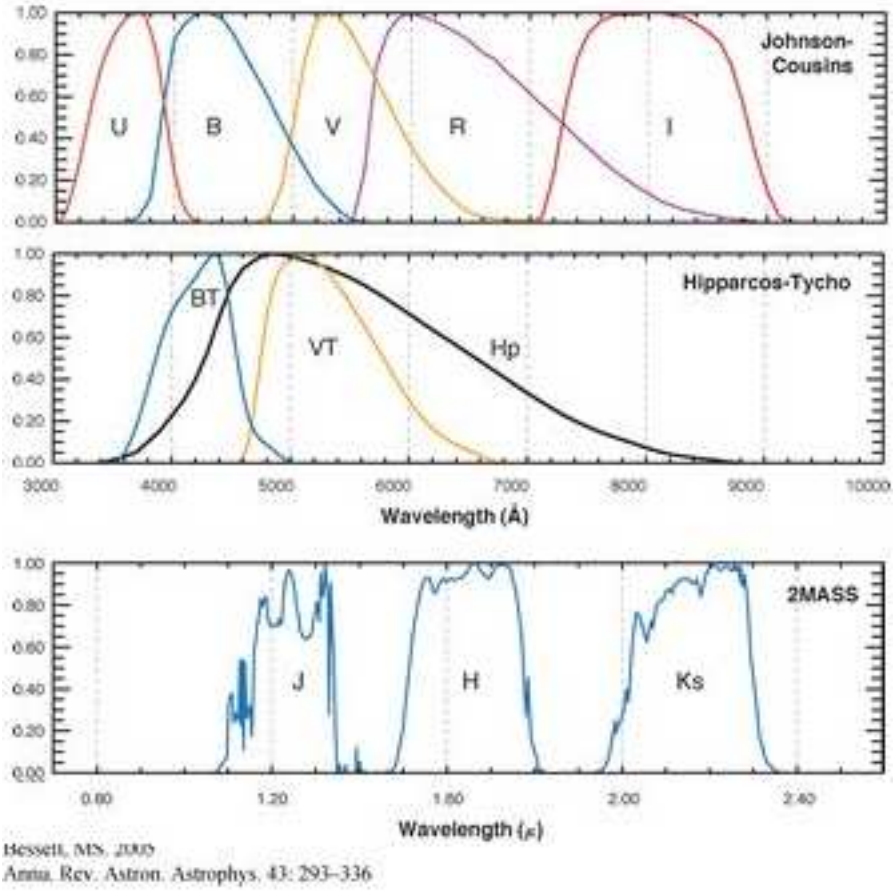

Figure 3.3: Filter responses as a function of wavelength for *Johnson-Cousins-Glass UBVRI* and *2MASS JHK*. Figure made from figures in Bessell (2005).

3.4 Membership selection

Wide field instruments have enabled simultaneous photometry to be collected for large numbers of stars covering a wide field of view. These instruments use CCDs to collect photons (limited in wavelength by a filter) from many stars at once. However as comparison to theory relies on the locations within this CMD of pre-MS and young stars of a given coeval population, we must be able to preferentially select stars which are most likely to be associated with a common formation point (in time) from the background and foreground field stars of very different ages.

The definition of a coeval population is a delicate one. An intrinsic spread in age will be present of order the formation time (see Section 2.3). Further age spreads may be included and confuse the data if close regions derived from a different star formation episode are included. This has been demonstrated in Jeffries et al. (2006a) where the previously assumed associated coeval group in σ Orionis was shown to be actually two kinematically distinct populations with different ages. Therefore when selecting target stars it must be borne in mind that some methods do not discriminate against absolute membership but are only indicators of youth. The inference of youth makes a given star unlikely to be a foreground or background field object, which are in general much older.

In this section I discuss various youth and membership indicators and criteria, with emphasis on their bias and applicability. I begin with general youth indicators (Section 3.4.1) and then move on to methods of identifying stellar memberships from more accurate kinematics (see Section 3.4.2).

3.4.1 pre-MS star selection

Pre-MS stars exhibit various characteristics that can identify them as young stars, which allow us to distinguish them from an older field star population. However this does not allow separation from different populations of young stars within the field-of-view (FOV). Methods to do this are discussed in Section 3.4.2. Throughout the subsequent sections I refer to Figure 3.4 (Hartmann, 2001), a schematic of a CTTS. Reference to this figure can be made for WTTS which are similar, the notable difference being a lack of a significant accretion disc.

3.4.1.1 Photometric CMD selection

Several of the physical aspects of pre-MS stars distinguish them from older field stars within a CMD. As discussed in Section 3.2 pre-MS stars appear over-luminous when compared to similar mass (or spectral type) stars at the ZAMS (due in part to their larger radii). In addition interstellar material left over from the pre-natal cloud absorbs and re-emits radiation from the parent stars, lowering the intensity and decreasing the peak wavelength. Contamination from field stars at different distances and behind different densities of ISM can be separated from a pre-MS population using a CMD. This method of selection has been employed in many studies (Pozzo et al., 2003; Béjar et al., 1999) and was shown in Burningham et al. (2005b) to not include or exclude a significant number of non-members and members respectively. However, this method of selection is complicated by the age spreads in young clusters. If one accepts a SSF model, this could result in

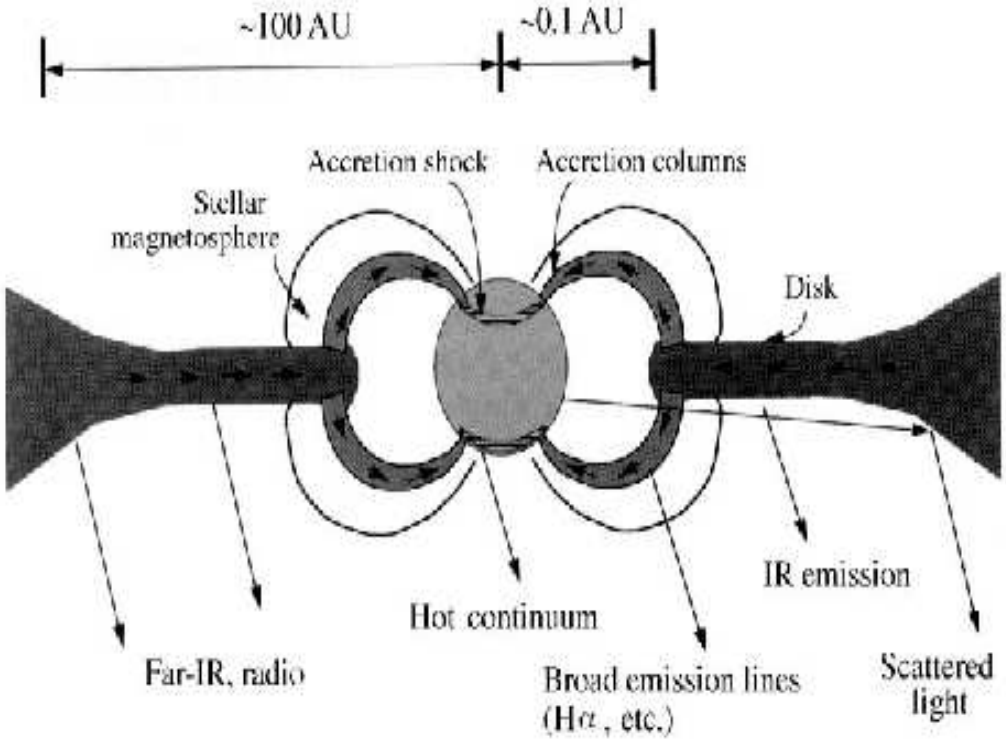

Figure 3.4: A schematic of a CTTS pre-MS star showing the disc, accretion columns, infalling envelope and central star from Hartmann (2001).

a spread of ≈ 10 Myrs, covering a large area of the CMD. On the other hand if we adopt a RSF model the photometric spreads observed are perhaps less well understood (see Chapter 4). MS stars at lower masses often lie in the contamination, with only the hottest and shortest lifetime stars lying blue-ward and brighter than the field stars (field stars are generally much older and therefore HM stars would already have evolved away from the MS). The approximate positions of these stars in an apparent CMD of h and χ Persei can be seen in Figure 3.5. Selections based on positions in a CMD are complicated by degeneracies (see discussion in Section 3.6.1) and are more often used as a selection tool for follow up observations.

3.4.1.2 IR excess or disc indicators

As explained in Section 2.4.1 pre-MS stars with circumstellar material show IR and NIR excesses (now defined as bands JHKL in the *Glass* photometric system). These excesses are caused by thermal emission of dust grains around the star (Bertout et al., 1988). As seen in Figure 3.4, the excess moves from far-IR to IR and then NIR as the material moves closer to the star and therefore hotter. In terms of selecting pre-MS candidates from a CMD, infrared colours can be used to construct the CMD, and from these data sources with excess NIR, IR or far-IR can be selected.

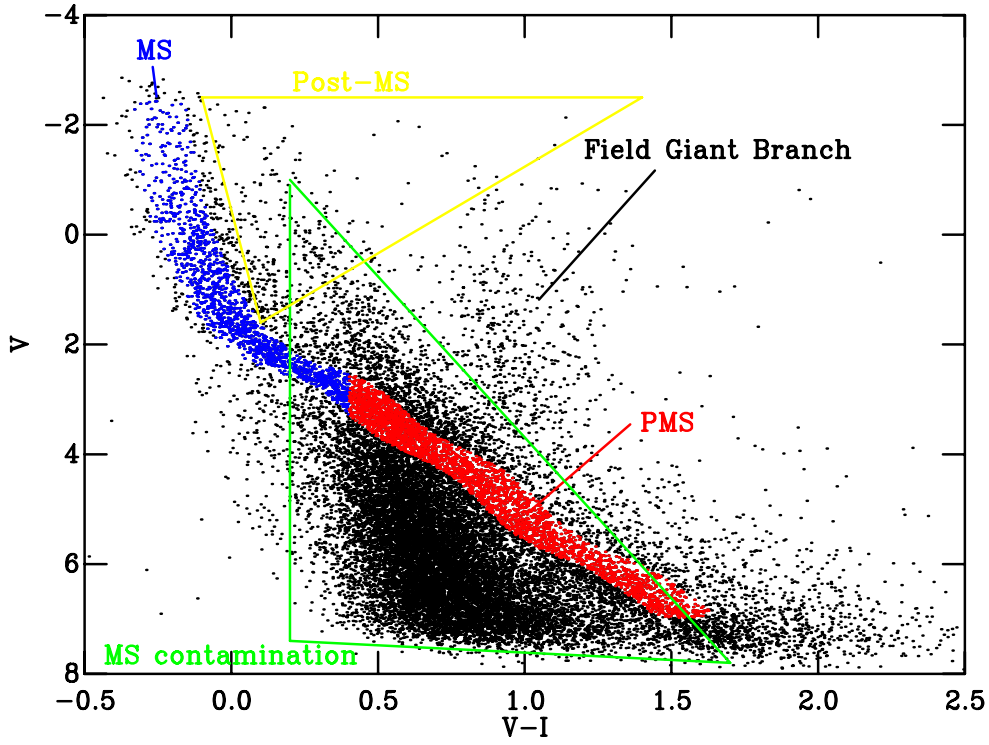

Figure 3.5: A CMD of h and χ Persei combined and adjusted to absolute magnitude and intrinsic colour. This figure shows a strong MS blue-ward and brighter than the contamination, then a pre-MS joining this in the contamination. The post-MS stars evolving red-ward and brighter than the MS are shown and the giant branch of large (bright) and cool (red) stars.

3.4.1.3 Hα

As discussed in Section 2.4.1 young stellar objects or pre-MS stars show $H\alpha$ emission. The classification of WTTS and CTTS is driven by the $H\alpha$ signature itself. For an equivalent width (EW) of $H\alpha$ greater than 10 Å the pre-MS star is classified as a CTTS (Appenzeller & Mundt, 1989). WTTS stars are classified as having $EW(H\alpha) < 10$Å. If $H\alpha$ emission is linked to accretion, evidence of infalling material should correlate with $H\alpha$ emission. A correlation of this sort was found by Cabrit et al. (1990). This selection mechanism will be inherently biased towards objects with discs.

The large magnetic fields present in TTS (see discussion in Section 2.4) are thought to disrupt the stellar disc and channel the ionised material down through magnetically driven accretion columns (Koenigl, 1991; Camenzind, 1990). These accretion columns (shown schematically in Figure 3.4) shed new light on the further classification of TTS found in Section 2.4. For CTTS stars the presence of these accretion columns falling onto the star at velocities of 100 km s^{-1} resulting in a blue- and red-shifting of the Balmer lines dependent on the line of sight and rotation of the star. This leads to the broader $H\alpha$ profile of CTTS (Muzerolle et al., 1998). For WTTS stars the $H\alpha$ emission is probably due to chromospheric activity from enhanced surface magnetic fields (see discussion in Walter et al., 1988).

3.4.1.4 X rays

Both WTTS and CTTS are thought to have enhanced magnetic fields, which although difficult to measure or infer appear much larger than those of our sun (Basri et al., 1992). These magnetic fields cause enhanced X-ray emission from the stellar chromosphere. Pre-MS stars have been observed with enhanced X-ray emission (Feigelson, 1983), and in addition X-ray flares have been found associated with pre-MS stars and YSOs (Feigelson & Montmerle, 1985; Guenther & Ball, 1999; Smith et al., 2003). This X-ray enhancement is strongest for fully convective stars where the magnetic field generation is of an α^2 type, deduced from rotation period correlation to X-ray emission (Feigelson et al., 2003). Solar-like stars with a tachocline-driven magnetic field generation show much less X-ray emission (see discussion in Section 2.5.1.2) (Preibisch & Feigelson, 2005).

Many studies of pre-MS populations have used the enhanced X-ray emission of these stars to select them from the contamination (e.g Flaccomio et al., 2006). Interestingly the low-mass members of the cluster σ Orionis and the sub-group Cep OB3b were both discovered through X-ray surveys (Walter et al., 1998; Naylor & Fabian, 1999). Feigelson et al. (2003) shows that there is little evidence for a bias in X-ray selected pre-MS stars to have an associated accretion disc and in fact they are most probably biased towards WTTS.

3.4.1.5 Periodic variability

For pre-MS stars as discussed in section 3.4.1.4 enhanced X-ray emission is found due to increased magnetic activity. As discussed in Section 2.5 magnetic effects can also create a variation in luminosity. This rotational variability is associated with three main accretion driven phenomena

(see for discussion Herbst et al., 1994; Bouvier et al., 1995; Herbst et al., 2007).

In CTTS only, as shown in Figure 3.4 magnetically driven accretion columns are channelled onto the stellar surface. From these areas of intense accretion continuum flux is emitted (often veiling other signatures within the spectrum of a star). As the star rotates the hot continuum emission is found to vary in accordance with this rotation. This suggests that the accretion impact points are fixed over several rotations (Bertout et al., 1988). This variation with rotation means that rotational periods can be extracted from the luminosity data.

However a much more easily detectable and long-lived source of luminosity variation (that found in wide-field photometric surveys, see Section 2.5) is due to cool spots. These are found in mainly WTTS but often CTTS stars as well. It is thought that magnetic activity on the surface creates cooler regions with lower plasma densities analogous to sun-spots (Bouvier et al., 1995). However, due to the much higher magnetic activity in pre-MS stars these single or groups of cool or plage spots have a much larger areal coverage. The amplitude of variation in flux is assumed to be linked to this areal coverage (Bouvier et al., 1995). In addition these spots are long lived, surviving over many years (Cohen et al., 2004) (pre-MS rotation periods are typically a few days, therefore they survive for many thousand rotations Lamm et al., 2005). Periods of rotation of the parent star can therefore be inferred from the variation of luminosity.

A highly irregular variation in luminosity can also be found, mostly in CTTS stars. These are thought to be variations caused by shifting accretion sites and are both much stronger and shorter lived than variability driven by cool spots. This sort of variability is not periodic and cannot be linked directly to the period of rotation of the parent star.

By far the most important form of rotational luminosity modulation is that of cool spots. This form of periodic variation is long-lived and easily detectable. Extracting robust periods from data of this sort is not a trivial task but is becoming more automated. Photometric surveys (such as Lamm et al., 2005, discussed in Section 2.4.1) provide an excellent and ubiquitous tool for selecting pre-MS stars. Selection of periodic variables of this sort is perhaps slightly biased towards WTTS.

All of the rotational accretion-driven phenomena are generated by large scale magnetic fields. The generation mechanism of these magnetic fields and indeed their strength appears to change with the formation of a radiative core (see discussion in Section 2.4.1). A delineation between the detectable variability in these two groups of stars should be apparent. This has been used as to trace magnetic field generation mechanisms in Saunders et al (in prep).

3.4.1.6 Li

The presence of Lithium can be identified from the Li I doublet ($\lambda = 6707.76$ and 6707.91Å) in the Solar spectrum (Grevesse, 1968) and TTS stars (Herbig, 1962, 1965). ^7Li is swiftly changed to He through nuclear reactions along the p-p chain, $^7Li + ^1H \rightarrow ^8Be \rightarrow ^4_2He$. This occurs at a temperature $T_{\rm Li} \simeq 2.5 \times 10^6$K (Bodenheimer, 1965a,b), at a rate very sensitive to the core temperature (Jeffries, 2004, $\propto T_c^{16-19}$ at typical pre-MS core densities). ^6Li has a lower critical temperature and faster reaction rate so is depleted much more rapidly (Hayashi, 1965).

Li abundances for our Sun (Grevesse & Sauval, 1998) are lower than for pre-MS stars

(Bonsack, 1961; Basri et al., 1991) which are in turn lower than for the ISM. It is clear from these observations that Li is depleted in the pre-MS phase and the MS phase of stellar evolution (Randich, 2006).

Lithium depletion is dependent on the temperature of the stellar core (T_c) and as pre-MS stars contract towards the main sequence their internal temperature increases with age. This rate of increase is controlled by the energy transport mechanism within the stars, which in turn is dependent on mass. This has been observed in IC2602 (Randich et al., 1997). Broadly speaking, the dependence on mass can be separated into three main regimes (see discussion in Jeffries, 2004). These mass ranges are extremely dependent on adopted distances and evolutionary models.

- **VLM stars** $0.06M_{\odot} < M_{\star} < 0.35M_{\odot}$. These stars remain in a fully convective state as they collapse towards the ZAMS. Li is depleted in the core. The material throughout the stellar interior can mix convectively on the Kelvin-Helmholz timescale, so Li is very swiftly depleted in these stars. As the stellar mass is increased the T_c at a given age is increased. Therefore, for stars in this mass regime the mass at which Li is depleted decreases with age. Li depletion can be observed between 10 and 200 Myrs. For stars $M_{\star} < 0.06M_{\odot}$ the temperature within the core never reaches the critical value for the Li depletion to proceed (Martin et al., 1994; Chabrier & Baraffe, 1997).

- **Intermediate Mass (IM) stars** $0.35M_{\odot} < M_{\star} < 1.2M_{\odot}$. IM stars all develop radiative cores before arriving at the ZAMS. As material mixing within the interior is then much less efficient subsequent Li depletion is slowed. In addition radiation transfer from the core to the convective envelope is slowed and the temperature there falls. For $M_{\star} < 0.6M_{\odot}$ the core becomes radiative at $T_c > T_{\rm Li}$ and hence these stars will show Li depletion at comparable levels to the VLM stars. However for stars above this range the Li depletion will be incomplete.

- **HM stars** $M_{\star} > 1.2M_{\odot}$ Stars in this mass range do not deplete Li significantly in the pre-MS phase. A radiative core is formed much before $T_c = T_{\rm Li}$ and the temperature in the convective envelope is not high enough to deplete the Li trapped there.

Therefore a specific mass for a given age describes a boundary between stars with significant and those with negligible Li depletion. As in the simplest sense the luminosity of an object and therefore its magnitude in an observable passband varies with mass, a magnitude or colour limit can be found. This is called the Lithium depletion boundary (LDB) and can be used to find ages for individual or groups of stars. Additionally, stars within the mass range $0.06M_{\odot} < M_{\star} < 1.2M_{\odot}$ having Li signatures must be youthful. This means Li signatures can be used as a membership indicator for young regions.

Li depletion is dependent on several assumptions within the stellar evolutionary model. Also in practice and LDB is found through luminosities in a given passband (or magnitude). This means absolute luminosities must be found through distance adjustments (see Section 3.6.1) and bolometric corrections (see Sections 4.4 and 3.2) each with associated uncertainties.

There are several critical studies of the various evolutionary assumptions and their effects on the LDB. The particular issues of ageing stars using this method are investigated in Jeffries

(2000) and Jeffries & Naylor (2001). Jeffries (2004) and Burke et al. (2004) provide a comprehensive discussion of the various model parameters and their effects on LDBs. These studies show that uncertainties in stellar structure, composition, equations of state, opacity and mixing-length parameters of convective models (Vitense, 1953) are negligible when compared to observational uncertainties. Complications of pre-MS atmospheres (grey or non-grey) would introduce time variable scatter into Li signatures which are not observed (Jeffries, 1999b). However, rotation has also been suggested as a cause for variation in the LDBs (Pinsonneault et al., 1992).

Scatters in Li abundances are observed in supposedly coeval stellar populations (Xiong & Deng, 2005). What could cause this scatter besides different ages? The first cause could be difference in the initial Li abundances between different regions of the ISM. A heterogeneous Li abundance cannot be ruled out with current data. Rotation rates have been observed to correlate with Li abundances, particularly in the Pleiades (Soderblom et al., 1993) at an age of ≈ 120 Myr. Subsequent studies (Garcia Lopez et al., 1994; Jeffries et al., 1998; Jeffries, 1998) found this correlation to exist only for IM stars. One theory is that as IM stars develop radiative cores some non-convective mixing is caused by angular momentum loss. This means pre-MS stars which are rapidly rotating will undergo less mixing (as they have lost less angular momentum) and therefore have higher Li abundances. Accretion could act to scatter the Li abundances, however it is unclear to what extent. Accretion of extra material before $T_c = T_{\rm Li}$ will hasten the onset of Li depletion whereas accretion after this point will serve to enrich the star (Jeffries, 2004). A final and perhaps telling contribution to Li abundance scatters could be caused by magnetic fields. The strong magnetic fields within pre-MS stars could act to suppress convective mixing and hasten the formation of a radiative core therefore reducing Li depletion (Ventura et al., 1998). Polosukhina & Shavrina (2007) have also observed Li spots on the surface of Ap-CP stars associated with magnetic fields and enhanced Li abundances in the atmospheres of these stars. Polosukhina & Shavrina (2007) suggest that strong magnetic fields may act to preserve Li in the atmosphere. In conclusion, at present the accuracy of LDB ages is believed to be limited by observational effects (Burke et al., 2004; Jeffries, 2004; Xiong & Deng, 2005).

Studies using Li signatures as an indicator of youth and therefore membership are numerous (e.g Jeffries, 1997; Dolan & Mathieu, 1999; Jeffries, 1999a; Kenyon et al., 2005). More recently ages have been derived for stars using LDB methods for both individual stars and groups of stars (e.g Jeffries et al., 2000; Jeffries & Oliveira, 2005). In particular studies have been used to advocate SSF (see Section 2.2.1) citing large Li depletion scatters and therefore age spreads within assumed coeval stellar populations (e.g Palla et al., 2007). It is important to note that LDBs for stars are subject to the same assumptions of stellar evolution that evolution in a HR diagram is. This makes ages for individual stars unreliable until the timescale of star formation is known. If one accepts SSF then these Li abundance scatters represent a real age spread in a given SFR. However for RSF these spreads must be derived from other effects (see discussion in Chapter 4).

3.4.2 Kinematic selection methods

Kinematic methods of membership selection rely on a star's motion inferred from observations. They rely on gravitationally bound objects having similar velocities through space. OB associa-

tions are gravitationally unbound so one would expect internal velocity difference to degrade any co-motion. However as OB associations are young the internal velocity dispersion is normally not large enough to disrupt co-moving populations significantly. Kinematic methods of membership selection are much more robust against contamination than most other forms of membership selection, with only foreground or background stars travelling along a coincident velocity vector erroneously included. Measurements of stellar movement come in two main sorts derived in very different ways, proper motions and radial velocities. These values represent the perpendicular (proper motion) and radial (radial velocity) components of a star's motion with respect to our line-of-sight.

3.4.3 Proper motions

As the stars are so distant they appear as a fixed background. However, even in antiquity some stars were noted as having peculiar motions, movement relative to the rest of the stars. From comparison of modern measurements with the data of the Greek astronomer Hipparchos Halley (1717) discovered proper motions of several stars. In more recent times photographic plates have been scrutinised to reveal proper motions of many stars, with the process becoming automated (Ducourant et al., 2006). With the launch of the *HIPPARCOS* satellite, designed to measure parallaxes, de Zeeuw et al. (1999) found proper motions for all OB associations within 1 kpc of the Sun. Proper motions are more precise and still commonly used to select members and study other astrophysical phenomena (Uribe et al., 2002; Oyama et al., 2007). Proper motions for young stellar objects can sometimes be small with data over long timescales required. In addition catalogues such as *HIPPARCOS* and later *TYCHO* are not sensitive enough in magnitude to detect the often faint pre-MS stars.

3.4.4 Radial velocity

Radial velocities can be calculated using the simple Doppler shift equation. As the star moves towards or away from us the emitted radiation is Doppler shifted according to equation 3.2, which was first developed by Christian Doppler in 1841. This method was first used by William Huggins in 1868 to measure the motion of the star Sirius.

Using standard stars which are moving at known radial velocities (RVs) the shift of a known emission/absorption line can be found (e.g $H\alpha$ or Li). This can then be converted to a velocity using

$$\frac{\Delta\lambda}{\lambda} = v \tag{3.2}$$

where λ is the wavelength, $\Delta\lambda$ the measured shift and v the radial velocity of the star. Many studies have utilised Rvs to classify pre-MS members (Dolan & Mathieu, 1999; Pozzo et al., 2003; Kenyon et al., 2005) and to study accretion discs or outflows (Echevarría & Michel, 2007; Coffey et al., 2007).

3.5 Summary

We require precise relative age orders (and later absolute ages) of many populations of pre-MS stars to apply constraints on star formation and evolution timescales (see Section 2.3 and 2.3). In Sections 3.1 and 3.4.1 I have discussed where and how to observe pre-MS stars. I have also discussed methods of comparing data to theoretical models using the HR and colour-magnitude diagram in Sections 3.2 and 3.6. Furthermore I have discussed methods of classifying pre-MS stars as members of a certain (coeval) group. In the next section I explore the practical aspects of fitting data in a CMD.

3.6 Timescales and ages from a CMD

As mentioned in Section 3.2 a star's evolution in the HR diagram ($L_{\rm bol}$ vs $T_{\rm eff}$ plane) is a function of age. Therefore once a star's intrinsic luminosity and effective temperature are known comparison with stellar models can be made to derive an age. However, as also mentioned in Section 3.2 it is better to compare data to a model in the natural plane of the data. Models (as a function of age) in the observational plane within a CMD (see Section 3.2) can be constructed using bolometric corrections and colour to $T_{\rm eff}$ relations.

The bolometric correction is, in magnitude space, an additive factor to convert the total luminosity to a luminosity in a given observable band (i.e. BC_V, the bolometric correction applied to L to derive V). This factor is often derived from standard stars and is more difficult to calculate in some bands for pre-MS stars due to the various excess emissions of pre-MS stars (see Section 3.4.1). A further discussion of this factor and its effect can be found in Section 4.4.

Colour to $T_{\rm eff}$ relations are also usually based on standard stars or on atmospheric models. This factor is a conversion of a given surface effective temperature to an intrinsic colour (e.g *V-I*). These conversions again suffer from uncertainties for pre-MS models both due to various excess emissions and the more complex cooler atmospheres. Again a further discussion of this factor can be found in Section 4.4.

Early fitting of absolute magnitudes and intrinsic colours of stars to models was carried out in conjunction with spectral type, such as those leading to the creation of the HR diagram (Hertzsprung, 1911; Russell, 1913). Later comparison was carried out using magnitudes and colours within a CMD. Early examples include studies such as Cuffey (1940) and then later Mitchell & Johnson (1957) which used the MK standard system (Morgan et al., 1943). In these early examples the MS stars of clusters such as the Hyades (Eggen, 1950a), Pleiades (Eggen, 1950b; Johnson & Morgan, 1951; Mitchell & Johnson, 1957) and Praesapes (Eggen, 1951) were fitted to models to derive distances rather than ages. Before it is possible to fit a selection of stars using modern theoretical models in the CMD we must first understand the impact of two other important variables, namely distance and extinction.

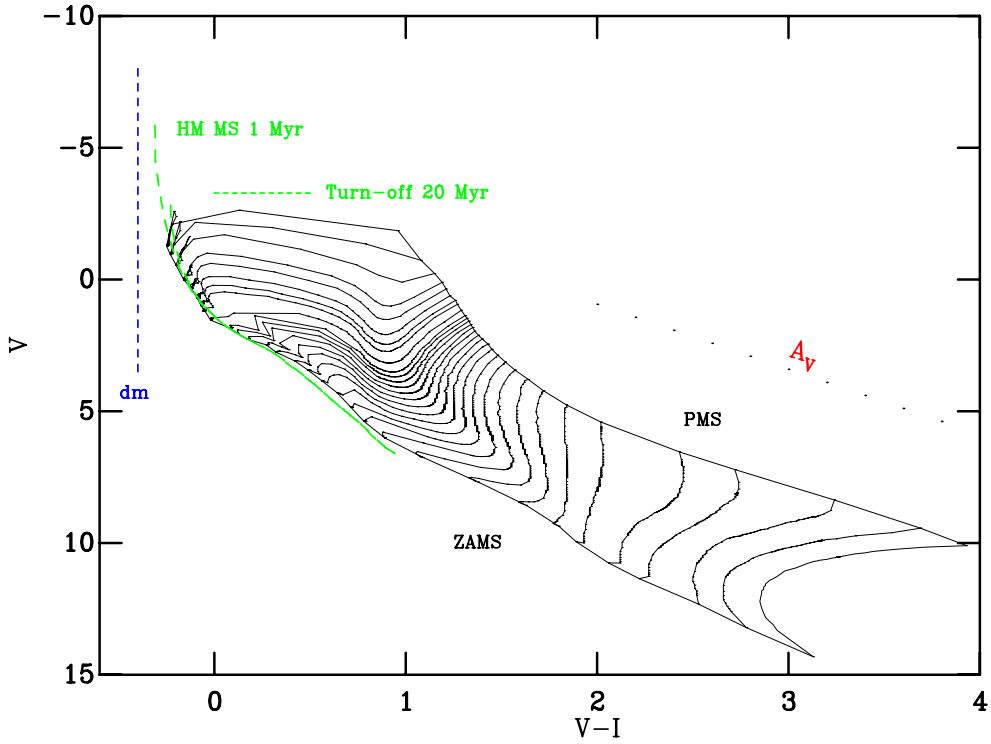

Figure 3.6: A CMD showing direction of the distance (dm) variable, vertical blue dashed line. The direction of the extinction (A_V in this plane), red dotted line. pre-MS mass tracks from Siess et al. (2000) for Masses $M_\star$ = 0.13, 0.16, 0.2, 0.25, 0.3 – 2.0 ($\Delta M_\star$ = 0.1) and 2.2, 2.5, 2.7, 3.0, 3.5, 4, 5, 6 and 7$M_\odot$, bold black lines. The mass tracks are bounded by the ZAMS and 0.1 Myr isochrones from Siess et al. (2000). Finally, the MS HM isochrones of Girardi et al. (2002) for 1 and 20 Myr, green dashed lines, with the turn-off for 20 Myrs shown. This figure shows that for HM fitting distance is degenerate with extinction only, and for LM or pre-MS fitting distance is degenerate with age only.

3.6.1 Degeneracies

A modern set of pre-MS, MS and a section of the post-MS isochrones are shown for different masses (for reference) in a V vs $V-I$ CMD in Figure 3.6. In addition, the effects of distance and extinction are shown which I now discuss.

3.6.1.1 Distance fitting

If the intrinsic luminosity (L_0) from a star is emitted isotropically (not always correct see Section 3.4.1.5) it is projected outwards on to the inner surface of a sphere. The surface area that the flux covers increases with distance to the observer (r) or effective radius of the sphere, reducing the flux arriving per second per area (or Luminosity, L). This effect is a simple geometric one, applies equally to all wavelengths and is given by

$$L_{app} = 4\pi r^2 L_0 \tag{3.3}$$

Distances derived using the $\propto \frac{1}{r^2}$ nature of equation 3.3 in conjunction with a model of

a stars intrinsic luminosity are called 'photometric' distances. This technique was put forward by James Gregory in (1668) and was first used by Sir Isaac Newton. Newton used the solar luminosity as a model for the intrinsic luminosty of any star. The solar luminosity was measured by its reflection from Saturn's surface. Newton used this technique to show that the stars were at a much greater distance than supposed at the time, this was published in *De mundi systemate* (On the system of the world) in 1685. In particular Newton calulated the distance to Sirius as one million astronomical units (AU), although this result is too large by roughly a factor two this was an important first step in deriving distances from stellar luminosities. As models of stellar intrinsic luminosities (and effective temperatures) increased in sophistication, and an evolutionary sequence began to emerge, photometric distances become more accurate.

If the luminosity of the star is converted to a magnitude (see Section 3.6) in a given band the effect of distance on this magnitude can be derived. If we take a star at an apparent magnitude m_1 at distance r_1 and move it to distance r_2 with fluxes at that wavelength of F_1 and F_2 respectively the change in magnitude will be (using $m = -2.5log\, f_\lambda$)

$$m_1 - m_2 = -2.5log(\frac{F_1}{F_2}) \tag{3.4}$$

Setting the flux equal to the luminosity (L_1 and L_2) at that distance (i.e using equation 3.3)

$$\frac{F_1}{F_2} = \frac{L_1}{4\pi r_1^2}\frac{L_2}{4\pi r_2^2} \tag{3.5}$$

Defining the absolute magnitude ($m_2 = M$) as the magnitude at 10 parsecs ($r_2 = 10$ pc) and d as the distance to the star in parsecs

$$dm = m - M = 5log(\frac{r_1}{10})\ and\ \therefore m - M = -5 + 5log(d) \tag{3.6}$$

Equation 3.6 defines the distance modulus dm. For the case of colours (i.e. $V - I$) in a CMD distance affect both bands equally. Therefore this effect cancels when the bands are subtracted to make the colour. Hence, adjusting the distance to a given sequence of stars only shifts the sequence in magnitude.

The section of stars on the relatively temporally stationary MS of a cluster can be fit to derive a distance, the traditional method is illustrated in Mitchell & Johnson (1957), effectively removing age as a parameter. This involves fitting a theoretical isochrone to the lower or single star sequence by adjusting the distance until one achieves a fit. The lower part of the sequence is used as unresolved binaries can shift the star up to ≈ 0.7 mags brighter. Fitting has largely been done 'by eye' and this technique is still used in modern work (Sanner et al., 2000; Pinsonneault et al., 2003). An example of a MS isochrone fitted to derive a distance can be seen as Figure 3.7 from Stauffer et al. (2007). This is discussed in more detail in Chapter 4.

If a sequence does not contain a well-populated MS then often pre-MS isochrone fitting must be used to determine an age and distance simultaneously. This is as there are many more lower mass stars in a given population than higher mass stars, given a standard initial mass function (IMF). Figure 3.6 shows that the variation of age is degenerate with distance in the pre-MS. This

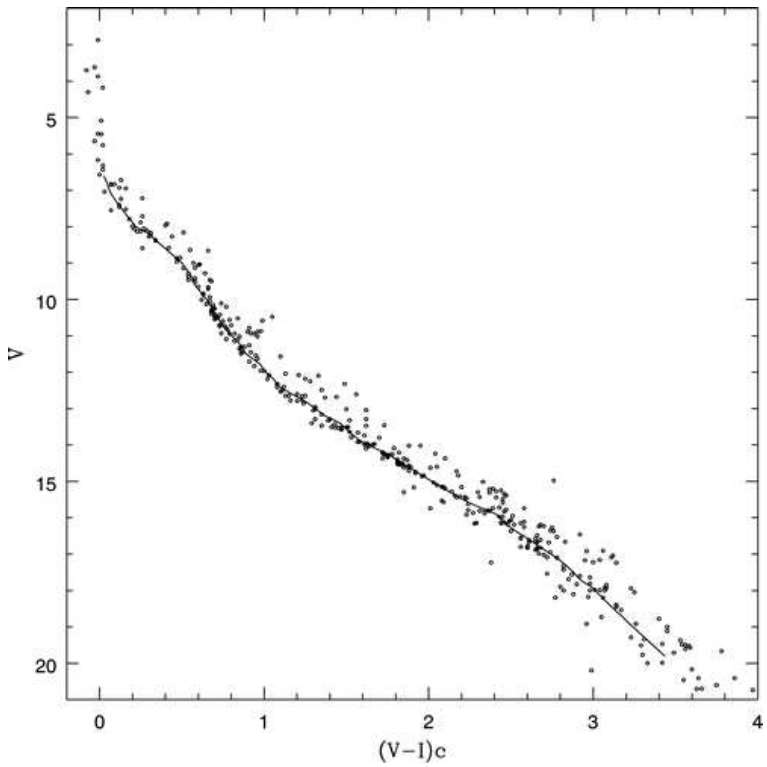

Figure 3.7: The MS isochrone distance fit to the Pleiades from Stauffer et al. (2007).

is discussed in Section 3.6.2.

Figure 3.6 shows that the extinction vector will have a component in the same direction as distance. This degeneracy means that extinctions must be known to derive precise distances. As there are no effects of distance on colour comparing data in a colour-colour plane allows us to remove this variable and solve for extinction.

3.6.1.2 Extinction fitting

ISM material between the observer and the target absorbs some of the light from the source and re-emits it, reducing its intensity differently for different wavelengths. The interstellar extinction absorption as a function of wavelength is shown as Figure 3.8. As interstellar extinction affects the magnitude in each band (A_λ; for example, A_V is extinction in the V band) differently its effect in a CMD will have a component in both colour and magnitude. The extinction is defined as a colour excess, e.g. $E(B-V)$ is the excess in $B-V$, and is given by, $(B-V)_0 = B-V+E(B-V)$, where $(B-V)_0$ is the intrinsic colour and $B-V$ the apparent colour. The gradient of this reddening vector depends on the colours used i.e. the relation $\frac{A_{\rm mag}}{E_{\rm col}}$. For the V vs $V-I$ CMD in Figure 3.6 the reddening vector lies almost parallel to the pre-MS. This is one of the advantages of using V vs $V-I$ for pre-MS analysis (see Chapter 5).

Extinctions can be found simultaneously with distances (Mitchell & Johnson, 1957) or by using colour-colour diagrams. The construction of colour-colour diagrams allows the removal of distance effects and the fitting of MS stars for extinctions along a theoretical extinction vector.

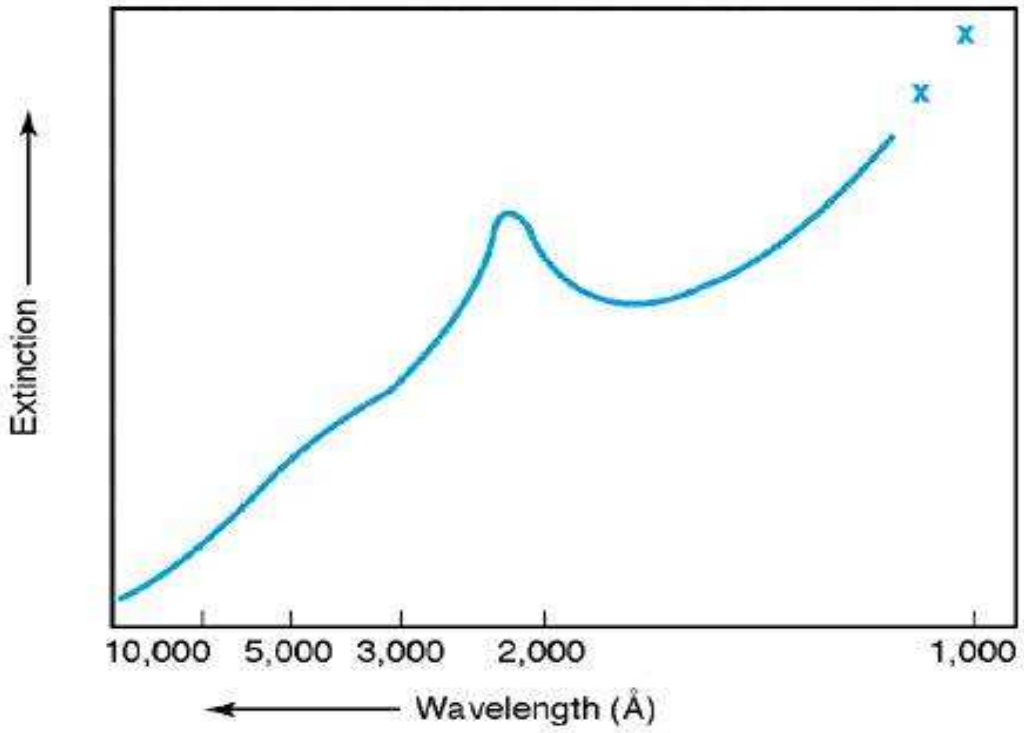

Figure 3.8: The extinction as a function of wavelength from URL:www.astro.livjm.ac.uk/courses/phys134/magcol.html.

This can be done for whole populations (Claria, 1982b) or individual stars using the Q-method (Johnson & Morgan, 1953). This aspect of CMD fitting is discussed in more detail in Chapter 4. A schematic showing how to fit a sequence of stars to an isochrone in a colour-colour diagram to derive a reddening and therefore extinction is shown in Figure 3.9.

3.6.2 Ages

The fitting to derive a distance or extinction from a relatively static and thus older MS is quite robust, as these sections of the stellar sequence do not move significantly with age. Finding a precise age from this part of the sequence is more difficult, this is as the shifts as a function of age within the CMD are small when compared to an average photometric uncertainty. Therefore, fitting for ages and indeed separating ages of sequences in a CMD requires more swiftly evolving (in CMD space) sections of the sequence, where the difference in magnitude and colour is large compared to the photometric uncertainty. Particularly for young populations as a well populated MS may not be available.

3.6.2.1 HM ages, nuclear or turn-off ages

HM stars evolve very quickly and move away from the MS on post-MS evolutionary tracks. As a coeval stellar population ages the mass at which stars are moving away from the MS lowers. The subsequent evolutionary tracks in their entirety are complicated, degenerate with distance (see

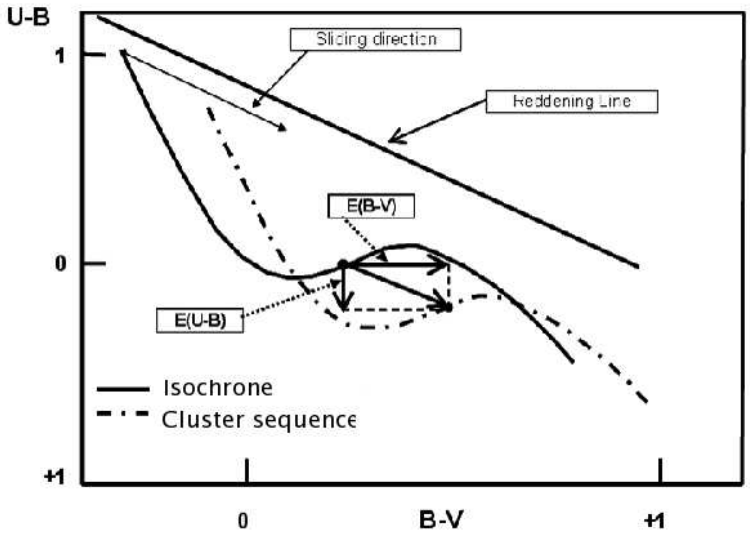

Figure 3.9: A schematic showing the fitting of a cluster sequence to an isochrone in a colour-colour diagram. This has been modified from the original source at URL:http://xoomer.alice.it/hrtrace/Geberal_Info_Wd_file/Geb1.png

Figure 3.6) and beyond the scope of this thesis. However, the highest mass star found on the MS can be fitted with post-MS models from which an age can be derived. These ages are based on the internal nuclear physics of the stars. As they exhaust their core hydrogen supply they turn away from the MS. These ages are called nuclear or turn-off ages and have been found for many stellar populations (Lindoff, 1968; Mazzei & Pigatto, 1989). These ages are necessarily based on the photometry of only a few stars and are degenerate with distance (see further discussion in Chapter 4). In addition these ages are often found not to be consistent with ages derived from other parts of the stellar sequence (Lyra et al., 2006b).

3.6.2.2 pre-MS ages, turn-on or contraction ages

With the advent of more sensitive CCD based photometry, superseding photoelectric photometry using photomultiplier tubes, observations of fainter stars became available. This developed the fitting of stellar models to the contracting pre-MS stars Current models of pre-MS isochrones are available from several groups (D'Antona & Mazzitelli, 1997; Siess et al., 2000; Baraffe et al., 2001b). However these models are particularly sensitive to the adopted conditions in the stellar interior of the fully convective star. In addition the atmospheres of LM pre-MS are not well understood. Meaning that the relation from effective temperatures (produced by the stellar interior models) to colours, after radiation passes through the atmosphere, is uncertain. Semi-empirical studies have attempted to tune this relation using data for the LM pre-MS stars in the Pleiades (Jeffries & Tolley, 1998).

The derivation of independent distances and ages from CMDs with higher precision than traditionally available is the subject of the remainder of this thesis.

3.7 Summary

It is apparent from Section 2.7 that at least in principle the timescales of star formation can be constrained by the ages and age spreads in young coeval populations. In particular more precise relative age orders of several stellar populations would enable us to conclude two contentious issues of stellar evolution. Firstly a universal disc lifetime and secondly possible effects of the local environment on these dissipation timescales. Further calibration to absolute ages would provide useful timescales to constrain planet formation models.

As described in Section 3.6 ages can be derived for young MS (turn-off) and pre-MS (turn-on) populations using isochrone fitting in a CMD. These ages are however degenerate with distance with distances in turn degenerate with extinctions. Therefore, to derive a set of precise relative age orders which can be calibrated into absolute ages, extinctions and then distances must be derived.

The rest of this thesis is given over to deriving relative extinctions and distances, and age orders for a range of young stellar populations. In Chapter 4 I describe firstly a new technique for deriving precise extinctions and distances from photometric data. Subsequently, these quantities are derived for several stellar populations using several model isochrones. This chapter also contains an investigation of the model dependency of these distances. In Chapter 5 I model the pre-MS using empirically constructed isochrones. Then in Chapter 6 I assign age orders using the distances and extinctions applied to the empirical isochrones. Chapter 6 also contains a discussion of the consequences of this new age order. In Chapter 6 I also report the discovery of a useful phenomenon that can be used to derive absolute and distance independent ages. This feature also has the potential to provide further insight on the stellar evolutionary and formation models. Finally, I draw conclusions and discuss possible future work in Chapter 7.

Chapter 4

Deriving Distances and Extinctions

This chapter describes the determination of distances and extinctions for several SFRs. This is done, for the most part, by using MS isochrone fitting described in Section 3.6.1.1. I employ a new fitting statistic to derive the most likely parameters and in the case of distance, uncertainties. In cases where this fitting technique is not applicable distances and extinctions from the literature are adopted.

4.1 Introduction

As discussed in Section 3.6 colour-magnitude diagrams (CMDs) of star-formation regions (SFRs) provide, in combination with model isochrones, an excellent tool with which to determine distances, ages and individual stellar masses.

Very precise photometry ($\approx 1\%$) is now routinely available, along with sophisticated stellar models. However, current parameter derivations from CMDs still have relatively large uncertainties and are model dependent (see the discussions in Bonatto et al., 2004; Pinsonneault et al., 2004; Naylor et al., 2002; Mayne et al., 2007). Thus current age, and distance, uncertainties all but 'wash-out' any environmental effects. Clearly more robust constraints would be available for current stellar theories if more precise parameters could be extracted from the CMDs of SFRs.

Previous distances have been derived using chiefly main-sequence (MS) isochrone fitting, pre-MS isochrone fitting or from *HIPPARCOS* parallax measurements. MS isochrone fitting provides distances based on the positions of MS stars in a CMD, which are independent of uncertainties in age. Pre-MS isochrone fitting also uses the positions of stars in a CMD, but in this method the derived distances are degenerate with age as discussed in Chapter 3, (see e.g. Naylor & Jeffries, 2006). Finally, distances derived from *HIPPARCOS* parallax measurements are only available for a few SFRs included in this chapter, σ Ori, NGC2547 and λ Ori, with all except λ Ori having large uncertainties.

Of those methods used to derive distances, the most suitable for the derivation of age orders is clearly MS isochrone fitting, once stars have crossed the radiative-convective gap, which is discussed in Chapter 6. However MS fitting has not yielded the precision one would expect in distance estimates. This is due to two significant problems. Firstly the position of MS isochrones, although temporally static, is model dependent, with different studies adopting different models.

Secondly distances are usually derived using 'by eye' fitting of models to the data, yielding ill-defined uncertainties.

In this chapter both of these problems are solved. First fitting is performed against a single MS isochronal model, which allows derivation of a set of accurate and self-consistent relative distances. However these distances are of course still dependent on the chosen model (although this model dependency is practically very small for the isochrones we have used, see Section 4.7). Second the τ^2 fitting technique (Naylor & Jeffries, 2006), a new rigorous and self-consistent method of fitting stars to isochrones is used. This statistic is defined in Section 4.5.1 and its use in MS fitting for distances and extinctions is described in Section 4.5. This fitting routine also yields statistically meaningful uncertainties. This presents the opportunity to achieve more precise distances from the fitting of high-mass (HM) or MS stars.

The rest of this chapter is laid out as follows. Section 4.2 introduces and characterises the sample of SFRs, in particular, results for distance and extinction derivations and lists ages for the set of SFRs. Section 4.3 describes the preparation of the data, including their literature sources, membership selection and photometric cuts required for fitting the MS. In Section 4.4 the different models used are discussed and their various calibrations. Then in Section 4.5 the fitting statistic is introduced and the fitting process described using an example. Some practical issues associated with the fitting are also discussed in Section 4.5. Alternative derivations of extinctions for individual stars are discussed in Section 4.6. The results for all the model isochrones and calibrations are shown and briefly discussed in Section 4.7. The result for one adopted model are then displayed in Sections 4.8 and the implications of these results are discussed in Section 4.9. Finally a summary of this chapter can be found in Section 4.10 along with the parameters adopted for the rest of this thesis.

4.2 Sample characterisation: Literature distances, extinctions and nominal ages

The sample of 15 SFRs within this thesis was chosen from available archive data, with the added restriction of being young (< 100 Myrs), and preferably well studied. All of the SFRs lie within $\approx$ 2.5 Kpc from the Sun in or slightly above or below the galactic plane and exhibit a reasonably clear pre-MS in a CMD.

Distances and extinctions from the literature have been obtained for comparison with those derived in this chapter. In adopting literature distances the most comparable are those derived preferably from MS isochrone fitting or at the very least methods as free from pre-MS (Pre-Main Sequence) fitting as possible. The following section details the general SFR characteristics, and the distances and extinctions previously derived in the literature. Table 4.1 summarises the discussed distances and extinctions and lists some previous age estimates.

4.2.1 h and χ Per

h and χ Per (NGC 869 & NGC884), named using the Bayer convention from 1603, comprise a double cluster at the core of the Per OB1 association. Each cluster has an approximate diameter of

around 30 arcmin and contains around 400 stars, the brightest of which is at around a $V = 7$ mag. These clusters have total masses of $3700 M_{\odot}$ and $2800 M_{\odot}$ for h and χ Per respectively (Slesnick et al., 2002). The clusters (and Per OB1) are located within the Perseus spiral arm, with central positions (defined in Chapter 5) of α=2 22' 5.02" δ=+57 7' 43.44" (χ Per), α=2 18' 58.76" δ=+57 8' 16.54"(h Per), J2000.

Capilla & Fabregat (2002) derive an extinction of $A_V = 1.71$ for χ Per and between $A_V = 1.71$ and $A_V = 1.99$ for h Per. Both clusters were found to have a distance modulus of $dm = 11.7 \pm 0.1$. This study fitted narrow-band photometry with MS isochrones. The values of extinction and distance modulus are in line with other recent determinations such as: Marco & Bernabeu (2001) $E(b-y) = 0.39 \pm 0.05$ and $E(b-y) = 0.44 \pm 0.02$ for χ and h Per respectively, with the same distance for both of $dm = 11.56 \pm 0.20$; Slesnick et al. (2002) find identical distances and reddening of $dm = 11.85 \pm 0.05$ and $E(B\text{-}V) = 0.56 \pm 0.01$ ($A_V = R * E(B-V)$, $R \approx 3$)for both clusters. The values adopted for comparison are $dm = 11.7 \pm 0.1$ for both clusters and $A_V = 1.71$ for χ Per with $A_V = 1.71 - 1.99$ for h Per.

4.2.2 NGC2547

NGC2547 is a southern open cluster associated with Vela, it was first discovered and studied from South Africa by Abbe Lacaille in 1751-1752. It has an apparent size of approximately 20 arcmins with the brightest star at around $V = 4-5$ mags. The cluster contains around 100-150 stars and has a total mass of $190 M_{\odot}$ or $370 M_{\odot}$ (Naylor et al., 2002). NGC2547 has a central position of α=08 10' 25.70" δ=-49 10' 03.00", J2000.

Claria (1982b) undertook a photoelectric survey in *UBV* and found 22 probable radial velocity members with (B-V) < 0.1. Using individual reddenings to MS intrinsic colours he derived $A_V = 0.192$, from $E(B\text{-}V) = 0.06 \pm 0.02$ mags, with $dm = 8.27$ mags. Robichon et al. (1999) used *HIPPARCOS* parallax data to calculate a $dm = 8.18^{+0.29}_{-0.26}$ pc. The latter distance used an alternative method to isochronal or intrinsic colour fitting, so will be most useful here. The studies used for memberships in Chapter 6 all contain derivations of distance and extinction in agreement with those found in these two cases. The initially adopted values are; $dm = 8.18^{+0.29}_{-0.26}$ mags and $A_V = 0.192$.

4.2.3 The ONC

The ONC (NGC1976) is part of the Orion molecular cloud complex and the large scale Orion OB association. The association comprises the southern "A" and Northern "B" clouds. For this study we adopt the definition of the ONC used in Hillenbrand (1997). This selection of the inner 20 arcmin includes the central Trapezium Cluster. The ONC, so defined, contains around 1600 stars (Hillenbrand, 1997) with the brightest stars at a $V = 4$ mag and lies ≈ 160 pc above the galactic plane. The ONC has an estimated total mass of $930 M_{\odot}$ (Hillenbrand, 1997) with a central position of $\alpha \approx$05 35' 0" $\delta \approx$-05 29' 0", J2000.

H_2O MASER measurements are used in Genzel et al. (1981), where expansion velocities of molecular clouds were used to infer the distance. A result of $dm = 8.38 \pm 0.37$ mags was obtained. This along with values of the extinction from Hillenbrand (1997) are initially adopted for this field.

4.2.4 NGC2264

NGC2264 is surrounded by the Cone nebula in the Orion arm. The cluster itself extends over ≈ 60 arcmins and contains around 600-800 stars, the brightest of which are at $V = 4-5$ mag. The estimated total mass of the cluster is $> 430 M_{\odot}$ (Dahm & Simon, 2005) and has a central position of $\alpha \approx$ 06 41' 0" $\delta \approx$+09 59' 0", J2000.

In Dahm & Simon (2005) a summary of values from previous studies is presented along with the methods of calculation. All the entries listed are from forms of isochrone fitting, but only those studies fitting the main sequence are considered here. Sung et al. (1997) used colour-magnitude selection in $R - H\alpha$, then fitted the ZAMS to those stars assumed to be B type stars. An average distance modulus of 9.40 ± 0.25 mags and extinction of $A_V = 0.23$ resulted. Perez et al. (1987) used shifts of individual OB type stars to intrinsic colours leading to $A_V = 0.19$ and $dm = 9.88 \pm 0.17$ mags. Park et al. (2000) selected stars using Hα and X-ray emission, then used MS isochrone fitting with the bright stars, deriving a distance modulus of 9.4 ± 0.10 mags and $E(B\text{-}V) = 0.066 \pm 0.034$. An average of these values has been taken giving $dm = 9.6$ mags and $A_V = 0.21$, which is adopted initially.

4.2.5 σ Ori

σ Ori is a small cluster of stars first recognised by Garrison (1967) and Lynga (1981), but was not studied further until Wolk et al. (1996), and later Walter et al. (1998). Where Walter et al. (1998) re-discovered the clusters through X-ray observations. This cluster is associated with the Orion molecular complex, in particular the Ori OB 1b association (or Orion Belt) and has a diameter of around 50 arcmin. More recent studies have interestingly separated the previously assumed single coeval population into two kinematically distinct populations (Jeffries et al., 2006a). This cluster contains around 400 stars (in the two groups) with the brightest at $V = 4$ mags, and has a total mass of approximately $225 \pm 30 M_{\odot}$ (Sherry et al., 2004). The central position of this cluster is $\alpha \approx$ 05 38' 0" $\delta \approx$-02 36' 0", J2000.

Brown et al. (1994) derived parameters using the lower part of the sequence, without the direct use of isochrones. Measurements of surface gravity from narrow band photometry were calibrated to intrinsic colours of the theoretical and empirical models of Straizys & Kuriliene (1981). Brown et al. (1994) used MK spectral types in conjunction with effective temperature and absolute bolometric magnitudes to calculate surface gravities and radii of stars. In Straizys & Kuriliene (1981) however the calibrations did not take into account pre-MS or post MS objects, as they only provide intrinsic colours for MS stars. Brown et al. (1994) applied these calibrations to all spectral types, clearly at the age of around 3 Myr many of these stars are indeed pre-MS objects. A set of subgroups were selected and the subgroup 1b of Brown et al. (1994) covers the SFR chosen in this thesis. The values for this subgroup were given as $dm = 7.80 \pm 0.39$ mags, with a value of $E(B\text{-}V) = 0.06$. The distance from *HIPPARCOS* parallax measurements is quoted as $dm = 7.73^{+0.84}_{-0.60}$ to the star σ Orionis. The large uncertainties make this value unusable. Therefore the values initially adopted are from Brown et al. (1994), namely $dm = 7.80 \pm 0.39$ mags and $E(B\text{-}V) = 0.06$ ($A_V = 0.18$).

4.2.6 NGC7160

NGC7160 is located in the Cepheus OB2 region. It has an apparent diameter of 7 arcmin with the brightest stars at $V = 6$ mag. The number of stars in this cluster and the total mass are not well studied quantities. The central coordinates are $\alpha \approx$ 21 53' 40" $\delta \approx$+62 36' 12", J2000.

Sicilia-Aguilar et al. (2004) and Sicilia-Aguilar et al. (2005) used spectroscopically derived spectral types and intrinsic colours to calculate the extinctions, and MS isochrone fitting for the distance. The resulting values which I adopt are $A_V = 1.17$ and $dm = 9.77$ mags.

4.2.7 Cep OB3b

Cepheus OB3b is a subgroup of the Cepheus OB3 association, within which the discovery of a well populated pre-MS was made in Pozzo et al. (2003). This subgroup could be evidence of triggered star formation from an expanding atomic hydrogen shell centred on a supernova remnant in the close, and older, subgroup Cep OB3b (Simonson & van Someren Greve, 1976; Assousa et al., 1977). Cep OB3b covers an apparent diameter of < 5 arcmin and contains upwards of 900 stars, the brightest at $V = 6 - 7$ mags. The subgroup central coordinates are α=22 55' 43" δ=+62 40' 14", J2000.

Moreno-Corral et al. (1993) used optical and IR photometry of O, B and A type stars. These were compared with MS calibrations to calculate individual extinctions and distance moduli, which were then averaged. Pozzo et al. (2003) recalculated these parameters from the Moreno-Corral et al. (1993) individual extinctions and distance moduli, but excluded star 11 from Blaauw et al. (1959) which is of dubious membership. The resulting values which I adopt are $dm = 9.65 \pm 0.20$ and $A_V = 2.81 \pm 0.10$.

4.2.8 IC348

IC348 is a cluster associated with the Per OB2 complex in the perseus spiral arm. This young cluster spans a region approximately < 15 arcmin in diameter. IC348 contains upwards of 300 stars, but is a site of low-mass star formation containing no O-type stars. The total mass of the IC348 cluster is estimated to be $\approx 200 M_{\odot}$ (Luhman et al., 2003). The central position of the cluster is α=03 44' 30" δ=+32 00' 00", J2000.

The distance of Strom et al. (1974) was derived using *UBVKL* photometry of 20 stars with $V < 14$ believed to be cluster members, in conjunction with various literature spectral types and MK classifications, resulting in a distance of $7.5^{+0.14}_{-0.16}$ mags. This is the same distance as that derived to the Per OB2 association, $dm = 7.5$ mags, and is adopted here (see Herbig, 1998, for a discussion of the distance to IC348). The extinctions adopted for this field are individual star extinctions from Herbig (1998) and Luhman et al. (2003).

4.2.9 λ Ori

λ Ori is a cluster at the centre of the λ Ori association. The cluster spans a diameter of approximately 10 arcmin and its brightest objects reach $V = 3$ mags. Dolan & Mathieu (2001) provide evidence showing that this cluster may have undergone triggered star formation along a radially

expanding shell centred on a supernova remnant. The cluster contains around 200 stars and has an estimated total mass of $> 500 M_{\odot}$ Dolan & Mathieu (2001). The central position of the cluster is α=05 35' 08" δ=+09 56' 00", J2000.

The *HIPPARCOS* distance modulus to this cluster is $dm = 7.90 \pm 0.17$, which I adopt. The extinction adopted to this cluster is calculated in Diplas & Savage (1994) as E(B-V)=0.12, equating to $A_V = 0.36$.

4.2.10 NGC2362

NGC2362 (Tau Canis Majoris cluster) is a cluster first discovered by Giovanni Battista Hodierna in 1654 and studied later by William Herschel in 1783. This cluster is associated with the outer edge of the Orion-Cygnus arm of the galaxy. The cluster spans a diameter of around 11 arcmin and its brightest stars are at $V = 4$ mags. The cluster comprises of around 300 stars and has an estimated total mass of $> 500 M_{\odot}$ (Dahm, 2005; Damiani et al., 2006). The central position of this cluster is $\alpha \approx$07 19' 00" $\delta \approx$-24 57' 00", J2000.

Balona & Laney (1996), use narrow-band photometry of B-type stars to derive $A_V = 0.31$ and $dm = 10.87 \pm 0.03$. Moitinho et al. (2001) also used the B-type stars to obtain $A_V = 0.31$ and $dm = 10.85$. The values adopted here are 10.87 ± 0.03 and $A_V = 0.31$.

4.2.11 IC5146

IC5146 or the Cocoon nebula is associated with dense molecular material of the Cygnus region, the cluster spans a diameter of approximately 10 arcmin with the brightest stars reaching $V = 7$ mags. Estimates of the total mass of this cluster are not available , although estimates from ^{12}CO and ^{13}CO emission lines have been used to estimate the mass of the associated dark cloud, $\approx 4500 M_{\odot}$ (Dobashi et al., 1992). The cluster probably contains around 200 stars Damiani et al. (2006). The central position of this cluster is $\alpha \approx$21 53' 24" $\delta \approx$+47 12' 00", J2000.

Herbig & Dahm (2002) derived a distance from a comparison of the early-type, specifically B type stars with MS models yielding $dm \simeq 10.4$. They then calculated the reddening by assuming their distance and using the known spectral types of a selection of 38 stars, to yield $A_V = 3.0 \pm 0.2$. I have adopted $dm \simeq 10.4$. The individual extinctions used for the B type stars to calculate distance have been adopted, and an average extinction adopted for the remaining stars.

4.2.12 NGC6530

NGC6530 is a young open cluster located in front of the M8 giant molecular cloud (also referred to as the Lagoon nebula). NGC6530 was discovered by Hodierna before 1654 and was observed later by Flamsteed in 1680. This cluster spans an apparent diameter of 14 arcmin and contains > 800 stars, the brightest of which have a $V = 4 - 5$ mags (Prisinzano et al., 2005). The total mass estimate for this cluster, using X-ray sources is $700 - 930 M_{\odot}$ (Prisinzano et al., 2005). The central position of this cluster is $\alpha \approx$18 04' 48" $\delta \approx$-24 20' 00", J2000.

Prisinzano et al. (2005) used MS fitting of the stars in the blue envelope. These are MS stars assumed to be at the cluster distance or closer. They calculate $dm \simeq 10.48$ and use the value of the

extinction from Sung et al. (2000). Sung et al. (2000) use the Q-method (detailed in Section 4.6.3) for early-type stars yielding $A_V \simeq 1.09$. Sung et al. (2000) then fitted a ZAMS relation individually to 30 of these early-type stars, yielding two different average distances, assuming one was due to binarity they adopted the further distance, $dm = 11.25 \pm 0.1$ mags. In Prisinzano et al. (2005) a useful summary table of the distances calculated to this cluster is presented along with a summary of the literature of the field. For comparison I have adopted $dm \simeq 10.48$.

4.2.13 NGC1960

NGC1960 (or M36) was also first discovered by Hodierna and is not associated with dense molecular material. The cluster has an apparent diameter of 12 arcmin and the brightest stars are at $V = 6$ mags. The central position of this cluster is α=05 36' 18" δ=+34 08' 24", J2000.

Sanner et al. (2000) used proper motion memberships for stars brighter than V=14 and statistical field star subtraction below this down to V=19. MS isochrone fitting was used, with an isochrone fit to the MS yielding values of $A_V = 0.77 \pm 0.06$ (from $E(B\text{-}V) = 0.25 \pm 0.02$) and $dm = 10.6 \pm 0.2$ mags.

4.2.14 NGC2244

NGC 2244 or the Rosette nebula is associated with the Mon OB2 association. The cluster spans an apparent diameter of 24 arcmin and contains at least 30 OB-type stars (Park & Sung, 2002), the brightest of which are at $V = 4-5$ mags. The central position of this cluster is $\alpha \approx$21 53' 24" $\delta \approx$+47 12' 00", J2000.

Hensberge et al. (2000) used eclipsing binaries to derive a distance of $dm = 10.72^{+0.16}_{-0.15}$. Previous MS isochrone fitting studies placed this SFR at $dm = 11.11^{+0.16}_{-0.16}$ (Perez et al., 1987), and $dm = 11.1$ (Park & Sung, 2002). Literature derivations of extinctions include the values of $A_V = 1.49$ (Perez et al., 1987) and $A_V = 1.46$ (Park & Sung, 2002). The initially adopted values are $dm = 10.72^{+0.16}_{-0.15}$ and $A_V = 1.46$.

Table 4.1 contains a summary of the best current literature distances and extinctions for the studied SFRs.

Field	A_V	Source	Method	dm(mags)	Source	Method	Nominal Age (Myrs)	Source
NGC2547	0.15	1	Q-method	$8.18^{+0.29}_{-0.26}$	11	HIPPARCOS	30-45	27
h & χ Per	1.57 ± 0.079	2	Q-method	11.7 ± 0.1	10	MS fitting	12.6	2
NGC2264	0.371	4	Q-method	9.6	13	Avg	3	Avg
NGC7160	1.17	5	Intrinsic colours	9.77	14	Isochrone fitting	10	5
Cep OB3b	2.882	6	Q-method	9.65 ± 0.20	15	Spectroscopy	5.5	20
σ Ori	0.18	8,9	Iso fitting	7.8 ± 0.39	17	HIPPARCOS	3	17
The ONC	$A*$	19	Spectral classes	8.38 ± 0.37	18	H_2O MASER	≈ 0.8	19
IC348	A*	7	Spectral classes	$7.5^{+0.14}_{-0.16}$	16	HIPPARCOS	2-3	7
λ Ori	0.37	24	Spectral classes	7.90 ± 0.17	24	HIPPARCOS	4, 6-7	28
NGC2362	0.31	25	Avg	10.87 ± 0.03	26	MS fitting	$\simeq 1.8, 3.5-5$	25
IC5146	3.0 ± 0.2	23	Spectral classes	10.4	23	MS fitting	1	23
NGC6530	1.09	22	MS fitting	10.48	22	MS fitting	2.3,1.5 or 0.5-1.5	29, 30 and 31
NGC2244	1.46	32	MS fitting	$10.72^{+0.16}_{-0.15}$	33	Eclipsing binaries	2.3 ± 0.2	33
NGC1960	0.77	34	MS fitting	10.6	34	MS fitting	16	34

Table 4.1: Extinction, *dm*, ages and sources. A* = Individual values from sources indicated.
Sources as follow. 1 Claria (1982b), 2 Slesnick et al. (2002), 3 Sanner et al. (2000), 4 Mendoza V. & Gomez (1980), 5 Sicilia-Aguilar et al. (2004), 6 Jordi et al. (1996), 7 Herbig (1998) and Luhman et al. (2003), 8 Béjar et al. (1999), 9 Sherry et al. (2004),Brown et al. (1994), 10 Capilla & Fabregat (2002), 11 Robichon et al. (1999), 12 Sanner et al. (2000), 13 Dahm & Simon (2005), 14 Sicilia-Aguilar et al. (2004), 15 Pozzo et al. (2003), 16 Herbig (1998), 17 Sherry et al. (2004), 18 Genzel et al. (1981), 19 Hillenbrand (1997), 20 Jordi et al. (1996), 21 Diplas & Savage (1994), 22 Prisinzano et al. (2005), 23 Herbig & Dahm (2002), 24 Diplas & Savage (1994), 25 Dahm (2005), 26 Balona & Laney (1996), 27 Jeffries & Oliveira (2005), 28 Murdin & Penston (1977) and Dolan & Mathieu (2001), 29 Siess et al. (2000), 30 Sung et al. (2000), 31 Damiani et al. (2004), 32 Park & Sung (2002), 33 Hensberge et al. (2000) and 34 Sanner et al. (2000).

SFRs	Data type	Source
The ONC	VI photometry and $Log(T_{\rm eff})$	Hillenbrand (1997)
NGC6530	$UBVI$ photometry	Sung et al. (2000)
NGC2244	$UBVIH_{\alpha}$	Park & Sung (2002)
NGC2264	$UBVRI$ photometry	Mendoza V. & Gomez (1980)
NGC2362	UBV photometry	Johnson & Morgan (1953)
λ Ori	UBV photometry	Murdin & Penston (1977)
σ Orionis	$V_T B_T$ photometry(1)	Caballero (2007)
chi Per	UBV photometry	Slesnick et al. (2002)
h Per	UBV photometry	Slesnick et al. (2002)
NGC1960	UBV photometry	Johnson & Morgan (1953)
NGC2547	UBV photometry	Claria (1982a)

Table 4.2: Literature sources for data. Notes as follows. (1) *TYCHO* VB bands.

4.3 The data

Most of the SFRs from table 4.1 can be fitted using photometry of the MS for a distance and extinction. For IC5146, CepOB3b and IC348 the MS is either not well populated, as in IC348 and IC5146, or the SFR reddening is prohibitively variable, CepOB3b. The sources of photometry of the MS for the SFRs where it is available are detailed in Table 4.2.

4.3.1 Memberships and photometric cuts

This section describes cuts made to the data prior to fitting. Although the literature sources often provide membership criteria further photometric cuts are required. These cuts are needed to remove non-members stars which may have satisfied the criteria in the original source from Table 4.2. In addition stars must be cut due to fitting limitations, for instance where the colour-$T_{\rm eff}$ relationship is no longer defined for *TYCHO* photometry. Some stars have also been lost from the source photometric catalogues due to missing values of photometry in some bands. Most importantly, to avoid distance-age degeneracy problems and to minimise the effect of age assumption on the distance derivations only HM stars on or near the MS are fitted (as explained in Chapter 3). Therefore, these photometric cuts must isolate the required section of the sequence from which reliable distances and extinctions can be derived.

If stars which are too red are included they may be pre-MS stars, if stars which are too bright are included they may have evolved away from the MS. Therefore the photometric cuts must effectively isolate the stars between the turn-off and turn-on. As the MS lies clear of the contamination and is easily identifiable in the studied SFRs these cuts can be placed empirically. CMDs of all the SFRs studied showing the population selected for fitting are presented in Section 4.3.1.3.

4.3.1.1 The turn-off cut

If stars which are too bright are included they may have evolved away from the MS (turn-off), so a photometric cut must be made at the turn-off, for the nominal age, despite the fact that in

SFR	B-V Cut	$E(B-V)$	$(B-V)_0$		Nominal Age (Myrs)
			Empirical	Theoretical	
The ONC[(1)]	-	-	0.1	-0.13	1
NGC6530[(2)]	0.5	0.32	0.18	-0.17	1
NGC2244[(2)]	0.45	0.47	-0.02	-0.13	2[(3)]
NGC2264	-0.02	0.03	-0.05	-0.1	3
NGC2362	0.04	0.09	-0.05	-0.1	3
λ Ori	0.20	0.11	0.09	-0.1	3
σ Orionis[(4)]	0.03	0.06	-0.03	-0.06	4-5
chi Per	0.7	0.50	0.2	0.2	13
h Per	0.74	0.54	0.2	0.2	13
NGC1960	0.25	0.20	0.05	0.2	16[(5)]
NGC2547	0.1	0.04	0.06	> 0.2	38[(6)]

Table 4.3: The empirical and theoretical cuts for each SFR. The apparent cut has been converted into intrinsic colour using the $E(B-V)$ derived in Section 4.8. Also shown the nominal age adopted for each SFR. The notes are as follows. (1) Individual extinctions derived from $T_{\rm eff}$, see Section 4.6. (2) Individual extinctions derived using Q-method (see Section 4.6.3) for distance result adopted, mean extinctions also used see Sections 4.6.3 and 4.4. (3) Age from Park & Sung (2002). (4) Data in *TYCHO* photometric system. (5) Age from Sanner et al. (2000). (6) Age from Naylor & Jeffries (2006).

some cases the MS appears to extend above the turn-off (see Section 4.9 for a discussion of this discrepancy).

There is also a shift in the position of the MS as the isochronal age increases, as the stars are 'preparing' to turn-off. I have examined this effect and the result of assuming the wrong age for the model sequence. The effect is found to be negligible in this experiment as explained in Section 4.5.3.

4.3.1.2 The turn-on cut

The colour at which stars join the MS (turn-on) and hence where the pre-MS cut should be made is predicted by pre-MS isochrones. Figure 4.1 shows the pre-MS isochrones of Siess et al. (2000) for ages of 1, 3, 5, 15 and 40 Myrs (the latter being age of the oldest SFR). The colour of the turn-ons are shown in Figure 4.1. However for the younger SRFs the observed MS in a CMD often appears to extend redder and fainter than predicted by the pre-MS isochrones. Positions of the cuts have been decided empirically, that is to say the bottom of the MS in the data has been identified and the cut placed there, at the blue edge of the radiative-convective (R-C) gap (a separation between the fully convective pre-MS and MS discussed in Chapter 6). Table 4.3 shows the positions of the cuts predicted from the isochrones of Siess et al. (2000), the extinction (see Sections 4.5.2.1 and 4.8), the actual cut employed and the age assigned for each SFR. These are discussed in more detail in Chapter 6. Placing the turn-on cuts empirically results in significantly more precise distances where there is a disagreement between these and the theoretically predicted positions i.e. for the younger SFRs. The fact that the theoretical prediction for the turn-on does not match the empirical position of the MS terminus has important ramifications. An extended discussion of the implications of colour cut positions can be found in Chapter 6.

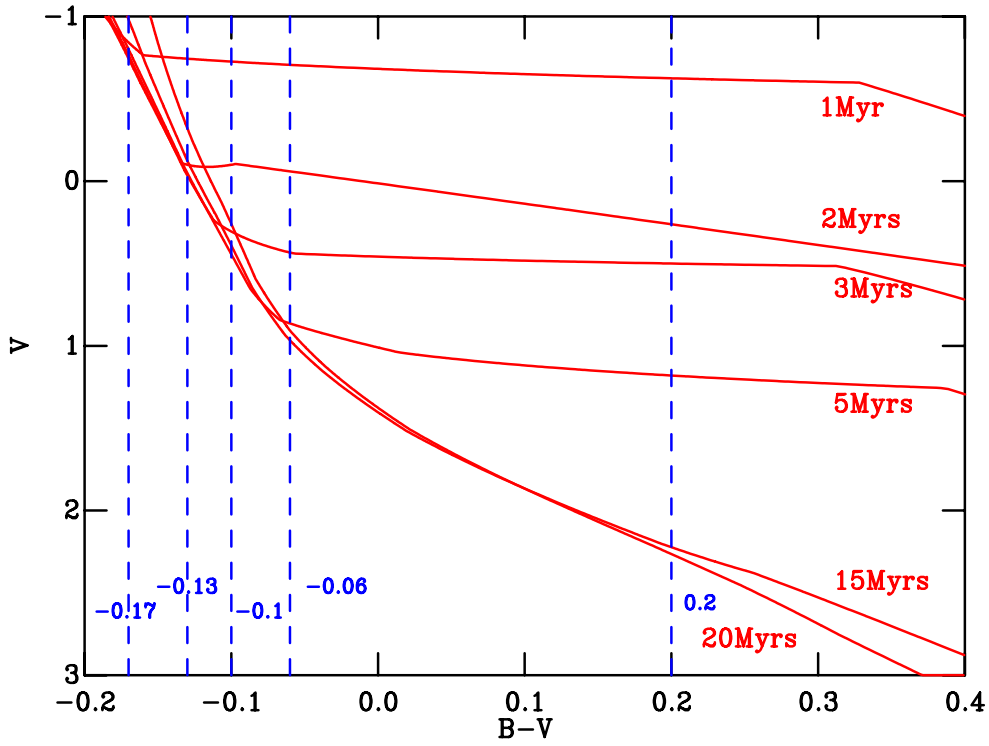

Figure 4.1: 1, 3, 5, 15 and 20 Myr isochrones from Siess et al. (2000) showing the MS, and pre-MS. $B-V$ colour cuts are shown for each age to isolate the MS. These are: -0.17, -0.1, -0.06 and 0.2 for 1, 3, 5, and older sequences respectively.

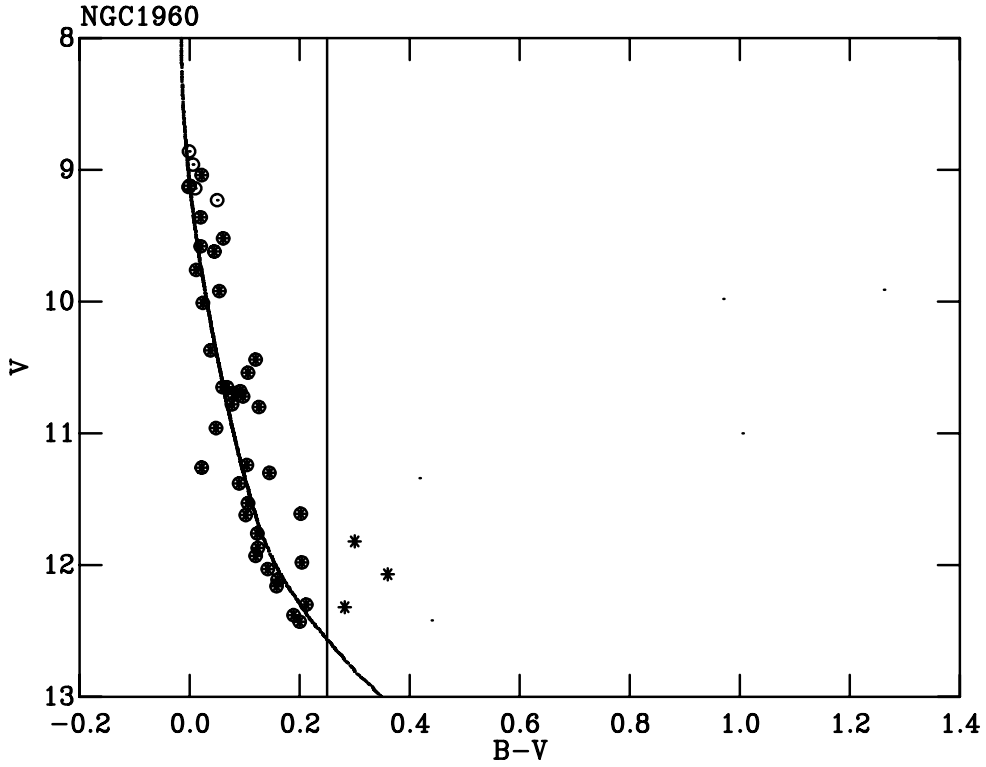

Figure 4.2: NGC1960. Photometry of Johnson & Morgan (1953) plotted as dots, with the stars used for the distance derivation plotted as asterisks and the stars used for extinction derivation circled. Filled circles therefore represent stars used for both distance and extinction derivation. The bold line is the photometric cut used for the distance determination. The 20 Myr MS isochrone of Lejeune & Schaerer (2001) is also shown, adjusted by the approximate distance and extinction of the cluster, as a guide.

4.3.1.3 Fitted stars

- **NGC1960**: For NGC1960 the photometry of Johnson & Morgan (1953) is used, employing only photometric cuts. Figure 4.2 shows the stars used for the extinction and distance derivations.
- **NGC2264**: Photometry for NGC2264 comes from Mendoza V. & Gomez (1980) and as with NGC1960 photometric cuts have been used. Figure 4.3 shows the stars selected.
- **NGC2362**: Johnson & Morgan (1953) provide photometry for NGC2362 and only photometric cuts have been employed for this cluster. Figure 4.4 shows the stars used.
- **NGC2547**: Photometry for this cluster is from Claria (1982a). Members were selected based on proper motions from Claria (1982a) and subsequent photometric cuts. The selected stars are shown in Figure 4.5.
- **NGC6530**: Sung et al. (2000) provide photometry and target stars have been photometrically selected, shown in Figure 4.6.
- χ **Per**: Photometry for this cluster is from Slesnick et al. (2002). Here those stars given as

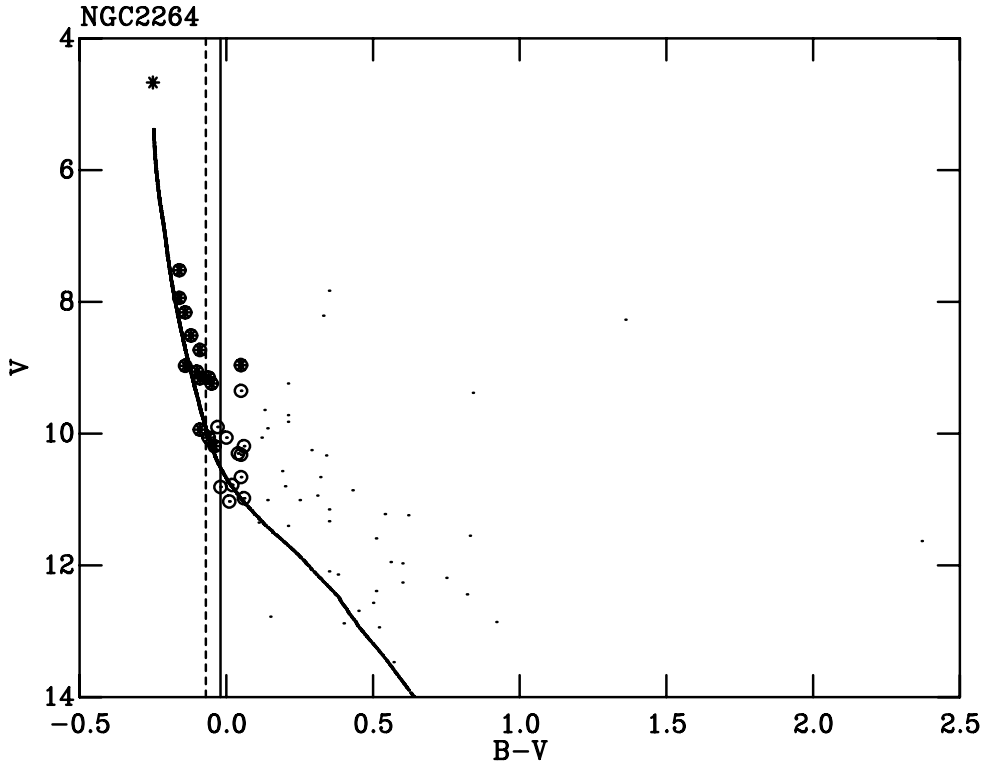

Figure 4.3: NGC2264. Photometry of Mendoza V. & Gomez (1980) plotted as dots, with the stars used for the distance derivation plotted as asterisks and the stars used for extinction derivation circled. Filled circles therefore represent stars used for both distance and extinction derivation. The bold line is the empirical photometric cut and the dashed line is position of the turn-on predicted by theory. The 3 Myr MS isochrone of Lejeune & Schaerer (2001) is also shown, adjusted by the approximate distance and extinction of the cluster, as a guide.

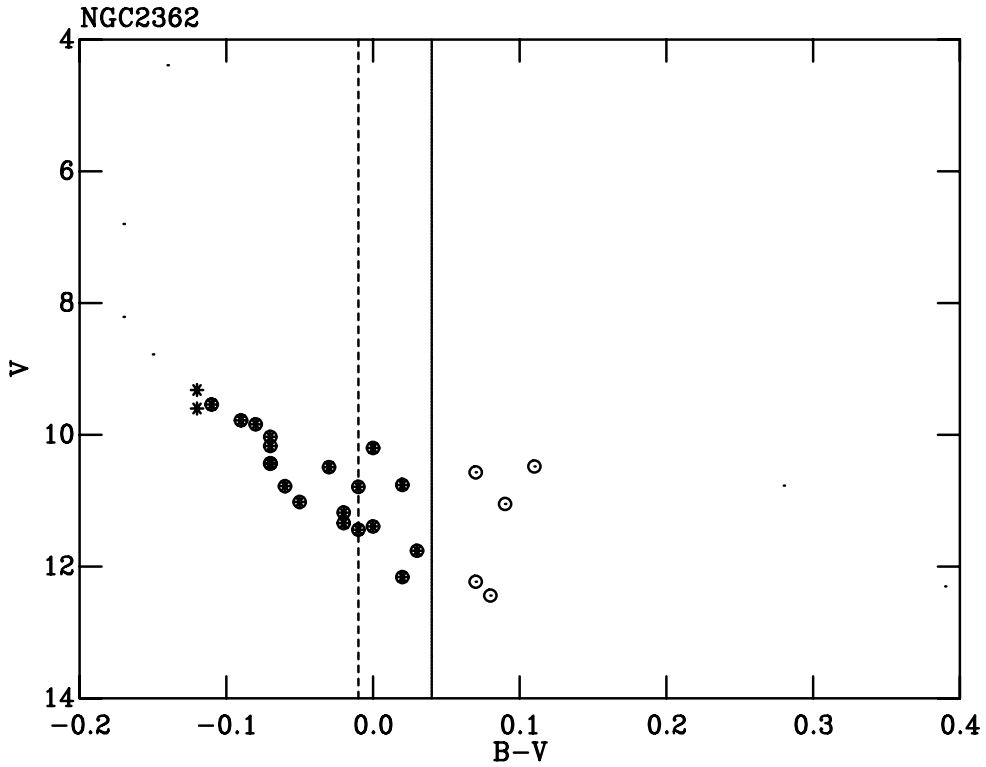

Figure 4.4: NGC2362. Photometry of Johnson & Morgan (1953) plotted as dots, with the stars used for the distance derivation plotted as asterisks and the stars used for extinction derivation circled. Filled circles therefore represent stars used for both distance and extinction derivation. The bold line is the empirical photometric cut and the dashed line is position of the turn-on predicted by theory. The approximate isochrone has been removed for this and subsequent figures for clarity.

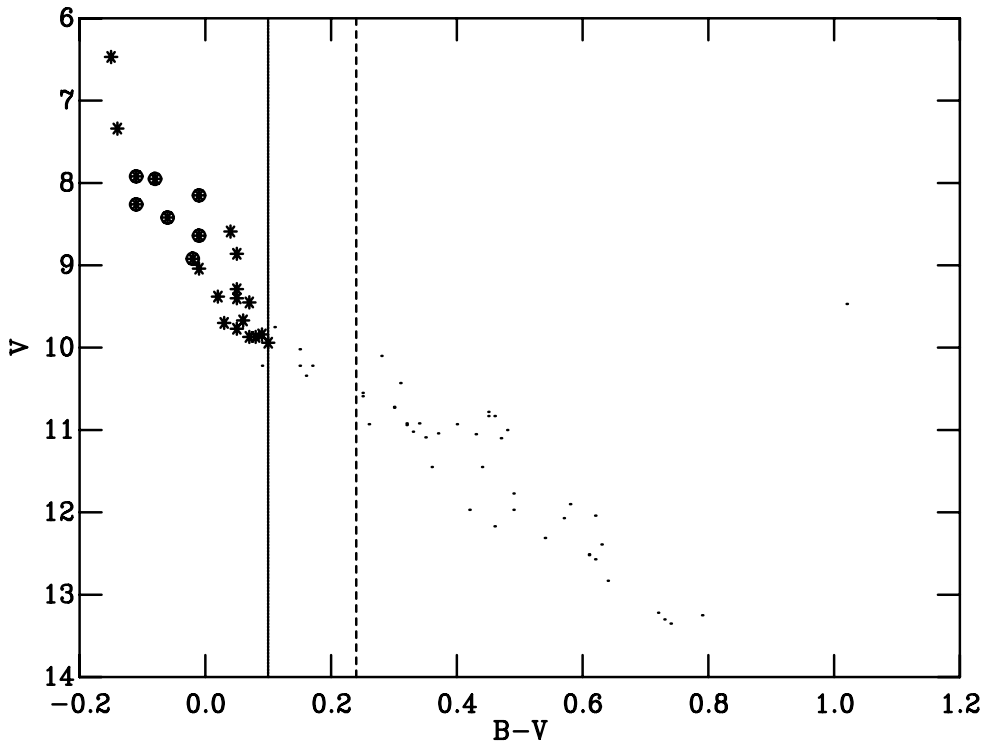

Figure 4.5: NGC2547. Photometry of members from Claria (1982a) plotted as dots, with the stars used for the distance derivation plotted as asterisks and the stars used for extinction derivation circled. Filled circles therefore represent stars used for both distance and extinction derivation. The bold line is the empirical photometric cut and the dashed line is position of the turn-on predicted by theory.

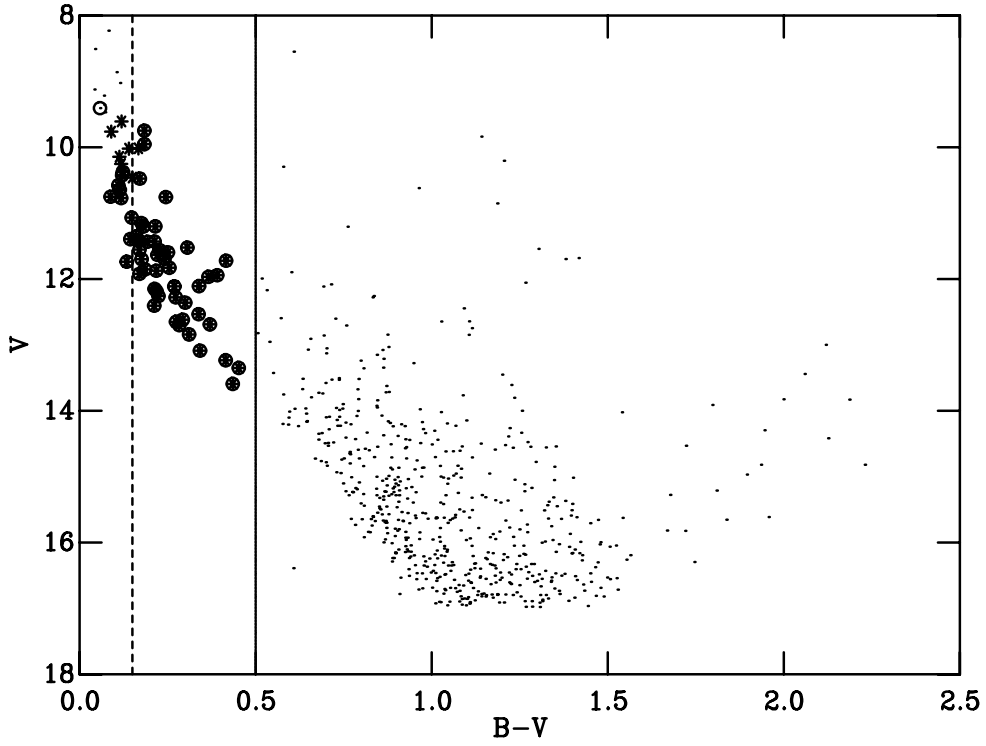

Figure 4.6: NGC6530. Photometry of Sung et al. (2000) plotted as dots, with the stars used for the distance derivation plotted as asterisks and the stars used for extinction derivation circled. Filled circles therefore represent stars used for both distance and extinction derivation. The bold line is the empirical photometric cut and the dashed line is position of the turn-on predicted by theory.

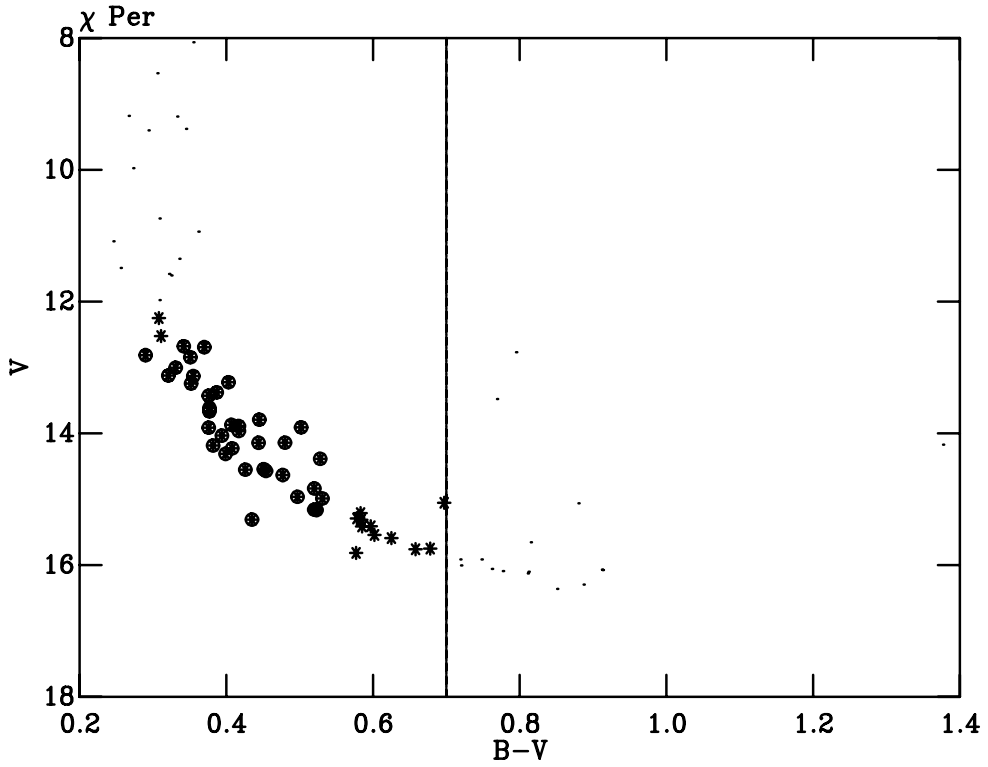

Figure 4.7: χ Per: Photometry of stars defined as members in Slesnick et al. (2002) and within 2' (radius) of (α=2 22' 5.02" δ=+57 7' 43.44") plotted as dots, with the stars used for the distance derivation plotted as asterisks and the stars used for extinction derivation circled. Filled circles therefore represent stars used for both distance and extinction derivation. The bold line is the photometric cut used.

members in Slesnick et al. (2002) were initially selected. After this only those stars within a radius of 2' from the central position defined in Chapter 5 (α=2 22' 5.02" δ=+57 7' 43.44"), based on the positions of HM stars, were retained. Further photometric cuts were made and the used stars can be seen in Figure 4.7.

- **h Per**: The selection process for h Per is as given for χ Per, but using the central coordinates of α=2 18' 58.76" δ=+57 8' 16.54" (J2000). The target stars can be seen in Figure 4.8.

- λ **Ori**: Photometry from Murdin & Penston (1977) has simply been cut photometrically for fitting, the selected stars are shown in Figure 4.9.

- **NGC2244**: Photometry from Park & Sung (2002) has been cut photometrically for fitting, the selected stars are shown in Figure 4.10.

- **The ONC**: Photometry for the ONC is from Hillenbrand (1997). Stars with membership probability in Hillenbrand (1997) of $\geq$ 90% were selected. For only those stars with a $log(T_{\rm eff}) > 3.900$ an absolute magnitude and intrinsic colour were derived using the $T_{\rm eff}$ provided in Hillenbrand (1997) as explained in Section 4.6. Photometric cuts were also made, with the resulting stars used presented in Figure 4.11 in apparent magnitude and colour.

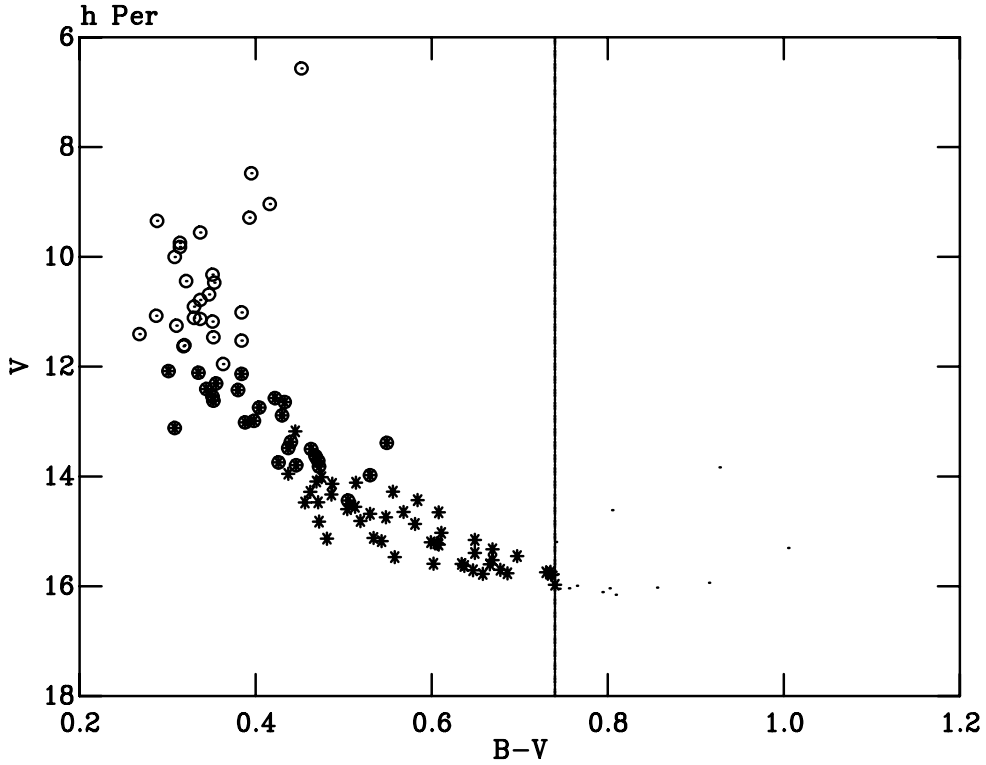

Figure 4.8: h Per. Photometry of stars defined as members in Slesnick et al. (2002) and within 2' (radius) of (α=2 18' 58.76" δ=+57 8' 16.54") plotted as dots, with the stars used for the distance derivation plotted as asterisks and the stars used for extinction derivation circled. Filled circles therefore represent stars used for both distance and extinction derivation. The bold line is the photometric cut used.

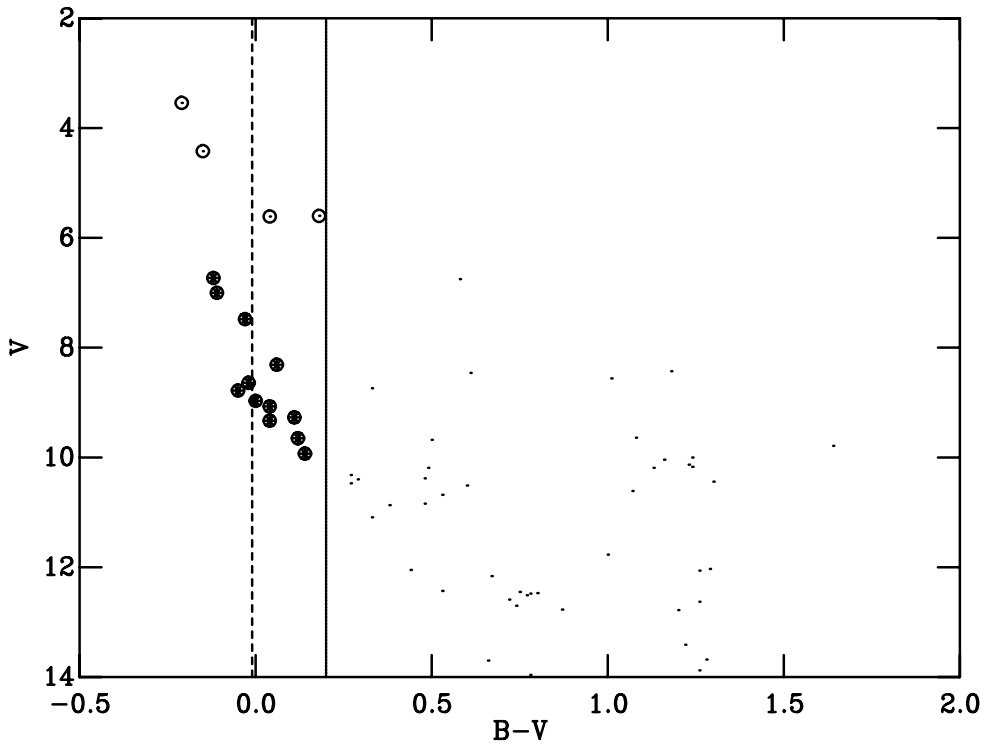

Figure 4.9: λ Ori. Photometry of Murdin & Penston (1977) plotted as dots, with the stars used for the distance derivation plotted as asterisks and the stars used for extinction derivation circled. Filled circles therefore represent stars used for both distance and extinction derivation. The bold line is the empirical photometric cut and the dashed line is position of the turn-on predicted by theory.

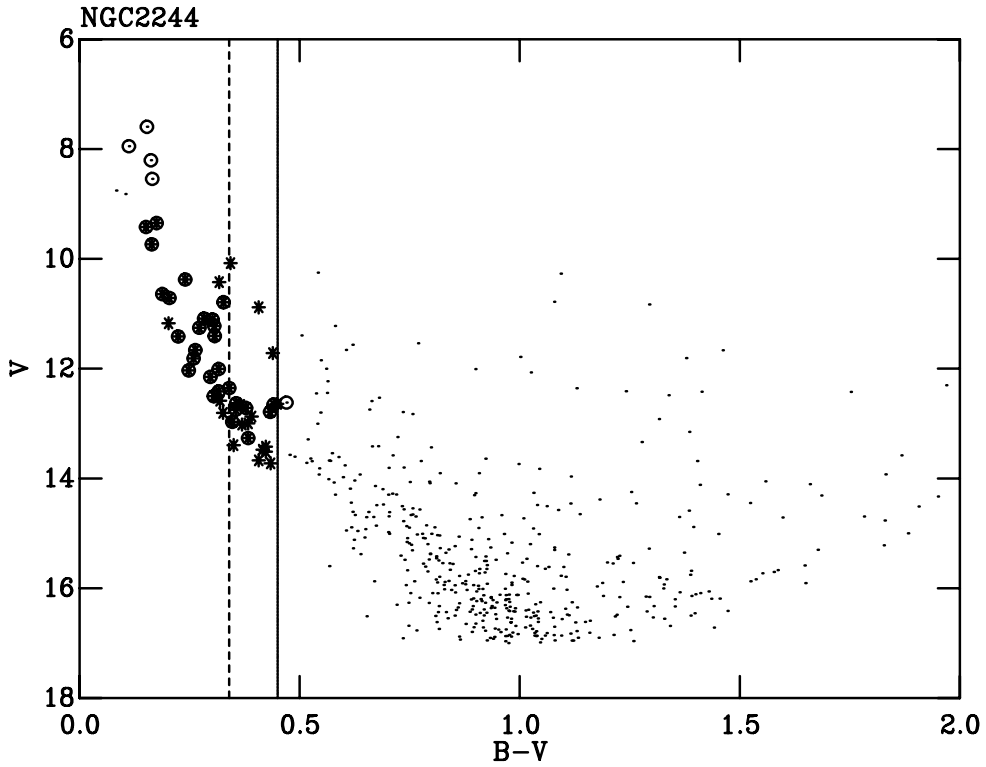

Figure 4.10: NGC2244. Photometry of Park & Sung (2002) plotted as dots, with the stars used for the distance derivation plotted as asterisks and the stars used for extinction derivation circled. Filled circles therefore represent stars used for both distance and extinction derivation. The bold line is the empirical photometric cut and the dashed line is position of the turn-on predicted by theory.

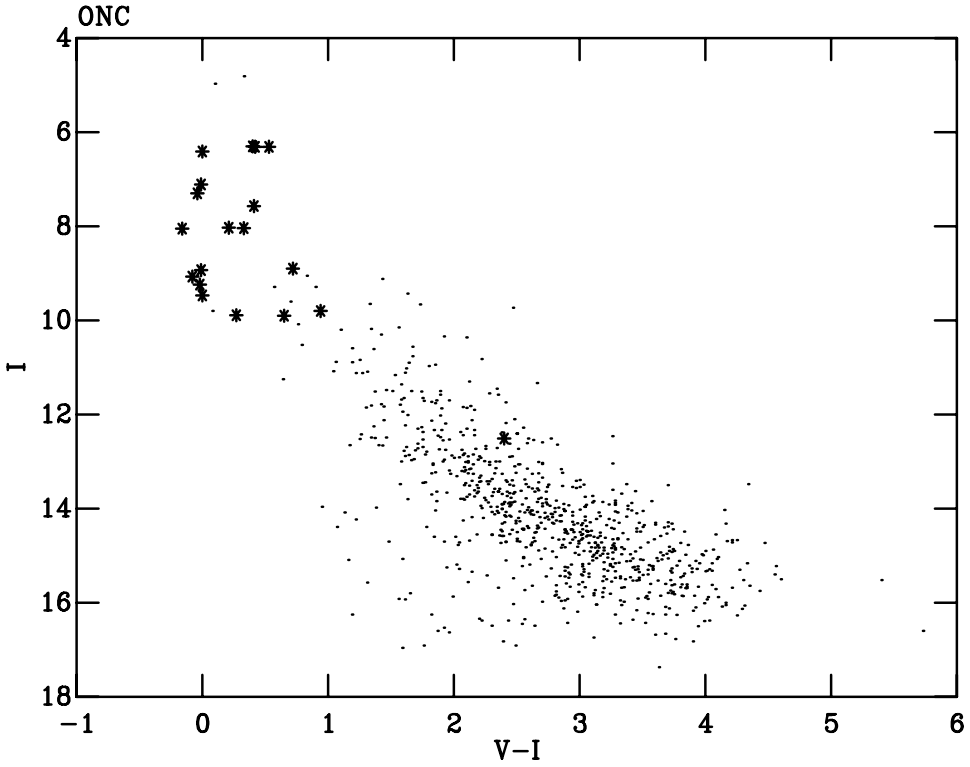

Figure 4.11: The ONC. Photometry of Hillenbrand (1997) plotted as dots with the stars used for the distance derivation appearing as asterisks. Here the stars have been cut using the $T_{\rm eff}$ values.

- σ **Orionis**: The photometry for this cluster is in the *TYCHO* photometric system and is from Caballero (2007). Photometric cuts have been made and the stars used for the distance derivation are shown in Figure 4.12.

4.4 The models

The MS stellar interior models of the Padova (Girardi et al., 2002) and Geneva (Lejeune & Schaerer, 2001) groups have been used. These interior models are amongst the most recent and widely used formulations. These models provide an effective temperature ($T_{\rm eff}$), luminosity and surface gravity. These values must then be converted into colours and magnitudes in the required photometric system (Johnson-Cousins-Glass) to allow the fitting of photometric data. Colours are found using a $T_{\rm eff}$-colour relation, and magnitudes using the bolometric correction to the luminosity. Both the $T_{\rm eff}$-colour relation and bolometric correction come from using the parameters from a stellar interior model to find the correct model atmosphere and then folding the resulting flux distribution through appropriate photometric filter responses. Once this is achieved the photometric colours and magnitudes must then be calibrated to a standard scale, using defined colours of Vega in the calibrated system. Three main isochrone and extinction systems calibrated to two different Vega colour systems are used, the details of each follow.

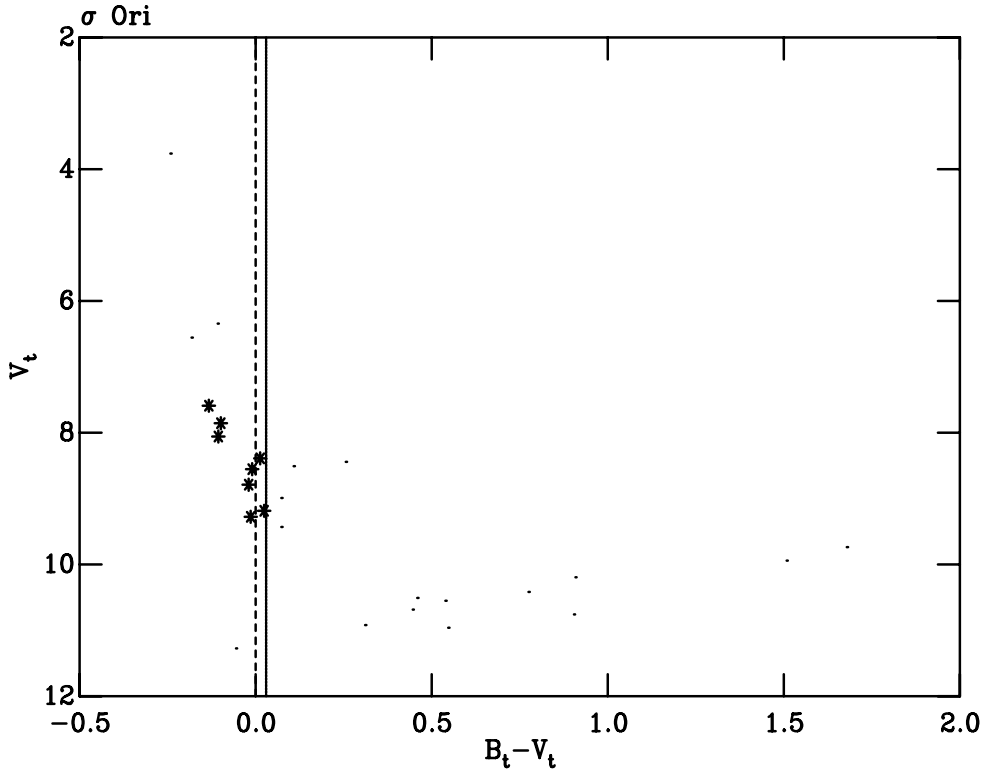

Figure 4.12: σ Ori. Photometry of Caballero (2007) plotted as dots with the stars used for the distance derivation plotted as asterisks. The bold line is the empirical photometric cut and the dashed line is position of the turn-on predicted by theory.

4.4.1 Geneva

The Geneva isochrones (as provided in Lejeune & Schaerer, 2001) are from the Geneva stellar interior models, basic set ("c") generally applicable for stars with $M < 12M_{\odot}$, in conjunction with the updated BaSeL-2.2 model atmospheres from Westera et al. (1999). To derive photometric magnitudes (V) they have adopted the bolometric corrections from Lejeune et al. (1998) which are defined to fit the empirical scale of Flower (1996) (not calibrated to the Sun). Colours have then been calculated for Johnson-Cousin photometry using the filter response functions of Buser & Kurucz (1978) (UBV) and Bessell (1979) (RI). The colours and magnitudes of the isochrone are then calibrated to a Vega colour of zero. The extinctions for these isochrones use the canonical extinction vectors, namely $E(U-B)/E(B-V) = 0.73$, $A(V)/E(B-V) = 3.1$ and $A(V)/E(V-I) = 0.41$.

4.4.2 Geneva-Bessell

For the Geneva-Bessell isochrones the interior models of Lejeune & Schaerer (2001) were used. Their conversion to photometric colours follows that of Bessell et al. (1998). Bessell et al. (1998) use the ATLAS9 atmosphere models of Castelli et al. (1997) (at solar metallicity only) and the filter responses of Bessell (1990) ($UBVRI$), to calculate the colour-$T_{\rm eff}$ relations and bolometric corrections. The resulting Johnson-Cousins-Glass photometry is then calibrated to a Vega colour of zero. Although Lejeune & Schaerer (2001) provide isochrones in intrinsic colour and absolute magnitude in this system in practice these conversions are carried out in the fitting code, since that allows calibration to what I term a non-zero system where $(B-V)_{Vega} = -0.002$ and $(U-B)_{Vega} = -0.004$. The colour dependent extinction vectors of Bessell et al. (1998) are consistent with these isochrones.

4.4.3 Padova-Bessell

For the Padova-Bessell isochrones the stellar interior models of Girardi et al. (2002) were used. The colours and magnitudes are then calculated using the conversions of Bessell et al. (1998) as for the Geneva-Bessell isochrones. The resulting Johnson-Cousins-Glass photometry is then calibrated to either a Vega colour of zero or the non-zero system. As with the Geneva-Bessell isochrones these isochrones use the colour-dependent extinction vectors of Bessell et al. (1998) for the Padova-Bessell isochrones is possible.

4.4.4 Extinction vectors in the Bessell system

It is well known that extinction vectors are actually a function of intrinsic colour (or spectral type), as shown in Bessell et al. (1998) and Dean et al. (1978). Bessell et al. (1998) provide extinction vectors as a function of colour based on the extinction curves of Mathis (1990) for an $E(B-V) = 0.3$. These extinction vectors as stated above can be used for the Geneva-Bessell and Padova-Bessell models.

4.4.4.1 The extinction dependence of the extinction vector

As these extinction vectors are provided for an $E(B-V) = 0.3$, it is important to confirm that larger extinction values, as found in some of the studied SFRs, do not significantly alter the vectors. This analysis was performed by Tim Naylor. The solar abundance ATLAS 9 spectra with the "new" opacity distribution function (Castelli & Kurucz, 2004) were folded through the band-passes of Bessell et al. (1998). The spectra were then reddened using the method of Cardelli et al. (1989), to achieve an $E(B-V) \approx 0.3$. The function of Cardelli et al. (1989) is that used in Bessell et al. (1998) after tabulation by Mathis (1990). An R_v of 3.2 (where $R_v = \frac{A_V}{E(B-V)}$) was chosen to match the extinction vectors of Bessell et al. (1998) in the BV pass-bands. The highest extinction of the studied SFRs is, $E(B-V) \approx 1$. The resulting differences in R_v between $E(B-V) = 0.3$ and $E(B-V) = 1$ were calculated over the colour range of interest ($B-V < 1.5$). This resulted in a maximum difference in applied extinction of -0.02 mags.

4.4.5 *TYCHO* photometry

For σ Orionis the data were taken in the *TYCHO* photometric system. These data were fitted using the conversion of Bessell (2000) to transform the Geneva-Bessell isochrones into the *TYCHO* system. Tim Naylor also used a similar technique to that of Section 4.4.4.1 to derive extinction vectors in the *TYCHO* photometric system. The zero-points for these vectors were derived by matching the resulting colour-$T_{\rm eff}$ relation (for $B-V$) of Bessell (1990) and the transformation of Bessell (2000). For values of $(B-V)_T < 0.065$ this gave,

$$\frac{(A_V)_T}{E(B-V)_T} = 3.358 + 0.237(B-V)_T, \tag{4.1}$$

and for $0.065 < (B-V)_T < 0.5$

$$\frac{(A_V)_T}{E(B-V)_T} = 3.387 - 0.207(B-V)_T. \tag{4.2}$$

The worst deviation of these fits from the curve is 0.05 mag at a $B-V = 1$, with a typical deviation around $B-V = 0$ of 0.01 mag. These extinction vectors have been used to apply a literature extinction ($E(B-V) = 0.06$, Brown et al., 1994) as fitting for an extinction in a colour-colour diagram is not possible (only V_t and B_t are available).

It is useful to calculate the difference in distance if these changes are unaccounted for. A population was simulated in the *TYCHO* photometric system at 10 Myr and fitted using a Johnson-Cousins-Glass system. The resulting difference in distance modulus is $dm \approx -0.12$ (or with a cut at $B-V = 0.2$, $dm \approx -0.19$).

4.5 Fitting

Once the stars for fitting have been selected, as shown in Section 4.3 the derivation of the extinction and distance can be undertaken. This section describes the details of this procedure. A practical example is used to describe the details involved in the fitting for a distance and mean extinction in

Section 4.5. Throughout this section and later sections in this chapter all isochrone fits displayed and test undertaken use the Geneva-Bessell isochrones unless otherwise stated. This choice is somewhat arbitrary as the model dependency between the studied models is small (as shown in Section 4.7.

4.5.1 Fitting statistic

The fitting statistic used in this work is τ^2, which is introduced in Naylor & Jeffries (2006). Fitting of MS data using this technique is described in Jeffries et al. (2007). τ^2 is essentially a generalised χ^2 statistic including uncertainties in two dimensions, and models with a two-dimensional distribution as opposed to a single isochronal line. The best fitting model is found by minimising τ^2.

4.5.1.1 τ^2 definition

The τ^2 statistic is constructed by first simulating a coeval population of stars, including binaries, using a given isochrone. A probability map of each position in colour-magnitude space ($\rho(c_i, m_i)$) is created by normalising the simulated data at each magnitude. Effectively the integral along each magnitude in colour is normalised to unity. The data are then overlaid on this grid at different distances, with the multiplicative sum of the probability (ρ) evaluated at the position of each data point used as a fitting statistic, D. The actual value of τ^2 is then defined as $-2lnD$. Meaning maximising D or minimising τ^2 provides the best fit parameter.

The uncertainties for each data point are assumed to be a two-dimensional Gaussian profile, U_i. This means in practice that the probability sum of a given model and parameter must include not simply the value of ρ at a given point ($c_d m_d$), but also the integral of the $U_i \rho_i$ distributions to provide the new probability grid P. This results in $\tau^2 = -2ln\Pi P_i$, from the definition of τ^2. A complication of the uncertainties in a CMD being related (as in V vs $V-I$) means that in effect each Gaussian uncertainty distribution, U_i has skewed axes within the CMD space.

As P_i is defined as the integration of the probability grid, ρ_i, with the uncertainties, U_i, the value of P_i at a given data point (c_i, m_i) is given by

$$P_i = \int U_i(c - c_i, m - m_i)\rho(c, m)\mathrm{d}c\ \mathrm{d}m. \tag{4.3}$$

Where the integration is over both an incremental colour, dc, and magnitude, dm. The total likelihood of the the model is then D, the multiplicative sum of P_i,

$$D = \prod_{i=1,N} P_i = \prod_{i=1,N} \int U_i(c - c_i, m - m_i)\rho(c, m)\mathrm{d}c\ \mathrm{d}m. \tag{4.4}$$

Since τ^2 is defined as $-2lnD$ and $lnA \times lnB = ln(A+B)$, equation 4.4 becomes

$$\tau^2 = -2 \sum_{i=1,N} ln \int U_i(c - c_i, m - m_i)\rho(c, m)\mathrm{d}c\ \mathrm{d}m. \tag{4.5}$$

In most case the uncertainties are Gaussian in nature and can be described by

$$U_i(c-c_i, m-m_i) = e^{-\frac{(c-c_i)^2}{2\sigma_{c_i}^2} - \frac{(m-m_i)^2}{2\sigma_{m_i}^2}}. \quad (4.6)$$

Equation 4.5 therefore provides a maximum likelihood statistic where each data point is blurred by its uncertainties.

4.5.1.2 A generalised χ^2

Why has the definition of τ^2 been chosen as $\tau^2 = -2ln\Pi P_i$? Using the described formalism τ^2 fitting reduces to the χ^2 case for uncertainties in one-dimension and a one-dimensional model. This allows the τ^2 fitting statistic to be viewed as a generalised χ^2. If the effect of uncertainties in one axis, for instance colour, are removed the fitting should be equivalent to χ^2 fitting. In this case the observed value of c can only take one value and the uncertainty distribution is a δ function. Practically, $c = c_i$ and U_i is only a function of m. U_i is now

$$U_i = e^{-\frac{(m-m_i)^2}{2\sigma_{m_i}^2}}, \quad (4.7)$$

as the dependence on c_i has been removed. Substituting equation 4.7 into 4.5 yields

$$\tau^2 = -2 \sum_{i=1,N} ln \int e^{-\frac{(m-m_i)^2}{2\sigma_{m_i}^2}} \rho(m) \mathrm{d}m. \quad (4.8)$$

If the δ function for each point is normalised to one equation 4.8 reduces to

$$\tau^2 = -2 \sum_{i=1,N} ln(e^{-\frac{(m-m_i)^2}{2\sigma_{m_i}^2}}) = \sum_{i=1,N} \frac{(m-m_i)^2}{\sigma_{m_i}^2}. \quad (4.9)$$

Equation 4.9 is the standard for χ^2. Thus τ^2 is a generalised form of χ^2, where model and data uncertainties exists on only one dimension for χ^2.

4.5.2 Example distance fit: χ Per

It is most instructive to describe the fitting method via an example. The cluster χ Per which is approximately 13 Myrs old, at a distance modulus of 11.85 with an $A_V \approx 1.6$ (Slesnick et al., 2002) (the extinction is reasonably uniform). First, the derivation of distance is described. Deriving a distance does require a known extinction, the derivation of which is described later in this section.

Once a model is selected (from those described in Section 4.4), in this case Geneva-Bessell, a Monte-Carlo method is used to generate the colour-magnitude probability grid. The model is then adjusted through a range of distances and the values of τ^2 for each star summed to calculate a total value of τ^2 for each distance step, as detailed in Naylor & Jeffries (2006). These τ^2 contributions were clipped, i.e. the contribution to the total τ^2 for any single data point value is capped at some set value. Clipping avoids erroneously included non-members or anomalous objects many σ from a given model overwhelming the result. The lowest total τ^2 was then selected as the best fitting model.

Once a given fit was completed a probability of obtaining the resulting τ^2, $P_r(\tau^2)$, was calculated. If $P_r(\tau^2)$ is far from 50%, the fitting is repeated with an additional systematic uncertainty added to the data. This is analogous to scaling data error bars to achieve a $\chi^2_\nu = 1$. This process ensures the model is a good fit to the data and then parameter uncertainties can be derived. To derive these uncertainties, a bootstrap method described in Naylor & Jeffries (2006) is used, repeating the fitting 100 times and deriving 68% confidence intervals.

The best fit for χ Per is shown in Figure 4.13. The distance modulus and 68% confidence interval is $11.79 < 11.83 < 11.88$. This agrees with the result of 11.85 ± 0.05 from Slesnick et al. (2002), which of course uses the same dataset. In addition the τ^2 space resulting from this distance fit is shown in Figure 4.14, this plot shows the value of reduced-τ^2 (τ^2_ν) against the distance modulus. τ^2_ν is defined in Naylor & Jeffries (2006) as the sum of τ^2 over all points ($\sum_{i=1,N} \tau^2$) divided by the value of this which you would expect to exceed 50% of the time i.e. divided by the value of $\sum_{i=1,N} \tau^2$ when $P_r(\tau^2) \approx 0.50$. τ^2_ν for the 68% confidence interval is also shown as a dashed horizontal line. Figure 4.14 clearly shows two minima in τ^2_ν an inflection point, a steep increase towards lower distance moduli, and a shallow increase towards larger distance moduli. The lowest value is achieved when the single-star and equal-mass-binary sequences, being usually the most populated, lie over the corresponding section of the model, at $dm \approx 11.83$. As the distance modulus is decreased the equal-mass-binary sequence contribution maximises and another minima is found as stars from the single-star sequence pass through the unequal-mass binary sequences of the model, at $dm \approx 11.79$. A small inflection is then present as the single-star sequence moves over the equal-mass-binary sequence of the model, this is indeed separated from the absolute minimun by approximately 0.7 mags, positioned at $dm \approx 11.76$. The steep climb in τ^2_ν, towards lower distance moduli, is observed as the probablity density falls sharply to zero below the single-star sequence. Towards larger distance moduli however, the increase is much shallower as the single star sequence moves through the area occupied by the unequal-mass-binary sequences of the model.

Figure 4.13 and all subsequent figures showing fitted data have several elements requiring explanation. The shaded area shows the probability density of finding a star at a particular colour and magnitude (or colour and colour for extinction fitting). This density, ρ is that from Equation 1 of Naylor & Jeffries (2006) generated for a specific isochrone, in this case Geneva-Bessell. The circles show the positions of the photometry and the bars give the uncertainties in magnitude and colour. For all the figures showing fitted data (except those using individual extinctions, see Section 4.6) the models have been adjusted to the natural space of the data i.e. apparent colour and magnitude.

4.5.2.1 Mean extinction fitting

To allow the derivation of a distance, an extinction is required and is indeed crucial as changing it will change the distance derived for the stars being fitted. A mean extinction can be derived by fitting the data to an isochrone in a colour-colour diagram. Where *UBV* photometry is available to construct a colour-colour diagram, thereby removing the effects of distance (as discussed in Chapter 3), the sequence in $U-B$ vs $B-V$ is simply fitted in a similar fashion as that for a distance. The resulting fit can be seen in Figure 4.15, with a best fitting $E(B-V) = 0.50$. Figure

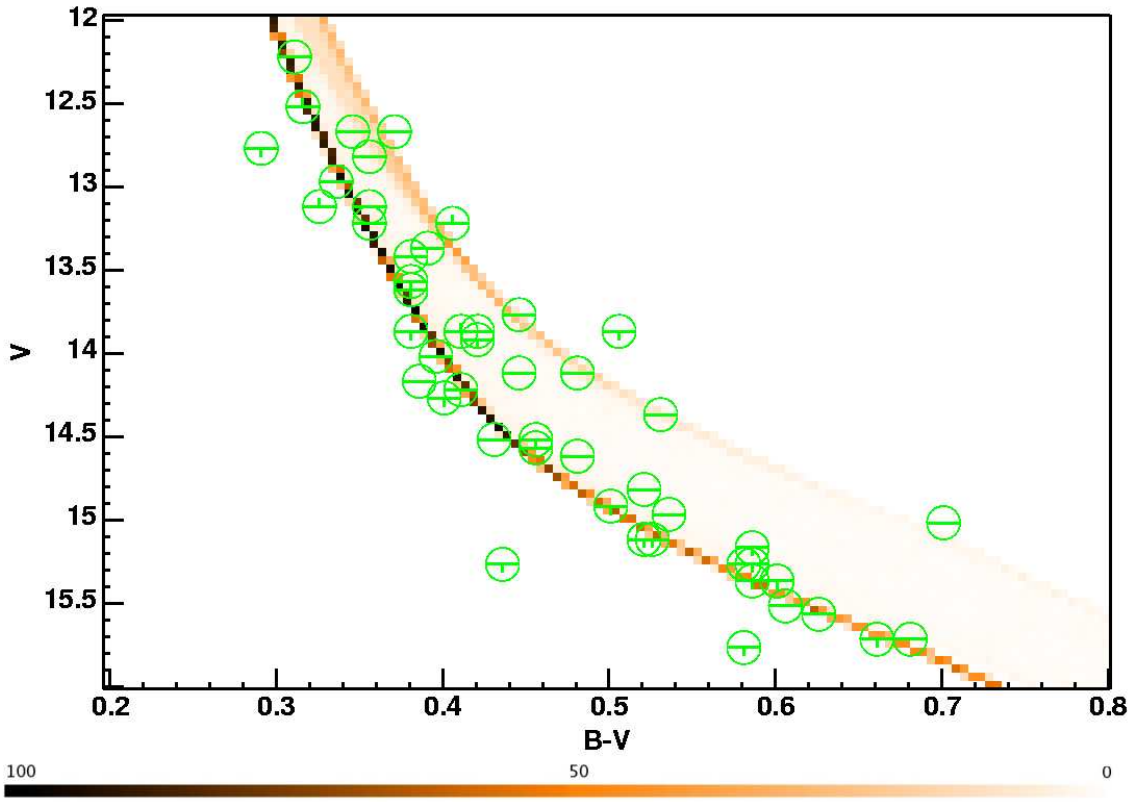

Figure 4.13: The distance fit for χ Per to the Geneva-Bessell isochrones. The colour bar shows the probability density (ρ from Naylor & Jeffries, 2006) for the contours in the figure, generated using the isochrone. The circles are the positions of the photometric points with the bars showing the uncertainties where available.

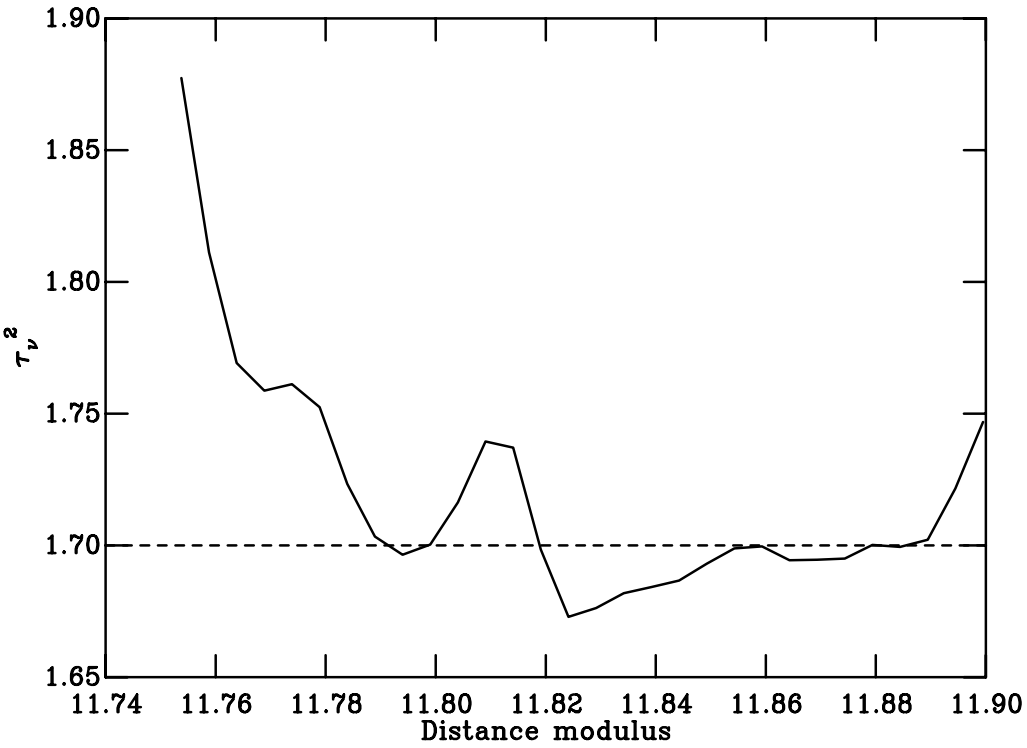

Figure 4.14: τ_ν^2 value shown as a function of distance modulus. With minima at $dm \approx 11.79$ and 11.83 and an inflection point at $dm \approx 11.76$. Towards lower distance moduli the slope is much sharper than the shallow incline towards higher distance moduli. These features are discussed in Section 4.5.2.

4.15, and all subsequent figures for extinction fitting using τ^2, contain the same components as those of Figure 4.13.

In general, fitting for an extinction using the τ^2 method is desirable as individual extinction methods rely on the star being either a single star or unresolved equal-mass binary. However, in some cases the dispersion in $E(B-V)$ is too large, i.e. the scatter around the isochrone in the $U-B$ vs $B-V$ is too large to confidently assign one mean extinction. This is the case where there is significantly variable reddening across a SFR. Here it is possible to derive extinctions for each star from *UBV* photometry alone using the Q-method (Johnson & Morgan, 1953). This is the case for NGC6530, NGC2244 and λ Orionis. Both the τ^2 fitting and the Q-method require three colour photometry. If three colour photometry is unavailable extinctions can be derived using surface temperatures, this is the case for the ONC. I return to discuss individual extinctions in more detail in Section 4.6.

4.5.3 Practical effect of assumptions

During fitting three main assumptions have been made about the fitted stellar populations and it is important to examine the validity of each. Firstly an isochrone at an assumed nominal age is used which could be inaccurate for a given SFR. This may be important both just prior to turn-off and at the turn-on. Secondly, the subject population is implicitly assumed to comprises only MS stars by fitting using MS isochrones. Lastly, isochrones of an approximately solar composition ($Z = 0.02$) were used.

4.5.3.1 Age assumption

As a (coeval) stellar population ages, stars of a decreasing mass turn-off from the MS. In addition, stars close to but nominally below the turn-off age also move slightly red-wards in position in a CMD. As the position of isochrones brighter than the turn-off is not fitted, the age dependency of this region is avoided, but the age dependency of the upper-MS is retained. This shift of the upper-MS is small and furthermore in principle is modeled as a MS at the nominal age of the SFR is used. However it is important to quantify this effect to ensure the derived distances are robust against assuming an incorrect age.

To test this upper-MS age dependency photometry of a population based on a 1 Myr Geneva-Bessell isochrone has been simulated. These data are then fitted (as described in Section 4.5.2) across a typical colour range, specifically blue-ward of $(B-V)_0 = 0.2$ (as shown in Table 4.3 cuts in all our SFRs are blue-ward of this), to a 10 Myr Geneva-Bessell isochrone. This provides a measure of any extra uncertainty one accrues if the age assumption is incorrect. The resulting distance modulus and extinction derived are $dm \approx 0.001$ and $E(B-V) \approx -0.028$, for this factor ten in age. The effect of assuming an incorrect age on a derived distance and $E(B-V)$ is therefore negligible even for a large error in assumed age.

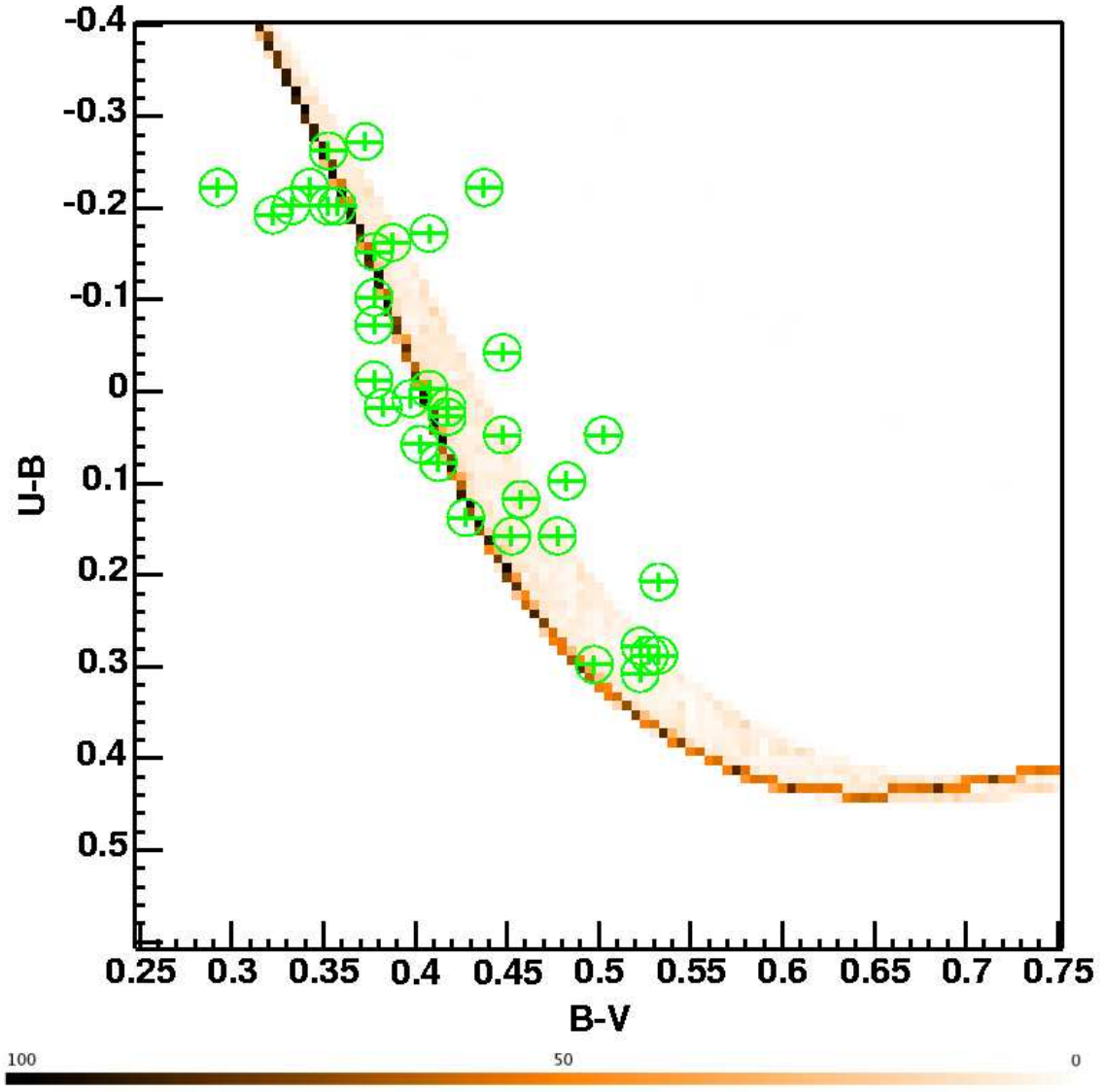

Figure 4.15: Figure showing $E(B-V)$ fit of χ Per to the Geneva-Bessell isochrones. See Section 4.5.2.1 for details of the symbols. Here a systematic shift in $E(B-V)$ as a function of colour $(U-B)$ is evident, as in Figure 4.37. This is probably due to a difference in the photometric systems of Bessell et al. (1998) and Slesnick et al. (2002) (see Section 4.6.3). The colour bar shows the probability density (ρ from Naylor & Jeffries, 2006) for the contours in the figure, generated using the isochrone. The circles are the positions of the photometric points with the bars showing the uncertainties where available.

4.5.3.2 MS isochrones for a possible pre-MS population

As pre-MS stars approach the MS, just prior to the onset of hydrogen burning they enter a quasi-equilibrium state as hydrogen ignition starts. This delays their arrival onto the MS. The rate at which this phase progresses is a function of stellar mass and is, over the mass range of interest, very short in comparison to the evolution of the pre-MS. However, as such stars are slightly brighter than MS stars, the distances derived may be systematically reduced as a function of age.

Some stars in our selected sequence may still be in this pre-MS phase even though appearing to be on the MS. This effect is greatest for the younger SFRs. However within the colour cuts used the deviation from the MS is a maximum of ≈ 0.05 mag (in magnitude) and only affects a limited number of stars. Therefore the overall effect will be $<< 0.05$ mags.

4.5.3.3 Composition

As compositions are not available for all the SFRs studied, solar metallicity ($Z = 0.02$) is assumed. However there is evidence to suggest that some SFRs have a metallicity as low as half-solar (see Section 4.9.2). Therefore quantifying the possible effect varying composition could have on derived relative distances is necessary. To do this again a population is simulated, this time at 10 Myr, using the Geneva isochrones with $Z = 0.008$ (the closest match in the library to half-solar) and these data were fitted for extinction and distance with solar composition isochrones (as described in Section 4.5.2). The resulting differences are, for extinction $E(B-V) = 0.005$ and for distance modulus, $dm \approx 0.41$. This is a negligible difference in extinction but a significant error in distance modulus. In addition χ Per has been fitted using the half-solar metallicity isochrones. Here the colours and photometric system provided with the Geneva isochrones must be used as the Geneva-Bessell isochrones utilise atmospheres of solar metallicity. The resulting distance modulus is $11.32 < 11.36 < 11.41$ and an extinction of $E(B-V) = 0.51$ (using uncertainties of 0.018 for a $P_r(\tau^2) \approx 0.5$). This means that if the metallicity is indeed $Z \approx 0.01$ the distance modulus to χ Per is actually ≈ 0.5 mags less, making the stars older. This could have a major effect on the distances and ages of star-forming regions. Therefore composition information is vital in the future for more accurate SFR parameters. A further discussion of this problem can be found in Section 4.9.

4.6 Individual intrinsic colours

As stated in Section 4.5.2.1 it is sometimes not desirable or possible to derive a mean extinction using τ^2 fitting. In this section cases where individual extinctions are derived are detailed. Source by source extinctions have been used for six SFRs, using two methods. In all of these cases the extinctions applied will change the relative positions of the stars in colour magnitude space, as opposed to applying a mean extinction where the entire dataset is simply translated (shifted). Therefore, in the case of individual extinctions these must be applied prior to fitting, and the resulting figures show the data and model in intrinsic colour and extinction free magnitude.

4.6.1 The ONC

For the ONC *UBV* photometry is unavailable. However Hillenbrand (1997) provides *VI* photometry and effective temperatures derived from spectra of stars within 15' from the centre of the ONC. I used the effective surface temperatures of Hillenbrand (1997) with an assumed surface gravity ($log(g) = 4.5$) and interpolated these to obtain intrinsic colours from the $T_{\rm eff}$ relations in Bessell et al. (1998). This allows derivation of an A_V from $E(V-I)$ using $A_V = ((3.26 + 0.22(B-V)_0)/(1.32 + 0.06(V-I)_0)) \times E(V-I)$ (derived from the extinction vectors of Bessell et al., 1998) and therefore allows calculations of an unredenned magnitude. These resulting magnitudes and colours can then be fitted to derive a distance as in Section 4.5.2. For the main analysis in this chapter the ONC data have been fitted using the intrinsic $B-V$, but they have also been fitted using $V-I$, the result of which can be found in Section 4.7.

4.6.2 h and χ Per

Deriving extinctions, and subsequently distances, in this way can be compared to the results achieved in Sections 4.5 and Section 4.7 the clusters h and χ Per. The $T_{\rm eff}$ data from Slesnick et al. (2002) has been used to derive intrinsic colours for these clusters. However, as the $T_{\rm eff}$ information is only available for the hottest stars, the colour range for fitting is small. Practically this means the uncertainties are large, particularly towards larger distance moduli. To increase the colour range the intrinsic colours for the stars with $T_{\rm eff}$ data from Slesnick et al. (2002), were supplemented with stars from the main catalogue dereddened to intrinsic colours using the mean extinction from the τ^2 fitting. The results from both these methods are consistent (see Table 4.7), however fitting of the $T_{\rm eff}$ data supplemented with photometry is more precise. Although distances derived using the latter method are more precise they are not adopted as a self-consistent set of distances for the studied SFRs is more desirable.

4.6.3 Q-method

4.6.3.1 NGC6530, NGC2244 and λ Orionis

For the SFRs NGC6530, NGC2244 and λ Ori the Q-method has been used to derive source by source extinctions, as the reddening is highly variable in these cases and $T_{\rm eff}$ data are not available. Once the extinctions are derived and applied the distance fitting proceeds as described in Section 4.5.1.

The Q-method is a widely used method to derive individual source-by-source extinctions using a $U-B$ vs $B-V$ colour-colour diagram. It was introduced in Johnson & Morgan (1953). Whilst very successful, the use of the Q-method has not been changed since its inception in 1953. There are several inherent problems with its use and areas which require updating.

Johnson & Morgan (1953) developed the Q-method empirically using photometry of bright stars from NGC2362, the Pleiades and Praesepe. Firstly photometry of stars from these clusters is adjusted to absolute magnitude and intrinsic colour by fitting them to a sequence of nearby bright stars and applying a mean extinction (adopting $E(U-B)/E(B-V) \approx 0.72$, the reasons for which are shown later). This provides an empirical MS in V vs $B-V$ and V vs $U-B$ CMDs. The

unredenned photometry of NGC2362 and the Praesepe stars are then used to construct an empirical MS in a $U-B$ vs $B-V$ colour-colour-diagram (the Pleiades are omitted due to differential reddening). Then reddened stars are moved onto this sequence in the colour-colour-diagram. The effective extinction vector connecting stars of the same spectral type was observed to be a constant. This is the first derivation, for the subsequently adopted as canonical, extinction vector of $E(U-B)/E(B-V) = 0.72 \pm 0.03$. Therefore the reddening independent quantity Q was defined as

$$Q = (U-B) - E_{(U-B)}/E_{(B-V)} * (B-V). \tag{4.10}$$

This quantity is effectively the intercept along the extinction vector with the $(B-V) = 0$ axis, or in other words the value of $(U-B)$ at $(B-V) = 0$ along the extinction vector. The values of Q for B stars in NGC2362, M36 and the nearby bright stars were then plotted against B-V and observed to lie on a straight line defined as

$$B-V = -0.009 + 0.337Q. \tag{4.11}$$

This results in a colour excess of $E_{(B-V)} = (B-V) - 0.337Q + 0.009$. Effectively this method involves the empirical derivation of a pseudos-MS straight line relationship in a $(U-B)$ vs $(B-V)$ CMD and an extinction vector. Stars are then essentially moved onto the sequence along this vector.

The Q-method is stated to be valid over the range $-0.80 < Q < -0.05$, this is the range covered by B stars and so defined empirically, it is also interesting to note that the authors of Johnson & Morgan (1953) point out that the straight line fit in Q vs *B-V* degrades at low Q, or Q=0. To use the Q-method to derive extinctions for our τ^2 fitting routine the all possible sources of error and the problems affecting validity must first be explored fully.

4.6.3.2 Pseudo-MS straight line

The use of the Q-method entails the assumption that a section of the MS is a straight line in a $U-B$ vs $B-V$ diagram. This straight line is at a different gradient and intercept to any straight line drawn through a section of the Geneva-Bessell (or indeed Padova-Bessell) isochrones. The gradient and intercept of this pseudo-MS line can be derived using Equations 4.10 and 4.11, adopting $E_{(U-B)}/E_{(B-V)} = E_m$ and using a MS line in the form $y = mx + c$ ($y = (U-B)_0$, $x = (B-V)_0$, $m = MS_M$ and $c = MS_c$). We have a MS line of

$$(U-B)_0 = MS_m * (B-V)_0 + MS_c, \tag{4.12}$$

substituting for Q into Equation 4.10 into 4.11 we have

$$(B-V)_0 = 0.337((U-B) - E_m(B-V)) - 0.009, \tag{4.13}$$

rearranging Equation 4.13 into the form $y = mx + c$, assuming $(U-B) = (U-B)_0$ results in

$$\therefore (U-B)_0 = (B-V)_0(0.337E_m + 1)/0.337 - 0.009/0.337. \tag{4.14}$$

Age	$U-B$	$B-V$
1	$-0.17 < -1.15$	$-0.06 < -0.30$
3	$-0.17 < -1.12$	$-0.06 < -0.29$
5	$-0.17 < -1.08$	$-0.06 < -0.28$
15	$-0.17 < -0.90$	$-0.06 < -0.23$
30	$-0.17 < -0.72$	$-0.06 < -0.22$

Table 4.4: The approximate validity range (not including multiple value solutions) for several ages derived from the Geneva-Bessell isochrones, defined as regions where the real isochrone moves more than 0.01 in colour away from the straight line model.

As $E_m = 0.72$, the resulting implicit pseudo-MS straight line assumed in Johnson & Morgan (1953) is

$$\therefore (U-B)_0 = (B-V)_0 * 3.687 - 0.027. \tag{4.15}$$

One can replace the original Q-method MS line with a new version fitted to the modern isochrones and can therefore derive a formula for Q as provided in the original work. The validity of this formula is a function of age (see Section 4.6.4.2) and some approximate values are given in Table 4.4. Using this formula of course does not account for various other problems explained in the rest of this section. The formula for the updated Q using the Geneva-Bessell isochrones and the extinction vectors from Bessell et al. (1998) is (using a MS line of $(U-B)_0 = 3.967(B-V)_0 + 0.015$ from the Geneva isochrones):

$$Q = 0.24(B-V)^2 + 3.257(B-V) + 0.015 \tag{4.16}$$

The difference between the original Q-method and a modern isochrone results in a maximum change of $\delta A_V \approx 0.10$.

4.6.3.3 Extinction vectors

The traditional Q-method used an empirically derived extinction vector, $E(U-B)/E(B-V) = 0.72 \pm 0.03$, which is still widely used. Given extinction vectors as a function of colour in the adopted photometric system, $E(U-B)/E(B-V) = 0.71 + 0.24(B-V)$ and $R = 3.26 + 0.22 \times (B-V)_0$ ($A_V = R \times E(B-V)$) any difference in derived extinction with the canonical values can be found. The difference in extinction derived using the extinction vectors of Bessell et al. (1998) compared to those of the original Q-method for an $E(B-V) = 0.3$, of the reddest typical star ($B-V \approx 0$), is $\delta A_V = 0.078$. This also has an important effect on the shape of the sequence in the resulting CMD. The two extremal extinction vectors over the range of Q validity are shown in Figure 4.18.

4.6.4 Revised Q-method

The "revised Q-method", used for some clusters in Section 4.8, increases the sophistication of the Q-method by using a real isochrone in place of the straight line. The original Q-method line and a Geneva-Bessell 10 Myr isochrone are displayed in Figure 4.18, which also shows the difference in derived A_V obtained when deredenning stars onto either line.

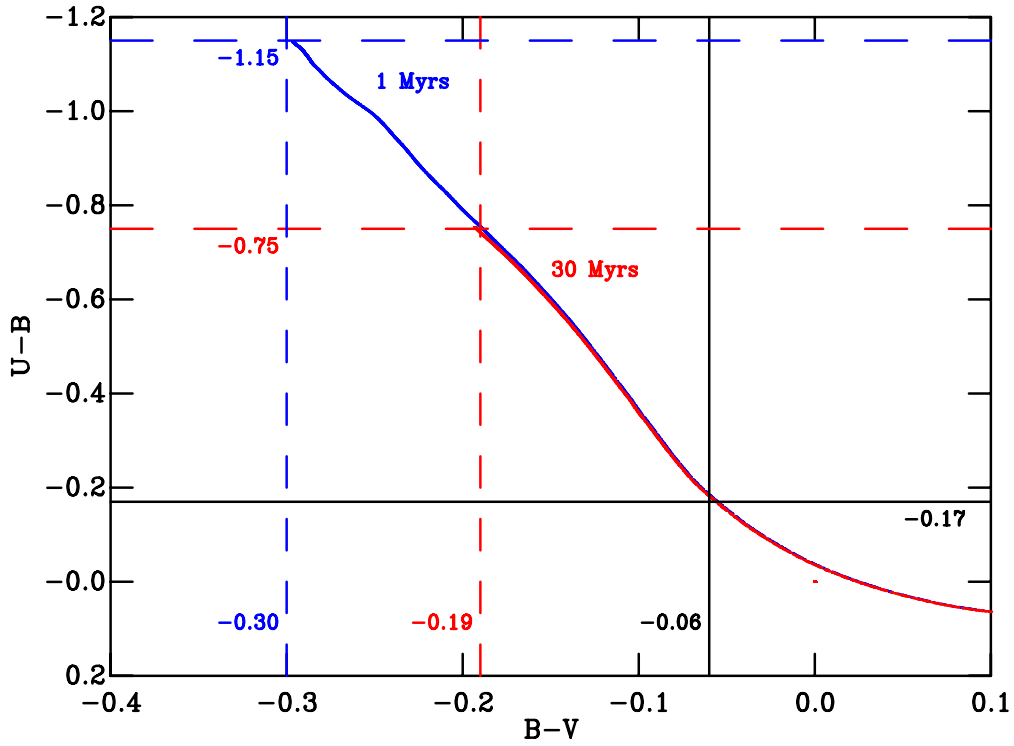

Figure 4.16: Geneva isochrones of 1 and 30 Myrs (limited to $30M_{\odot}$ and $7M_{\odot}$ respectively, the masses at which stars depart the pseudo-MS for these ages) showing the negligible shift of the MS line with age, the inflection point and the shift in the post-MS section. The bold lines are the validity ranges for the reddest stars, with the dashed lines the upper validity ranges for the bluest stars, for the two different age isochrones. Approximate validity ranges for different age isochrones for straight lines drawn from these isochrones are shown in Table 4.4.

4.6.4.1 Stationary or inflection point

Stellar sequences in a colour-colour diagram red-ward of a certain $B-V$ (as discussed in Delgado et al., 2007), which is a function of the reddening vector and isochrone, have multiple solutions for $E(B-V)$. Using 1 Myr isochrone and assuming a simple gradient of $E(U-B)/E(B-V) = 0.72$ this value is $(B-V)_0 > -0.12$. This can be solved by simply selecting the $E(B-V)$ closest to the cluster mean, for stars within the range of this problem. A cluster mean extinction can be calculated using OB stars where the effect of binarity (see Section 4.6.4.4) is least.

4.6.4.2 Age assumption

As extinctions are derived using a real isochrone an age must be assumed. However, the pseudo-MS straight line shifts negligibly with age at the inflection point and along the straight line central section. More important are the changes at the post-MS end of the isochrone in $U-B$ vs $B-V$, where the tracks have a strong age dependency and are complex. Clearly, deredenning these stars onto a MS will result in an incorrect extinction. The colours at which the stars evolve away from the MS are shown in Figure 4.16. These values are also shown as part of Table 4.4.

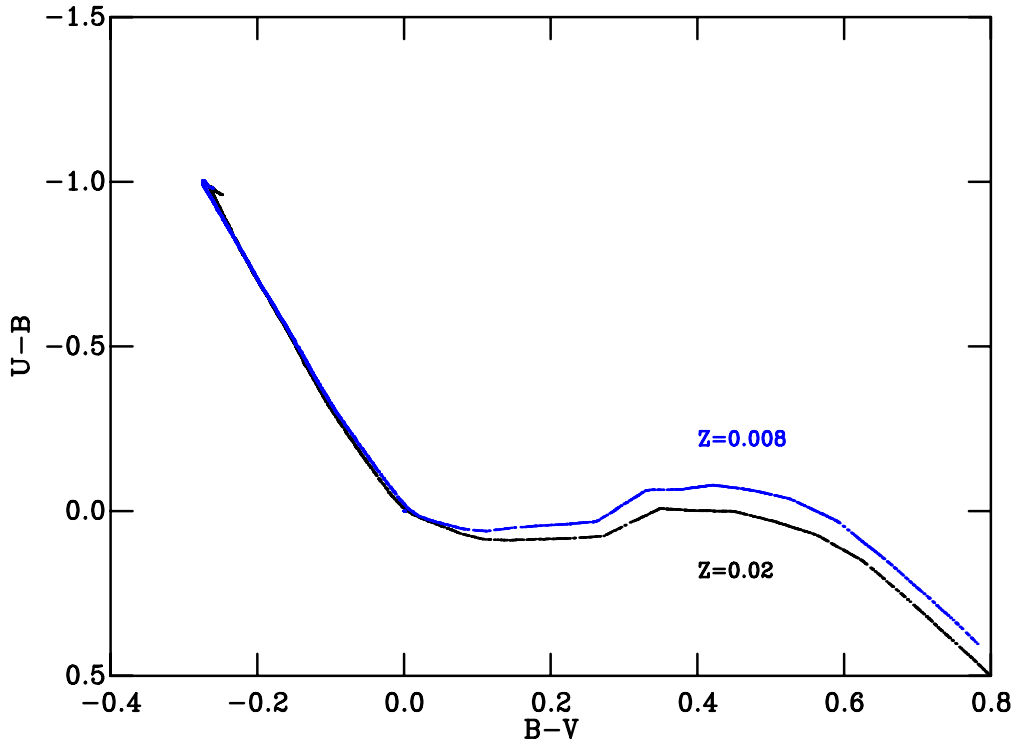

Figure 4.17: 10 Myr Geneva isochrones of $Z = 0.02$ and $Z = 0.008$, the line are almost coincident until the inflection point.

4.6.4.3 Metallicity

The original Q-method was derived empirically and thus contains no assumptions about metallicity. Any differences in composition will shift the positions of the stars in a colour-colour diagram. The shift is very small over the straight section of the MS, however metallicity changes do perturb the position of the isochrone at values blueward of $B - B = 0$. As shown in Figure 4.17, using Geneva $Z = 0.02$ and $Z = 0.008$ isochrones alone (as the Bessell et al., 1998, colours are defined using atmospheres at solar metallicity, see Section 4.4), will yield a significantly different $E(B-V)$ for stars redder than the limits in Table 4.4, where the isochrone is red-ward of its first minimum. Therefore without composition information it is important to avoid this part of the isochrone. Since this corresponds to the multivalued region of the extinction solution, this is not a critical limitation.

4.6.4.4 Binarity

A final significant problem is that of multiplicity. Binary stars of unequal mass do not lie on the same locus as single and equal-mass binary stars in a $U-B$ vs $B-V$ colour-colour diagram. This is unaccounted for in the original Q-method, or by using an updated straight line relationship or model isochrone. As can be seen in Figure 4.15 it is unclear whether a star should lie on the single-star or equal-mass binary sequence or or in the region occupied by unequal-mass binaries. Crucially, as shown in Kouwenhoven (2005), around 80% of OB stars are found in binary systems.

The effect and range of this problem is shown in Figure 4.18. The outer envelope of the binary sequence has been modeled with a curve and A_V values derived using the binary line. These can then be compared to those A_V values found using the original Q and the single star sequence. Figure 4.18 shows that binarity has a non-negligible effect of up to $\delta A_V \approx 0.15$ in the derived extinction. This effect becomes increasingly significant as one moves down (redder in $U-B$) the MS isochrone.

As the revised Q-method does not account for the scatter binaries produce in a CMD, or colour-colour diagram, it is a statistically ill-defined process. Effectively most of the intrinsic scatter from the binary sequence and photometric uncertainties is removed, in addition to that caused by variable extinction. Therefore, only when there is good evidence, from the mean extinction fitting method, that the extinction in a SFR is large and variable is the revised Q-method applied. Thus the null hypothesis that the reddening or extinction is uniform is formulated. The SFR is fit to derive a mean extinction and subsequently a distance. These results can be found in Table 4.8 and are discussed in Section 4.7. However, in some cases of distance fitting, after applying a mean extinction, the addition of large systematic uncertainties was required to return a $Pr(\tau^2) \approx 50\%$. In these cases I am forced to reject the null hypothesis and use the revised Q-method to derive individual extinctions. Additional systematic uncertainties of up to 2% are credible, therefore the revised Q-method was applied in cases where the added systematic uncertainties exceed this level.

4.6.5 Example of SFRs with signifi cant variable reddening

In Figures 4.19 , 4.20 and 4.21 the τ^2 mean extinction fits for NGC6530, NGC2244 and λ Ori, respectively, are shown. There is clearly a large scatter in each fit, which is also reflected in the corresponding distance fit, Figures 4.22, 4.23 and 4.24. This scatter improves significantly when the revised Q-method is applied, as shown in Figures 4.29, 4.30 and 4.31. In addition the uncertainties in distance are significantly smaller when using the revised Q-method. In Section 4.8 all three clusters are fitted using extinctions from the revised Q-method. For completeness the parameters derived for these three clusters using both methods are presented in Section 4.7. The resulting distance moduli derived using a mean extinction or the revised Q-method are consistent within the uncertainties.

Figures 4.25, 4.26 and 4.27, show the positions of the target stars in apparent colour and intrinsic colour before and after application of the revised Q-method. The scatter is greatly reduced after application of the revised Q-method. This results in much more precise distances as shown in Table 4.9. These distances have been adopted in Section 4.8 and the resulting best fitting distances are shown in Section 4.8 as Figures 4.29, 4.30 and 4.31.

I also attempted to use the revised Q-method for h Per, as it satisfied the criteria for non-uniform redenning. However, the $E(B-V)$ was found to vary systematically as a function of colour. This systematic shift in extinction with colour is evident in Figure 4.37. It shows that to fit the hotter stars and cooler stars simultaneously would require a change in the gradient of the isochrone. The same trend is observed for χ Per in Figure 4.15. Therefore, this behaviour can be attributed to differences between the photometric systems of Slesnick et al. (2002) and Bessell et al. (1998). Moreover, as this systematic shift in $E(B-V)$ is not present in V vs $B-V$ fit (see

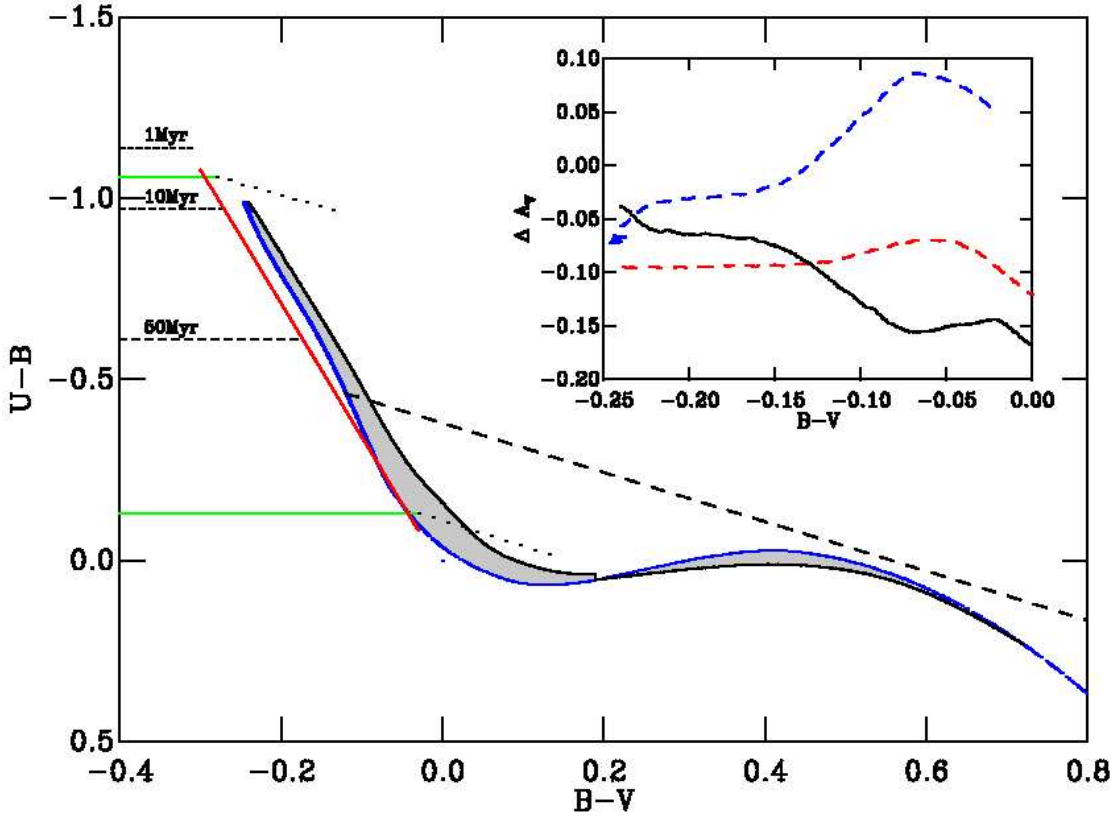

Figure 4.18: Geneva-Bessell 10 Myr isochrones with the outer binary envelope (gray region enclosed by black line) and the Q-method straight MS line (red line). The horizontal dashed lines are the points at which the Geneva-Bessell isochrones evolve away from the MS (see Figure 4.16). The horizontal bold lines are the validity region of the original Q-method given in Johnson & Morgan (1953). The two angled dotted lines are the extinction vectors of Bessell et al. (1998) at each end of the Q-method validity range. Finally, the large dashed line shows the region below which (redder $U-B$) the solution for a given star can be multi-valued. The inset figure shows the approximate differences in derived A_V. The top dashed line is the revised Q-method minus the old Q-method, the lower dashed line is that derived from the outer binary envelope minus the old Q-method, and the bold line is that derived from the binary envelope minus the revised Q-method to the single star sequence.

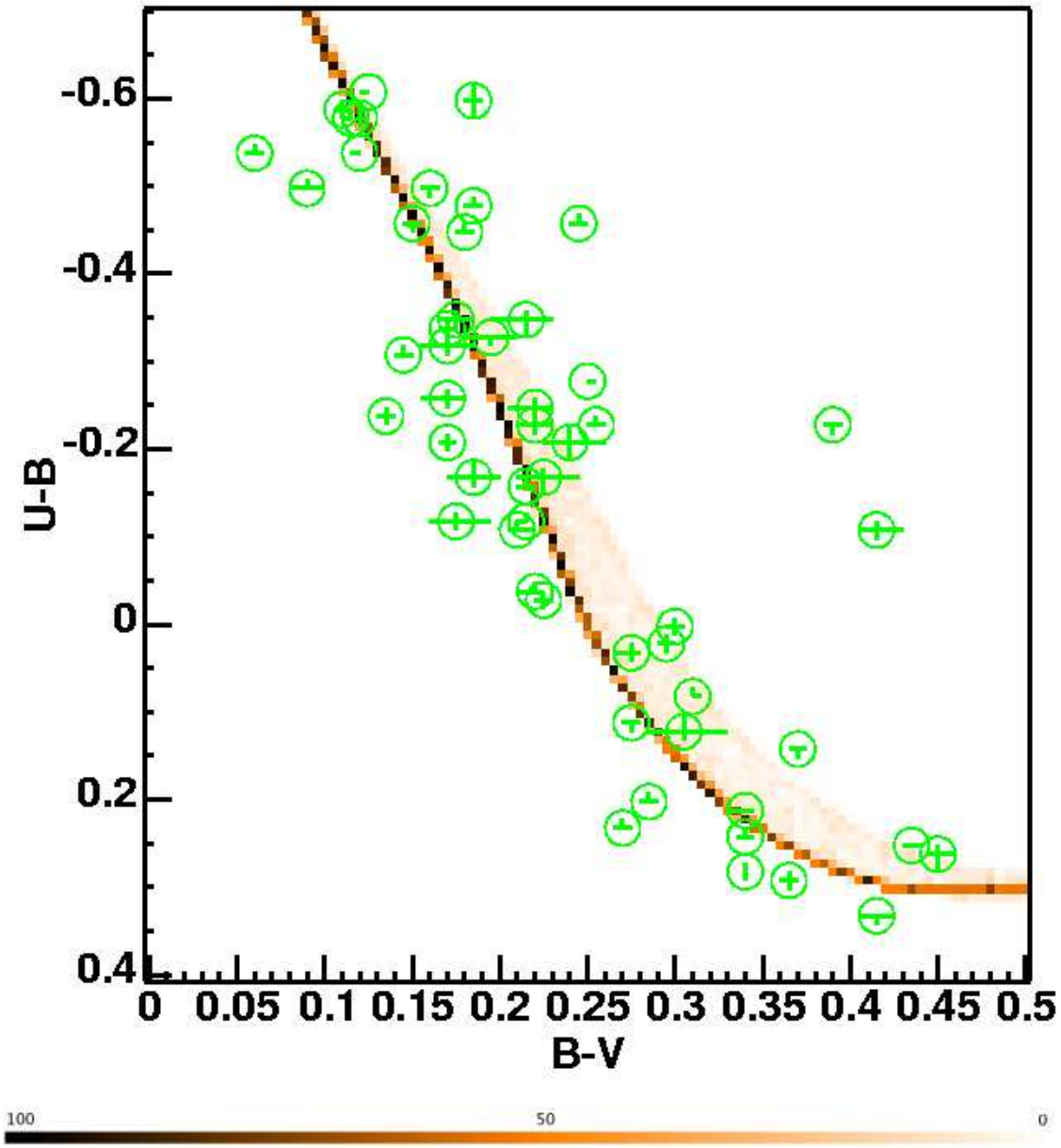

Figure 4.19: NGC6530 $E(B-V)$ fit. The colour bar shows the probability density (ρ from Naylor & Jeffries, 2006) for the contours in the figure, generated using the isochrone. The circles are the positions of the photometric points with the bars showing the uncertainties where available.

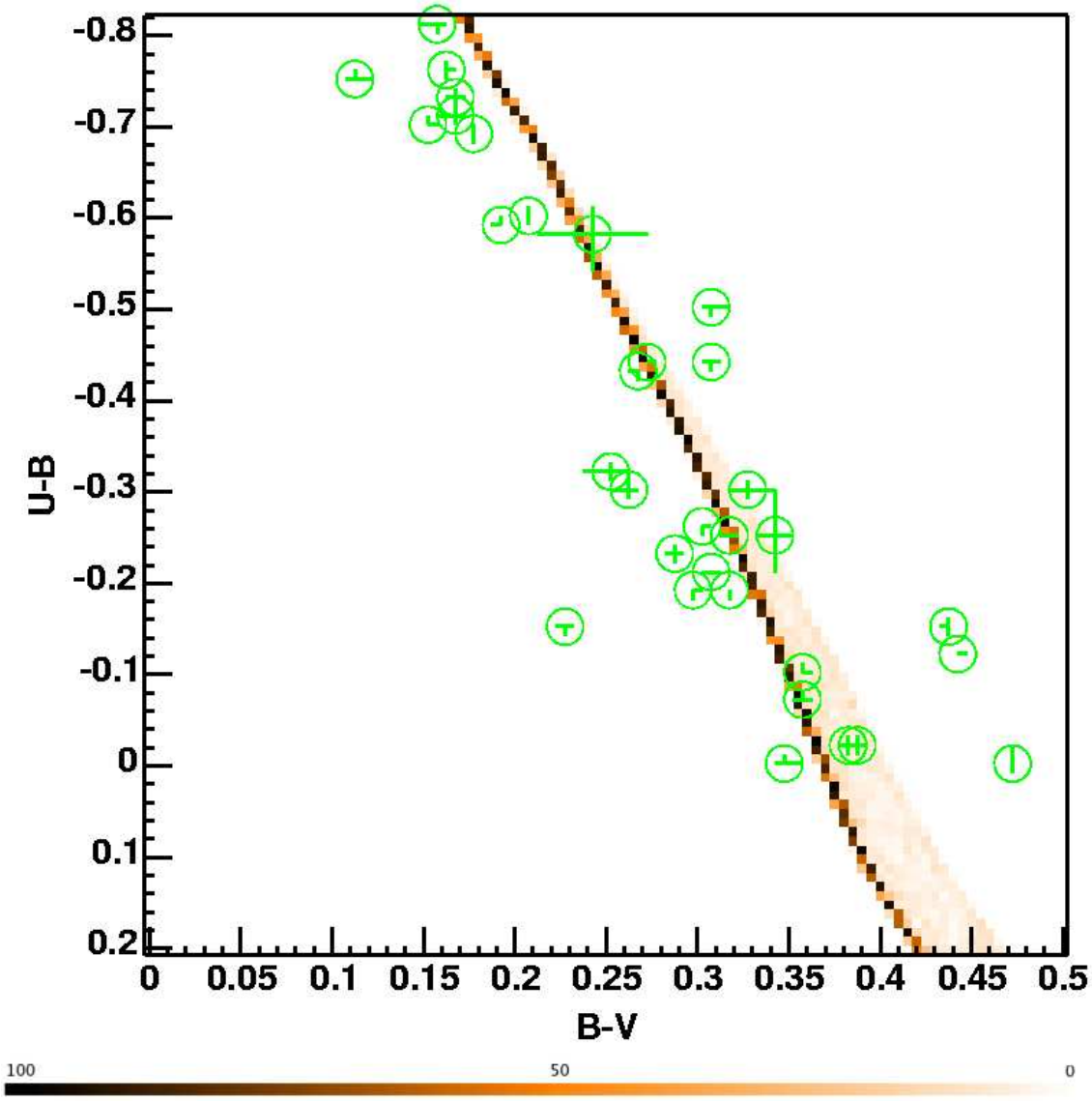

Figure 4.20: NGC2244 $E(B-V)$ fit. The colour bar shows the probability density (ρ from Naylor & Jeffries, 2006) for the contours in the figure, generated using the isochrone. The circles are the positions of the photometric points with the bars showing the uncertainties where available.

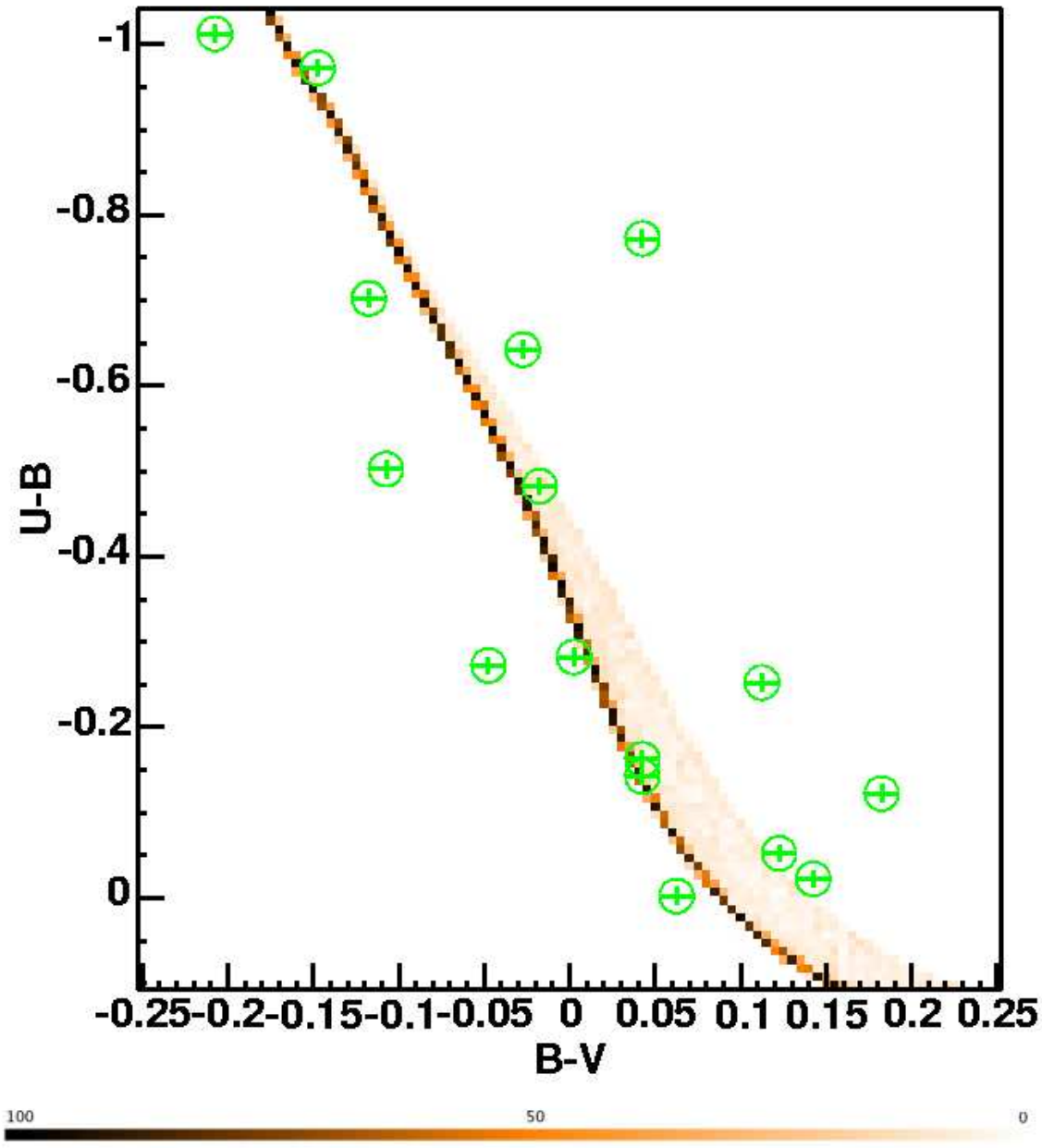

Figure 4.21: λ Ori $E(B-V)$ fit. The colour bar shows the probability density (ρ from Naylor & Jeffries, 2006) for the contours in the figure, generated using the isochrone. The circles are the positions of the photometric points with the bars showing the uncertainties where available.

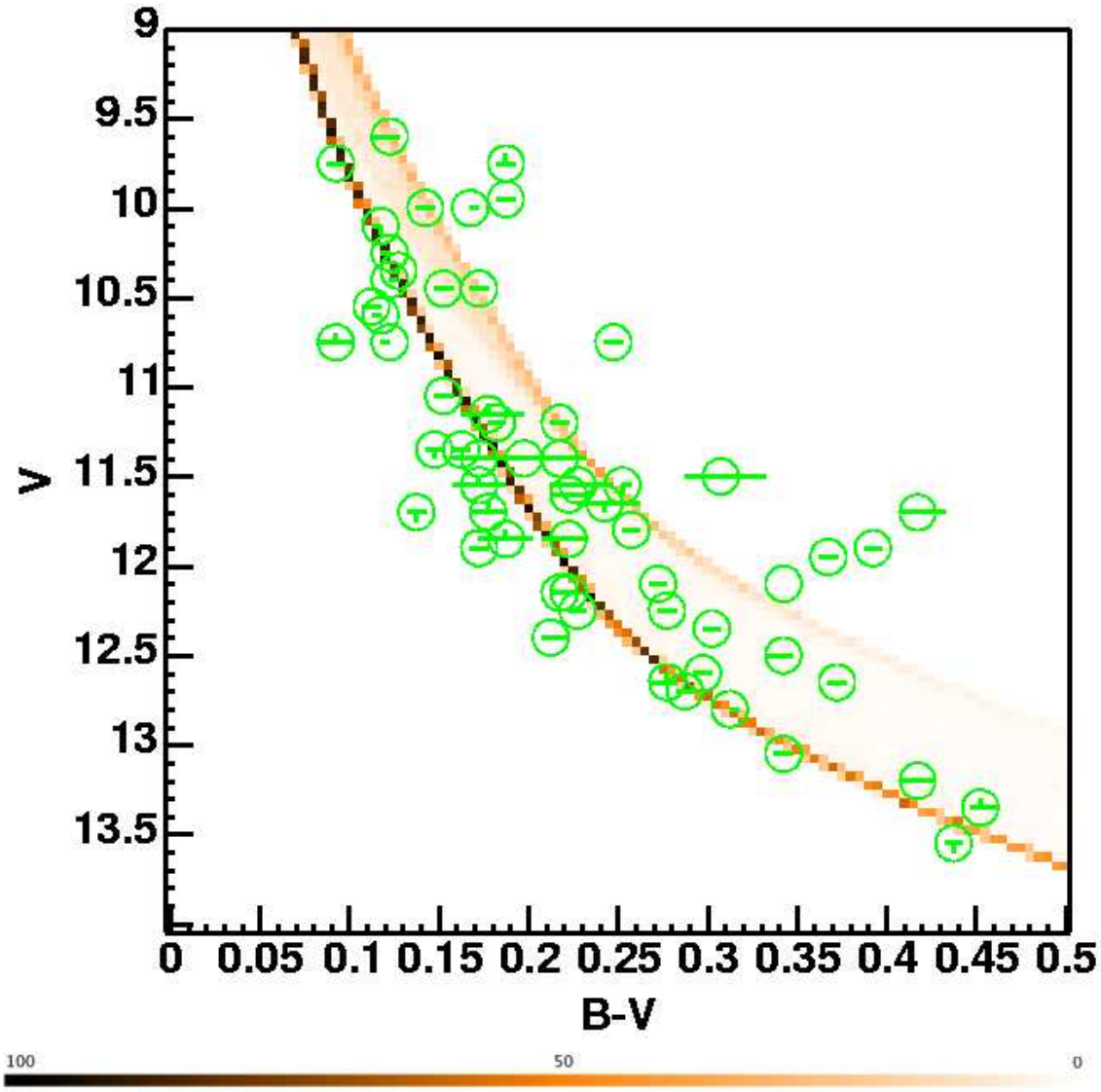

Figure 4.22: NGC6530 distance fit using mean extinction, the fit for which is shown as Figure 4.19. The colour bar shows the probability density (ρ from Naylor & Jeffries, 2006) for the contours in the figure, generated using the isochrone. The circles are the positions of the photometric points with the bars showing the uncertainties where available.

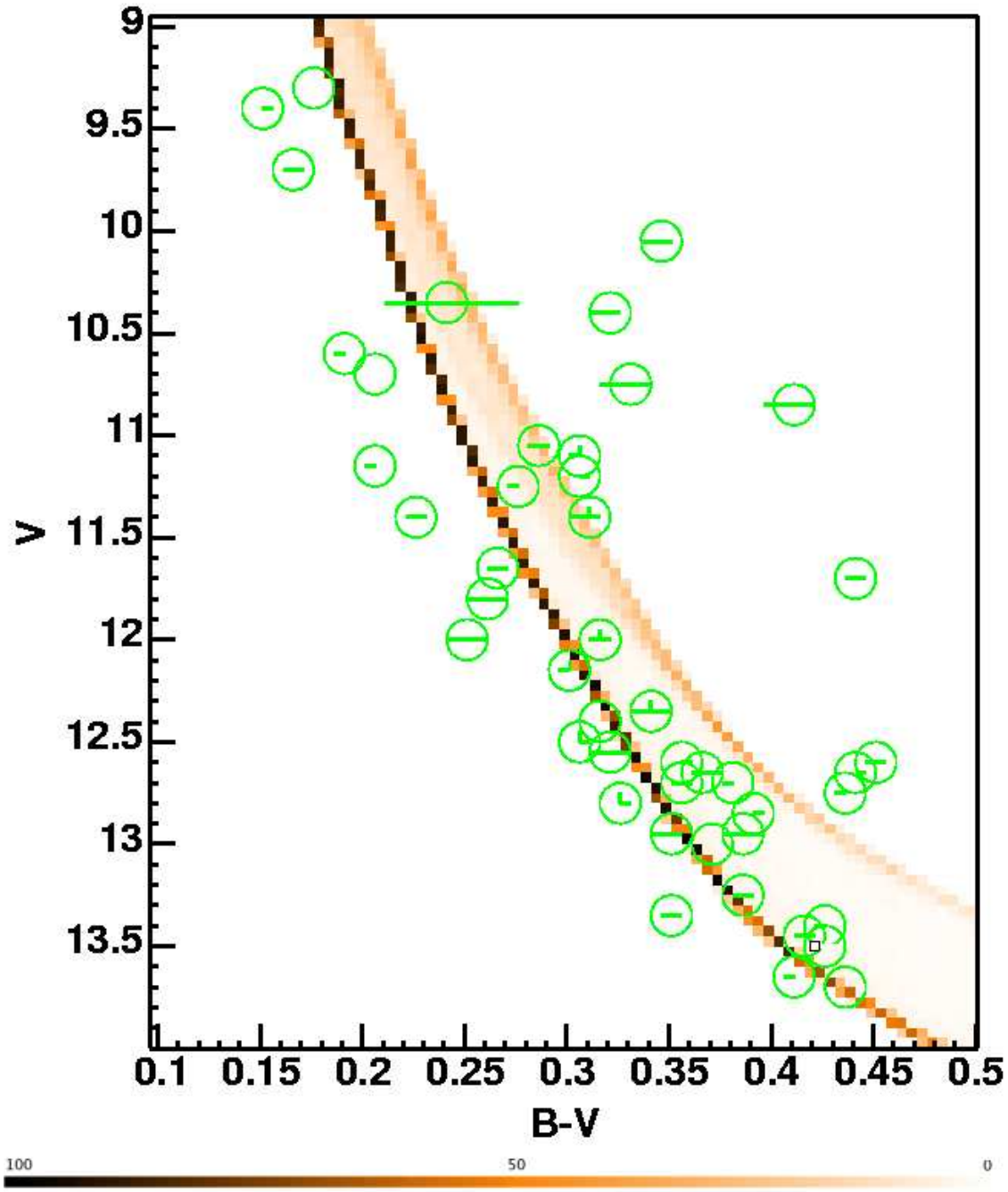

Figure 4.23: NGC2244 distance fit using mean extinction, the fit for which is shown as Figure 4.20. The colour bar shows the probability density (ρ from Naylor & Jeffries, 2006) for the contours in the figure, generated using the isochrone. The circles are the positions of the photometric points with the bars showing the uncertainties where available.

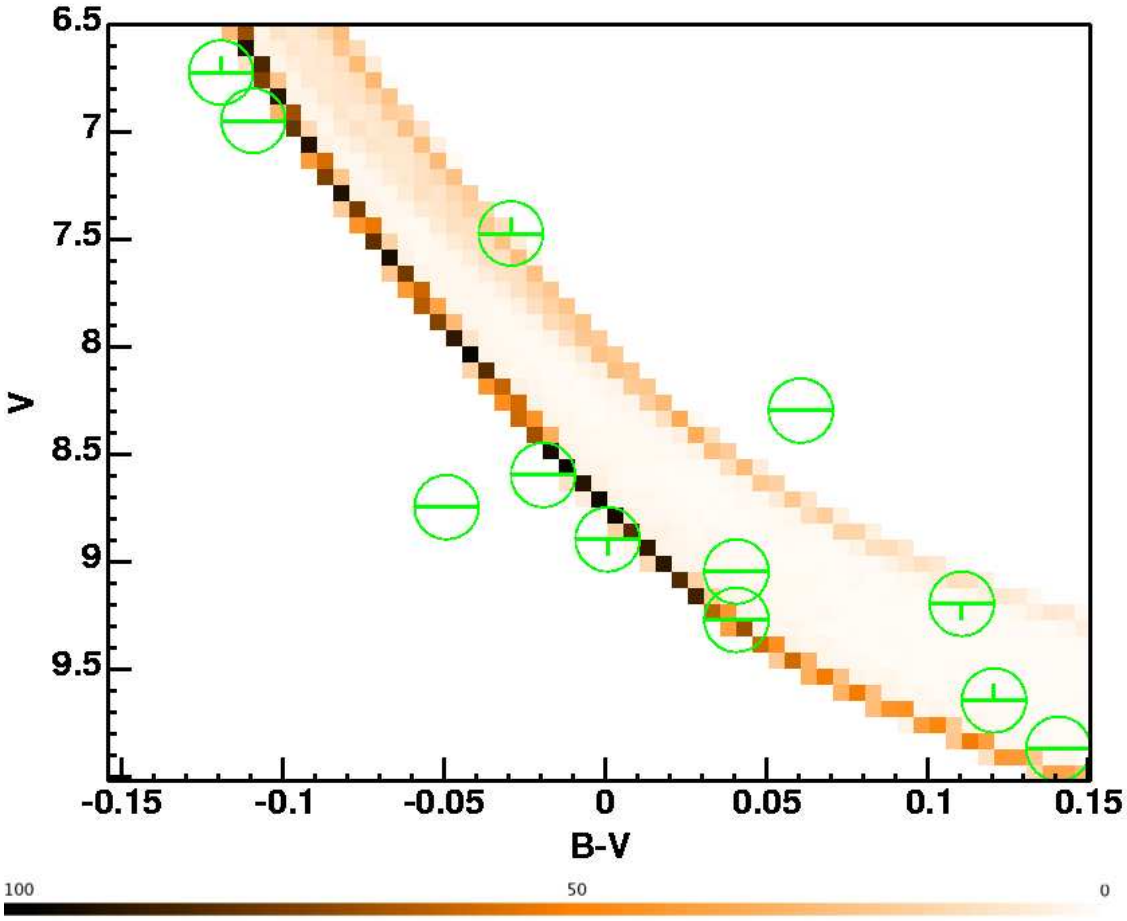

Figure 4.24: λ Ori distance fit using the mean extinction, the fit for which is shown as Figure 4.21. The colour bar shows the probability density (ρ from Naylor & Jeffries, 2006) for the contours in the figure, generated using the isochrone. The circles are the positions of the photometric points with the bars showing the uncertainties where available.

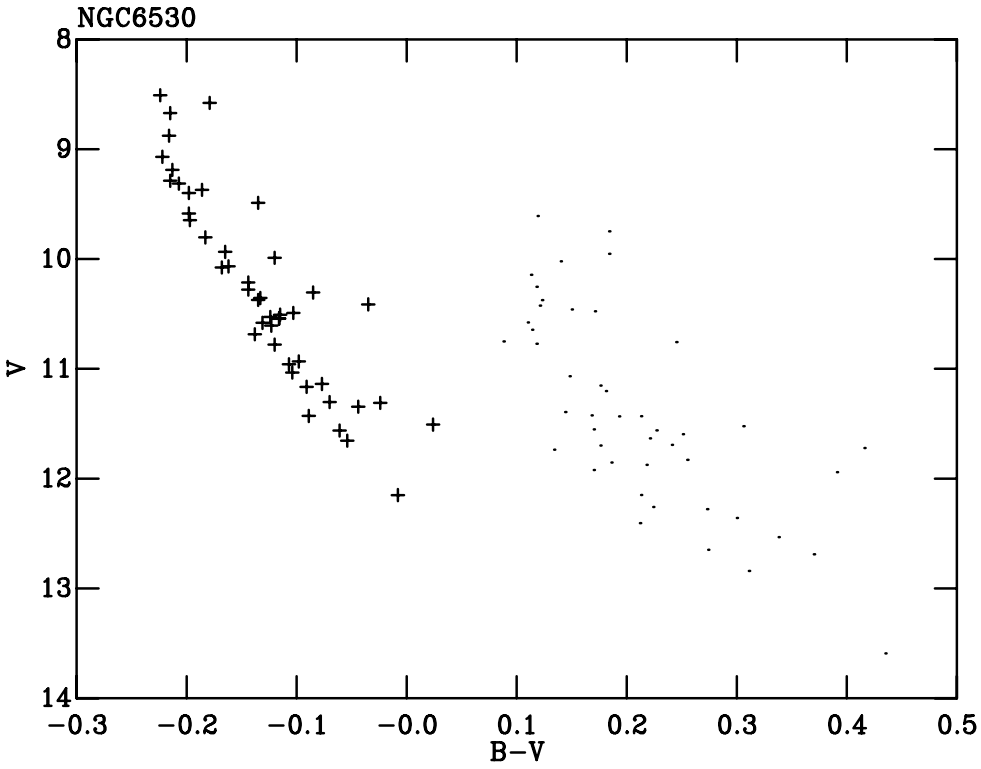

Figure 4.25: NGC6530: photometry of Sung et al. (2000). Dots show the stars apparent colour and magnitude and the crosses are the stars positions after application of individual extinctions derived using our revised Q-method.

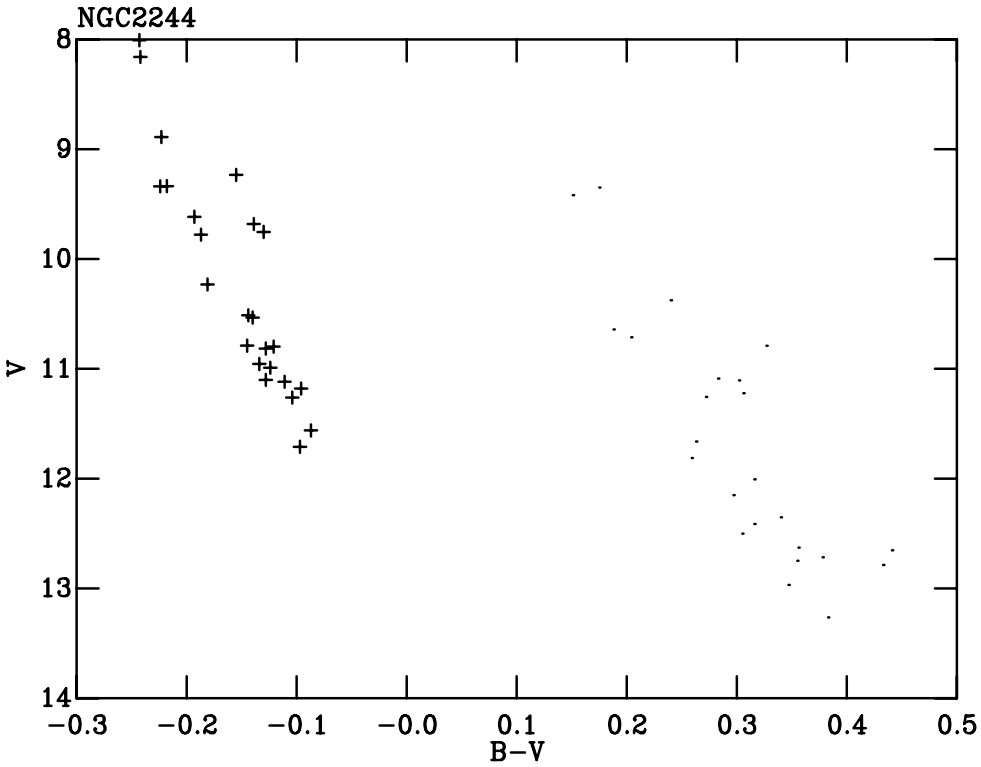

Figure 4.26: NGC2244: photometry of Park & Sung (2002). Dots show the stars apparent colours and magnitudes and the crosses are the stars positions after application of individual extinctions derived using our revised Q-method.

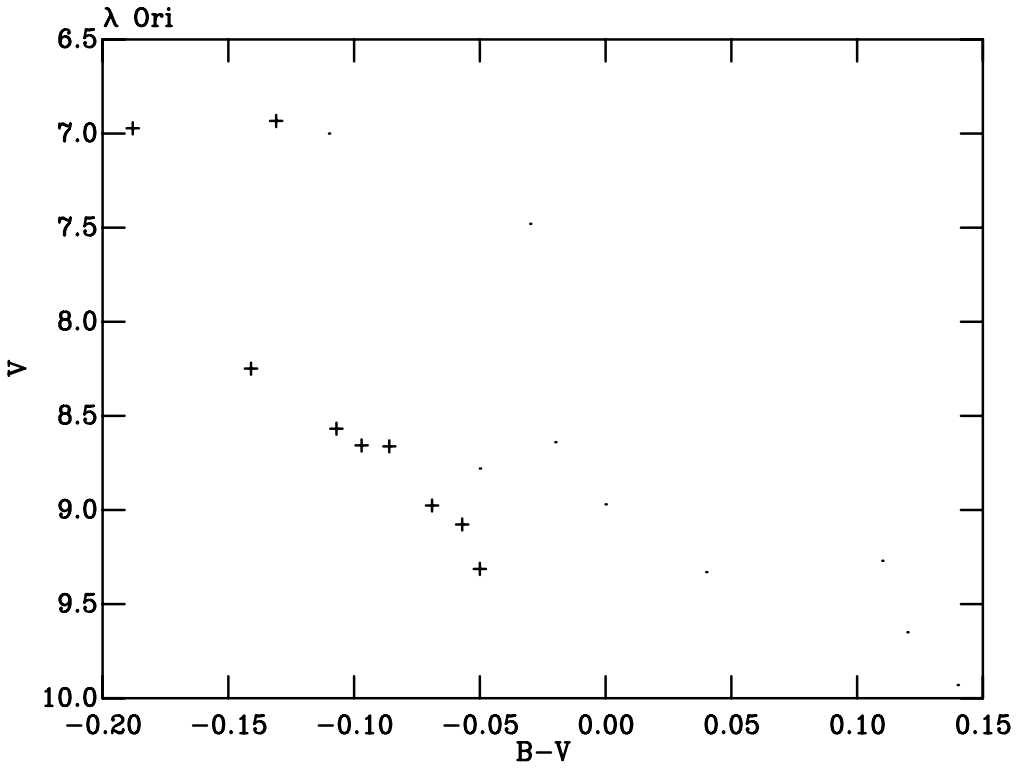

Figure 4.27: λ Ori: photometry of Murdin & Penston (1977). Dots show the stars apparent colours and magnitudes and the crosses are the stars positions after application of individual extinctions derived using our revised Q-method.

TYCHO photometry			
SFR	σ Ori		
Model (Vega cal)	dm	Δdm	Unc
Geneva-Bessell(0)	$7.84 < 7.94 < 8.10$	0.26	0.00
Padova-Bessell(0)	$7.72 < 7.93 < 8.03$	0.31	0.00
Geneva-Bessell(/ = 0)	$7.79 < 7.94 < 8.07$	0.28	0.005
Padova-Bessell(/ = 0)	$7.72 < 7.93 < 7.98$	0.26	0.005

Table 4.5: The distance moduli derived for σ Ori in the *TYCHO* photometric system for the different models and calibrations to Vega colours of zero or Vega $B-V=-0.002$ and $U-B=-0.004$. Uncertainties required to achieve $0.40 < P_r(\tau^2) < 0.60$ are also shown.

Figure 4.13) the problem can be further constrained to a difference dominated by the U band.

4.7 Model dependency

In this section the results of fitting all models given in Tables 4.5-4.9. The fits have been optimised by adjusting the systematic uncertainties in colour and magnitude such that the $Pr(\tau) \approx 50\%$ (actually 44%-66%). The values for the extinction and distance modulus with 68% confidence limits and the added systematic uncertainties are shown. Table 4.5 shows the distances derived for σ Orionis using the Geneva and Padova models (with canonical extinction vectors) after conversion to the *TYCHO* photometric system of Bessell (2000) (see Section 4.4.5). Tables 4.6 and 4.7 contain the results of distance fitting SFRs using a direct conversion from $T_{\rm eff}$ to colour and subsequent derivation of an extinction (see Section 4.6.1). Table 4.6 contains distances to the ONC using the two colour indices $V-I$ and $B-V$, whereas for Table 4.7 the results are for h and χ Per fitted in $B-V$ (see Section 4.6.2). Tables 4.8 and 4.9 show the distances and extinctions derived for each SFR using a a mean extinction, and the revised Q-method respectively.

These data can be used to compare the different sets of model isochrones. Figure 4.28 shows the derived distances and associated uncertainties (68% confidence intervals) for each SFR and each set of isochrones, where a mean extinction has been derived. Figure 4.28 shows that for any given SFR the scatter between models is smaller than the uncertainties from the data. However, one could argue for a systematic shift of ≈ 0.05 in distance modulus depending on the choice of Vega zero point. These results show that any model dependency in the derived distances and extinctions is small. In addition, as can be seen from the results in this section, the systematic uncertainties added to achieve a $Pr(\tau^2) \approx 50\%$ do not favour any particular model. This statistical justification shows, in conjunction with the small model dependency, that the choice of model is arbitrary for these data.

Extinction from *UBV* fitting				
SFR	NGC6530			
Model (Vega cal)	dm	Δdm	Unc	$E_{(B-V)}$
Geneva(0)	$10.29 < 10.38 < 10.48$	0.19	0.0330	0.35
Geneva-Bessell(0)	$10.16 < 10.34 < 10.43$	0.27	0.0305	0.32
Padova-Bessell(0)	$10.15 < 10.35 < 10.46$	0.31	0.0308	0.32

Geneva-Bessell(/ = 0)	10.25 < 10.27 < 10.34	0.09	0.0330	0.32
Padova-Bessell(/ = 0)	10.26 < 10.28 < 10.32	0.08	0.0330	0.32
SFR	NGC2244			
Model (Vega cal)	dm	Δdm	Unc	$E_{(B-V)}$
Geneva(0)	10.62 < 10.78 < 10.94	0.32	0.0470	0.47
Geneva-Bessell(0)	10.68 < 10.89 < 11.09	0.41	0.0450	0.46
Padova-Bessell(0)	10.73 < 10.81 < 11.00	0.27	0.0450	0.45
Geneva-Bessell(/ = 0)	10.54 < 10.78 < 10.94	0.40	0.0400	0.46
Padova-Bessell(/ = 0)	10.50 < 10.74 < 10.90	0.40	0.0400	0.45
SFR	NGC2264			
Model (Vega cal)	dm	Δdm	Unc	$E_{(B-V)}$
Geneva(0)	9.15 < 9.40 < 9.53	0.38	0.018	0.06
Geneva-Bessell(0)	9.26 < 9.37 < 9.52	0.26	0.0160	0.04
Padova-Bessell(0)	9.27 < 9.34 < 9.51	0.24	0.0140	0.04
Geneva-Bessell(/ = 0)	9.18 < 9.39 < 9.51	0.33	0.0160	0.04
Padova-Bessell(/ = 0)	9.18 < 9.40 < 9.50	0.32	0.0160	0.04
SFR	NGC2362			
Model (Vega cal)	dm	Δdm	Unc	$E_{(B-V)}$
Geneva(0)	10.48 < 10.58 < 10.69	0.21	0.0150	0.12
Geneva-Bessell(0)	10.51 < 10.67 < 10.70	0.19	0.0130	0.10
Padova-Bessell(0)	10.47 < 10.66 < 10.77	0.30	0.0120	0.10
Geneva-Bessell(/ = 0)	10.49 < 10.57 < 10.70	0.21	0.0120	0.10
Padova-Bessell(/ = 0)	10.47 < 10.55 < 10.72	0.25	0.0120	0.10
SFR	λ Ori			
Model (Vega cal)	dm	Δdm	Unc	$E_{(B-V)}$
Geneva(0)	7.77 < 7.87 < 8.03	0.26	0.022	0.12
Geneva-Bessell(0)	7.89 < 7.98 < 8.16	0.27	0.025	0.11
Padova-Bessell(0)	7.81 < 7.98 < 8.15	0.34	0.026	0.11
Geneva-Bessell(/ = 0)	7.86 < 7.96 < 8.13	0.27	0.024	0.11
Padova-Bessell(/ = 0)	7.79 < 7.92 < 7.99	0.20	0.025	0.11
SFR	h Per			
Model (Vega cal)	dm	Δdm	Unc	$E_{(B-V)}$
Geneva(0)	11.77 < 11.78 < 11.85	0.08	0.0250	0.57
Geneva-Bessell(0)	11.77 < 11.78 < 11.84	0.07	0.0260	0.54
Padova-Bessell(0)	11.63 < 11.65 < 11.74	0.11	0.0310	0.52
Geneva-Bessell(/ = 0)	11.76 < 11.78 < 11.80	0.04	0.0270	0.54
Padova-Bessell(/ = 0)	11.67 < 11.74 < 11.75	0.08	0.0300	0.52
SFR	χ Per			
Model (Vega cal)	dm	Δdm	Unc	$E_{(B-V)}$
Geneva(0)	11.82 < 11.82 < 11.85	0.03	0.010	0.52

Geneva-Bessell(0)	$11.79 < 11.82 < 11.88$	0.09	0.005	0.50
Padova-Bessell(0)	$11.77 < 11.79 < 11.86$	0.09	0.012	0.50
Geneva-Bessell($/ = 0$)	$11.80 < 11.82 < 11.85$	0.05	0.011	0.50
Padova-Bessell($/ = 0$)	$11.79 < 11.80 < 11.82$	0.03	0.010	0.50
SFR	NGC1960			
Model (Vega cal)	dm	Δdm	Unc	$E_{(B-V)}$
Geneva(0	$10.21 < 10.22 < 10.30$	0.09	0.0170	0.22
Geneva-Bessell(0)	$10.27 < 10.35 < 10.46$	0.19	0.0164	0.20
Padova-Bessell(0	$10.17 < 10.29 < 10.43$	0.26	0.0164	0.20
Geneva-Bessell($/ = 0$)	$10.21 < 10.23 < 10.31$	0.10	0.0164	0.20
Padova-Bessell($/ = 0$)	$10.20 < 10.31 < 10.40$	0.20	0.0164	0.20
SFR	NGC2547			
Model (Vega cal)	dm	Δdm	Unc	$E_{(B-V)}$
Geneva(0)	$7.85 < 7.93 < 7.97$	0.12	0.012	0.053
Geneva-Bessell(0)	$7.98 < 8.05 < 8.09$	0.11	0.018	0.038
Padova-Bessell(0)	$7.97 < 8.04 < 8.06$	0.09	0.018	0.038
Geneva-Bessell($/ = 0$)	$7.92 < 8.03 < 8.07$	0.15	0.020	0.034
Padova-Bessell($/ = 0$)	$7.92 < 7.99 < 8.05$	0.13	0.020	0.034

Table 4.8: The distance moduli and $E(B-V)$ values , derived using $U-B$ $B-V$ fitting, for each SFR using the different models and calibrations to Vega colours of zero or Vega $B-V=-0.002$ and $U-B=-0.004$. Uncertainties required to achieve $0.40 < P_r(\tau^2) < 0.60$ are also shown.

4.8 Results

As stated in Section 4.7 the choice of model, from those studied, is largely arbitrary. To discuss the implications of a single self-consistent set of distances and extinctions, one model must be adopted. The Geneva-Bessell isochrones for a Vega colour zero system are adopted here. The results of the distance and extinction fits using the Geneva-Bessell models are displayed as Figures 4.13, 4.15 and 4.29-4.43. Table 4.10 provides a comparison of the newly derived distances, with the 68% confidence intervals, to the distances adopted from the literature (see Section 4.2). The best fitting $E(B-V)$ is also provided.

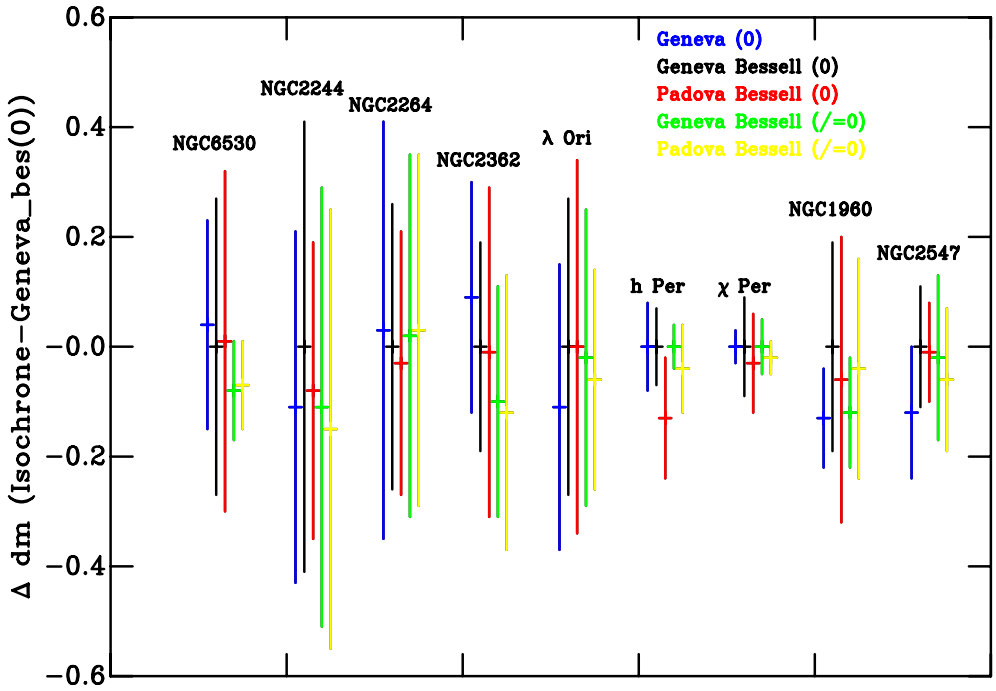

Figure 4.28: The distances and uncertainties (68% confidence intervals) derived for all SFRs and all isochrones, where a mean extinction has been derived. The results shown for each cluster are for, from left to right, Geneva (0) (blue), Geneva Bessell (0) (black), Padova Bessell (0) (red), Geneva Bessell (/=0) (green) and Padova Bessell (/=0) (yellow). All the resulting distances agree within the uncertainties for all models.

Intrinsic colours from $T_{\rm eff}$			
SFR	The ONC		
Model (colour used)	dm	Δdm	Unc
Geneva-Bessell($B-V$)	$7.91 < 7.96 < 8.03$	0.12	0.010
Geneva-Bessell($V-I$)	$7.88 < 7.96 < 8.00$	0.12	0.013

Table 4.6: The distance moduli derived for the ONC using intrinsic colours derived from T_eff values of Hillenbrand (1997) in different colour indices. Uncertainties required to achieve $0.40 < P_r(\tau^2) < 0.60$ are also shown.

Intrinsic colours from $T_{\rm eff}$, $B-V$			
SFR	χ Per		
Model (stars used)	dm	Δdm	Unc
Geneva-Bessell(Hot)	11.70 < 11.78 < 11.93	0.23	0.003
Geneva-Bessell(Hot and cool)	11.83 < 11.84 < 11.87	0.04	0.00
SFR	h Per		
Model (stars used)	dm	Δdm	Unc
Geneva-Bessell(Hot)	11.76 < 11.78 < 11.94	0.18	0.004
Geneva-Bessell(Hot and cool)	11.83 < 11.83 < 11.84	0.01	0.019

Table 4.7: The distance moduli derived for h and χ Per using intrinsic colours derived from $T_{\rm eff}$ values of Slesnick et al. (2002) alone or supplemented by cooler stars dereddenned using an average extinction. Uncertainties required to achieve $0.40 < P_r(\tau^2) < 0.60$ are also shown.

Revised Q-method				
SFR	NGC6530			
Model (Vega cal)	dm	Δdm	Unc	$\overline{E_{(B-V)}}$
Geneva-Bessell(0)	10.49 < 10.50 < 10.60	0.11	0.011	0.33
Padova-Bessell(0)	10.47 < 10.48 < 10.58	0.11	0.011	0.35
Geneva-Bessell(/ = 0)	10.36 < 10.41 < 10.49	0.13	0.011	0.34
Padova-Bessell(/ = 0)	10.48 < 10.52 < 10.57	0.09	0.009	0.34
SFR	NGC2244			
Model (Vega cal)	dm	Δdm	Unc	$\overline{E_{(B-V)}}$
Geneva-Bessell(0)	10.66 < 10.77 < 10.81	0.15	0.01	0.44
Padova-Bessell(0)	10.68 < 10.76 < 11.84	0.16	0.013	0.45
Geneva-Bessell(/ = 0	10.67 < 10.76 < 10.89	0.22	0.014	0.42
Padova-Bessell(/ = 0)	10.70 < 10.81 < 10.92	0.22	0.013	0.43
SFR	λ Ori			
Model (Vega cal)	dm	Δdm	Unc	$\overline{E_{(B-V)}}$
Geneva-Bessell(0)	7.99 < 8.01 < 8.12	0.13	0.005	0.10
Padova-Bessell(0)	7.93 < 8.01 < 8.09	0.16	0.007	0.10
Geneva-Bessell(/ = 0)	7.95 < 7.97 < 8.11	0.16	0.007	0.17
Padova-Bessell(/ = 0)	7.94 < 7.97 < 8.08	0.14	0.007	0.12

Table 4.9: The distance moduli and mean $E(B-V)$ values , after application of Q, for each SFR using the different models and calibrations to Vega colours of zero or Vega $B-V=-0.002$ and $U-B=-0.004$. Uncertainties required to achieve $0.40 < P_r(\tau^2) < 0.60$ are also shown.

SFR	Adopted literature distance(dm)	Range	This work dm	Range	$\Delta\overline{dm}$	Δ range	$E(B-V)$
the ONC	8.01 < 8.38 < 8.75	0.76	7.91 < 7.96 < 8.03	0.12	-0.42	-0.64	$\approx 0.40^{(1)}$
NGC6530[(2)]	10.48[(4)]	$\approx 0.40^{(3)}$	10.15 < 10.34 < 10.44	0.29	-0.14	-0.11	0.32
NGC6530[(4)]	10.48[(4)]	$\approx 0.40^{(3)}$	10.49 < 10.50 < 10.60	0.11	+0.02	-0.29	0.33
NGC2244[(2)]	10.55 < 10.72 < 10.87	0.33	10.68 < 10.89 < 10.94	0.26	+0.17	-0.07	0.46
NGC2244[(4)]	10.55 < 10.72 < 10.87	0.33	10.66 < 10.77 < 10.81	0.15	+0.05	-0.18	0.44
NGC2264	9.6[(5)]	$\approx 0.40^{(4)}$	9.26 < 9.37 < 9.52	0.26	-0.23	-0.14	0.04
NGC2362	10.84 < 10.87 < 10.90	0.06	10.51 < 10.67 < 10.70	0.19	-0.20	+0.13	0.10
λ Ori[(4)]	7.73 < 7.90 < 8.07	0.34	7.99 < 8.01 < 8.12	0.13	+0.11	-0.21	0.10
λ Ori[(2)]	7.73 < 7.90 < 8.07	0.34	7.89 < 7.98 < 8.16	0.27	+0.08	-0.07	0.11
σ Ori	7.41 < 7.80 < 8.19	0.78	7.84 < 7.94 < 8.10	0.26	+0.14	-0.52	$0.06^{(6)}$
χ Per	11.69 < 11.70 < 11.71	0.20	11.79 < 11.82 < 11.88	0.09	+0.12	-0.11	0.50
h Per[(7)]	11.69 < 11.70 < 11.71	0.20	11.77 < 11.78 < 11.84	0.07	+0.08	-0.13	0.54
NGC1960[(9)]	10.40 < 10.60 < 10.80	0.40	10.27 < 10.35 < 10.46	0.19	-0.25	-0.21	0.20
NGC2547[(10)]	7.92 < 8.18 < 8.47	0.54	7.98 < 8.05 < 8.09	0.11	-0.13	-0.43	0.038

Table 4.10: Distance moduli and range adopted and those derived in this chapter. Notes are as follows. (1) Individual extinctions from $T_{\rm eff}$ value given is approximate mean. (2) Distance derived using mean extinction derivation from τ^2 fitting. (3) No uncertainties given in literature source, typical uncertainties adopted. (4) Distance derived after application of extinctions derived using revised Q-method (see Section 4.6.3), mean extinction quoted. (5) Mean of many values, assumed typical uncertainties. (6) $E(B-V)$ from Brown et al. (1994). (7) Assumed to be at the distance of χ Per.

4.8.1 Notes on results

CepOB3b has a sufficiently populated MS for MS fitting of the type in this chapter. However, CepOB3b has heavy and extremely variable extinction (as mentioned in Section 4.3) but after application of the Q-method the resulting colour range of the target stars was prohibitively low for distance fitting. Literature derivations of extinction for this sub-group (Garrison, 1970; Blaauw et al., 1959) rely on intrinsic colours derived from other isochrones so cannot be fitted to the Geneva-Bessell isochrones.

4.9 Implications

In the previous Section a self-consistently derived set of distances (and extinctions) were presented in general, to a higher precision than those existing in the literature, with statistically meaningful uncertainties for these distances. Now these distances have been derived some of the key implications of both the individual distances and the impact of the entire dataset can be discussed.

4.9.1 Individual Distances

Of the SFRs studied, distances derived for eight are of particular note. Here the distance moduli have been converted to a distance in parsecs to allow more obvious comparisons. It is however important to note that it is difficult to compare two derived distances without a full knowledge of the additional systematic and unaccounted for uncertainties. For instance in this work I adopt a best fitting extinction (without uncertainties) and assume all of the stars selected are on the MS. In practice, however, I have shown most extra uncertainties are small, i.e. those from the different choice of isochrones and the settling of some stars onto the MS. Additionally, Literature results often include the adoption of one isochrone with no multi-model fitting or adopt a mean extinction for a given SFR. Therefore to discuss the precision of my results I compare them to quoted literature uncertainties using the uncertainties derived from the fitting routine ignoring any additional uncertainties. Distances derived using trigonometric parallaxes are free from assumptions of a model, however both isochrone fitting and distances derived from eclipsing binaries are not, requiring the use of model atmospheres or theoretical mass-radius relations.

4.9.1.1 The ONC

The precision of the distance estimate for the ONC has been increased by a factor of 7 compared to that adopted from the literature. This new distance is also closer than the previously accepted result from the maser measurements of Genzel et al. (1981), by 0.42 mag. Conversely this new distance, 391^{+12}_{-9} pc agrees superbly with several recent derivations in the literature. Firstly, Jeffries (2007a) finds a distance of 392 ± 32 pc from the rotational properties of low-mass pre-MS stars (after removing accreting objects). Secondly, a parallactic distance of 389^{+24}_{-21} pc from very long baseline array observations has been found by Sandstrom et al. (2007). Lastly, Kraus et al. (2007) find a distance of 434 ± 12 or 387 ± 11 pc by modeling the orbit of the θ^1 Ori C binary system. They adopt 434 pc as the likely result after comparison to the distance obtained by Jeffries (2007a) for

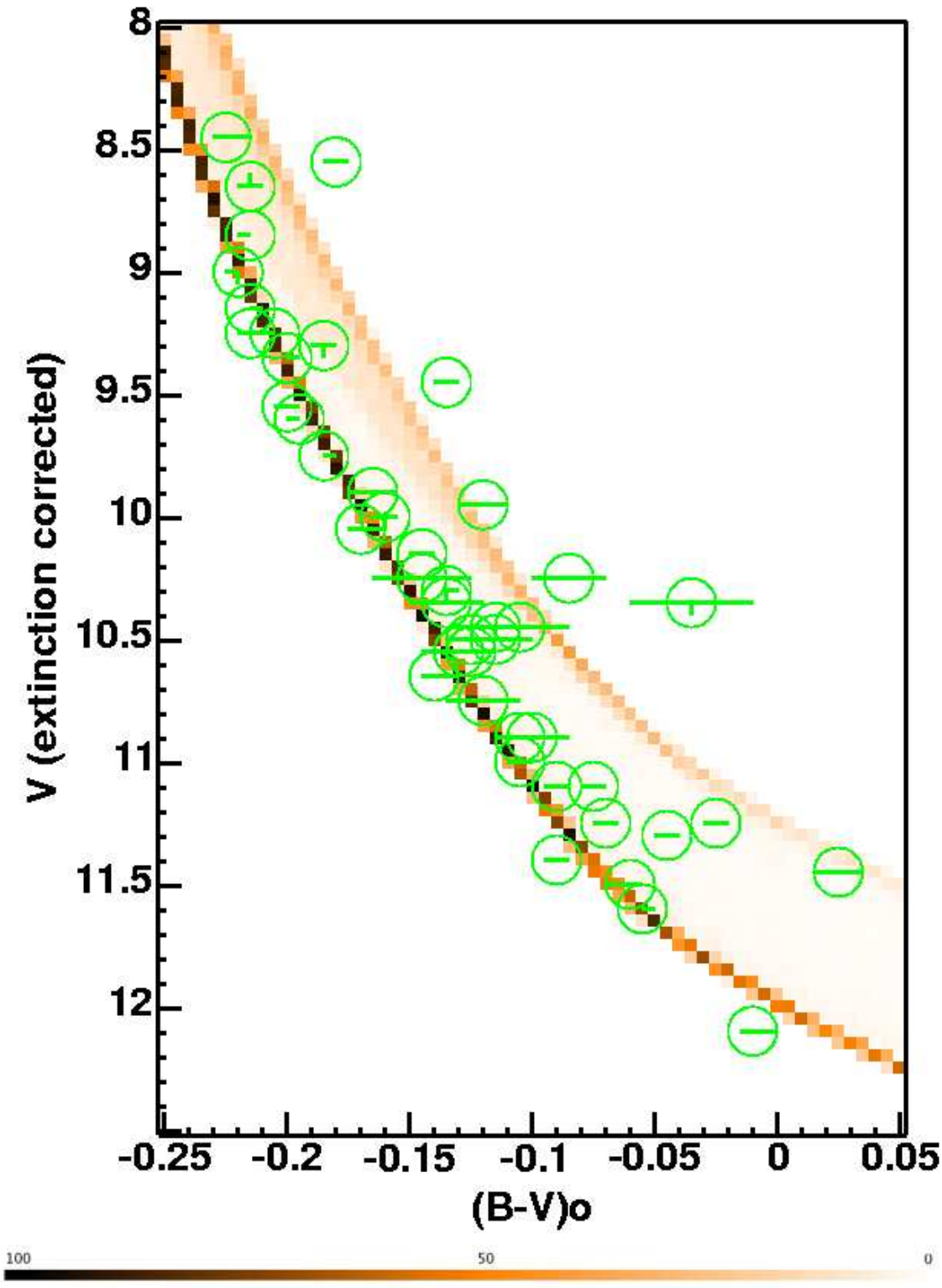

Figure 4.29: NGC6530 distance fit using Q-method extinctions (see Section 4.6.3). Figure shown in intrinsic colour and extinction corrected magnitude. The colour bar shows the probability density (ρ from Naylor & Jeffries, 2006) for the contours in the figure, generated using the isochrone. The circles are the positions of the photometric points with the bars showing the uncertainties where available.

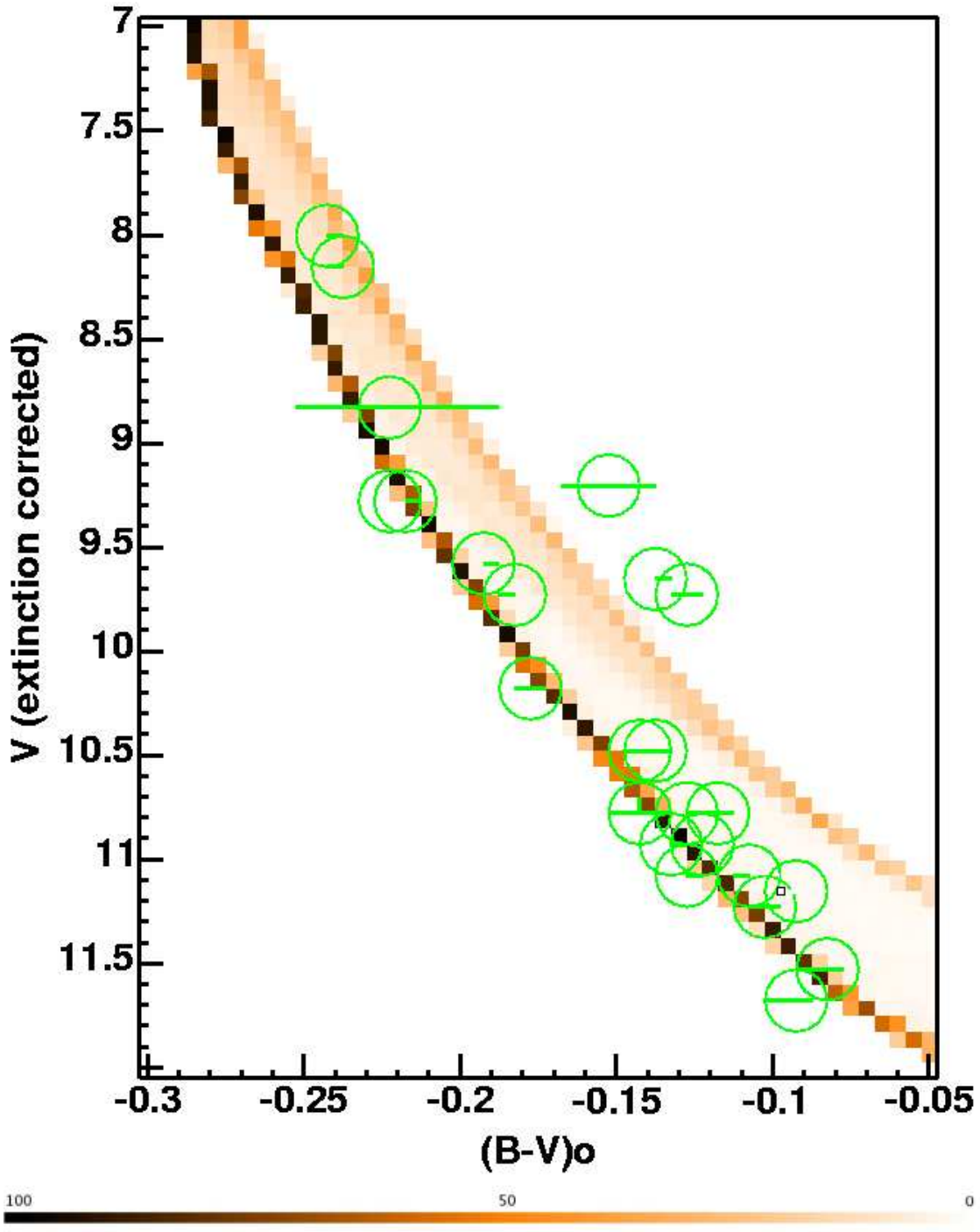

Figure 4.30: NGC2244 distance fit using Q-method extinctions (see Section 4.6.3). Figure shown in intrinsic colour and extinction corrected magnitude. The colour bar shows the probability density (ρ from Naylor & Jeffries, 2006) for the contours in the figure, generated using the isochrone. The circles are the positions of the photometric points with the bars showing the uncertainties where available.

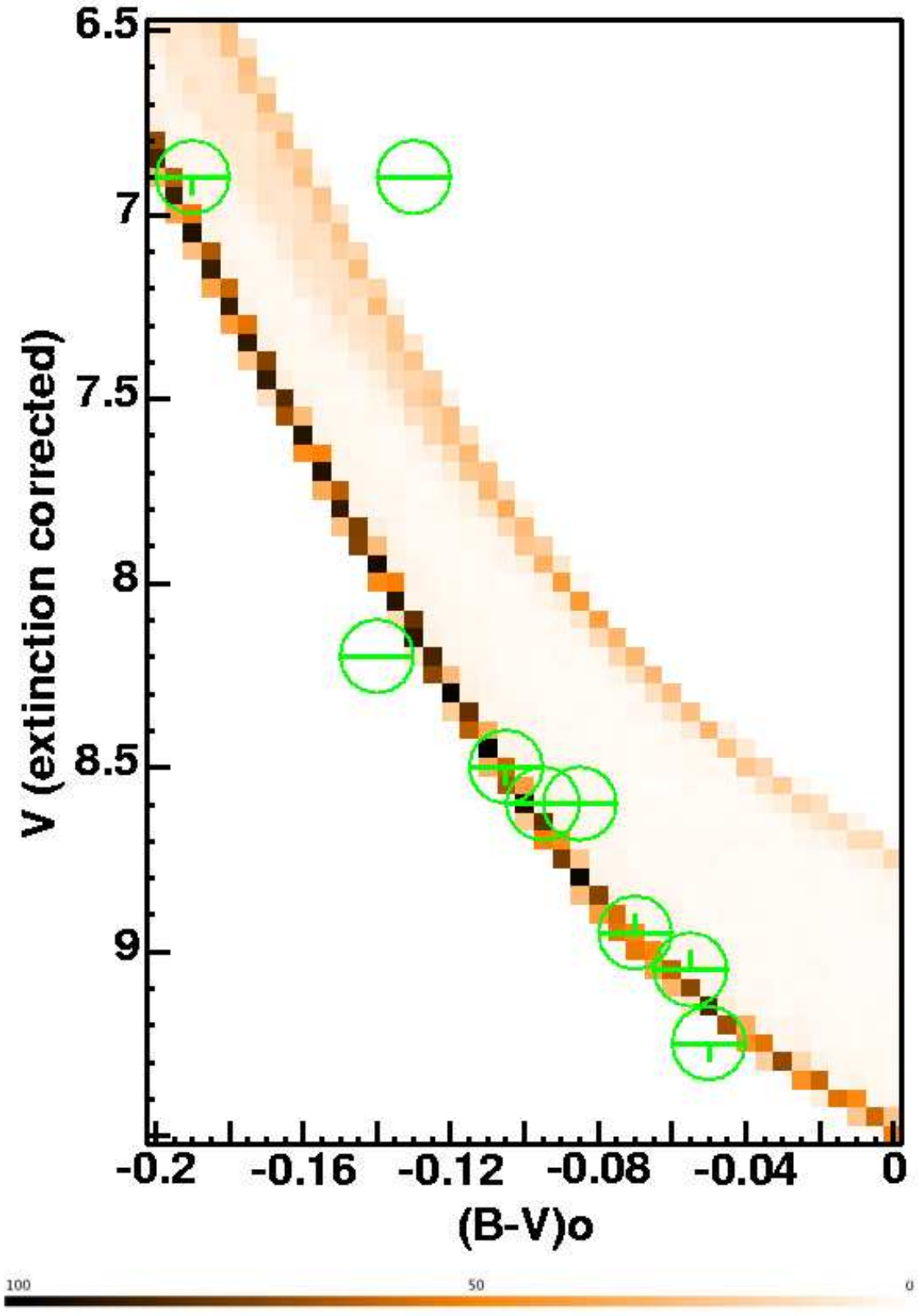

Figure 4.31: λ Ori distance fit using the Q-method extinctions (see Section 4.6.3). Figure shown in intrinsic colour and extinction corrected magnitude. The colour bar shows the probability density (ρ from Naylor & Jeffries, 2006) for the contours in the figure, generated using the isochrone. The circles are the positions of the photometric points with the bars showing the uncertainties where available.

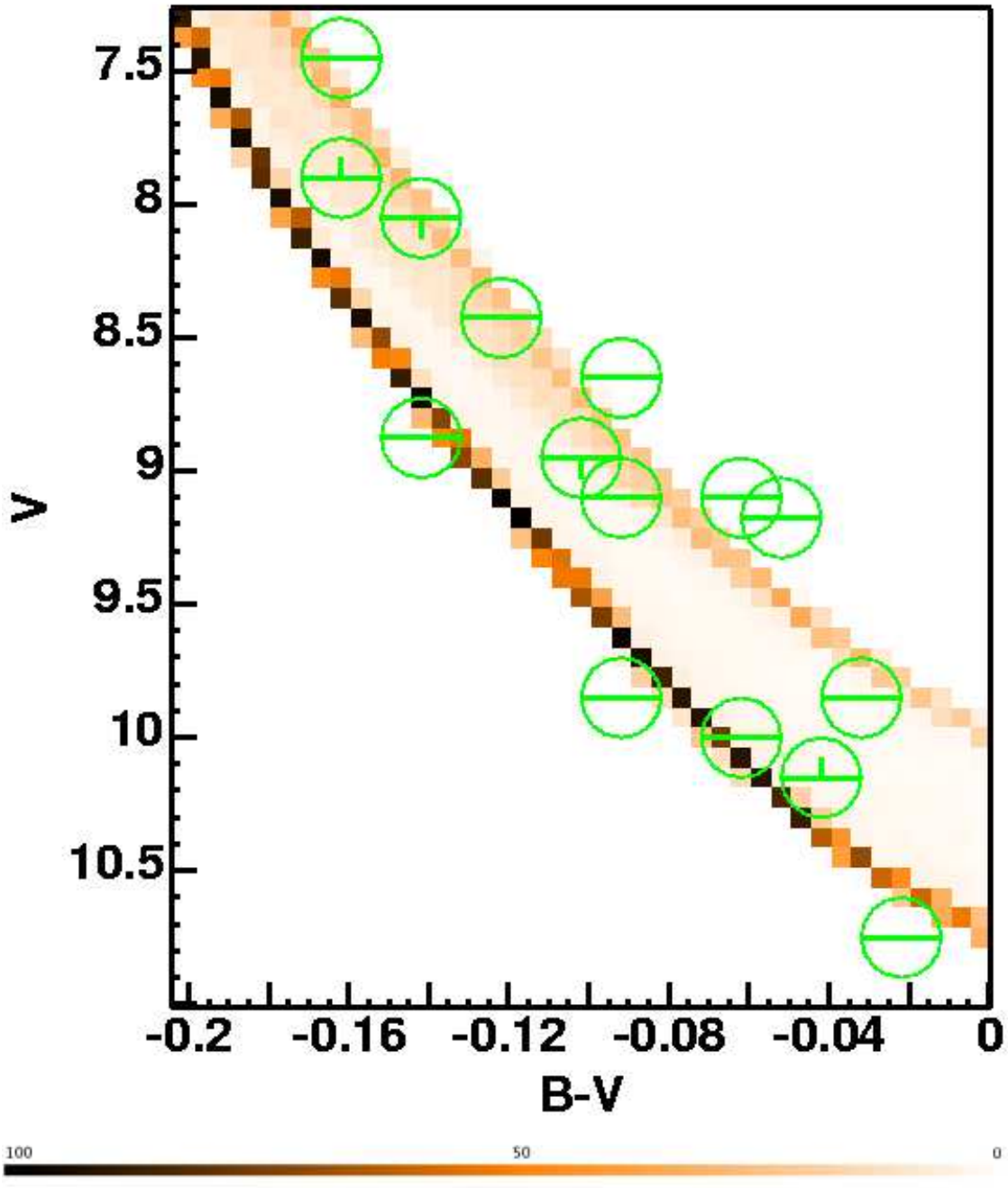

Figure 4.32: NGC2264 distance fit. The colour bar shows the probability density (ρ from Naylor & Jeffries, 2006) for the contours in the figure, generated using the isochrone. The circles are the positions of the photometric points with the bars showing the uncertainties where available.

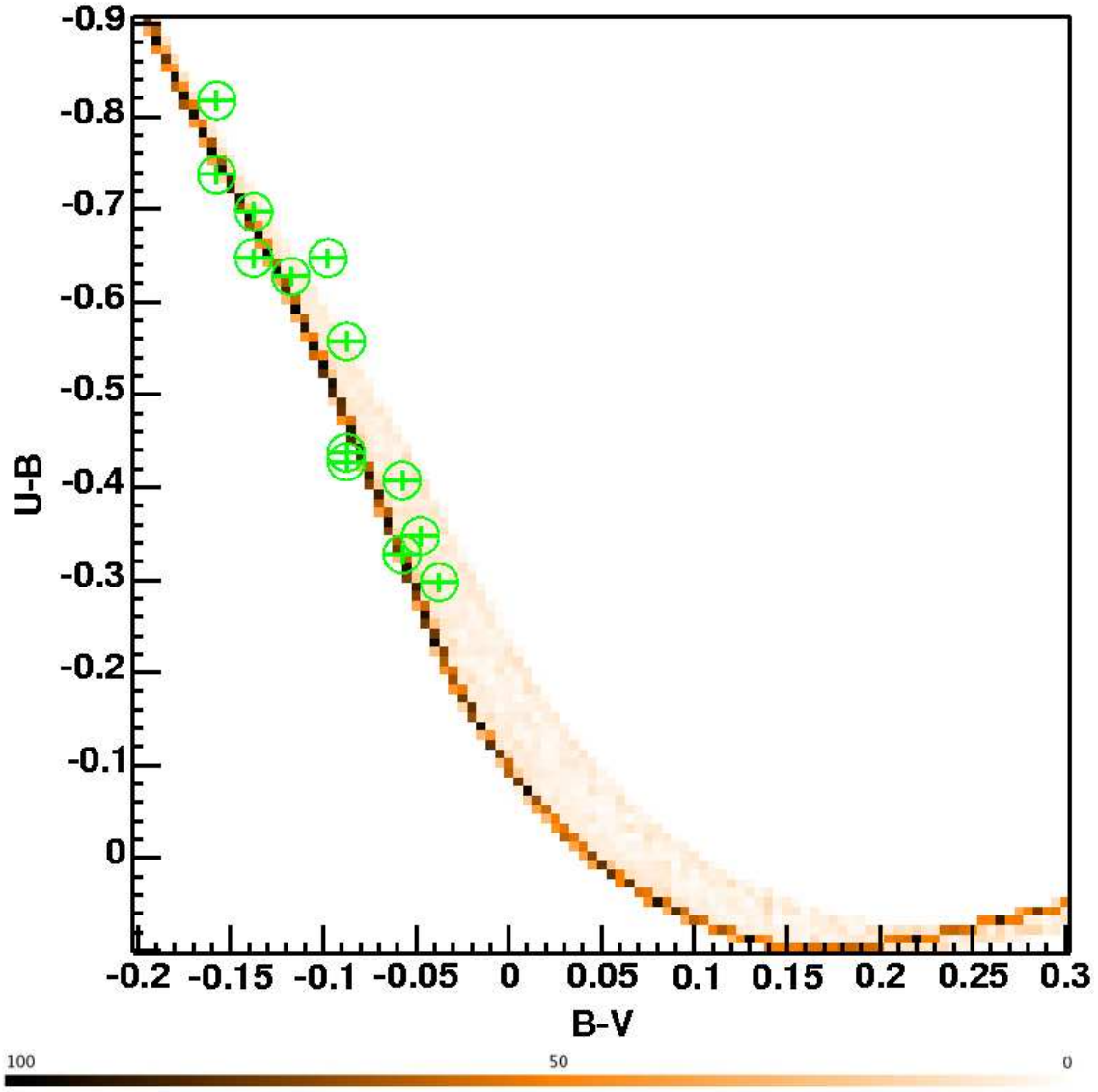

Figure 4.33: NGC2264 $E(B-V)$ fit. The colour bar shows the probability density (ρ from Naylor & Jeffries, 2006) for the contours in the figure, generated using the isochrone. The circles are the positions of the photometric points with the bars showing the uncertainties where available.

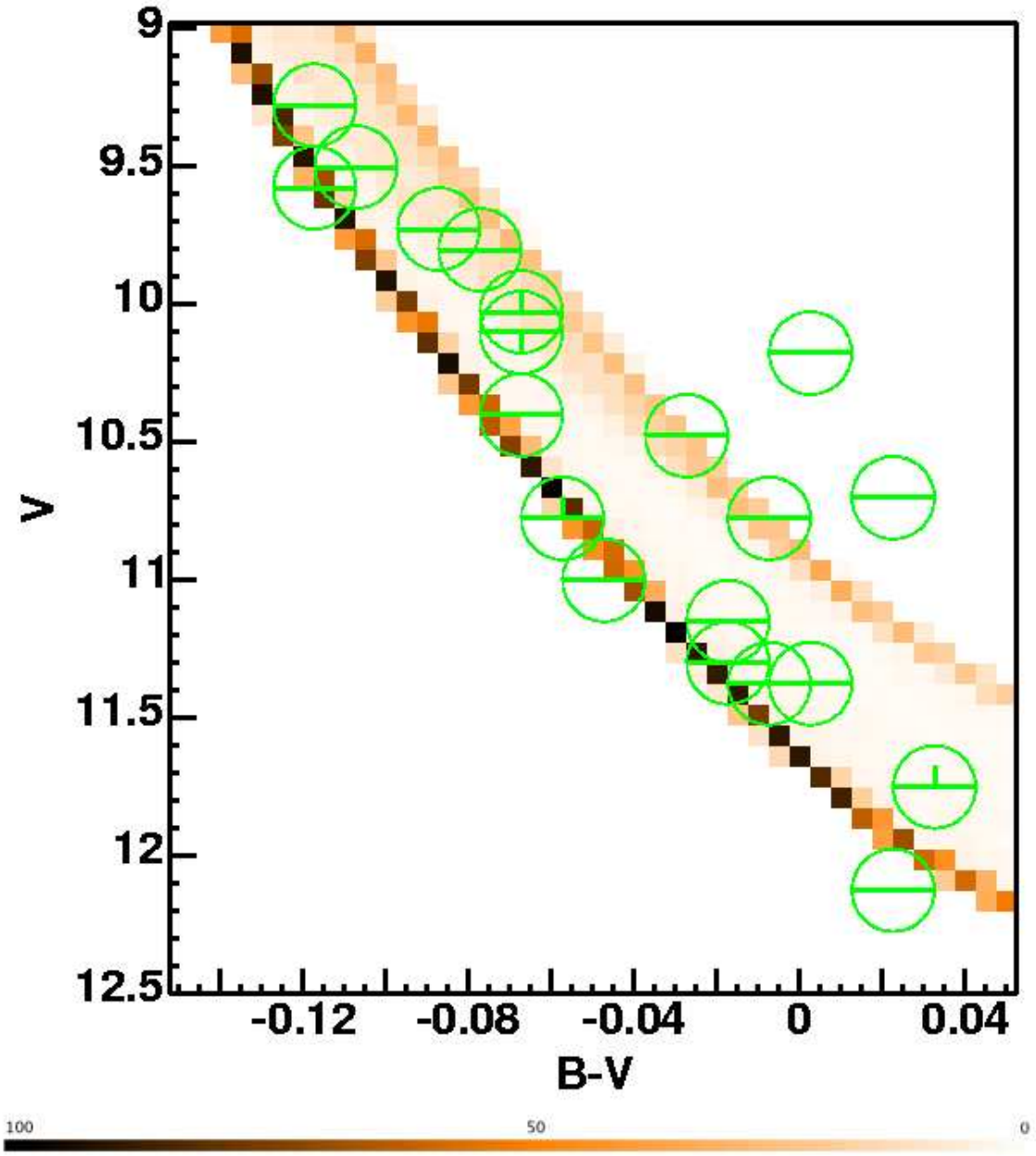

Figure 4.34: NGC2362 distance fit. The colour bar shows the probability density (ρ from Naylor & Jeffries, 2006) for the contours in the figure, generated using the isochrone. The circles are the positions of the photometric points with the bars showing the uncertainties where available.

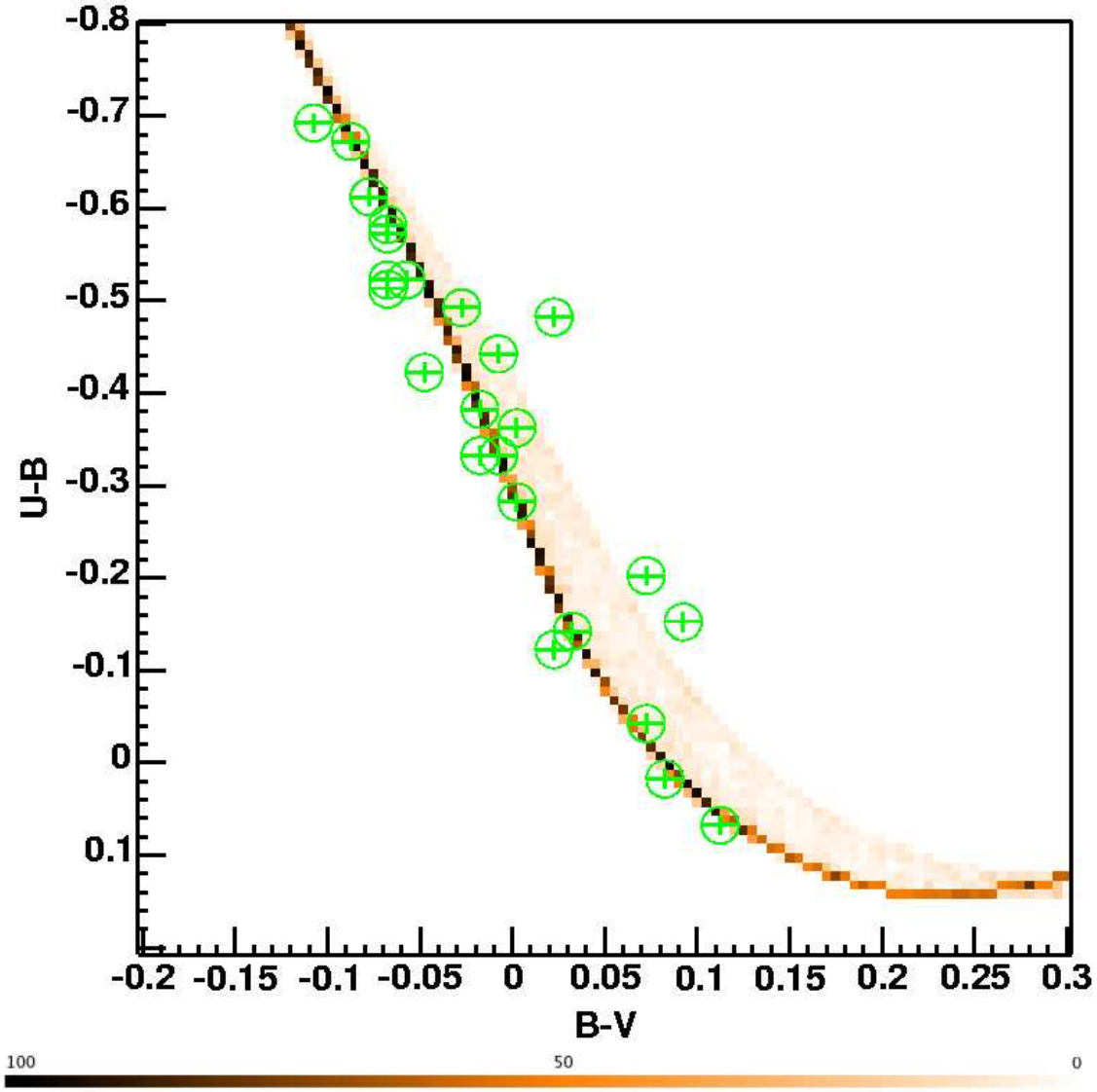

Figure 4.35: NGC2362 $E(B-V)$ fit. The colour bar shows the probability density (ρ from Naylor & Jeffries, 2006) for the contours in the figure, generated using the isochrone. The circles are the positions of the photometric points with the bars showing the uncertainties where available.

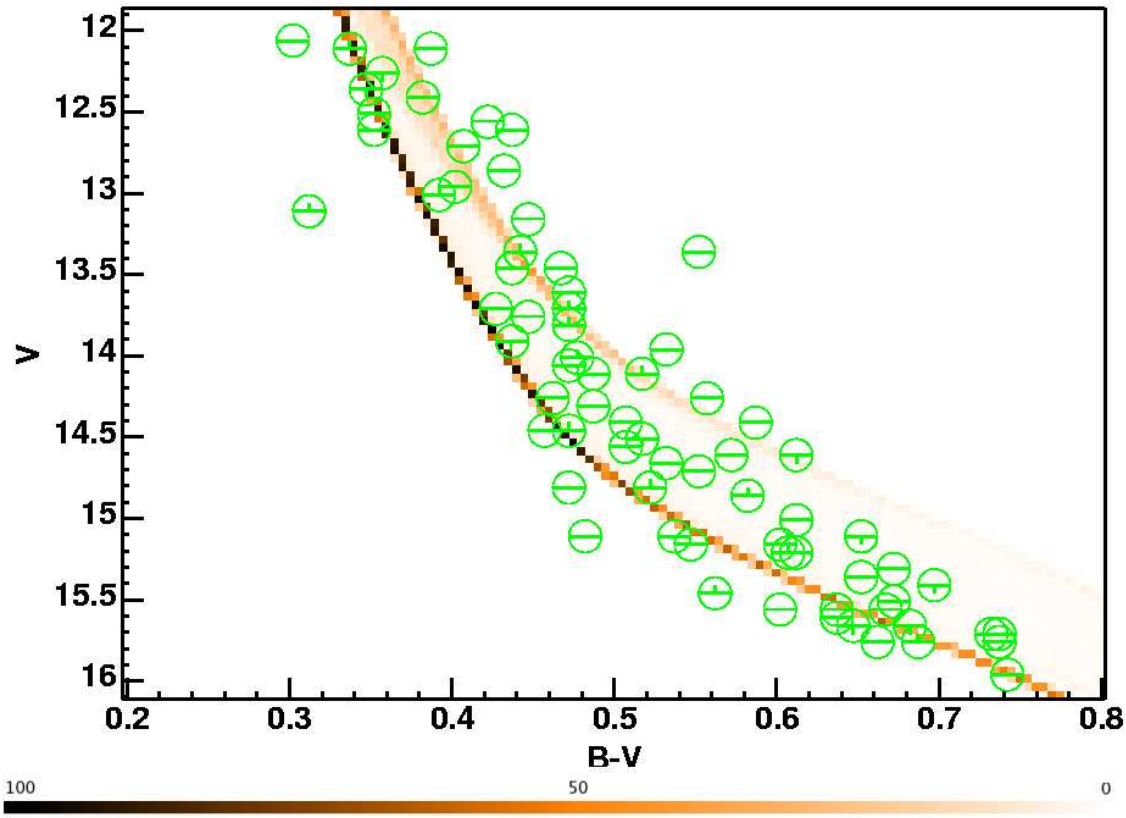

Figure 4.36: h Per distance fit. The colour bar shows the probability density (ρ from Naylor & Jeffries, 2006) for the contours in the figure, generated using the isochrone. The circles are the positions of the photometric points with the bars showing the uncertainties where available.

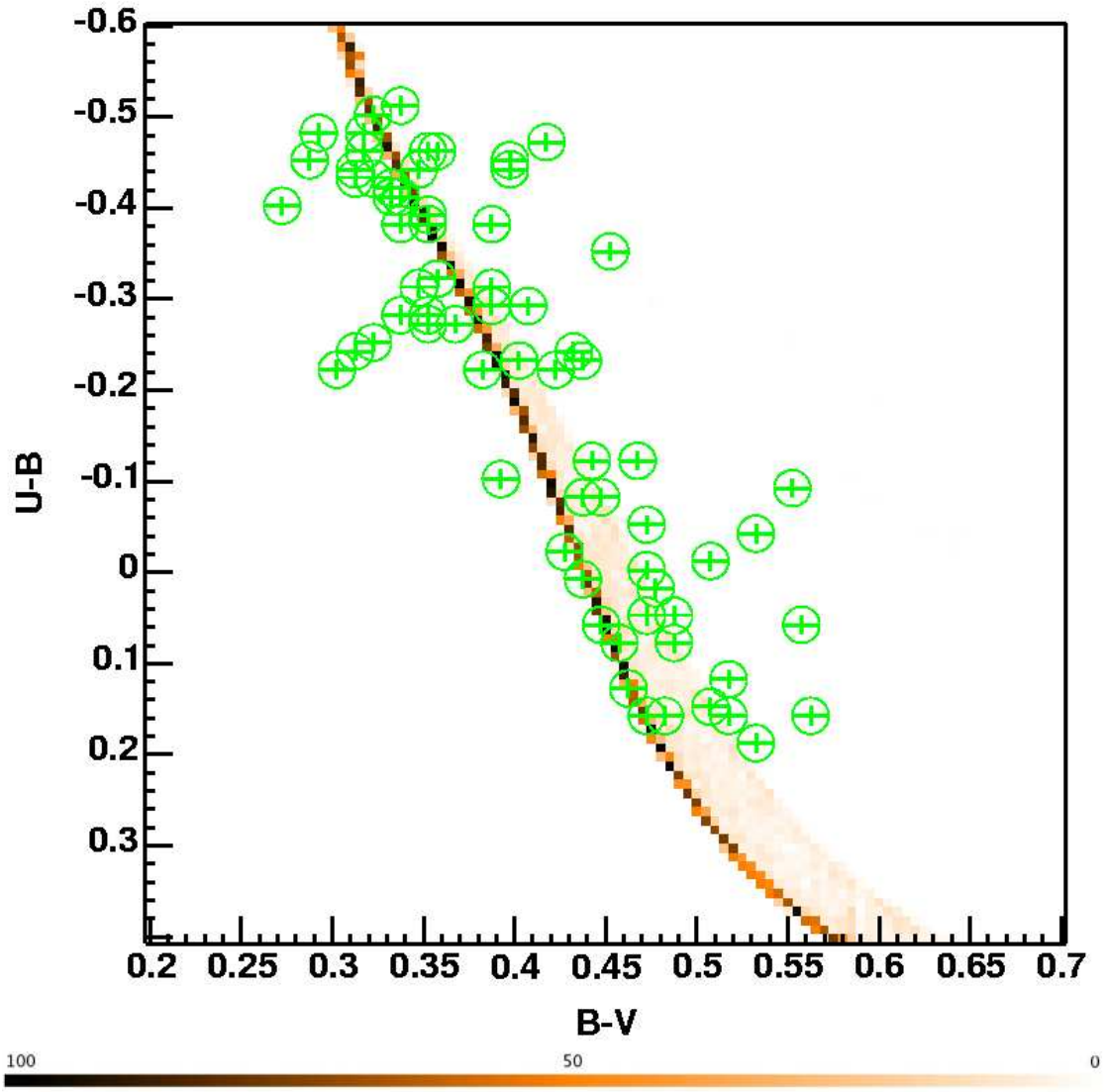

Figure 4.37: h Per $E(B-V)$ fit. Here a systematic shift in $E(B-V)$ as a function of colour $(U-B)$ is evident. This is probably due to a difference in the photometric systems of Bessell et al. (1998) and Slesnick et al. (2002) (see Section 4.6.3). The colour bar shows the probability density (ρ from Naylor & Jeffries, 2006) for the contours in the figure, generated using the isochrone. The circles are the positions of the photometric points with the bars showing the uncertainties where available.

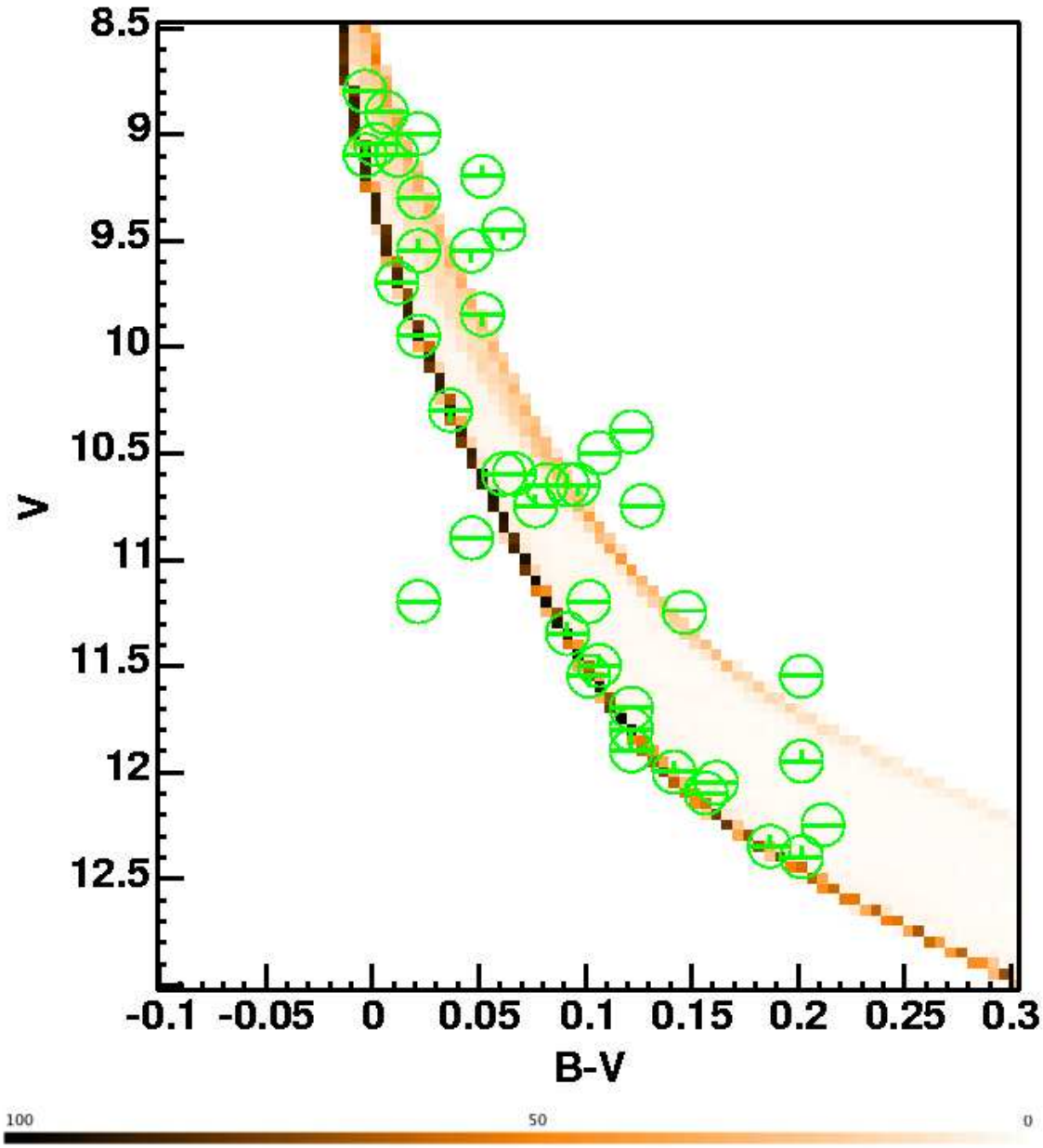

Figure 4.38: NGC1960 distance fit. The colour bar shows the probability density (ρ from Naylor & Jeffries, 2006) for the contours in the figure, generated using the isochrone. The circles are the positions of the photometric points with the bars showing the uncertainties where available.

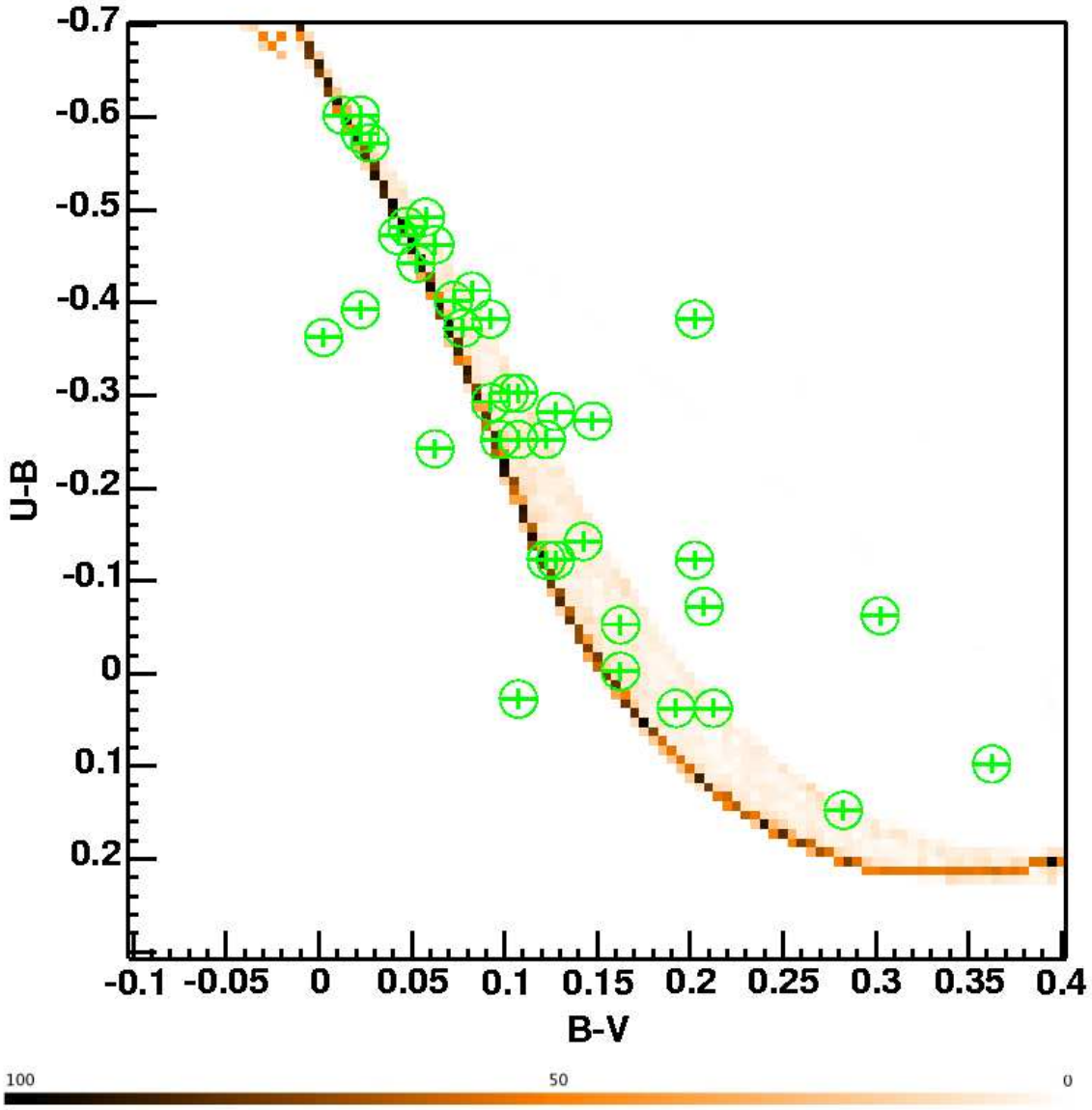

Figure 4.39: NGC1960 $E(B-V)$ fit. The colour bar shows the probability density (ρ from Naylor & Jeffries, 2006) for the contours in the figure, generated using the isochrone. The circles are the positions of the photometric points with the bars showing the uncertainties where available.

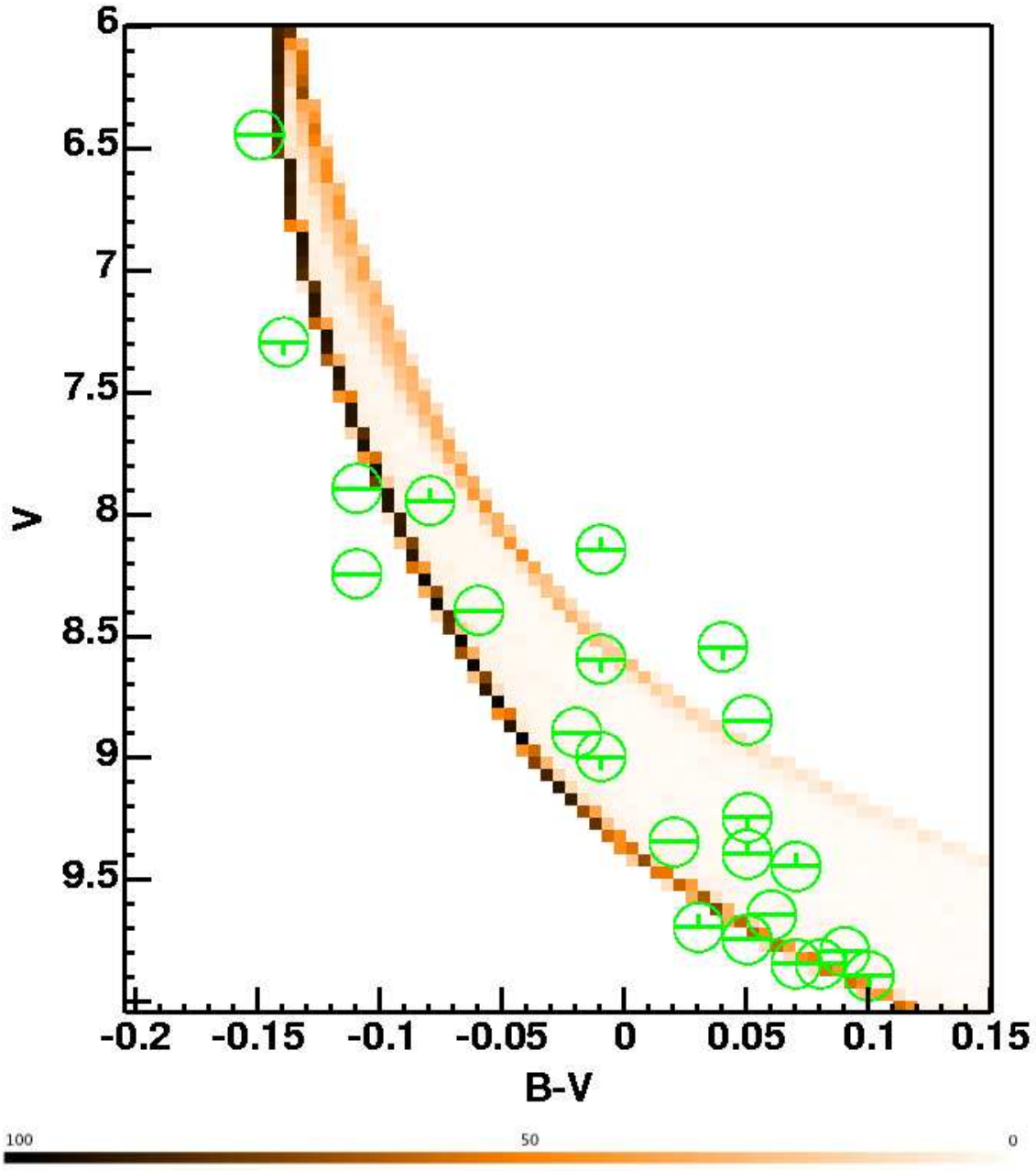

Figure 4.40: NGC2547 distance fit. The colour bar shows the probability density (ρ from Naylor & Jeffries, 2006) for the contours in the figure, generated using the isochrone. The circles are the positions of the photometric points with the bars showing the uncertainties where available.

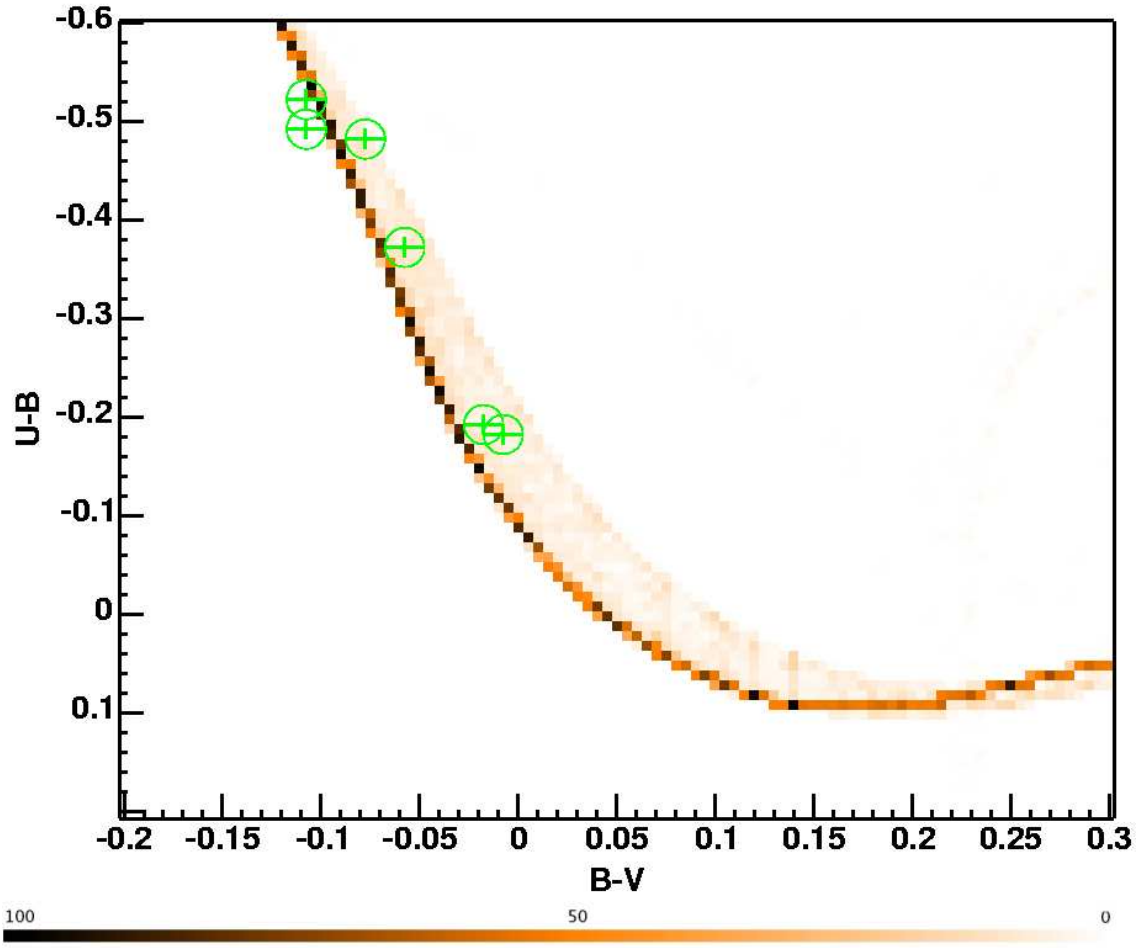

Figure 4.41: NGC2547 $E(B-V)$ fit. The colour bar shows the probability density (ρ from Naylor & Jeffries, 2006) for the contours in the figure, generated using the isochrone. The circles are the positions of the photometric points with the bars showing the uncertainties where available.

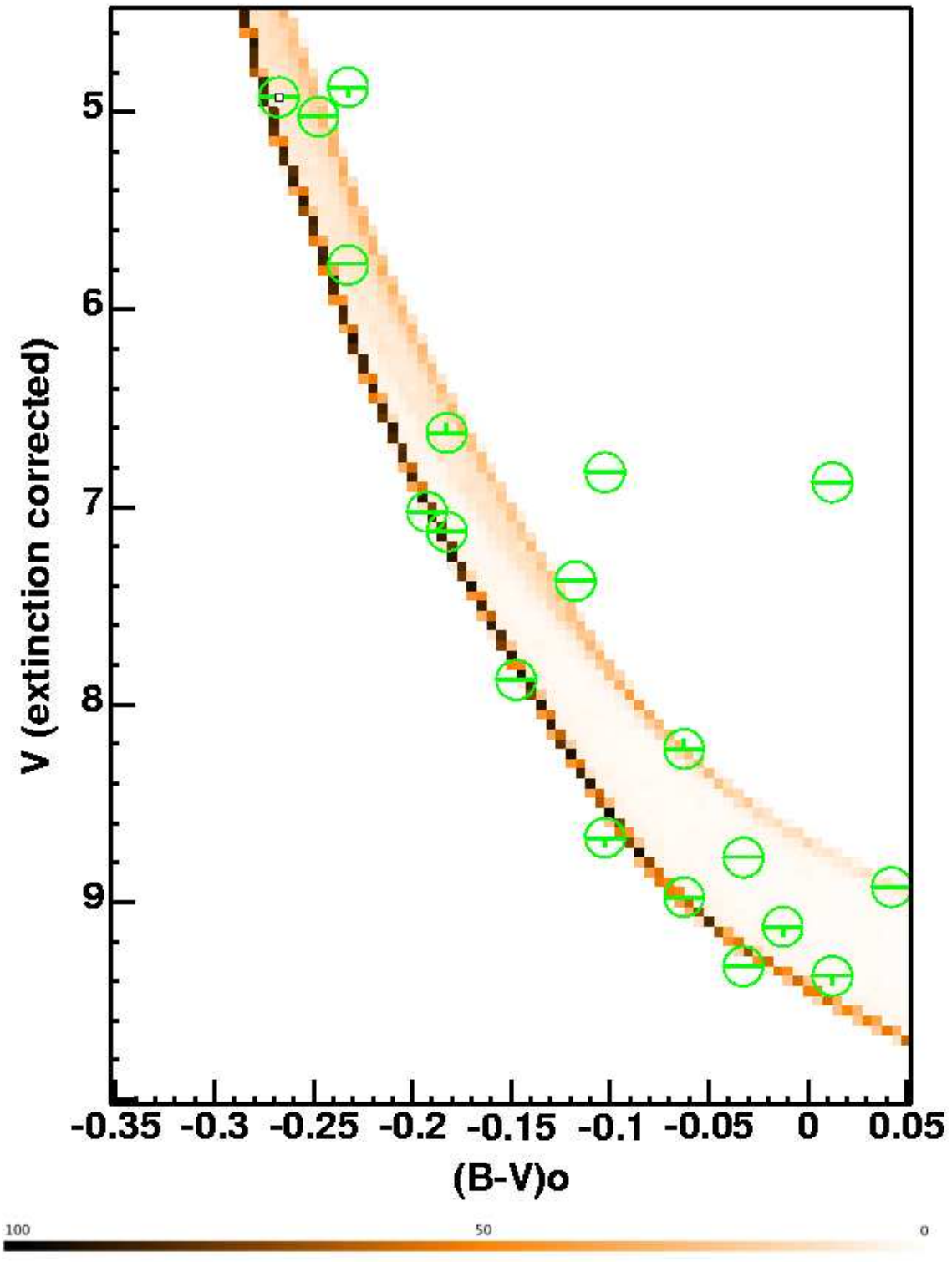

Figure 4.42: The ONC distance fit. Figure shown in intrinsic colour and extinction corrected magnitude. The colour bar shows the probability density (ρ from Naylor & Jeffries, 2006) for the contours in the figure, generated using the isochrone. The circles are the positions of the photometric points with the bars showing the uncertainties where available.

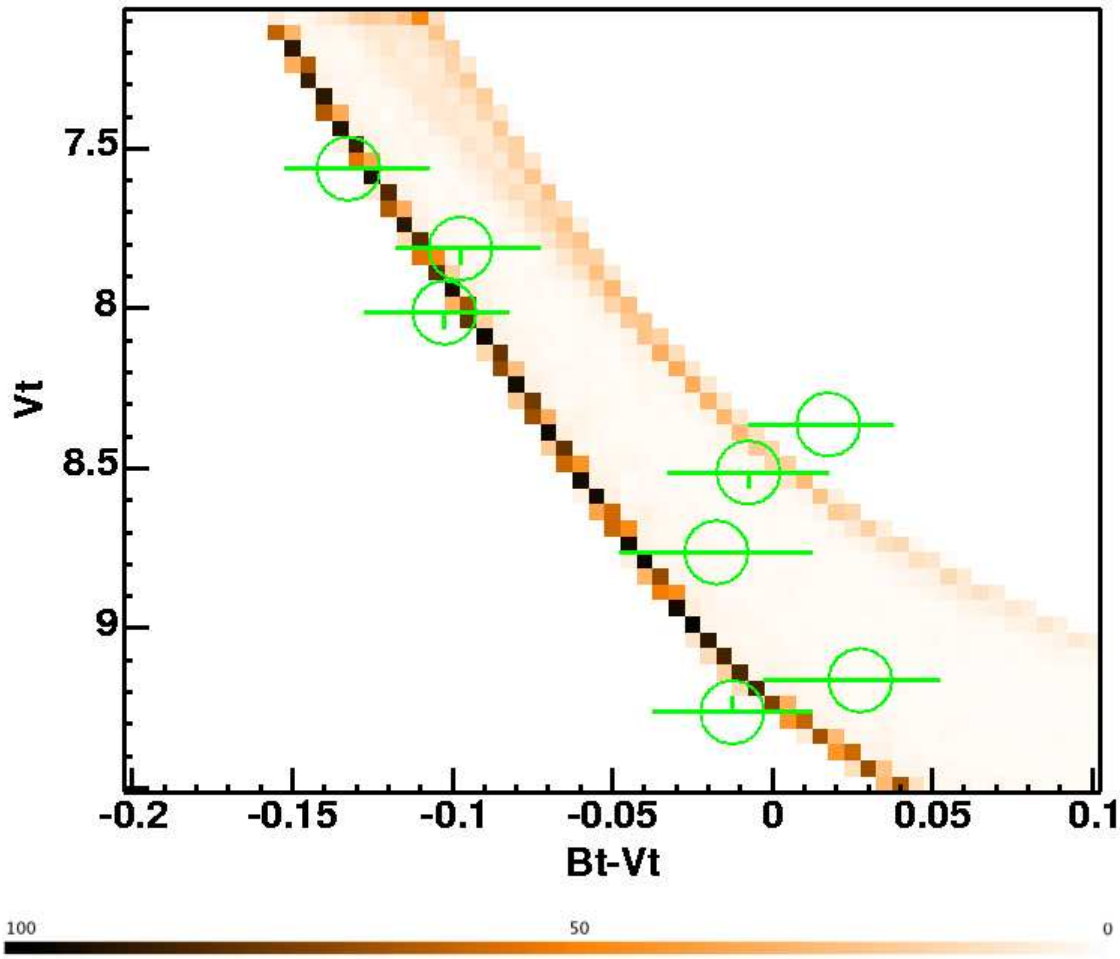

Figure 4.43: σ Orionis distance fit. The colour bar shows the probability density (ρ from Naylor & Jeffries, 2006) for the contours in the figure, generated using the isochrone. The circles are the positions of the photometric points with the bars showing the uncertainties where available.

all objects including those showing evidence of accretion. Clearly, my result favours the solution yielding 387 pc.

This closer distance (391^{+12}_{-9} pc compared to 480 ± 80 pc) has important implications for the stellar population of the ONC. It means the pre-MS population lies 0.42 mags fainter in absolute magnitude in the CMD. This will force the isochronal age of stars older, but perhaps more importantly increase their spread (see the discussion in Palla et al., 2005) in isochronal age derived from a CMD. This is due to the bunching of older isochrones towards the zero-age-main-sequence (ZAMS). In fact there is also evidence of a spread in the CMD from the MS members used to derive a distance. This is discussed further in Chapter 6.

4.9.1.2 σ Orionis

The precision of the distance estimate adopted for σ Orionis has been improved by a factor of 2. Caballero (2007) derives a distance based on *TYCHO* photometry of 360^{+70}_{-60} pc. Although *TYCHO* photometry is also used here, updated photometric conversions from Bessell (2000) are used. A distance of 389^{+34}_{-24} pc was derived, a more precise value in agreement with that of Caballero (2007).

4.9.1.3 NGC2547

For NGC2547 the precision in distance compared with that adopted has been increased by a factor of 5. I derive a distance of 407^{+8}_{-13} pc, which compares favourably with the *HIPPARCOS* result of 433^{+62}_{-49} pc from Robichon et al. (1999). However, Naylor & Jeffries (2006) use pre-MS isochrones to obtain a distance of 361^{+19}_{-8} pc. The age and distance derivation in Naylor & Jeffries (2006) is consistent with the Li depletion boundary, which is also based on pre-MS models. Therefore the difference in distance is probably attributable to a model-dependent difference between the MS and pre-MS models. Interestingly a different extinction is also obtained, $E(B-V) = 0.038$ to that of Claria (1982a), $E(B-V) = 0.06 \pm 0.02$ which is used in Naylor & Jeffries (2006). However, this does not have a significant impact on their distance, and so does not explain the discrepancy between the MS and pre-MS distances.

4.9.1.4 NGC2244

The distance to NGC2244 derived is $1\,425^{+27}_{-70}$ pc, using individual extinctions from the new Q-method (see Section 4.6.3). This compares well to the literature result of $1\,390 \pm 100$ pc from the study of an eclipsing binary, Hensberge et al. (2000). Previous MS isochrone fitting studies placed this SFR at $1\,667^{+128}_{-118}$ pc (Perez et al., 1987), and 1 660 pc (Park & Sung, 2002, , the photometric dataset adopted in this chapter). This result confirms the closer distance of Hensberge et al. (2000) and is marginally consistent with the studies yielding a greater distance, meaning the cluster pre-MS will be moved fainter or older in absolute magnitude by ≈ 0.3 mags.

4.9.1.5 NGC2362

The derived distance for NGC2362, $1\,361^{+19}_{-97}$ pc is closer and less precise than that adopted from the literature, the incredibly precise distance of $1\,493^{+21}_{-20}$ pc, from Balona & Laney (1996), derived using effectively MS fitting to narrow-band photometry. Balona & Laney (1996) derive these uncertainties if "the five most discordant stars are removed" after transformation to a theoretical HR diagram, within which the data show an RMS scatter about the ZAMS of 0.17 mag, the method of obtaining the uncertainties is not stated.

4.9.1.6 h and χ Per

The distance derived for χ Per of $2\,312^{+65}_{-32}$ pc agrees well with the recent literature result of $2\,344^{+55}_{-53}$ pc of Slesnick et al. (2002), as stated in Section 4.5.2. They employ spectroscopy as well as the Q-method (with what appears to be an updated MS line, but canonical reddening vectors) combined with MS isochrone fitting to derive this distance. Interestingly they also derive a spectroscopic parallax distance of 3 162 pc. This method involves dereddening stars with known spectral types onto an intrinsic MS; they conclude that recalibration of these intrinsic colours is required. Also Slesnick et al. (2002) find h and χ Per to be at approximately the same distance, agreeing with the majority of the literature (e.g Keller et al., 2001). The new distance derivations for h and χ Per are also consistent with both these clusters being at the same distance.

4.9.2 Metallicity

There is little work on the metallicity of SFRs. James et al. (2006) show that the metallicity is solar or very slightly sub-solar for the majority of stars in three star-forming-regions, Lupus, Chamaeleon and CrA in the southern hemisphere. Conversely recent eclipsing binary results suggest a metallicity of more like half-solar for h and χ Per and Collinder 228 (Southworth et al., 2004,a; Southworth & Clausen, 2007), with a solar metallicity found in NGC6871 (Southworth et al., 2004b, $Z = 0.02$). If compositions do indeed vary as is suggested from the above results then distances derived to these SFRs must be re-derived after a comprehensive composition survey. As discussed in Section 4.5.3.3, adopting a half-solar composition for χ Per (for example) results in a fall of the derived distance modulus by ≈ 0.5 mags. A similar result would apply for h Per. This will have a significant affect on the ages and age ordering of pre-MS populations, and in addition on any conclusions drawn from studies of secular evolution, such as disc lifetimes.

4.10 Summary

In this chapter a set of consistent and statistically robust distances and extinctions for a range of SFRs have been derived. These have been derived by fitting the young MS between the turn-off and turn-on, the most temporally static part of the isochrone. These distances and extinctions are therefore robust to changes in adopted age. Furthermore, the model dependency of MS isochrones over this age range (0-40 Myrs) has been shown to be negligible. For some SFRs derivation of new

SFR	dm	Extinction ($E(B-V)$)
IC5146[(1)]	10.4	0.97 ± 0.06
ONC	$7.91 < 7.96 < 8.03$	≈ 0.40[(2)]
NGC6530[(3)]	$10.49 < 10.50 < 10.60$	0.33
NGC2244[(3)]	$10.66 < 10.77 < 10.81$	0.44
NGC2264	$9.26 < 9.37 < 9.52$	0.04
CepOB3b[(4)]	$9.45 < 9.65 < 9.85$	≈ 0.93
IC348[(5)]	$7.34 < 7.5 < 7.64$	≈ 0.90
NGC2362	$10.51 < 10.67 < 10.70$	0.10
λ Ori[(3)]	$7.99 < 8.01 < 8.12$	0.10
σ Ori	$7.84 < 7.94 < 8.10$	0.06[(6)]
NGC7160[(7)]	9.77	0.39
χ Per	$11.79 < 11.82 < 11.88$	0.50
h Per	$11.77 < 11.78 < 11.84$	0.54
NGC1960	$10.27 < 10.35 < 10.46$	0.20
NGC2547	$7.98 < 8.05 < 8.09$	0.038

Table 4.11: Distances and extinctions adopted for the chosen SFRs. Notes are as follows. (1) Distance and extinction from Herbig & Dahm (2002). (2) individual extinctions used from Hillenbrand (1997) mean extinction quoted. (3) distance after application of individual extinctions using the Q-method mean extinction quoted. (4) Distance and extinction from Pozzo et al. (2003). (5) Distance from Herbig (1998) and individual extinctions from Herbig (1998) and Luhman et al. (2003) mean extinction quoted. (6) Extinction from Brown et al. (1994). (7) Distance and extinction from Sicilia-Aguilar et al. (2004) and Sicilia-Aguilar et al. (2005).

distances and extinctions was not possible. For these regions, namely IC348, IC5146, CepOB3b and NGC7160 literature extinctions and distances have been adopted.

In addition, metallicity information has been shown to be vital for accurate distances (and relative distances) to SFRs. This is especially true if one is attempting to characterise evolutionary indicators such as disc fractions as a function of age, or trying to uncover environmental effects (such as the effect of ionising winds from massive stars on planet formation in discs).

These distances can now be used to derive a age order for a range of SFRs. First, a method of modeling the pre-MS must be developed due to large model dependencies in this region of the CMD, this is done in the next chapter. The derived distances and extinctions or those adopted from the literature for each SFR are summarised in Table 4.11.

Chapter 5

Empirical isochrones, modeling the pre-MS

5.1 Introduction

Most ages for stellar groups, sub-groups, clusters or associations are derived from fitting observations to theoretical isochrones. It is well known that these models often deviate systematically from the data. For instance if an isochrone fits part of a sequence, it may systematically deviate from the observed sequence in other sections (e.g. Bonatto et al., 2004; Pinsonneault et al., 2004). In addition if a sequence of stars is fitted to an isochrone in one colour, derived parameters such as the age may be different from those derived in another colour (e.g. Naylor et al., 2002). In this chapter I create empirical isochrones. These have the advantage of necessarily fitting the entire data sequence, allowing the creation of an age ordered ladder. Ages can then be derived for fields where different regions of a sequence are available, by selecting appropriate fiducial sequences covering the required colour range. The obvious disadvantage of empirical isochrones is that they are unable to provide absolute age information. Although this is the first attempt to create such a ladder, carried out with data that use slightly different photometric systems and heterogeneous selection criteria, as I shall show later the method is clearly effective.

For this study the optical bands *V* and *V-I* are used. This enables the minimisation of the effects of accretion, the presence of discs and of chromospheric activity on the empirical isochrones. Accretion will generally affect the flux of the *B* band and those short-ward of *B*, (Gullbring et al., 1998) with disc emission important at longer wavelengths, first becoming significant in the *H* and *K* bands (Hartmann, 1998). Lastly, Stauffer et al. (2003) have shown that magnetically generated chromospheric activity in young stars primarily causes perturbations and scatter in the *B-V* and *U-B* colours, whereas the *V, V-I* CMD is unaffected.

This chapter is laid out as follows. The data collection and reduction are detailed in Section 5.2. To create the empirical isochrones members are selected in each field using a variety of criteria detailed in Section 5.3. A curve is then fitted through these in a *V, V-I* CMD in Section 5.4. A summary of this chapter can be found in Section 5.5.

Field	Filter	Exposure time (secs) (×1 unless stated)
h Per	*I*	3 and 30
	V	1, 10 and 100
	B	2 and 20
χ Per	*I*	3 and 30
	V	1, 10 and 100
	B	2 and 20
NGC7160	*I*	3 and 30
	V	1, 10 and 100
	B	2 and 20
NGC2264 (4 fields)	*I*	2 and 20
	V	2 and 20
	B	4 and 40
NGC1960	*I*	3 and 30
	V	1, 10 and 100
	B	2 and 20
IC348	*I*	2 and 20
	V	2 and 20
	B	4 and 40
Cep OB3b	*I*	5(×2), 30(×2) and 300(×2)
	V	5, 30 and 350(×4)
σ Ori (Fields 1,2 and 4)	*I*	2 and 20
	V	2, 10, 100 and 350(×4)
σ Ori (Field 3)	*I*	2 and 20
	V	2, 10, 100 and 350
	B	4

Table 5.1: Exposure times for each field.

5.2 Data collection

The data used in this chapter are from both new observations and literature sources.

5.2.1 New observations

The images for the majority of this dataset were obtained in *BVI* with the 2.5m Isaac Newton Telescope (INT), situated on La Palma, equipped with the four EEV CCD Wide Field Camera (WFC). The filters used were Sloan *i'* and Harris *V* and *B*. The datasets used were collected on the nights of the 27th September and the 5th of October 2004, when the range of seeing was 1-2" and 1-1.5" on each night respectively. Both nights were photometric. The observational details are given in Table 5.1. Standards from Landolt (1992) were observed on these photometric nights, tying our calibration to *B*,*V* and I_c Landolt standards.

5.2.2 Data reduction

First the pixel counts in electrons were changed to photon counts using the gain. The images were then debiased, and flat fielded using median stacks of many sky flat frames. Known bad pixels

Region	Table reference number (#) at CDS archive or Cluster Collaboration page[(1)]	Data	Source (as table 5.3)
NGC2547	3	Members	1 (X-ray)
	4	Members	2 (Spectroscopy)
NGC7160	5	Full catalogue	
	6	Members	3 (Extinction)
NGC2264	7	Full catalogue	
	8	Members	6 (Periodic Variables)
	9	Members	4 (X-ray)
	10	Members	5 (Hα)
	11	Members	26 (Proper Motion)
Cep OB3b	12	Full catalogue	
	13	Members	7 (X-ray)
	14	Members	8 (Spectroscopy)
	15	Members	18 (Periodic Variables)
	16	Members	19 (Hα)
	17	Members	25 (X-ray)
σ Ori	18	Full catalogue	
	19	Members	11 (X-ray)
	20	Members	12 (Spectroscopy)
IC348	21	Full catalogue	
	22	Aperture Photometry	
	23	Members	10 (Periodic Variables)
	24	Members	16 (X-ray)
	25	Members	15 (X-ray)
	26	Members	9 (Spectroscopy)
	27	Members	17 (Hα)
h and χ Per	30	Full catalogue (both)	-
	31	Positionally isolated	-
NGC1960	–[(2)]	Full catalogue	-
	–[(2)]	Positionally isolated	-

Table 5.2: The catalogues presented in this thesis with their corresponding table reference number. These reference numbers are those used on internet severs and are marked with a # when used in the text. Notes are as follows. (1) The address for the Cluster Collaboration webpage is: http://www.astro.ex.ac.uk/people/timn/Catalogues/description.html. (2) Data are currently not available at CDS archive or from the Cluster Collaboration web page.

were flagged and pixels marked as saturated where the counts exceed the limit of linear response of the CCD. The *i* band images were then defringed using a library fringe frame. Fringing is caused by airglow from OH ions in the atmosphere interfering with the thin film covering the CCD. This effect happens at characteristic wavelengths and peaks in the I band.

The data, including the standards, were then reduced following the optimal extraction algorithm detailed in Naylor (1998) and Naylor et al. (2002). This process involves extracting magnitudes for stars separately in each frame and combining them using a weighted mean, this avoids problems of summed images being dominated by spurious or noisy pixels from one image. Firstly, a list of stars must be found in each frame. These stars are used to positionally centre the frames and as a target list for the optimal photometry procedure. This star search is done using a summed image initially to maximise the number of stars identified. The sky background is fitted using a skewed Gaussian, which allows for the presence of contaminant stars in the background box, and then interpolated and smoothed across the pixels. Then peaks are found at $n\sigma$ above this background over several passes, iteratively reducing n. Each star position is found within a 2*FWHM (the full width half maximum of an estimated point spread function or PSF) box. Fainter stars within the box of brighter stars are removed by rejecting these stars during later iterations i.e. fainter stars at a lower $n\sigma$ above the background within the box of a previously identified star. Finally the flux in each star is summed and its ratio compared to that found within $0.5*$FWHM, objects where this ratio exceeds the median by 3σ are then marked as non-stellar. This process results in a list of stars and a list of bright candidates for modeling the PSF. This output is used to match stars between images and create a list of offsets between frames. This process, of identifying stars and finding their positions in multiple frames, is then repeated for all frames. This means that stars saturated in the summed frame can be positioned using the shorter exposure frames. Once positions have been found for all stars in all frames these positions are fixed before optimal extraction. The list of brightest stars identified are then used to fix the shape of the PSF using a 2-D elliptical Gaussian. Optimal photometry then uses a weight mask which weights each pixel by its signal-to-noise ratio. This weight mask is constructed by convolving the PSF (estimated from the brightest stars) with the pixel-to-pixel uncertainties for the faintest stars. A local background is also subtracted during this process. During the optimal extraction various flags are introduced depending on the quality of the data, these are explained in Burningham et al. (2003). Additional non-stellarity checks are also carried out at this point based on the shape or ellipticity of the star. The flux from each star can then be summed and converted to an instrumental magnitude using,

$$m = -2.5 * log_{10} \frac{C}{t_{\rm exp}}. \tag{5.1}$$

Where C is the measured counts, $t_{\rm exp}$ the exposure time and m the instrumental magnitude. However, to extract the flux and determine a local background some limit radius for the weight mask must be applied. This clipping of the weight mask requires an additive correction to the instrumental magnitude, termed the profile correction Naylor (1998). The profile correction is analogous to the aperture correction in aperture photometry. Essentially, as the weight mask for each star is constructed using the PSF from the brightest, and clipped at some radius, there will be a difference

between this mask and the true mask. This profile correction can be estimated by comparing the instrumental magnitudes of good candidate stars with those resulting from aperture photometry. These profile corrections are applied and the resulting magnitudes from each frame (adjusted by the airmass) can be summed (using the weighted mean) to provide a single instrumental magnitude for each star. During this summing it is necessary to apply a transparency correction based on the relative transparency between each frame, in a given band, and a chosen master frame. This transparency correction is a weighted mean of the difference in magnitude of the star in the target frame and that in the master frame. Additional flags can be assigned to data at this point. The coefficients derived from standard star observations are then applied to convert the instrumental magnitudes to magnitudes calibrated in the required photometric system. The final step is to derive the conversion from x, y pixel positions to RA and Dec values. This astrometry is done using the brightest stars in each frame and a 6-coefficient solution is derived allowing for pincushion and barrel distortion. These positions are based on the 2 Micron All Sky Survey (2MASS) providing an astrometric solution for each field accurate to $\simeq$0.1 arcsec. The final product of the reduction process is a catalogues of photometry with flags and uncertainties. The flags are explained in Burningham et al. (2003).

In the IC348 region, in all but the central CCD there were too few stars to perform a profile correction (see Naylor et al., 2002). Aperture photometry was therefore performed on all the stars in the region, using the same radius as that used for profile correction. The resulting measurements were then processed in an identical manner to the standard reduction, except for the non-stellarity check, which was carried out using a comparison of the flux within the large aperture with one of half this radius. All those stars flagged H (meaning a poor profile correction) in the optimally extracted catalogue were then selected from the aperture photometry catalogue, to create a new catalogue. All objects flagged and with uncertainties greater than 0.1 mags were then removed from this catalogue. This is the aperture photometry replacement catalogue presented in Mayne et al. (2007), for which it should be noted that some stars may have a second star in the aperture. In our analysis, where the optimal photometry has been flagged H the photometry was replaced by the value in the aperture photometry replacement catalogue.

Photometric calibration coefficients were calculated from the standards using the procedure detailed in Pozzo et al. (2003). The standards used had colour ranges of $-0.30 < V\text{-}I < 2.87$ and $-0.30 < V\text{-}I < 2.85$, with airmass ranges of $1.13 - 1.32$ and $1.14 - 1.22$, on September 27th and October 5th 2004 respectively. One star lying far from the fit locus was removed from the Landolt fit. This star (SA98 L5) was observed only three times by Landolt, and as a result the uncertainties are large. To define the reddest part of our colour system, values for SA98 L5 obtained with our coefficients are $V = 17.800 \pm 0.163$ and $V\text{-}I = 5.800 \pm 0.123$ (c.f. Landolt $V = 18.607 \pm 0.022$ and $V\text{-}I = 6.532 \pm 0.025$). An estimate of the combined uncertainty in profile correction and transformation to the Landolt system is achieved by adding a magnitude independent uncertainty to the measured standard star magnitudes which yields a reduced χ^2 of one. This gave values of 0.01 in V and $V\text{-}I$ and 0.02 in $B\text{-}V$. I also experimented with standards from Stetson (2000), but the scatter about a linear fit was larger than for the Landolt photometry.

In the cases where multiple fields were observed (NGC2264, σ Ori and h and χ Per) the

catalogues were combined using the method described in Naylor et al. (2002). Overlapping regions were used to normalise the photometry to provide a combined catalogue. As detailed in Naylor et al. (2002) the RMS of the overlap region is a good measure of the accuracy of the profile correction. This suggests a magnitude independent uncertainty of approximately 0.01 mags which should be added to all bands when comparing objects well separated on the CCDs. This uncertainty is not included in the catalogues. For all subsequent analysis the combined catalogues have been used.

All of the new catalogues used for this chapter are freely available from the cluster collaboration home page[1], and the CDS archive. For membership selection and CMD plots, stars with uncertainties greater than 0.1 mags in colour or magnitude are excluded. The machine readable catalogues retain all the data. To aid navigation through this chapter an index to the catalogues is included as Table 5.2.

5.2.3 Literature data

Literature observations were taken in all cases (except where stated) in the Johnson-Cousins photometric system using I_c (Cousins I). This raises the question of what effect the use of two different I filters has on any derived empirical isochrones. The difference is illustrated in Figure 5.1. Figure 5.1 shows the data for Sloan i, for stars in Cep OB3b with the data for Cousins I_c, taken from Pozzo et al. (2003). The symbol I from hereon will be used to represent data taken using a Sloan i (i') filter tied to the Landolt standards, with I_c being data taken in Cousins I_c tied to Landolt standards. The difference (V-I_c)-(V-I) is plotted as a function of (V-I_c) in Figure 5.1. The data can be represented by the following linear fit: (V-I) = 0.971(V-I_c) + 0.008. This result shows that two stars with an apparent V-I of 3 mags, one cool and unredenned i.e. a typical Landolt standard, and another hotter and more heavily reddened, need not have the same V-I_c. As demonstrated by the extreme example of CepOB3b ($A_V \simeq 3$ mags), even at a V-I = 3 the shift is < 0.1 mags; though note that the reddest standard in our V-I calibration is 2.87. This means over the colour range covered within this Chapter the effect is negligible.

5.3 Sequence isolation

For each field-of-view (FOV) the CMD includes a high proportion of background and foreground objects, therefore the common problem of identifying members is present. For most fields literature sources for members were used. The memberships for these fields and biases incurred are discussed in Section 5.3.1. For h and χ Per and NGC1960 literature memberships were not available for the pre-MS. For these SFRs the confidence in selecting the correct sequence can be increased by selecting a limited area of the field-of-view. This method will clearly include a higher proportion of non-members. This method is detailed in Section 5.3.2.

[1] http://www.astro.ex.ac.uk/people/timn/Catalogues/description.html

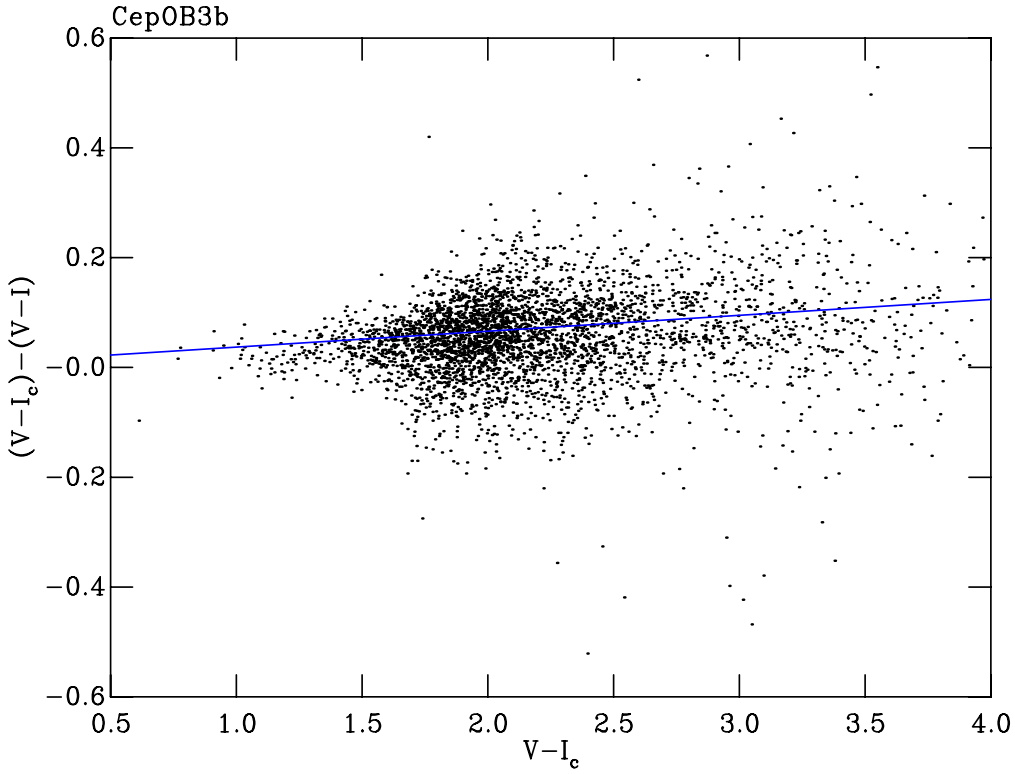

Figure 5.1: The difference in $V-I$ for Cep OB3b between data taken in the system used here and using Cousins I filter. The line is the best fit through the data.

5.3.1 Literature memberships

This section details the literature memberships for each field. Table 5.3 shows the cluster, the data type and the reference for each of the clusters in this section.

5.3.1.1 NGC2264

The X-ray sources (Table #9) pick out a reasonably clear sequence (see Figure 5.2), although there were also some X-ray active foreground and background objects. The spectroscopic members (Table #10) came from Dahm & Simon (2005) who selected members using Hα strength from narrow band imaging, a selection mechanism which is unbiased in colour-magnitude space. Spectroscopic observations were taken as follow up. The periodic variables (Table #8) came from Lamm et al. (2004) and Lamm et al. (2005). The entire periodic variable catalogue has been used here, whereas the final membership list of Lamm et al. (2005) imposed further isochrone driven selection. The photometry has been supplemented with the photometry for bright stars from Mendoza V. & Gomez (1980), as these stars were saturated in my catalogue. Only those stars with probability of membership greater than 90 percent from the proper motions of (Mendoza V. & Gomez, 1980) are included. Star W33 has also been excluded; the anomalous photometry of this star was also noted in Mendoza V. & Gomez (1980). The full CMD with each form of membership criterion added is shown here as Figure 5.2.

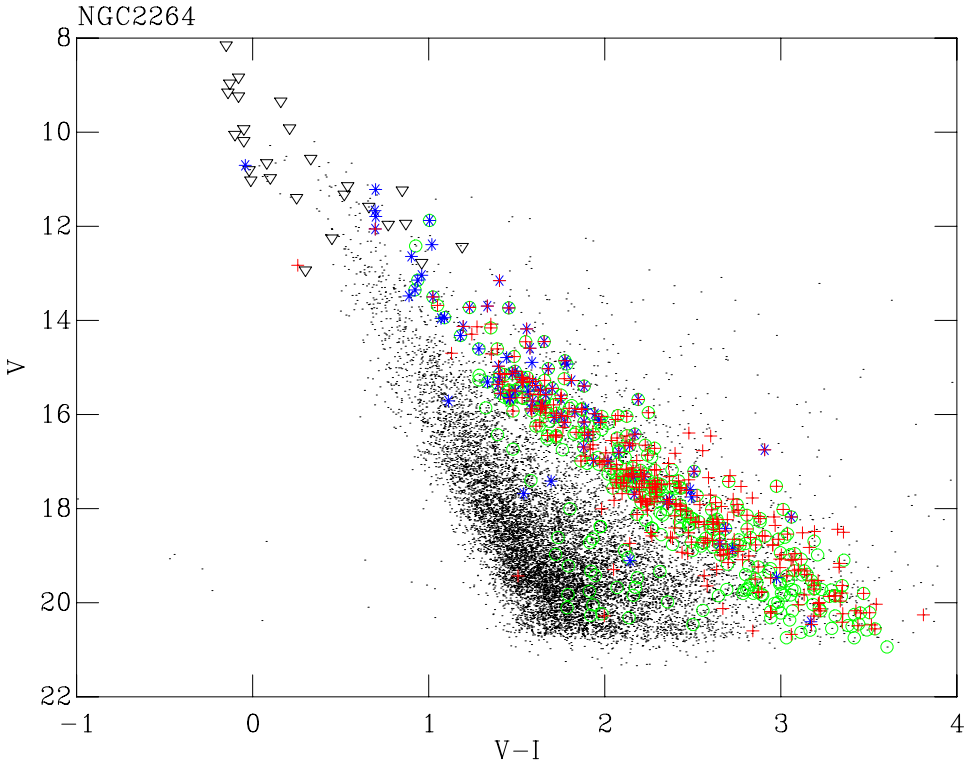

Figure 5.2: The full catalogue for the NGC2264 field (dots). Circles are the periodic variables from Lamm et al. (2004), asterisks are X-ray sources from Flaccomio et al. (1999) and crosses are Hα sources from Dahm & Simon (2005).

5.3.1.2 NGC2547

The observations of NGC2547 were taken from Naylor et al. (2002), using Cousins I (I_c). The photometry was calibrated with coefficients detailed in Naylor et al. (2002) with the reddest standard having a *V-I* of 2.7. Jeffries & Oliveira (2005) carried out spectroscopy (Table #4) of a photometrically selected sample. The photometric sequence was clear of the contamination in this instance and so the colour-magnitude selection should not have produced a bias in the CMD space. Radial velocity (RV) was used to define cluster memberships. The presence of Li below the Li boundary was also used. The X-ray members (Table #3) are from Jeffries & Tolley (1998).

5.3.1.3 ONC

The photometry (using I_c) and membership probabilities for this region come from Hillenbrand (1997). Hillenbrand (1997) calculated extinctions for a subset of stars, using spectroscopic measurements of stars already identified as members from a range of literature sources, in a spatially selected region encompassing the inner 15' radius. Only those stars with spectroscopically calculated extinctions and with assigned membership probabilities above 80% were used here. Periodic variables were from Herbst et al. (2002) and X-ray sources from Flaccomio et al. (2003).

5.3.1.4 NGC7160

Members were taken from Sicilia-Aguilar et al. (2004) and Sicilia-Aguilar et al. (2005) (Table #6). In these studies a photometric sample of stars was selected, initially by considering those lying above the 100 Myr isochrone in a *V*, *V-I* CMD and lying within a magnitude range of V=15-19 mags. A further selection was then made of stars with *RI* variability, then using U-band and 2MASS colours to select a pre-MS photometrically (which is biased to accreting stars). Spectroscopy was then used to measure extinctions and therefore assign memberships. The probability of membership was fixed to the distance in standard deviations (σ) from the average extinction value for the group. This relies on intrinsic colours. The members selected are those within 1σ of the average extinction.

5.3.1.5 σ Ori

Spectroscopic members were taken from Kenyon et al. (2005) and Burningham et al. (2005b). Kenyon et al. (2005) obtained spectroscopy of a photometrically selected sample using a "close" selection around the suspected sequence in a CMD, which is potentially photometrically biased. Memberships were then confirmed on the basis of measurements of RV and EWs (Equivalent Widths) of NaI consistent with the group mean. Burningham et al. (2005b) however, used a "broad" colour-magnitude selection. The memberships were also confirmed here via RV and NaI and LiI EWs. Burningham et al. (2005b) showed that using a "broad" selection does not reveal significantly more members, implying that using members from Kenyon et al. (2005) does not significantly bias the results. Of the members from Kenyon et al. (2005), only those satisfying all the criteria were included. In the case of Burningham et al. (2005b) a selection of > 80% probability of membership was applied to ensure a high percentage of genuine group members

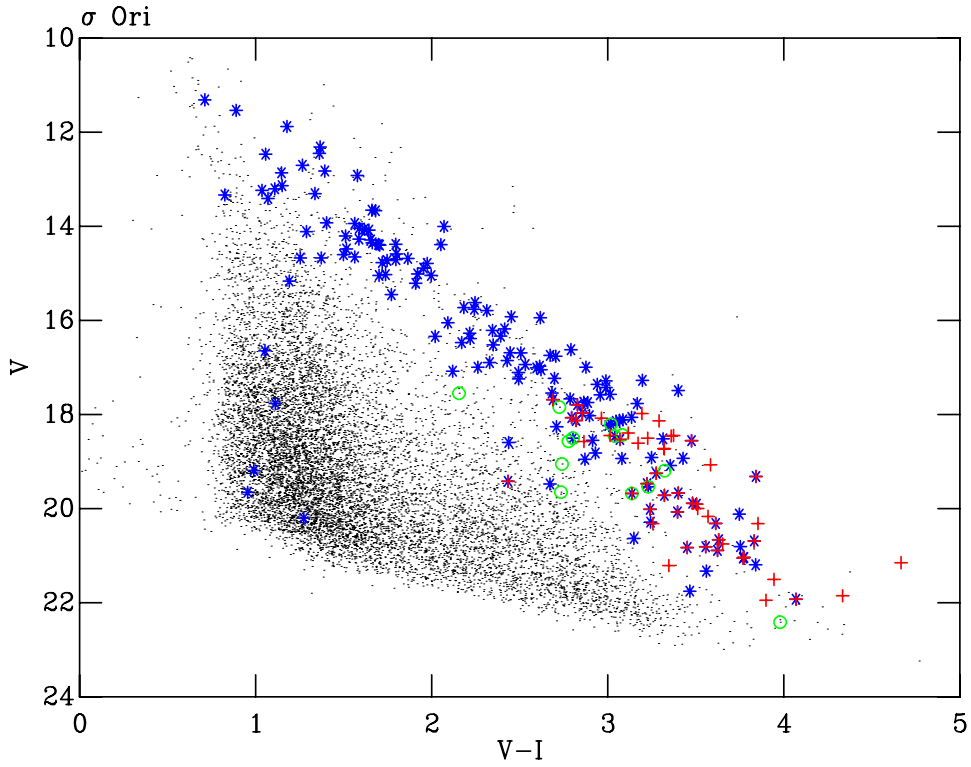

Figure 5.3: The full catalogue for the σ Ori field (dots). Circles are members from Burningham et al. (2005b), while asterisks are X-ray sources from Sanz-Forcada et al. (2004). Crosses are members from Kenyon et al. (2005).

(Table #20). X-ray positions were taken from Sanz-Forcada et al. (2004). Those for which Sanz-Forcada et al. (2004) (Table #19) found no optical counterpart are included after they were cross-correlated to positions with the new catalogue. The Sanz-Forcada et al. (2004) positions were used in preference to ROSAT data due to the higher spatial resolution of XMM-Newton. Jeffries et al. (2006b) shows that pre-MS members of this association are separated into two kinematic subgroups by heliocentric radial velocities, having different ages. In this work all but four stars from the sequence members are at a declination of less than δ=-2 18' 00.0". This area is dominated by members from group 2 as defined in Jeffries et al. (2006b). The resulting CMD is displayed as Figure 5.3.

5.3.1.6 Cep OB3b

Spectroscopic members were taken from Pozzo et al. (2003). They used a broad colour-magnitude selection with subsequent spectroscopic measurements of LiI EW, Hα and RV. Pozzo et al. (2003) then used the spectroscopic measurements in conjunction with X-ray measurements to compare each star to the group mean and assign memberships (Table #13). Hα memberships were taken from Ogura et al. (2002) (Table #16), who used a photometrically unbiased narrow band imaging survey. The X-ray data were taken from Naylor & Fabian (1999), supplemented with the second ROSAT PSPC catalogue. The latter contained two pointings; the one from Naylor & Fabian (1999), and a second, non-overlapping field. Both the unpublished and Naylor & Fabian (1999)

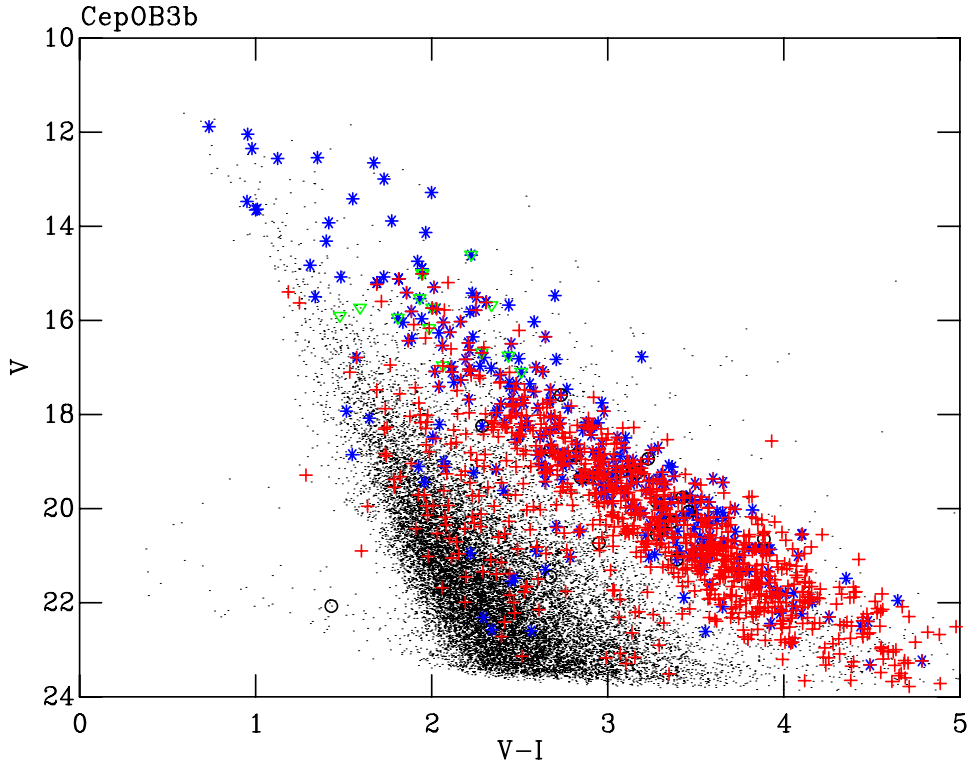

Figure 5.4: The full catalogue for the Cep OB3b field (dots). Asterisks are X-ray sources from Naylor & Fabian (1999), Getman et al. (2006) and the Second ROSAT PSPC catalogue. Triangles are members from Pozzo et al. (2003). Circles are Hα sources from Ogura et al. (2002). Crosses are the periodic variables from Littlefair et al. (2005).

catalogues were therefore used (Table #13), but where possible the positions from the Naylor & Fabian (1999) reduction have been adopted. In addition, the X-ray sources from Getman et al. (2006) have been included (Table #17). These sources are from the *CHANDRA ACIS* detector, and consequently have a much higher spatial resolution and sensitivity than ROSAT. Both the ROSAT and *CHANDRA* data have been used as the latter is centralised on a smaller field of view about the cluster core, while many of the ROSAT detections are outside this area. In the cases where a Getman et al. (2006) source lies within the positional error box of the sources from the ROSAT catalogues, the *CHANDRA ACIS* positions have been used. Periodic variables come from Littlefair (in prep) (Table #15).

5.3.1.7 IC348

Spectroscopic and Hα data were taken from Herbig (1998). He used photometry and a wide field Hα survey (grism spectrograph), discarding Hα EWs < 2Å(Table #27). Follow-up spectroscopy was undertaken on 80 stars within the field. Herbig (1998) classified the spectra by comparison with dwarf spectral standards, using these to derive extinctions (Table #26). The second set of spectroscopic members were taken from Luhman et al. (2003) (supplemented by Luhman (1999), Luhman et al. (2005), Luhman et al. (2005) and Luhman et al. (2003)) (Table #26). In Luhman et al. (2003) spectral types were assigned using various models and then extinctions calculated by

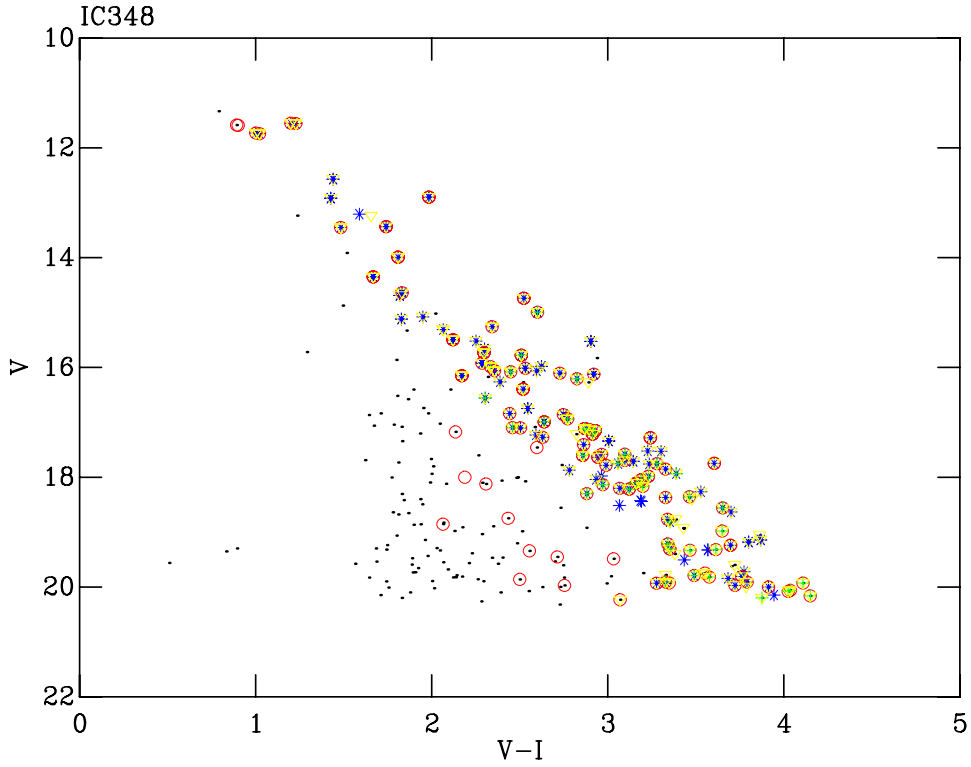

Figure 5.5: The full catalogue for the IC348 field (dots) The asterisks are X-ray sources from Preibisch & Zinnecker (2002) and the Second ROSAT PSPC catalogue. Circles are the periodic variables from Cohen et al. (2004) and Littlefair et al. (2005). Crosses are Hα sources from Herbig (1998). Triangles are spectroscopic members with extinctions from Luhman et al. (2003) and Herbig (1998).

deredenning the stars onto standard colours. The individual extinctions from Herbig (1998) and Luhman et al. (2003) are used here. X-ray members were taken from Preibisch & Zinnecker (2002) (Table #24), where Hα and *CHANDRA* data were presented with extinctions included. Preibisch & Zinnecker (2002) also include extinctions from a range of literature sources. The X-ray data from Preibisch & Zinnecker (2002) were supplemented with a portion of the Second ROSAT PSPC catalogue (Table #25). Periodic variables were taken from Cohen et al. (2004) and Littlefair et al. (2005) (Table #23), both being derived from *I* band wide-field surveys. The sequence with the members is displayed as Figure 5.5.

5.3.1.8 λ Ori

The data for λ Ori are from Dolan & Mathieu (2001) taken in the Johnson-Kron-Cousins system and calibrated to Landolt standards. Likely pre-MS members were selected from an *R*, *R-I* CMD. This sample was then spectroscopically observed using Li EW as an indicator of membership. Only those stars showing significant evidence for Li have been used.

5.3.1.9 NGC2362

The data for NGC2362 are from Dahm (2005), taken with an I_c filter and tied to Landolt standards. Dahm (2005) used a wide field Hα survey to identify a sample of 200 stars, which lay above the ZAMS in an optical CMD. This sample was then used for follow up spectroscopy, using Hα EW and Li EW as membership criteria. The members so identified are used here.

5.3.1.10 IC5146

The Cousins photometry for IC5146 comes from Herbig & Dahm (2002),this contains photometry from two areas approximately 10' apart. Herbig & Dahm (2002) used a wide field survey to identify any stars showing $W(H\alpha) > 5$Å. I used stars with known spectral types and exhibiting a $W(H\alpha) > 5$Å, discarding any stars lying below the Pleiades MS following Herbig & Dahm (2002).

5.3.1.11 NGC6530

The photometry for NGC6530 is from Prisinzano et al. (2005). X-ray members are from Prisinzano et al. (2005) using the *CHANDRA* ACIS detector. Hα members are taken from Sung et al. (2000).

5.3.1.12 NGC2244

The photometry and memberships for this cluster are from Berghöfer & Christian (2002). Berghöfer & Christian (2002) provide *BVRI* and Hα photometry. However, they only provide photometry of stars which are brighter than $V = 18$, which either appear in the catalogues of Walker (1957) or Kilambi (1977), or are matched to an X-ray source from Damiani et al. (2004).

5.3.1.13 Biases and summary

A wide range of membership criteria have been used, each of which will have an implicit bias. As the form of the sequences in CMD space is of interest it is important to be aware of and limit any bias incurred with respect to the CMD space. X-ray selection will be biased to weak lined T Tauri stars (WTTS) and binary systems (Preibisch & Feigelson, 2005). Variability exhibits a bias towards accreting objects, though periodic variability may exclude many classical T Tauri stars (CTTS) objects when observed over a long baseline. However periodic variability deduced from a short baseline does not carry this bias (Littlefair et al., 2005). The final frequently used data source was Hα, which is generally biased towards CTTS.

There is also a more subtle form of bias due to pre-selection. Because in many cases surveying all objects in a field is not possible, an observer will necessarily select a subset of objects. Often this initial selection is based on the positions of objects in CMD space thus introducing a bias in CMD space. This is particularly applicable to spectroscopic data. Where this form of sample selection has occurred the selection criteria are stated clearly in the previous section.

Samples derived from non-spectroscopic methods of membership selection have a higher probability of containing contamination from background or foreground objects. This leads to the

need for colour-magnitude selections to remove data points which lie far from the group sequence. Where this is done the number of discarded objects is small relative to the total number of objects and has little effect on the final sequence (see Section 5.4). In each section where such a selection was used, it is shown in the CMD and its effect on the result is discussed.

5.3.2 Isolating the sequence without memberships

For the fields of NGC1960 and h and χ Per no membership data of the form used previously is available, so colour-magnitude selections have been employed. As the groups in question are clustered in the FOV it was possible to remove a proportion of FG and BG objects by selection of a limited area of the FOV. However a guiding mechanism to allow the approximate central coordinates to select and a subsequent area to isolate is needed. The procedure to isolate the sequence is now explained for the example of h and χ Per.

5.3.2.1 h and χ Per: an example

1. **Lead Stars.** The CMD for the full h and χ Per catalogue is shown in Figure 5.6. The sequence is clearly visible and the brighter stars clearly lie blue-ward of the contamination. Therefore the positions of these stars on the sky were plotted, allowing the outline of the clusters to be traced. This can be seen in Figure 5.7.

   Three other sources of lead star candidates were explored. Uribe et al. (2002) where proper motions were presented, and photometry from Slesnick et al. (2002) and Muminov (1996). The coordinates from each set were carried forward through the following steps. However the central coordinates for all cases were very similar.

2. **Positional selection.** A circular positional selection was applied to the full catalogue around the central coordinates, with an inclusion radius varying from 5’ down to 1’ in increments of 1’. The CMDs for each were examined and a ‘by eye’ selection made for the CMD yielding the clearest sequence, optimising the member to field-object ratio. The best results were obtained with a radius of 2’. The final central coordinates for each cluster are: α=2 22’ 5.02” δ=+57 7’ 43.44” (χ Per), α=2 18’ 58.76” δ=+57 8’ 16.54”(h Per), J2000. The final areas selected can be seen overlaid on Figure 5.7.

   Since the measured ages in virtually all the literature for h and χ Per are the same, it was possible to increase our confidence of selecting the correct sequence in CMD space by combining the CMDs from both clusters. To achieve this any differences in extinction and distance modulus must be accounted for. Extinctions and distance modulus shifts in the sense h Per minus χ Per were calculated using the parameters from Chapter 4. The resulting shifts are $\Delta dm = 0$ and $\Delta A_V \approx 0.12$ This shift was applied to h Per, and the combined catalogue used from thereon (Table #30).

3. **Colour-magnitude selection and fitting.** The final sequence was then fitted as described in Section 5.4. Cuts in colour-magnitude space were then used to clip out stars lying far from the sequence.

Group	Data Type	Source	Matching radius	Offsets RA, DEC (arcsec)
NGC2547	X-ray (ROSAT)	1	From 1	0 0
	Spectroscopy	2	1 arcsec	0 0
NGC7160	Extinction	3	1 arcsec	0 0
NGC2264	X-ray (ROSAT)	4	6 arcsec	0 0
	Hα	5	1	0 0
	Periodic Variables	6	1 arcsec	0 0
Cep OB3b	X ray (ROSAT)	7	From 7 or 14 arcsec	0 0 (both)
	X ray (*CHANDRA*)	25	1	0 0
	Spectroscopy	8	1 arcsec (both)	0 0 (both)
	Hα	19	1 arcsec	0 0
	Periodic Variables	18	1 arcsec	0 0
σ Ori	X-ray (XMM)	11	6 arcsec	0 0
	Spectroscopy	12	1 arcsec (both)	0 0 (both)
ONC	Periodic Variables	13	1 arcsec	+1.5 -0.25 & 0 0
	X-ray (*CHANDRA*)	14	2 arcsec	0 0
IC348	Periodic Variables	10	1 arcsec	-0.1 -0.5
	X-ray (*CHANDRA*)	16	1 arcsec	-0.5 0
	X-ray (ROSAT)	15	14 arcsec	0 0
	Spectroscopy	9	1 arcsec (both)	0 0 & +0.2 -0.5
	Hα	17	1 arcsec	+0.2 -0.5
NGC2362	Hα (Li)	20	Members from 20	
λ Ori	Spectroscopy (Li)	21	Members from 21	
IC5146	Hα	22	1	0 0
NGC6530	Hα	23	Members from 23	
	X-ray (*CHANDRA*)	24	Members from 24	
NGC2244	X-ray & Hα	26	Members from 26	

Table 5.3: Literature sources and astrometric matching criteria. 1 Jeffries & Tolley (1998), 2 Jeffries & Oliveira (2005), 3 Sicilia-Aguilar et al. (2005), 4 Flaccomio et al. (1999), 5 Dahm & Simon (2005), 6 Lamm et al. (2004), 7 Second ROSAT PSPC catalogue and Naylor & Fabian (1999), 8 Pozzo et al. (2003) and Ogura et al. (2002), 9 Luhman et al. (2003) and Herbig (1998), 10 Cohen et al. (2004) and Littlefair et al. (2005), 11 Sanz-Forcada et al. (2004), 12 Burningham et al. (2005b) and Kenyon et al. (2005), 13 Herbst et al. (2002), 14 Flaccomio et al. (2003), 15 Second ROSAT PSPC catalogue, 16 Preibisch & Zinnecker (2002), 17 Herbig (1998), 18 Littlefair et al. (2005), 19 Ogura et al. (2002), 20 Dahm (2005), 21 Dolan & Mathieu (2001), 22 Herbig & Dahm (2002), 23 Sung et al. (2000), 24 Prisinzano et al. (2005), 25 Getman et al. (2006), 26 Mendoza V. & Gomez (1980) and 27 Berghöfer & Christian (2002).

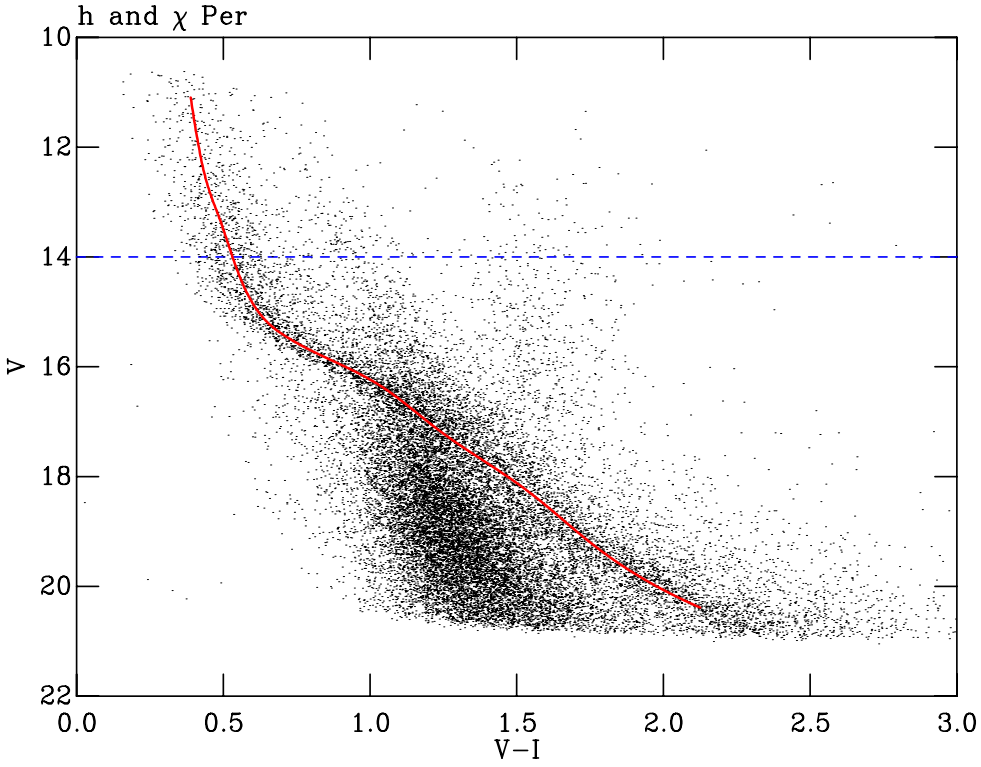

Figure 5.6: The full catalogue for the h and χ Per field (dots). The dotted line shows a colour-magnitude selection of $V < 14$th, showing the sequence clear of the contamination. The solid line is the best fitting spline, described in Section 5.4 to the selected sequence corrected to the mean extinction for the two clusters.

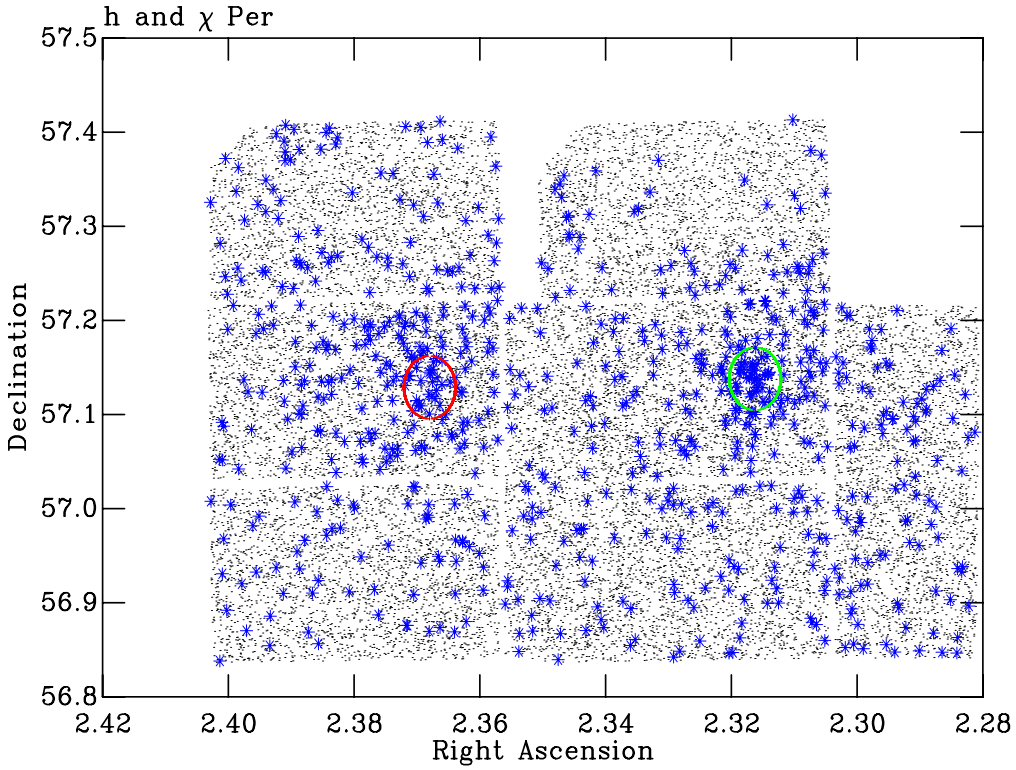

Figure 5.7: The positions of stars in the h and χ Per catalogue. Asterisks are stars with $V < 14$th, and the large circles show the regions selected.

5.3.2.2 NGC1960

The positional isolation method was again utilised here. The lead stars in this case were the high-mass (HM) stars from the FOV. The optimum radius was 7' centred at α=5 36' 20.41", δ=+34 7' 20.7", J2000. Photometry of the resulting stars is shown in Figure 5.17.

5.4 Fitting procedure

To explain the stages involved in producing the empirical isochrones an example cluster is used, NGC2264. This cluster is a good illustration as it has a large number of members from various sources.

5.4.1 NGC2264: an example

Once the sequence was finalised to stars having properties indicative of cluster membership (see Section 5.3.1.1) the median filtered sequence was fitted with a smooth curve. The median filter was used for two reasons. The median is necessarily tied to the values of real stars. In addition the median allows the effect of stars lying far from the sequence to be limited, as not all of our memberships are certain, for instance the X-ray sources in this group. The median sequence was calculated by binning the stars, from the full sequence, in V-band intervals and creating a median star for each bin. The median star was assigned the median V-I and V values from the stars within

the bin. The bin sizes were tailored to each field, and a minimum number of stars in each bin is enforced. A cubic spline was fitted through the resulting list of median stars, over the colour range of the stars selected, with the gradients at the ends tied to a quadratic. The resulting fit for NGC2264 is shown in Figure 5.8.

To remove BG and FG objects and spurious matches which lie below the pre-MS a colour-magnitude selection was applied before fitting. Removing objects lying below the dotted line in Figure 5.9. The effect of this colour-magnitude selection on the spline functions could be a concern. However, examining fits using data with and without a selection shows a negligible effect. The effect of removing the colour-magnitude selection for NGC2264 is shown in Figure 5.9. It has little effect on the resulting spline.

The resulting fit is clearly an average through the spread in the colour magnitude diagram (sometimes referred to as an age spread, see Burningham et al., 2005a, and references therein). Part of this spread will be due to unresolved binaries which lie above the single star sequence, lifting the spline above the single star sequence. Thus the splines do not necessarily follow the single-star sequence, although the displacement due to binarity should be the same for all fields. Furthermore the scale of this effect is small, as can be seen in the CMDs where there is a clear separation between the binary and single star sequence, e.g NGC2547 (Figure 5.10).

Sometimes the spline fit does not precisely follow the sequence the eye picks out, for example $0.5 < V\text{-}I < 1$ for NGC2264. Whether the spline or the eye is correct turns out to be immaterial. The deviations are never large enough to affect our conclusions.

Empirical sequences constructed from data have been created in previous works. In particular, Irwin et al. (2006) create an empirical MS line for V and $V-I$ photometric data of M34 using a similar method to that used here. Irwin et al. (2006) select candidate cluster members, initially 'by eye', then compute an iterative $k\sigma$ clipped median in 1 mag bins of V magnitude, at 0.5 mag spacings (from V = 14 to 24 mag). Once this line was created it was used to enforce a photometric cut to isolate members on the sequence. However, as with the method explained here the median-based line will follow the locus of the spread, and therefore be lifted above the single-star sequence. Therefore, to ensure a valid selection the line was shifted towards fainter magnitudes and bluer colours by a selected value of $0.1 + k\sigma(V-I)$ (with $\sigma(V-I)$ the uncertainty in colour of the point), this value effectively defines a user estimated 'width' for the sequence. As explained in Irwin et al. (2006) the choice of k is clearly arbitrary and the routine must be iterated until an aesthetically satisfactory sequence is isolated. Another example of an empirically constructed sequence using a different method is that found in Leggett (1992). Leggett (1992) create an empirical 'young disc' sequence by simply fitting candidate members of a young population from the galactic disc with a weighted least-squares polynomial fit. This method works well in this case as the data follow a smooth, continuous and quadratic-like curve, which is not the case for our sequences from MS to pre-MS.

5.4.2 NGC2547

The resulting fit, after sequence selection is shown in Figure 5.10. A colour-magnitude selection was used to clip out probable non-members. Only eight objects were removed, all lying far

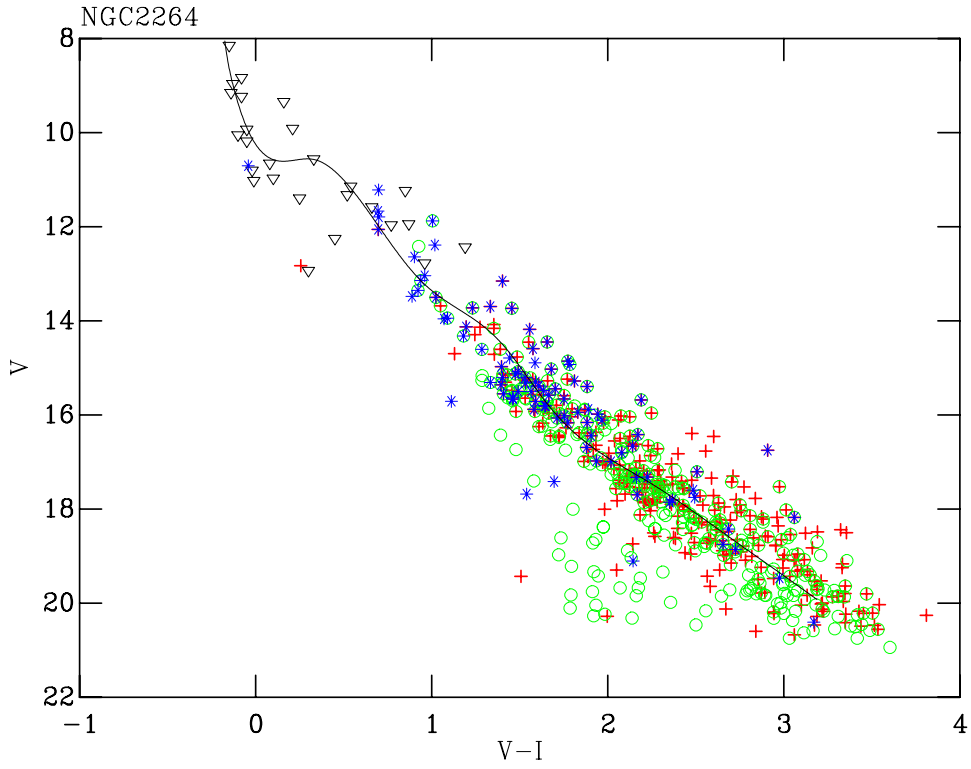

Figure 5.8: Stars selected as members of NGC2264. Circles are the periodic variables from Lamm et al. (2004), asterisks are X-ray sources from Flaccomio et al. (1999), crosses are Hα sources from Dahm & Simon (2005) and triangles are proper motion members from Mendoza V. & Gomez (1980). The spline fit to the sequence after a colour-magnitude selection is shown.

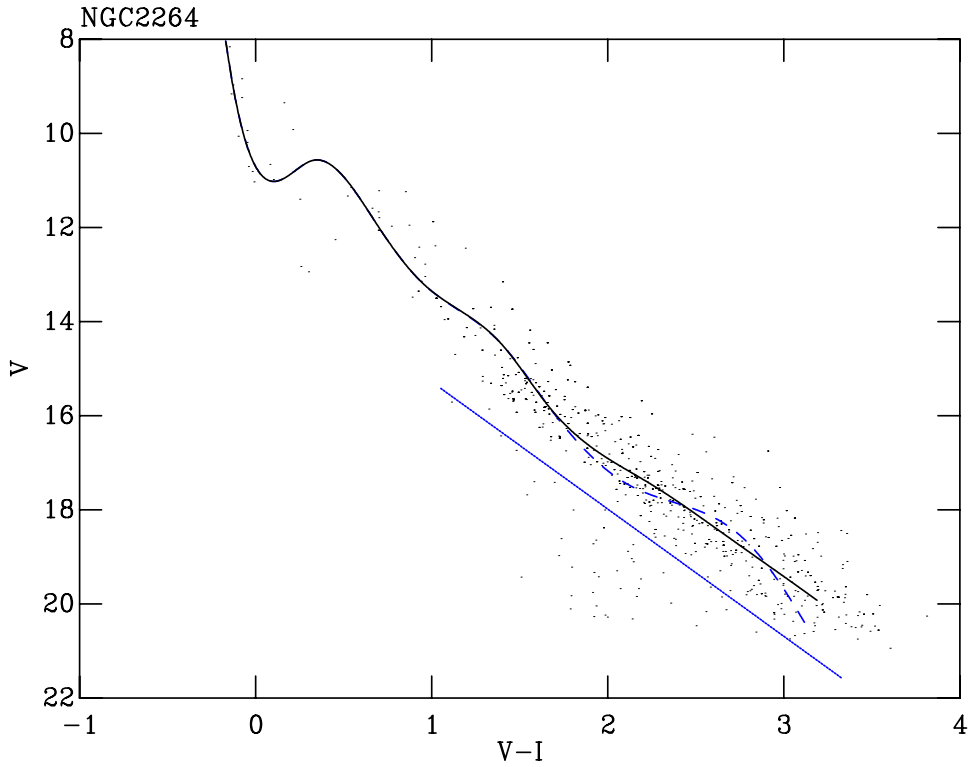

Figure 5.9: The effect of choosing a wider colour-magnitude selection in NGC2264. The effect is limited by the large number of sources within the sequence. The dashed curve is the result using no selection, with the dotted line being the colour-magnitude selection and the solid line the spline fit after the colour-magnitude selection is enforced i.e. only stars above the line were used to produce the spline curve.

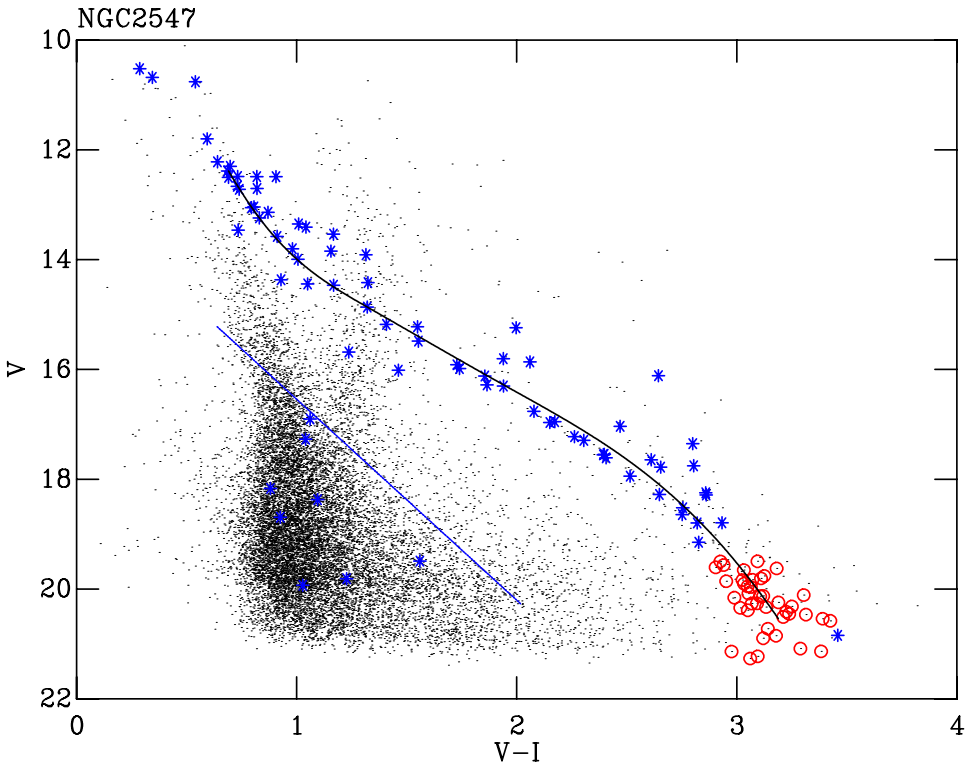

Figure 5.10: The full catalogue for the NGC2547 field (dots). Asterisks are the X-ray sources from Jeffries & Tolley (1998), circles are spectroscopic members from Jeffries & Oliveira (2005). The X-ray sources, some of which clearly lie in the BG MS contamination were removed using a colour-magnitude cut prior to fitting, shown here as the dotted blue line.

from the sequence and within the contamination. The fitted line lies slightly above the single star sequence, due to binary stars.

5.4.3 ONC

For the ONC the extinctions are calculated individually for each star, therefore the order in which the fitting and conversion to absolute colours and magnitudes is carried out is crucial. Where average extinctions have been used the entire space is simply translated by conversion to absolute magnitude and intrinsic colour, and the fitted spline curve will not change shape. If however individual extinctions are used shifts may therefore be different for each object, changing the shape of the sequence. Consequently, for the ONC the extinctions must be applied before the fitting procedure. This is also the case for the clusters IC348 and IC5146. The resulting sequence (extinction corrected) with additional membership information fitted is shown as Figure 5.11. All the stars shown were fitted to yield the spline curve shown. No colour-magnitude selection was utilised here as nearly all the stars within 15' of the centre are members of the ONC. This is because the background stars are largely obscured by the dense cloud behind the cluster.

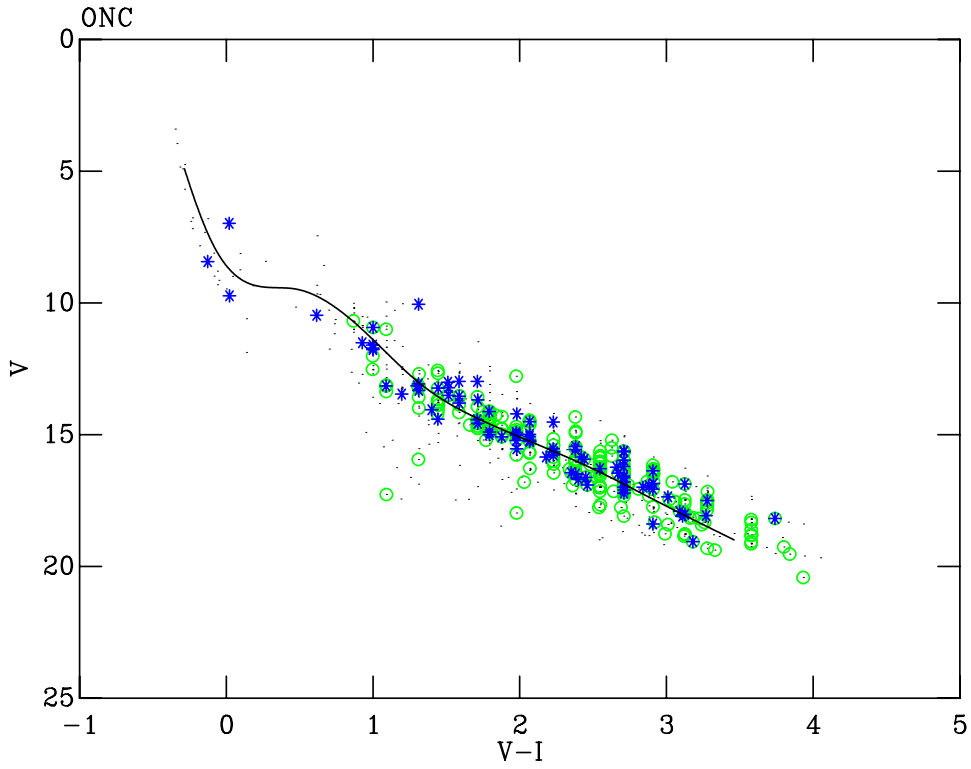

Figure 5.11: The ONC photometry from Hillenbrand (1997) (dots). Circles are objects which are periodic variables from Herbst et al. (2002). The asterisks are X-ray sources from Flaccomio et al. (2003). The best fit spline through all data points is also shown.

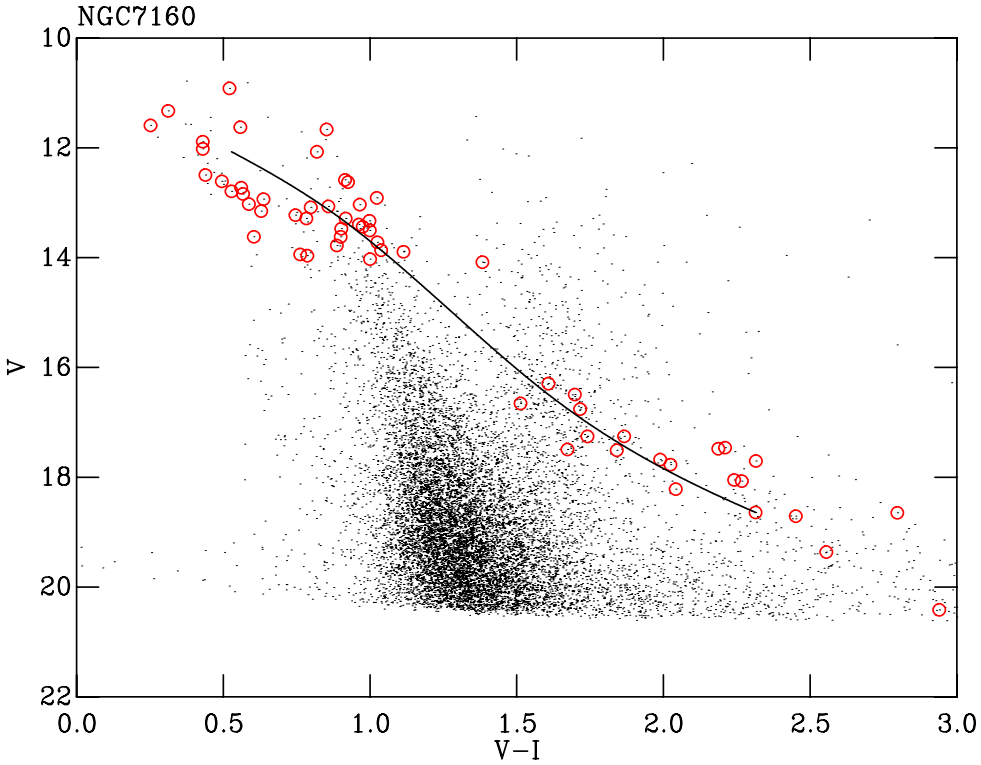

Figure 5.12: The full catalogue for the NGC7160 field (dots). Circles are members from Sicilia-Aguilar et al. (2004) and Sicilia-Aguilar et al. (2005).

5.4.4 NGC7160

The sequence and fit is displayed in Figure 5.12. The members, although sparse, represent a relatively unbiased sample in CMD space due to the 'wide' criteria applied to assign memberships (see Appendix 5.3.1.4).

5.4.5 σ Ori

For σ Ori a colour-magnitude selection was used to clip out the X-ray sources lying within the contamination. The resulting line fit is displayed in Figure 5.13. The applied colour-magnitude selection removed five objects all far from the sequence and within the contamination.

5.4.6 Cep OB3b

The selected members and fit for Cep OB3b are shown as Figure 5.14. A colour-magnitude selection has again been applied, although as in Section 5.4, since most objects lie in the sequence the effect on the fit is negligible.

5.4.7 IC348

For IC348 individual extinctions were available for all but 21 of the members. Therefore only those members with extinctions have been used. A colour-magnitude selection has been applied

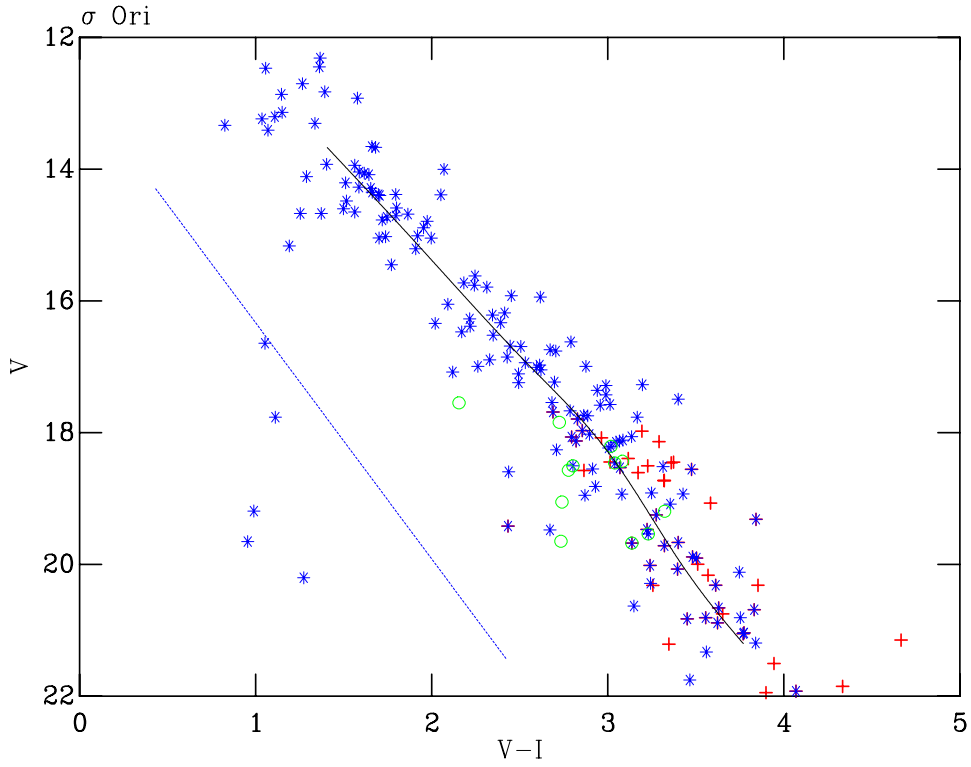

Figure 5.13: Stars selected as members in σ Ori. Circles are Burningham et al. (2005b) members. Asterisks are X-ray sources from Sanz-Forcada et al. (2004). Crosses are members from Kenyon et al. (2005). The fitted spline curve is shown. The colour-magnitude selection is shown as the dotted line.

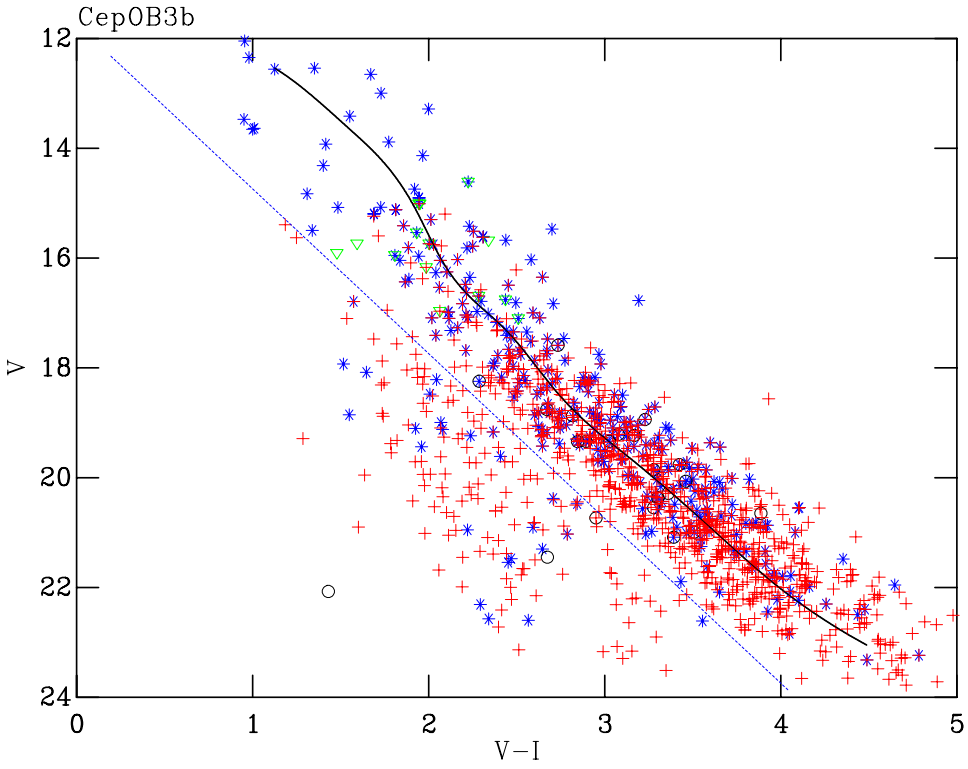

Figure 5.14: Stars selected as members in Cep OB3b. Asterisks are X-ray sources from Naylor & Fabian (1999), Getman et al. (2006) and the second PSPC catalogue. Triangles are members from Pozzo et al. (2003). Circles are Hα sources from Ogura et al. (2002). Crosses are the periodic variables from Littlefair et al. (2005). The fitted spline curve is shown.

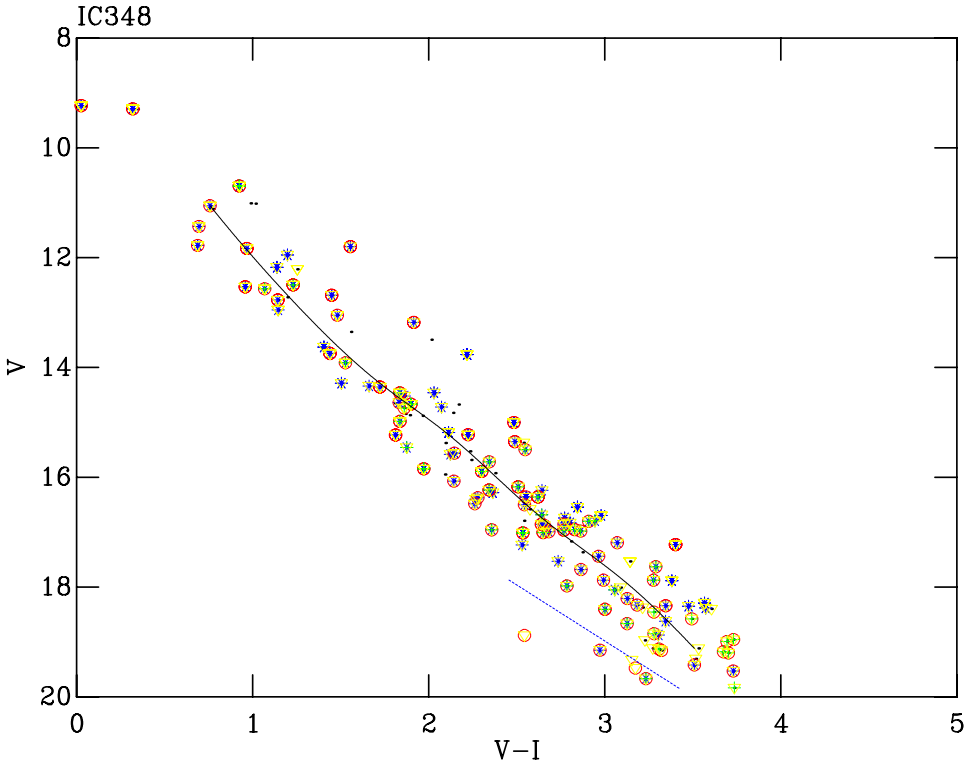

Figure 5.15: Stars selected as members in IC348. The asterisks are X-ray sources from Preibisch & Zinnecker (2002) and the Second ROSAT PSPC catalogue. Circles are the periodic variables from Cohen et al. (2004) and Littlefair et al. (2005). Crosses are Hα sources from Herbig (1998). Triangles are spectroscopic members with extinctions from Luhman et al. (2003) and Herbig (1998). Individual extinctions from Luhman et al. (2003) and Herbig (1998) have been applied before fitting. The colour-magnitude selection is shown as the dotted line.

removing five stars below the sequence. The individual dereddenings were applied prior to fitting. The dereddened sequence with the fitted curve can be seen as Figure 5.15.

5.4.8 h and χ Per

The positionally isolated stars for h and χ Per, as described in Section 5.3.2 were used for these clusters. Photometric cuts were then used to remove probable non-member stars. The cuts were varied until a best fit of the spline curve to the sequence was achieved. The final sequence, cuts and spline curve are shown in Figure 5.16. To further increase confidence in selection of the correct sequence the best fit spline was shifted to the mean extinction for both clusters and overlaid on the CMD showing the full catalogue. The spline curve clearly follows the sequence one would select by eye from this CMD, see Figure 5.6.

5.4.9 NGC1960

Again varying, wide colour-magnitude selections were applied during fitting of this cluster. The best resulting fit is shown as Figure 5.17. The spline fit is lifted above the sequence by around ≈ 0.3 mags, again due to the binary sequence in a similar way to NGC2547. This sequence is

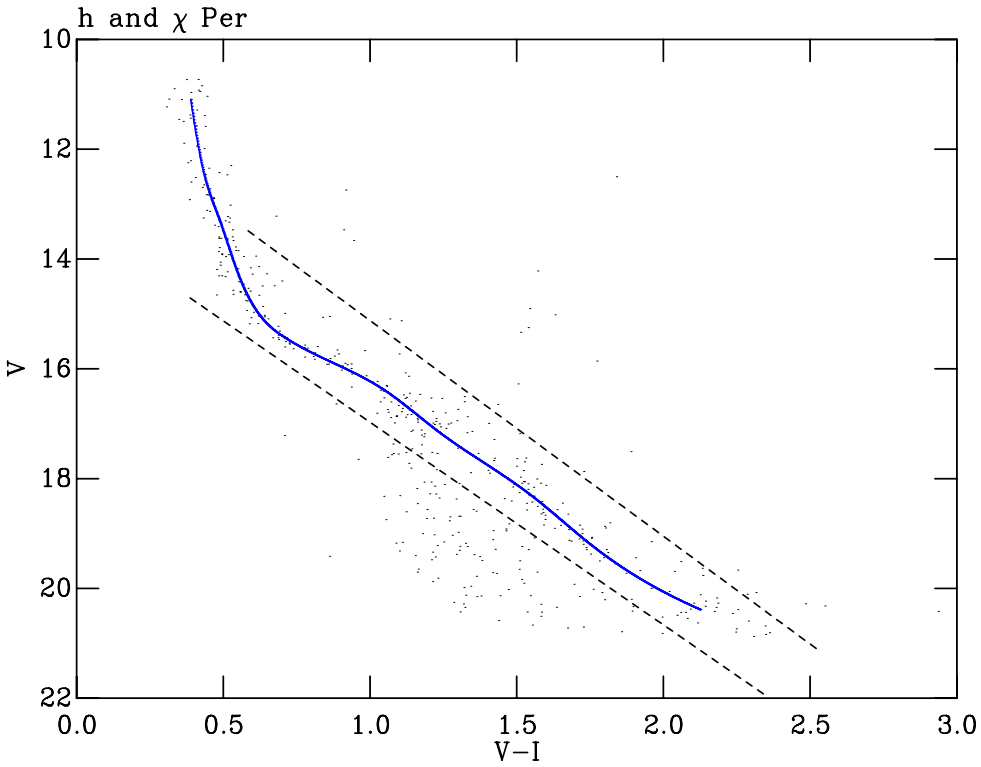

Figure 5.16: Stars within 2 arcmin radius of the centres of h and χ Per. Stars in the h Per region have been shifted in extinction to match those χ Per. The dotted lines are the colour-magnitude cuts used, and the solid curve the best fitting spline.

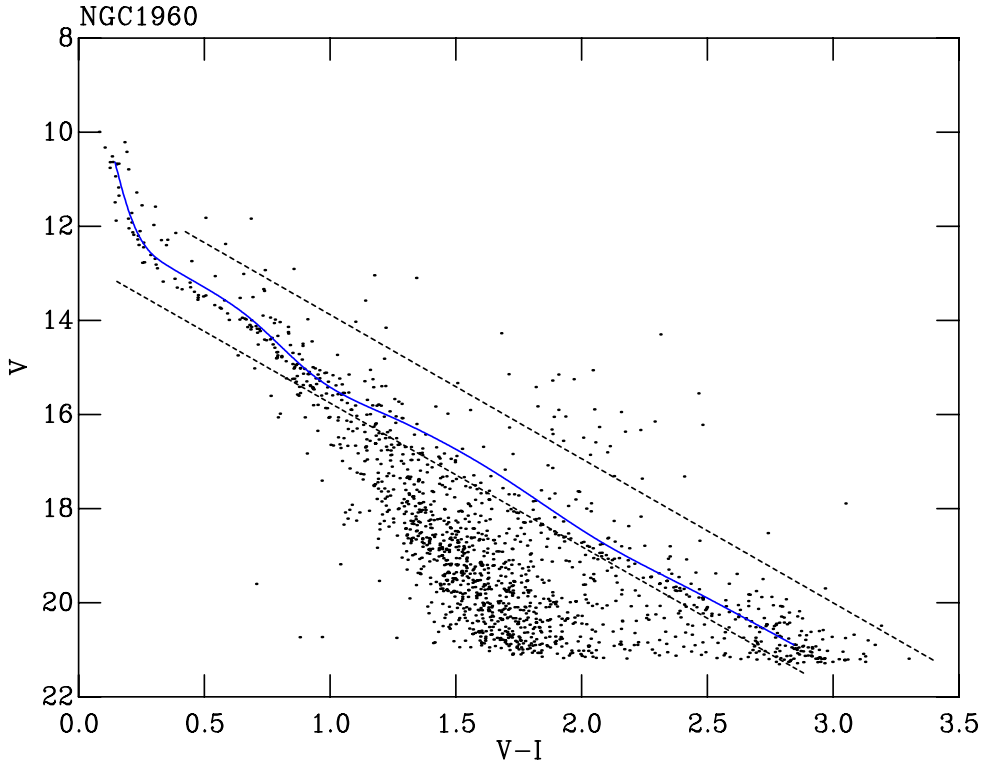

Figure 5.17: This spline curve lies around 0.3 mags above the sequence due to a clear binary sequence.

difficult to pick out, though the fact it lies close to a theoretical isochrone gives some confidence that the sequence has been correctly isolated.

5.4.10 λ Ori, NGC2362, IC5146, NGC6530 and NGC2244

For λ Ori a colour-magnitude selection has been applied removing three stars lying well above the sequence. For IC5146 only the stars shown as asterisks in Figure 5.19 were fitted. For NGC2244 two additional photometric cuts have been made, see Figure 5.20. For NGC2362 and NGC6530 no further cuts have been used. The members and spline fits for these fields can be seen as Figures 5.18 to 5.22.

5.5 Summary

In this Chapter likely pre-MS members have been selected for the chosen range of SFRs and empirical isochrones created for each. This provides a model of the pre-MS within a CMD which effectively removes the problems of age spreads for age order derivation. These empirical isochrones must now be converted to absolute magnitude and intrinsic colour to be compared and implications drawn. Absolute magnitudes and intrinsic colours can be derived using the parameters found in Chapter 4.

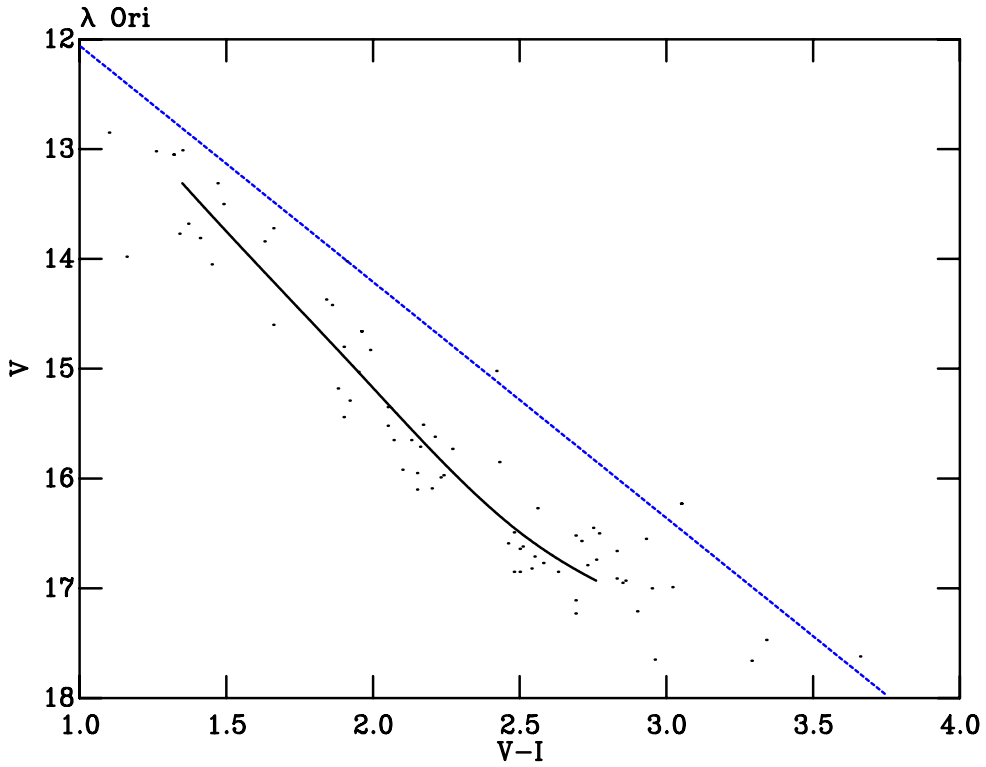

Figure 5.18: Stars selected as members in λ Ori. The dots are Li members from Dolan & Mathieu (2001).

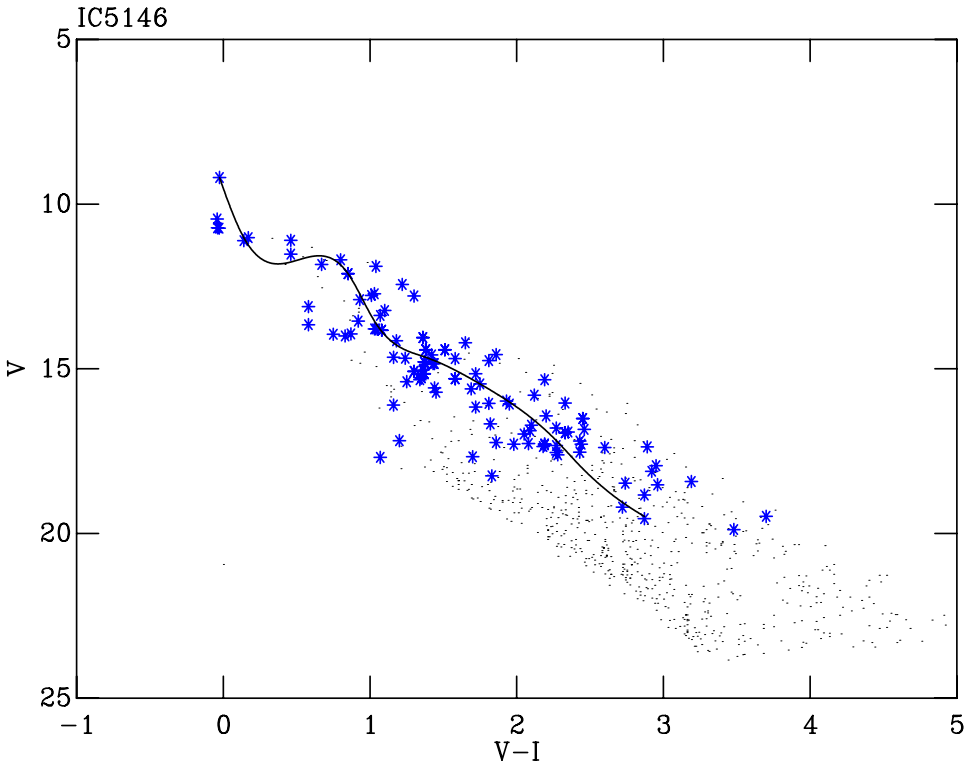

Figure 5.19: Stars selected as members in IC5146. Dots are likely pre-MS members from Herbig & Dahm (2002). Asterisks are Hα members from Herbig & Dahm (2002) with known spectral types excluding stars lying below the Pleiades MS. Only the asterisks were fitted.

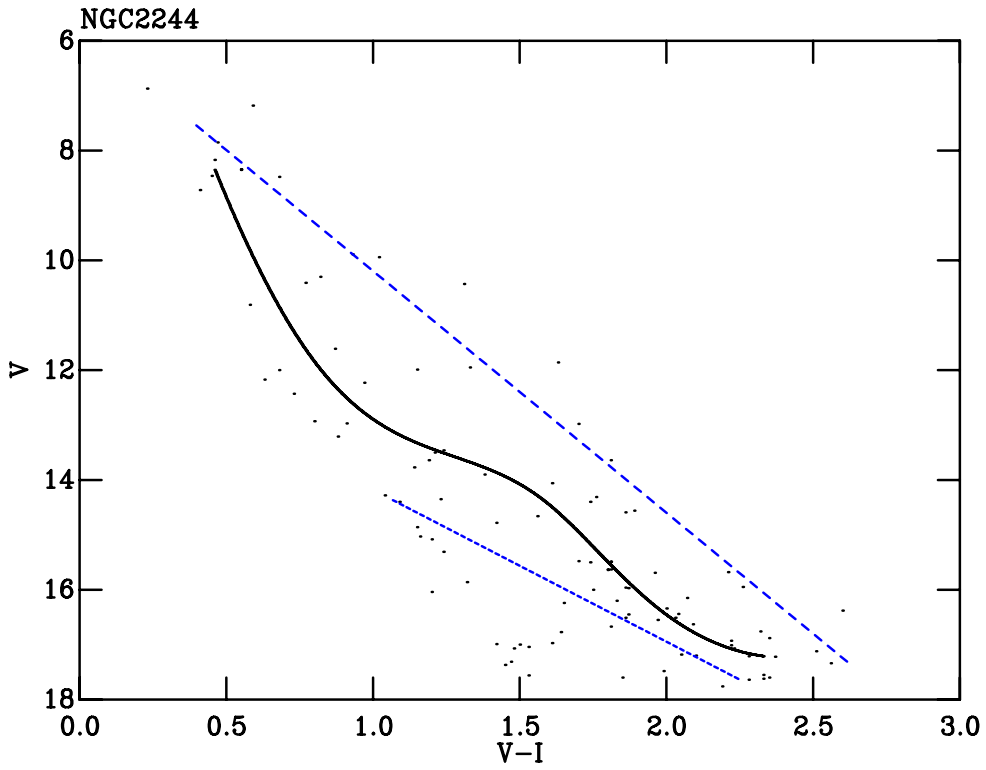

Figure 5.20: Stars selected as members in NGC2244. The dots are X-ray sources showing Hα emission from Berghöfer & Christian (2002).

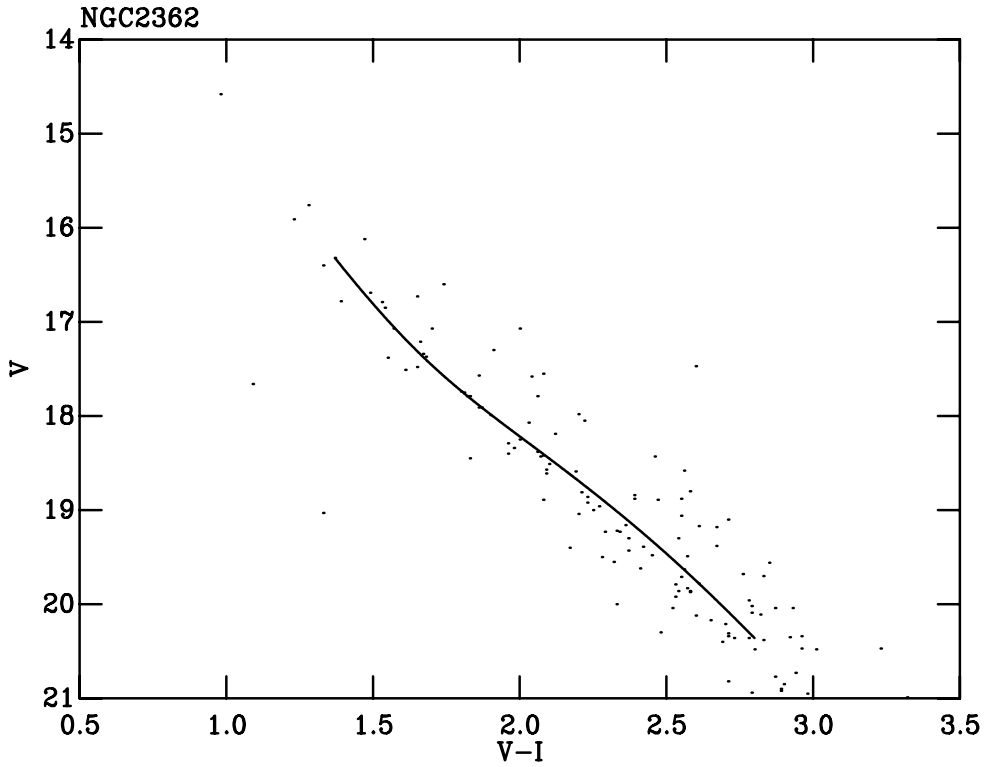

Figure 5.21: Stars selected as members in NGC2362. The dots are Hα and spectroscopically confirmed pre-MS members from Dahm (2005).

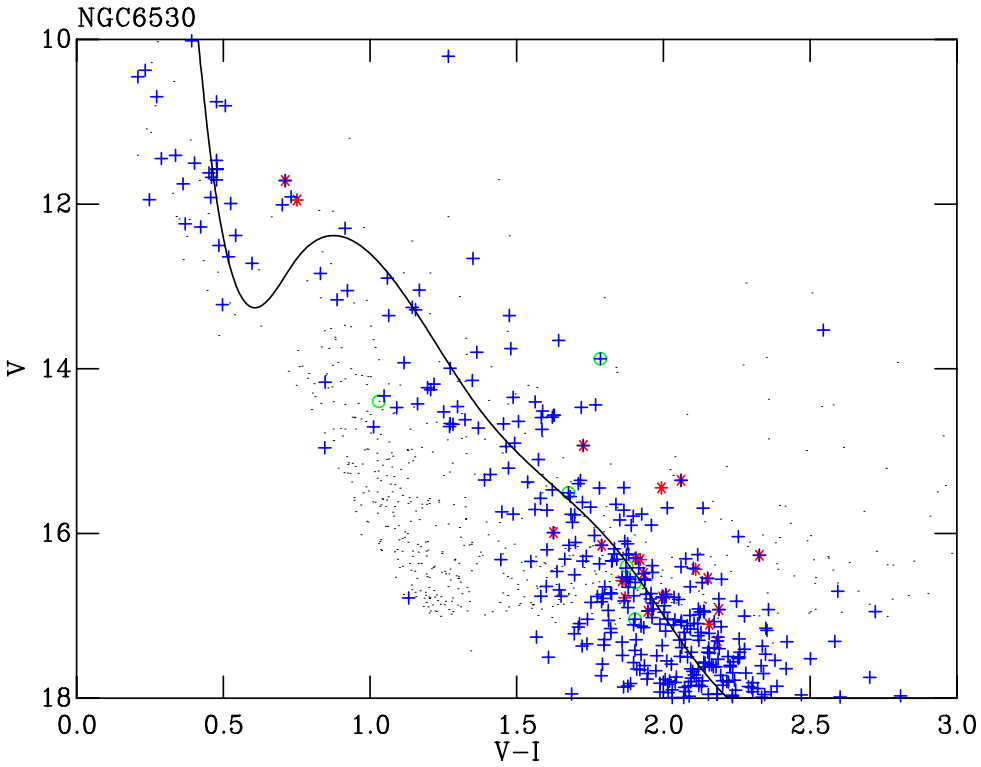

Figure 5.22: The photometry of NGC6530 from Prisinzano et al. (2005) (dots). Crosses are X-ray sources from Prisinzano et al. (2005). Circles are weak Hα stars from Sung et al. (2000). Asterisks are strong Hα stars from Sung et al. (2000).

Chapter 6

Age orders, nominal ages and the R-C gap

A distance and extinction has been derived or adopted for each SFR in Chapter 4 and each SFR sequence in CMD space has been modeled in Chapter 5. This allows firstly, a qualitative comparison of the sequences and photometry. This is discussed in Section 6.1. This comparison reveals an important feature of pre-MS populations in a CMD which is described and its uses discussed in Section 6.2. The empirical isochrones used to model the sequences can then be used after application of the assumed distance and extinction to provide a set of nominal ages using an age ladder. These nominal ages and their consequences in cases of particular interest are discussed in Section 6.3. Once the age orders have been derived they can be combined with supporting data to investigate aspects of the secular evolution between SFRs. The particular cases of rotational period distributions and disc fractions are discussed in Section 6.4. Finally the results and conclusions in this Chapter are summarised in Section 6.5.

6.1 Data comparison

The data from Chapter 5 present an opportunity to make a qualitative assessment of how the pre-MS changes with age. To enable this to be done the sequences were shifted by the adopted distances and extinctions (see Figure 6.1). Four of the best sequences spanning as large an age range as possible have been selected. Data for NGC2264 has been supplemented with photometry from Mendoza V. & Gomez (1980). They used radial velocities to assign membership probabilities, only those stars with membership probabilities of > 90% are considered here. This allows plotting of the sequence members above V_0=11, where the stars are saturated in the current catalogue.

6.1.1 Sequence spreads

The sequences in Figure 6.1 appear to “crystallise” with age. The absolute spread in CMD space of the sequences reduces as the age of the field increases. The trend appears to continue in the fields older than those presented in Figure 6.1. NGC2547 (≃30 Myrs) shows a clear sequence. Sequences older than 5 Myrs do not appear to show large spreads. However, sequences younger

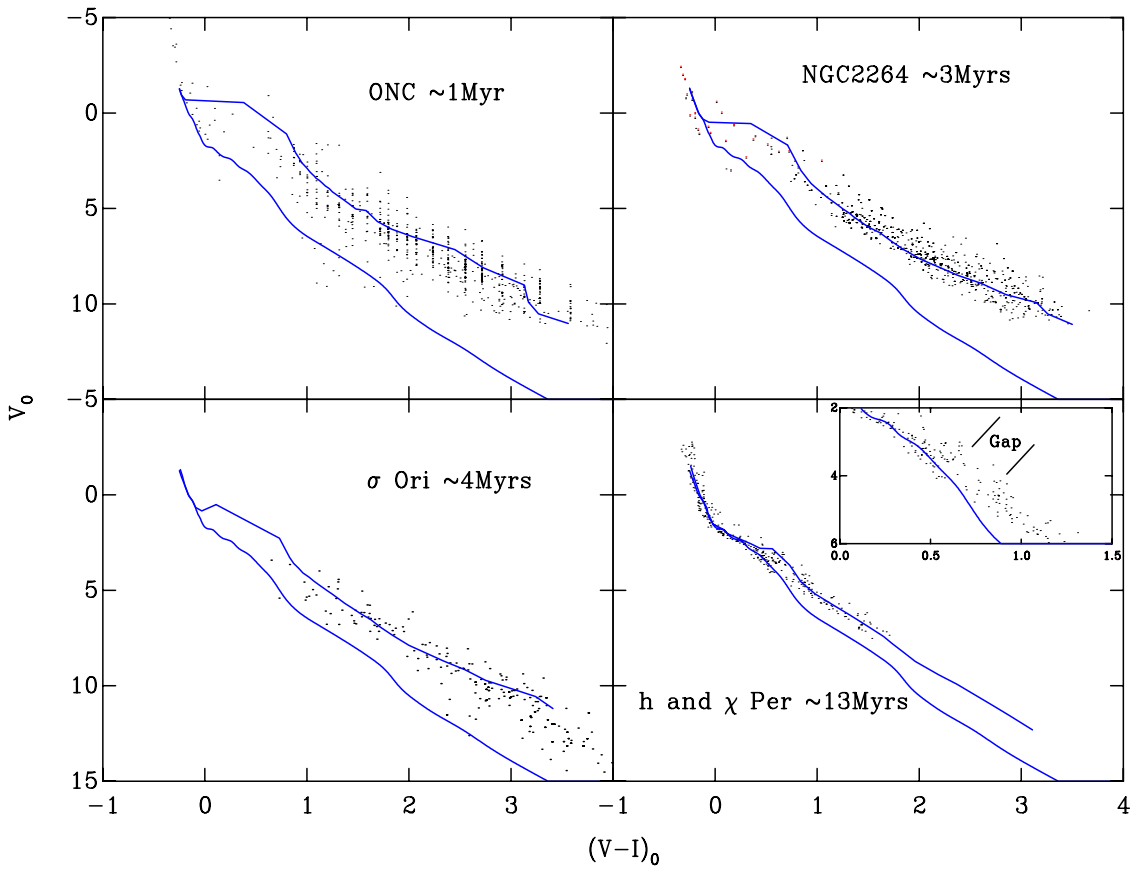

Figure 6.1: The likely PMS objects for fields of different ages, plotted in dereddened colours and absolute magnitudes. The spread in absolute colour magnitude space clearly decreases as age increases. The ZAMS and isochrones of approximately the correct age from Siess et al. (2000) are shown.

than this show large spreads not explicable by photometric errors, variability and binarity, as shown in the case of Cep OB3b and σ Ori by Burningham et al. (2005a). At $\simeq 5-6$ Myrs the Upper Sco-Cen OB association has an apparently wholly explicable photometric spread (Preibisch et al., 2002). It appears there is a change at about 5 Myrs.

This suggests a possible cause of the anomalous spreads; namely accretion. The half-life for accretion discs is estimated to be ≈ 3 Myrs, therefore for low mass objects one would expect the discs to have disappeared by $\simeq 6$ Myrs (Oliveira et al., 2006; Haisch et al., 2001). Active or current accretion from a disc, increases the continuum luminosity along with various other effects, possibly pushing the stars blue-ward, resulting in a scatter both temporally older and younger (Tout et al., 1999; Siess et al., 1999). This component of the spread would not be present in sequences older than $\simeq 6$ Myrs. It should be noted however that this half-life is derived from the presence of dust; the half-life of gas within these discs is less certain. If this is the case stars exhibiting Hα emission should lie above the main locus of stars in the pre-MS. This appears not to be the case as is demonstrated for NGC2264 in Figure 6.2. However, as discussed in Chapter 2, the effects of accretion events in the past are not removed over time. In other words photometric spreads within a CMD could be caused by varying levels of accretion much earlier in

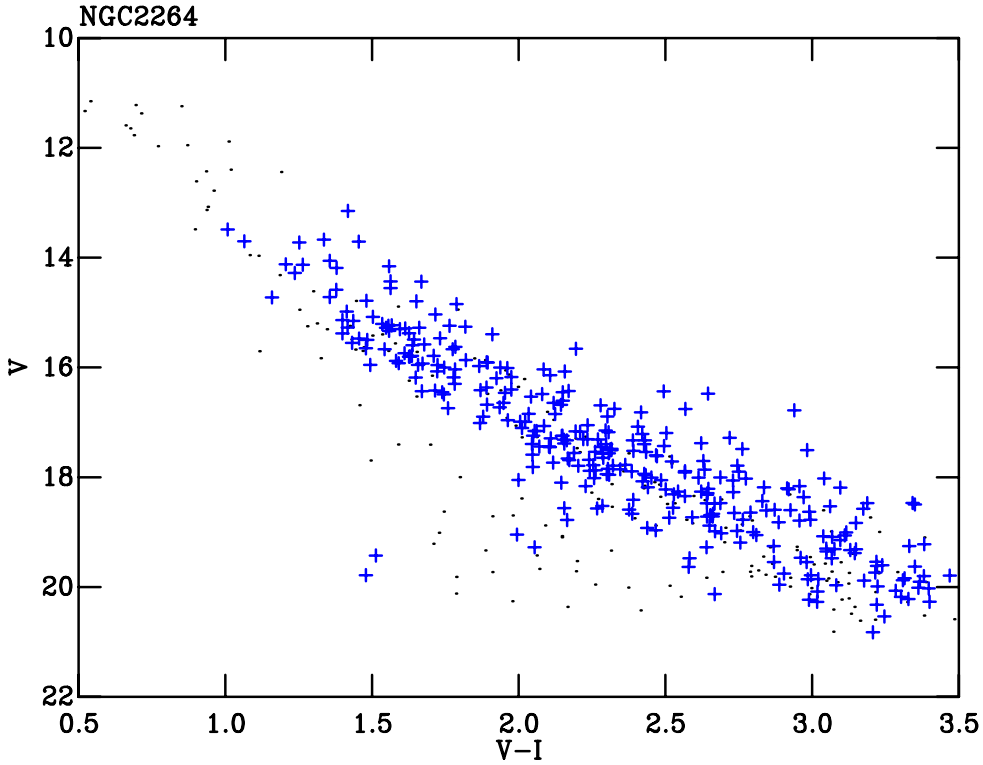

Figure 6.2: Dots are the combined photometric catalogue of NGC2264, photometry from Chapter 5 and > 90% members from Mendoza V. & Gomez (1980). The crosses are Hα emitters from Dahm & Simon (2005). The locus of the Hα emitting stars does not lie below the locus of the whole sequence. Meaning active accretion is not likely to play a major role in sequence spreads.

the star's history. Accretion causes the star to contract (Siess et al., 1999) moving the star along its evolutionary track. Subsequent evolution continues from this new position. Therefore, sequence spreads present in a given SFR could primarily be due to a range of past accretion rates and not necessarily correlate with current accretion. The crystallisation observed in the sequences would then solely be due to the bunching of the isochrones towards older ages.

6.2 R-C gap and the R-C gap overlap

A very useful and interesting feature of sequences in a CMD is apparent in Figure 6.1. The empirical isochrones and the underlying population in the CMDs of many SFRs reveal a clear gap between the convective lower-mass pre-main-sequence (pre-MS) and the radiative stars close to or on the main sequence (MS). I refer to this feature as the radiative-convective gap (R-C gap). This feature has the potential to provide a distance independent age indicator. Additionally it could provide a measure of the isochronal age spread or range of accretion histories (in slow-star-formation or rapid-star-formation models respectively).

6.2.1 Evidence for a gap in a *V*, *V-I* CMD

The ONC has a discernible gap between the pre-MS stars and the MS stars, at the point where the pre-MS isochrone meets the zero age main sequences (ZAMS), between a $(V-I)_0$ of $\approx 0-0.8$. This can be seen clearly in Figure 6.1. There also appears to be a gap, again where the pre-MS meets the MS in h and χ Per ($(V-I)_0 \approx 0.8-1.0$) and NGC2264 ($(V-I)_0 \approx 0-1.1$) in Figure 6.1. A gap is evident in the photometry for NGC6530 ($V-I \approx 0.5-1.5$) and perhaps IC5146 ($V-I \approx 0-1$, see Figures 5.22 and 5.19). A further excellent example of the gap can be seen in the CMD of NGC4755 in Lyra et al. (2006a).

To ascertain whether this gap between MS and pre-MS stars is a general feature, the isochrones can be used to find the position (in CMD space) of the pre-MS/MS connection. In some of the younger fields the gap is situated around the bright magnitude limit. In these cases one cannot be sure of the gap's existence. There is however a discernible dearth of members at the head of the pre-MS, which can be seen in Cep OB3b, σ Ori, IC348, NGC2362 and λ Ori. This explains the general shape of many CMDs of pre-MS regions, which appear to consist of a sequence parallel and red-ward of the contamination which disappears at brighter magnitudes. The brightest stars at the head of this sequence must represent the top of the pre-MS, with the MS appearing blue-ward of this. The MS, and therefore the gap, is often obscured by contamination.

Although rigorously characterising the gap will be the subject of future work it is useful at this point to provide some brief, and simple, statistical evidence for the gap. Figure 6.3 shows the histograms of star number as a function of intrinsic colour for the SFRs shown in Figure 6.1. This has been done to aid comparison of the position of the gap as a function of age. Then the stars have been collapsed onto the x-axis for the three younger sequences, where the R-C gap is nearly horizontal, and onto the spline for the older sequence, h and χ Per, as here the R-C gap lies diagonally in CMD space, overlapping in $V-I$ which would essentially foreshorten the gap if the x-axis were used. As can be seen in Figure 6.3 for each of the SFRs where the gap can be identified from the CMD a corresponding drop in the number of stars (or density) is found. The dashed lines on Figure 6.3 show the approximate centres of the gap positions taken from the CMDs, which move redward with age. For σ Ori the photometry saturates before the anticipated position of the gap and so only a decline in the density of stars is seen. One can do a very simple statistical test to confirm the existences of a drop in stars between the bins across the R-C gap by merely averaging the values in the bins either side of the gap and determining how many σ from the observed value this mean is, where σ is simply $\sqrt{N}$ with N=number of stars in the bin. This results in a gap being detected in the ONC, NGC2264 and h and χ Per at 10σ, 12.5σ and 6.7σ, respectively. The histogram for h and χ Per an increase in density in the bin redward of the R-C gap, this is most probably due to contamination as these stars were selected positionally, i.e. without membership information. This simple statistical test does not account for the effect of saturation and completeness on our photometric sample. For the three cases with a clear gap, however, these effects are not likely to cause a drop in density between two points. Although for σ Ori the drop in density be could be solely due to saturation effects. However in order to check this I have cross correlated stars in these data marked as saturated with stars from the Amateur all sky survey (Richmond et al., 1998) which is complete to $V = 14$ mag. This resulted in only thirteen

legitimate saturated stars above $V = 14$, not enough to change the decline towards the R-C gap. A further, rigorous, characterisation will be undertaken in the future.

The gap cannot definitely be detected in NGC7160, NGC1960 or NGC2547. In the case of NGC7160 the gap would fall in an area devoid of membership information. Finally for the oldest fields NGC2547 and NGC1960 the pre-MS and MS isochrones lie very close together meaning the gap, if present, would be very small compared to the younger fields.

It is apparent that this phenomena occurs in all datasets where one would expect to observe it. This feature delineates the transition from pre-MS to MS, hence Stolte et al. (2004) call this the pre-MS/MS transition region (they identified it in a J_s, $J_s - K_s$ CMD of NGC3603). The term radiative convective (R-C) gap is perhaps more fitting as this emphasizes the physics involved which is outlined in the next section.

6.2.2 The origin of the R-C gap

From the theoretical isochrones an explanation for this gap becomes apparent (see Figure 6.4). Physically the R-C gap is the transition phase of stars from a fully convective object to the development of a radiative core. The Hayashi tracks which the lower mass pre-MS stars descend in CMD space represent the gravitational contraction of a fully convective object. As the star heats and the core density gradually increases, at some stage the core becomes radiative, and the track changes to a Henyey track which is almost horizontal in a *V*/*V-I* CMD. For massive stars this happens earlier in the star's evolution than for low mass stars (Collins, 1989); a $7M_{\odot}$ star will develop a radiative core almost immediately.

The development and evolution of the radiative core causes the separation of the pre-MS and MS. As the transition proceeds the mass tracks become almost parallel to the isochrones, meaning evolution across the area of CMD space between the pre-MS and MS is rapid compared to the descent down the Hayashi tracks. The difference in motion in CMD space is clearly demonstrated in Figure 6.4. Here the distance between a 1 Myr and 3 Myr isochrone for a star on a fully convective track is small when compared to a star at the head of the pre-MS which will have joined the MS by 3 Myrs, moving much farther in CMD space. This means at any given age a sequence should have a relative sparsity of stars in this gap compared to the slowly evolving pre-MS and almost stationary MS (on these timescales).

As is visible from the data in Figure 6.1 and the theory in Figure 6.4 the size of the dislocation between the MS and pre-MS is a function of age. For the younger fields the pre-MS lies far from the MS and the transition occurs at high masses. The higher the mass of a star the earlier the formation of a radiative core and the sooner it changes to a Henyey track. Higher mass objects move to the MS more swiftly along these tracks. The reverse is also true; as the field becomes older, the mass at which the core develops falls and the evolution of the star progresses more slowly.

The age dependency of the size of the gap has important ramifications. If it is possible to identify the head of the pre-MS and the MS members for a given field, the separation of these will be a distance and reddening independent measure of the age. There are several restrictions. If the field is older than around 15 Myrs the gap becomes too small to detect reliably. The gap

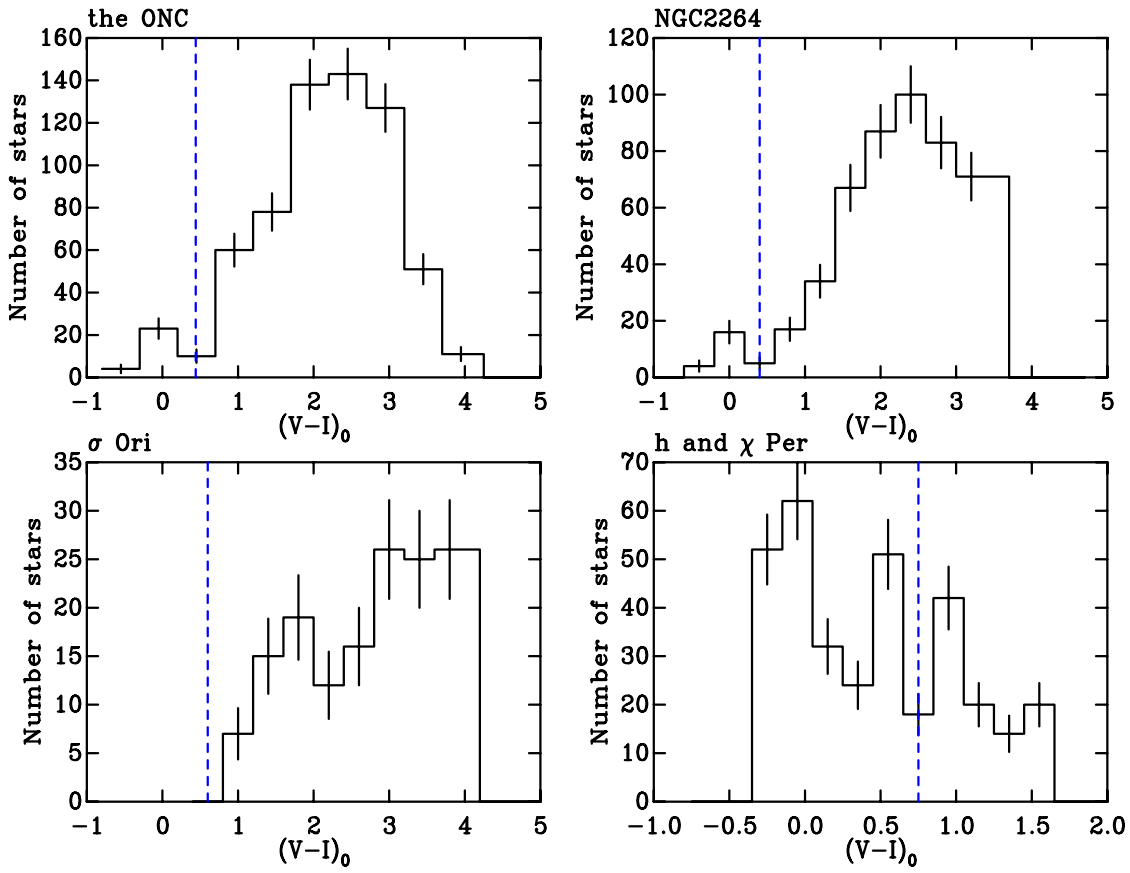

Figure 6.3: The histograms showing the number of stars as a function of intrinsic colour ($(V-I)_0$). For the young SFRs where the R-C gap is almost horizontal the stars have been collapsed onto the x-axis. For h and χ Per the stars have been collapsed onto the spline, as the R-C gap is diagonal in CMD space and using the x-axis effectively foreshortens the gap. The vertical dashed line shows the approximate central position expected for the R-C gap in each SFR, estimated from the CMD. For the ONC, NGC2264 and h and χ Per a simple statistical treatment confirms the observation of a gap at the expected position to the 10σ, 12.5σ and 6.7σ level respectively. For σ Ori only a decrease in the number of stars is seen. Note, in this simple example the effects of saturation and completeness have not been accounted for, however, for the three clear cases these effects could not cause the gap or drop in density. Further characterisation of the gap will be undertaken in future work.

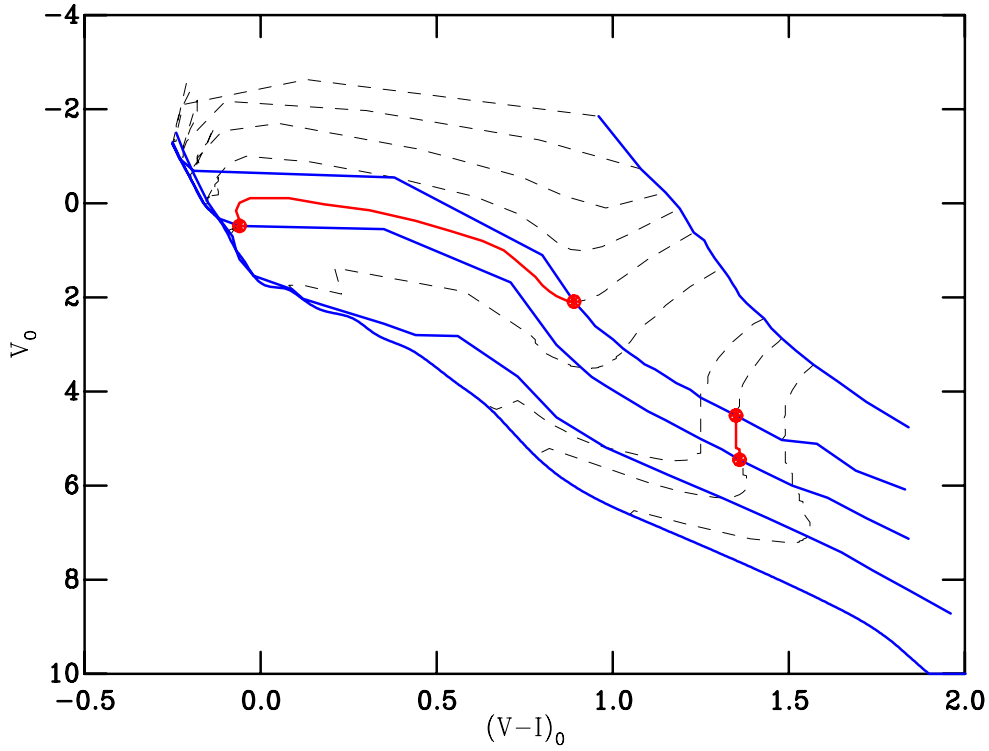

Figure 6.4: Isochrones (solid blue lines) from Siess et al. (2000) for the approximate ages of the four fields in Figure 6.1; 1, 3, 4 and 13 Myrs and two bounding isochrones, the ZAMS and 0.1 Myrs as a lower bound. Mass tracks (dashed lines) are show for 7, 6, 5, 4, 3, 2, 1.2, 1.0, and $0.8M_{\odot}$. The evolution between 1 and 3 Myrs of 3 and $1M_{\odot}$ stars are shown as filled circles, with the tracks highlighted in red.

may also lie within an area of high contamination, meaning many objects will need to be assessed for membership to be certain of detecting the gap. In some cases variable extinction will prevent photometric detection of the gap, as the relative positions of the stars shift in a CMD; in these cases individual extinctions will need to be found. As the size of the gap depends critically on the formation and growth of the radiative core, it may also represent an excellent test of the stellar interior models.

6.2.3 Age spreads and the R-C gap overlap

As discussed in Chapter 2 age spreads for SFRs in stellar populations have been used to support both rapid and slow star formation. Apparent spreads are clear in all the pre-MS populations presented in Chapter 5, indeed this provided the motivation for modeling these populations with empirical isochrones. In addition, apparent age spreads were present in the data and fitting contained in Chapter 4. In particular, as can be seen from Table 4.3, the faint red ends of the apparent MS invariably lie too red when compared with the theoretically predicted position i.e. the turn-on, for the younger SFRs. This is clearly visible in the CMDs of the younger SFRs in Section 4.3.1.3. This disagreement between the empirical and theoretical turn-on positions (in colour), is particularly clear for the ONC. As is clear in Figure 6.5, MS stars lie along isochrones suggesting ages of

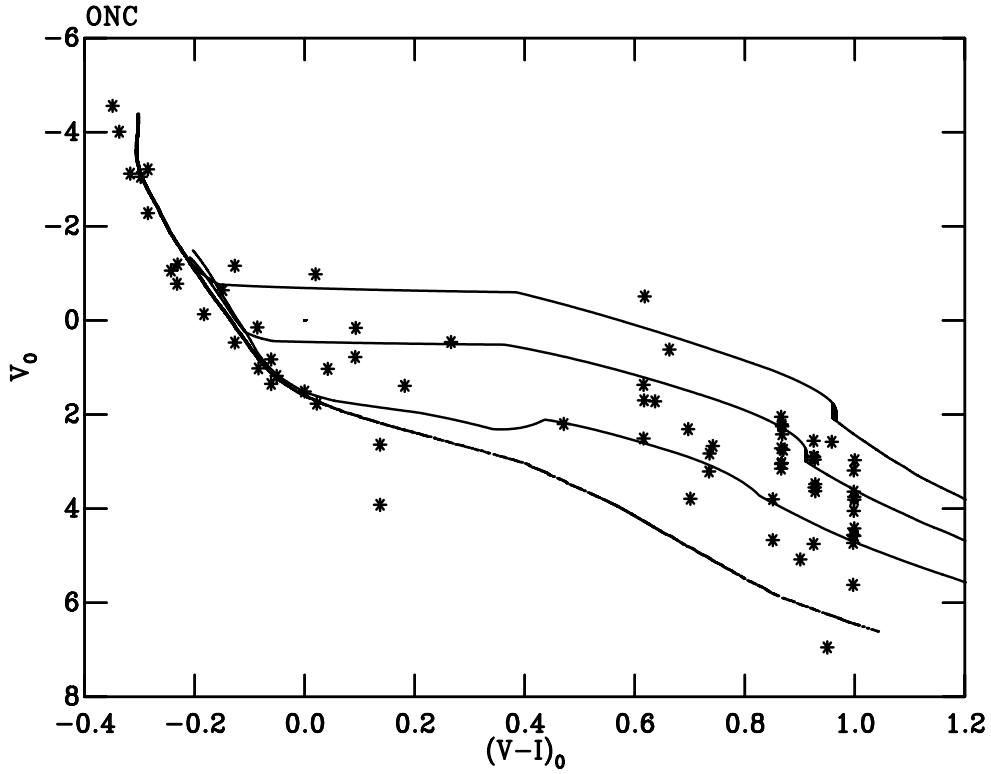

Figure 6.5: The ONC with a Geneva-Bessell 1 Myr MS isochrone and the Pre-MS isochrones of Siess et al. (2000) for 1, 3 and 10 Myrs. Stars appear to lie at the turn-on for an age of 10 Myr.

up to ≈10 Myrs.

This could be construed as evidence that the adopted age is incorrect. However, as shown in Figure 6.5 a turn-on age of 10 Myrs is at variance with a median pre-MS age of $\approx 2-3$ Myr. However, as suggested in Chapter 3, ages from pre-MS isochrones are unreliable. In Figure 6.5 there are no stars above and blueward of the turn-off with which to further constrain the age. Although any discrepancy between the apparent turn-on and the theoretical turn-on is harder to discern for the older SFRs, it can be seen for χ Per as shown in Figure 6.6. In addition to the discrepancy at the turn-on, a similar problem is clear at the turn-off. Figure 6.6 shows stars lying on an apparent MS above and bluewards of the theoretical turn-off for the adopted age of 13 Myrs. An inaccurate adopted age cannot account for both of these discrepancies. If one decreases the adopted age to fit the stars above the turn-off, the problem for stars below the turn-on is exacerbated.

Therefore, the extension of the apparent MS fainter than and redward of the theoretical turn-on appears a robust and ubiquitous feature. The fact that it is less apparent in the older SFRs is probably a consequence of the bunching of stars towards older ages. As the age of a coeval stellar population increases it becomes fainter and moves towards the ZAMS. Lower mass stars on the pre-MS contract more slowly as they age, therefore, the same difference in age for an older population produces a smaller change in V than for a younger isochrone. Thus this mis-match between the empirical and theoretical turn-ons would become smaller and harder to identify. Any extension of stars along an apparent MS above the theoretical turn-off will of course be difficult to observe in younger SFRs as only the most massive stars will have evolved away from the MS.

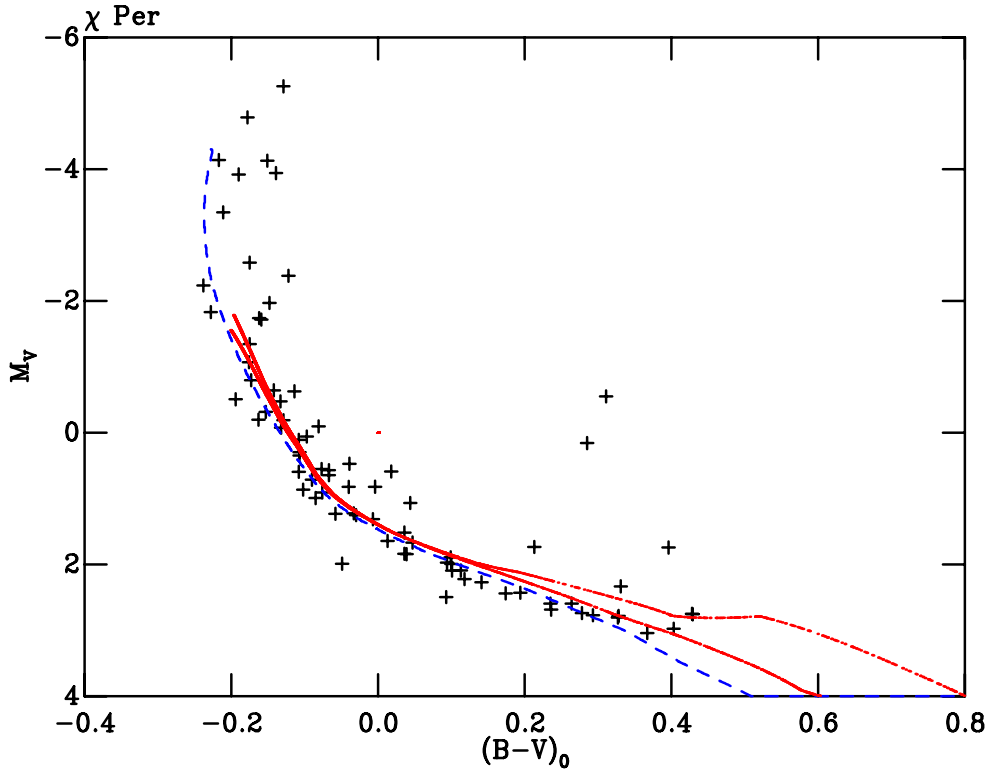

Figure 6.6: χ Per with a Geneva-Bessell 13 Myr MS isochrone (dashed line) and the pre-MS isochrones of Siess et al. (2000) for 13 and 23 Myrs (bold lines). Stars appear to lie below the turn-on and above and blueward of the turn-off for an age of 13 Myr .

If one is forced to accept that the adopted age cannot be changed to remove this discrepancy it must be construed as an apparent spread in age. If individual ages are assigned to each star using isochrones, this apparent extension (along a MS line) below the turn-on, for almost all SFRs, produces an age spread within the SFR, as exemplified by Figures 6.5 and 6.6. In addition Figure 6.7 shows a similar MS spread in NGC2264.

As this discrepancy at the turn-on happens across the R-C gap, and the apparent MS extends fainter than the apparent pre-MS effectively creating an overlap, I term this feature the R-C gap overlap. The highest mass object on the convective pre-MS and the lowest mass object which has already crossed the gap onto the radiative MS provide a precise measure of the apparent spread in isochronal age within a given SFR.

Age spreads within SFRs have of course already been postulated (see for example Palla et al., 2005; Slesnick et al., 2004). However, age spreads defined within the pre-MS are often based on pre-MS isochrones, which as discussed are unreliable, and the scatter could be dominated by errors in magnitude. Burningham et al. (2005a) however, found that photometric variability, photometric errors and binarity could not account for pre-MS age spreads. Part of this scatter could be driven by accretion, as Tout et al. (1999) show this acts to scatter a pre-MS star within a CMD.

To create an R-C gap overlap a star must move across the R-C gap before its assumed coeval counterpart of the same mass. The fact that motion across the R-C gap involves a large colour shift for a negligible change in magnitude, and the stars appear to lie along the MS isochrones, suggests that stars are unlikely to be scattered across this region by any of the effects discussed in Burningham et al. (2005a). In addition, Jeffries (2007b) finds a direct spread in the radii of pre-MS stars in the ONC, at a given effective temperature, using a method free from isochrone theory. This, in conjunction with the R-C gap suggests there is a real underlying spread in evolutionary states within the assumed coeval SFRs.

However, interpreting these spreads in isochronal age, or even in radii and evolutionary state, as real age spreads must be viewed with caution. As shown in Tout et al. (1999) accretion can act to force a star bluer and isochronally older, but additionally Siess et al. (1999) find that the evolution of an accreting star is accelerated, with the star having a smaller radius and therefore lower luminosity than a non-accreting coeval counterpart. So an apparent spread in age from a CMD, stellar radii or the R-C gap overlap, does not necessarily imply a real spread in age. This could be interpreted as a range of accretion histories within a SFR. Practically, at any given mass, two coeval stars can appear to have a different age due to differing accretion histories.

As discussed in Chapter 2 it is unclear whether star formation is rapid or slow. If star formation is rapid then apparent age spreads within a CMD do not represent real age spreads caused by slower star formation, but are driven by accretion history. Therefore isochronal ages for all parts of the sequence (based on turn-ons, turn-offs, or pre-MS fitting), for individual stars without a known accretion history do not represent the true age of the star and thus should not be used to support evolutionary theories. Indeed, it is even hard to argue that a median or mean age for a given SFR derived from isochrone fitting has any real meaning. Perhaps, following the results in Siess et al. (1999) and Tout et al. (1999), if accretion causes a decrease in a star's radius,

therefore increasing its isochronal age, the most accurate representative age for a given cluster is that of its youngest stars having the lowest accretion histories. However, this would mean a dramatic change in the ages for most SFRs, for example the youngest stars in the ONC are ≈ 0.1 Myrs (Hillenbrand, 1997) and many SFRs still contain embedded objects and sites of active star formation.

As stated in Chapters 2 and 3, examining secular evolution by, for example, deriving disc survival timescales, requires precise age orders for a range of SFRs. In Chapter 5, due to the fact that ages from pre-MS isochrones are unreliable, age orders from empirical isochrones were determined to be the best way to compare SFRs temporally. This argument is strengthened by the apparent spreads across the R-C gap overlap. As without a knowledge of the formation time one cannot rule out either model, and as suggested this undermines not only ages from pre-MS isochrone fitting but also fitting of other regions of a stellar sequence.

Given these additional problems with absolute ages, derived using isochrones, the best approach remains empirical, comparing observations of two different SFRs. Either by deriving age orders by assuming a similar range of accretion rates within each SFR, or by using the R-C gap overlap to derive approximate differences in the range of accretion rates. An example of this can be seen in Figure 6.7, showing the absolute magnitude and intrinsic colour for stars in the ONC and NGC2264. The locus of the pre-MS in NGC2264 clearly lies slightly below that of the ONC, but the MS section is strikingly similar. In addition Figure 6.7 shows the MS for the SFRs extending below the predicted turn-on. Moreover, the brightest MS stars in both populations are at similar magnitudes i.e. the turn-off is in a similar position, with stars lying on the apparent MS above the turn-off (as seen in Figure 6.6). The apparent MS and pre-MS in both clusters appear to extend to similar points i.e. the R-C gap overlap is similar, suggesting a similar range of accretion histories for each cluster. So, in conclusion, the MS sections imply a large **isochronal** age spread as seen in Figure 6.5, and deriving ages and age spreads from isochrone fitting to these sections of the sequence would lead to a similar result for the ONC and NGC2264. However, comparing the sequences as a whole show that NGC2264 is more evolved than the ONC. This is the basic process in construction of the age ladder, and is continued in the next section.

The R-C gap overlap effectively reveals the apparent age spreads in a SFR. This effectively means if one adopts SSF the R-C gap overlap provides an easy and precise tool with which to measure isochronal age spreads. If one adopts RSF then the overlap can be used to quantify the range of accretion histories within a given SFR. In either case empirical comparison can be enhanced by 'normalising out' this spread factor. This means once the R-C gap overlap spread is found for each cluster, the spreads around the median empirical isochrones can be reduced by a representative factor, meaning comparison of the sequence positions within an absolute CMD is enhanced. However, the R-C gap itself has not yet been reliably characterised. I return to this in Chapter 7 but for now I proceed with the assumption that all age spreads or ranges of accretion rate history are similar for the SFRs studied, and in the next section create an age ladder given this assumption.

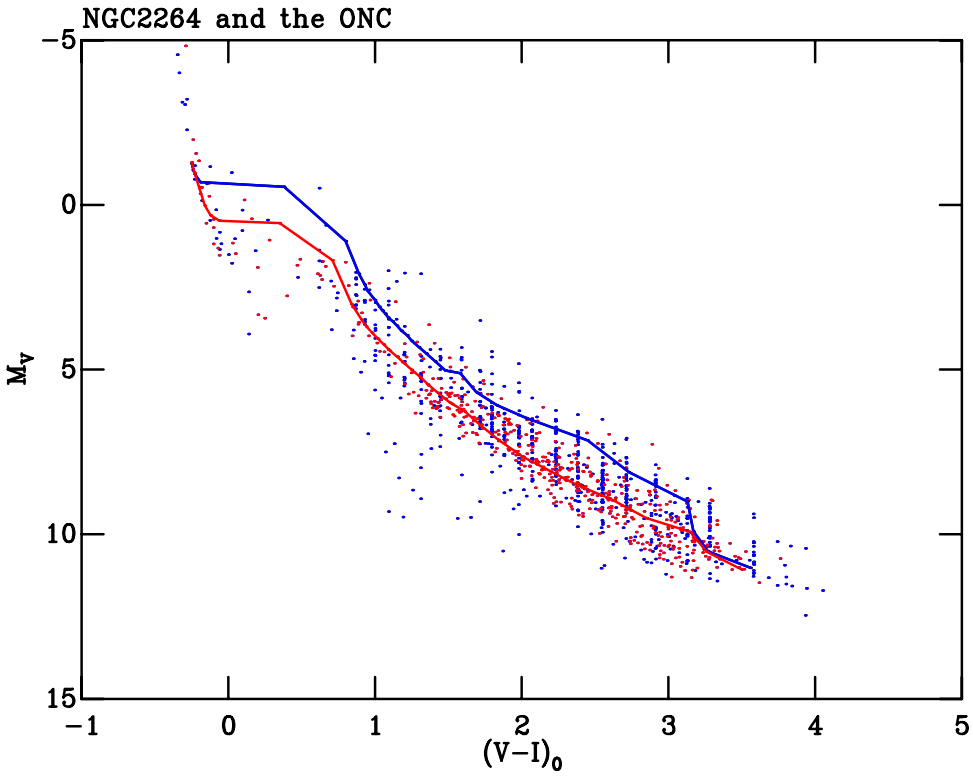

Figure 6.7: Absolute magnitude as a function of intrinsic colour for stars in the ONC and NGC2264 adjusted using a extinctions and distances from Chapter 4. The blue dots are the ONC and the red dots are NGC2264. The locus of points for NGC2264 can be seen to lay below the ONC, however the MS section is very similar in extent for each SFR, i.e. the turn-on appears coincident. The pre-MS isochrones from Siess et al. (2000) are shown for 1 and 3 Myrs. Most importantly in the MS section stars from both populations extend below the turn-ons and for both SFRs the peak of the MS (brightest stars) is similar i.e. the turn-offs do not appear significantly different, although this is based on only a few stars.

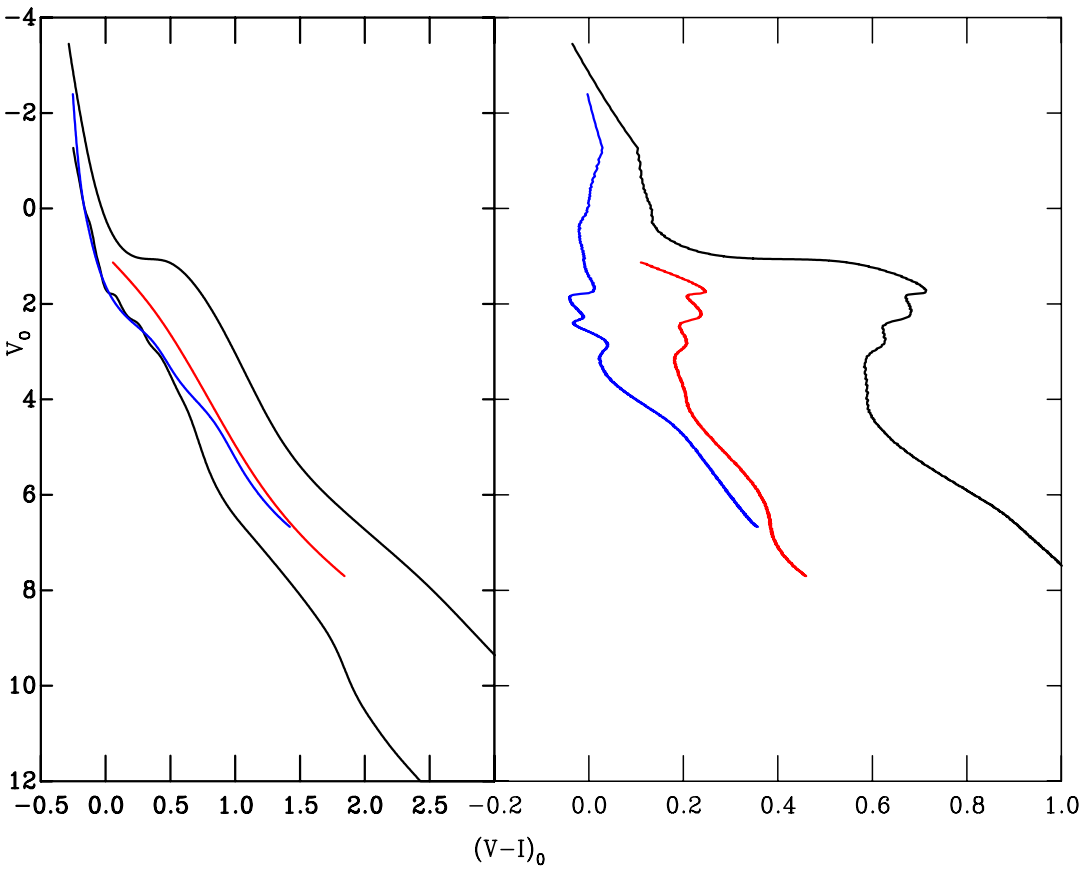

Figure 6.8: A sample of the empirical isochrones. Youngest to oldest, the ONC, NGC7160 and h and χ Per. The *left* panel is the empirical isochrones in an absolute *V*, *V-I* CMD, with the lowest curve the ZAMS relation of Siess et al. (2000). The *right* panel is the ZAMS subtracted space; at a given *V* the ZAMS *V-I* is subtracted from the *V-I* of the spline.

6.3 Age orders

The sequences displayed in Figure 6.1 are the results after membership selection. To create an age ladder however the sequences must appear on the same CMD, superimposed over one another. Such a figure would be confused due to the number of points and the spreads of the sequences, which could possibly be accounted for by use of the R-C gap overlap. At this stage however the sequences can be represented by the spline fits. To aid analysis a ZAMS subtracted CMD has been created, using the ZAMS relation of Siess et al. (2000). In these diagrams the points on the spline fits each have the *V-I* of the MS star at equivalent *V* subtracted from their *V-I*. This separates the sequences much more clearly. Figure 6.8 shows a sample of the empirical isochrones.

6.3.1 Theory comparison

It is useful at this stage to compare the empirical isochrones created to their theoretical counterparts. Although the isochrones from Siess et al. (2000) have been used, the effects described are apparent with all the other isochrones, though a complete investigation of all the models lies outside the scope of this thesis.

An approximately solar metallicity is adopted, $Z = 0.02$. James et al. (2006) show that for a number of star forming regions the metallicty is slightly subsolar. However it is possible that different clusters, associations, groups or sub-groups will have differing compositions. Therefore it is pertinent to ask what age difference would be obtained by fitting a higher or lower metallicity isochrone to our representative sequence of 3 Myrs. If we compare a 3 Myr $Z = 0.02$ isochrone with isochrones of $Z = 0.01$ and $Z = 0.04$ (using Siess et al., 2000, isochrones) the closest matches have approximate ages of 2.2 and 3.5 Myrs respectively. Thus changes in the metallicity by a factor two are too small to affect the discussion which follows.

In Figure 6.8 two minor problems are apparent. First for the ZAMS subtracted space diagram, at $V_0 \simeq 3$ mag many of the sequences show a "wave" effect. This effect is due to the subtraction of a smooth spline from the structured ZAMS. This could be a failure of the spline interpolation to follow the features of the sequence i.e. the spline curve is smoothed across this region whereas the ZAMS isochrone shows structure in this region.

In addition, our comparison reveals three serious concerns. (i) Figures 6.1 and 6.9 show that whilst an acceptable fit to the theoretical isochrones can be obtained over most of the sequence, the model isochrone lies above the data at the boundaries of the R-C gap. Furthermore the MS members overlap the pre-MS in magnitude space (the R-C gap overlap), in direct contradiction to the isochrones. (ii) For younger sequences a theoretical isochrone fitted to the pre-MS is a poor match to the MS. (iii) Although the young sequences have a large scatter, the pre-MS isochrones fail to consistently follow the centre of this spread. For example, in the ONC most stars lie below the isochrone at V-I=2.5, but above it at V-I=1. The conclusion is that when fitting isochrones to sequences across a limited colour range, one must be aware that the fit will not necessarily be good across the rest of the sequence. This implies that the age derived depends on which part of the sequence is fitted. This is why empirical isochrones are potentially superior to their theoretical counterparts.

6.3.2 Age ladder

Comparison of all the empirical isochrones in absolute magnitude and intrinsic colour as seen in Figure 6.8 can then provide an age ladder. The sequences can be separated into groups where the uncertainties in distances (typically $\approx \pm 0.1$ mags) are not sufficent to move a given SFR between age groups. In this section an age ladder is constructed using the best fitting distances and extinctions from Chapter 4. After this the distance uncertainties are examined and age groups delineated.

To aid the display of an individual SFR within an age ladder, empirical isochrone fiducial sequences are selected to 'bound' the age of the SFR. Nominal ages assigned to the well modeled fiducial sequences then allow a nominal age application to the chosen SFR. As the MS section of the sequences between turn-off and turn-on remains relatively static with age (see discussion in Chapter 4), the individual stars are shown in this region for the target SFR. The pre-MS empirical isochrone is only fit to the pre-MS members of the target. This effectively means the sequence is cut at the R-C gap with the individual MS or radiative stars plotted and the pre-MS or convective stars modeled by a spline line. For the bounding fiducial empirical isochrones a spline line fitted

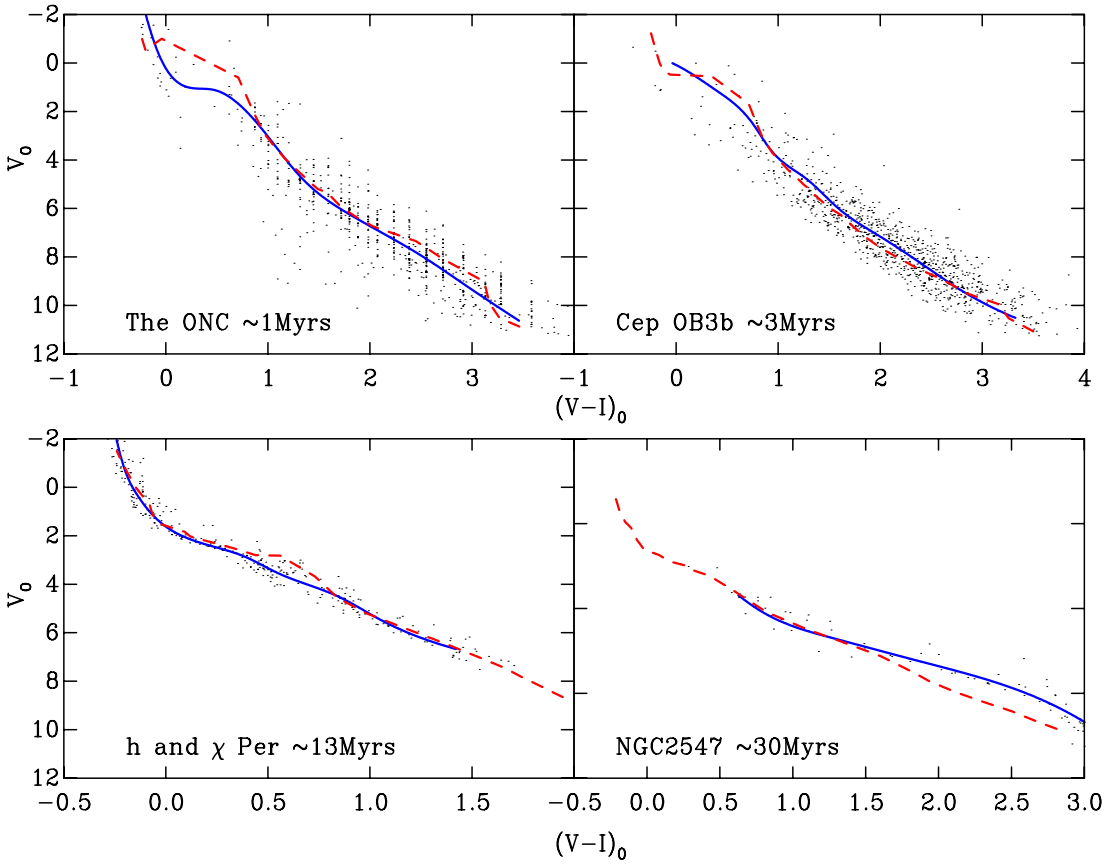

Figure 6.9: The selected members for the ONC, Cep OB3b, h and χ Per and NGC2547. The solid line is the empirical isochrone. The dashed line is the best fit isochrone (by eye) from Siess et al. (2000) ($\simeq$ 1, $\simeq$ 3, $\simeq$ 13 and $\simeq$ 16 Myrs respectively). The sequences and empirical isochrones can be seen to move away from the theoretical counterparts to varying degrees.

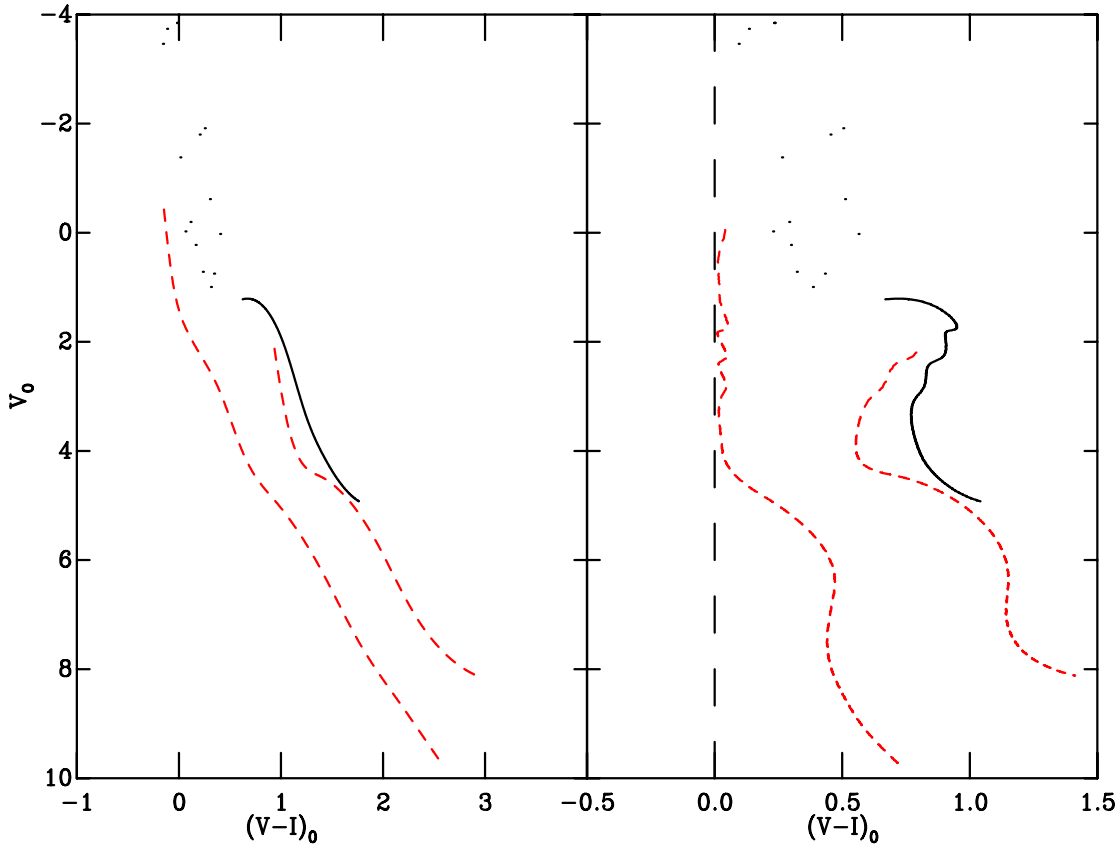

Figure 6.10: The solid line is the empirical isochrone of NGC2244, bounded by the dashed line of IC5146, with NGC1960 shown as a representative older cluster. The dots show stars in the MS section of the NGC2244 sequence, which lies redward of the empirical MS, most probably due to an underestimate of the extinction to this cluster.

to the pre-MS, or in some case the entire sequence, is shown for younger clusters. For the older sequences where the R-C gap is too small to identify, the empirical isochrones fitted to the entire sequences are shown. The age ladders for each SFR are displayed in the following sections. The fiducial empirical isochrones are displayed as dashed lines with the target isochrone plotted as a bold line and the MS members appearing as dots.

6.3.2.1 NGC2244

This cluster is the highest placed pre-MS in the age ladder meaning it is the youngest SFR modeled. The empirical isochrone of the pre-MS is shown bounded by the next youngest sequence, IC5146, with NGC1960 shown as a representative older cluster, in Figure 6.10. Figure 6.10 shows the MS points lying redward of the empirical MS. This could be explained by an underestimate of the extinction to these stars, reasonably likely as NGC2244 is an area of high and highly variable extinction. For the age ordering this is unimportant as the extinction vector lies parallel with the pre-MS in a V vs $V-I$ CMD.

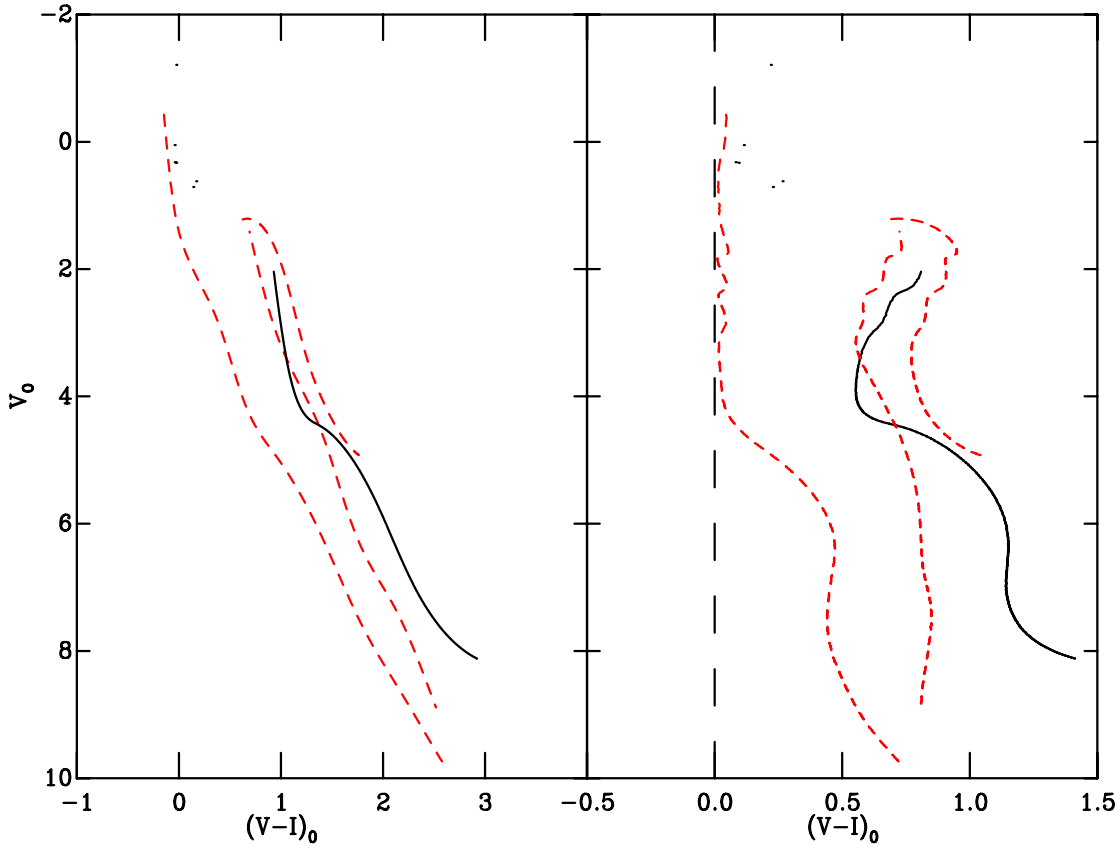

Figure 6.11: The solid line is the empirical isochrone of IC5146, bounded by the dashed lines of NGC2244 and NGC6530, with NGC1960 shown as a representative older cluster. The dots show stars in the MS section of the IC5146 sequence.

6.3.2.2 IC5146

IC5146 lies next below NGC2244 and is shown bounded by NGC2244 and NGC6530 with NGC1960 again representing an older cluster.

6.3.2.3 NGC6530

NGC6530 is the next sequence and is shown bounded by IC5146 and the ONC in Figure 6.12. Again NGC1960 is shown as a representative older cluster. Figure 6.12 shows the ONC and NGC6530 are practically coincident and certainly lie close enough for distance uncertainties (for NGC6530 and the ONC $\approx$ 0.1 mag) to make their ages indistinguishable.

6.3.2.4 The ONC

The ONC is shown in Figure 6.13 bounded by IC5146 (as NGC6530 is coincident with the ONC) and Cep OB3b. NGC1960 is included to show a representative older cluster. As can be seen in Figure 6.13 the ONC lies above Cep OB3b. However, they could be considered coincident within the given a distance uncertainty margin of 0.26 mags (with distances uncertainties of ±0.20 and

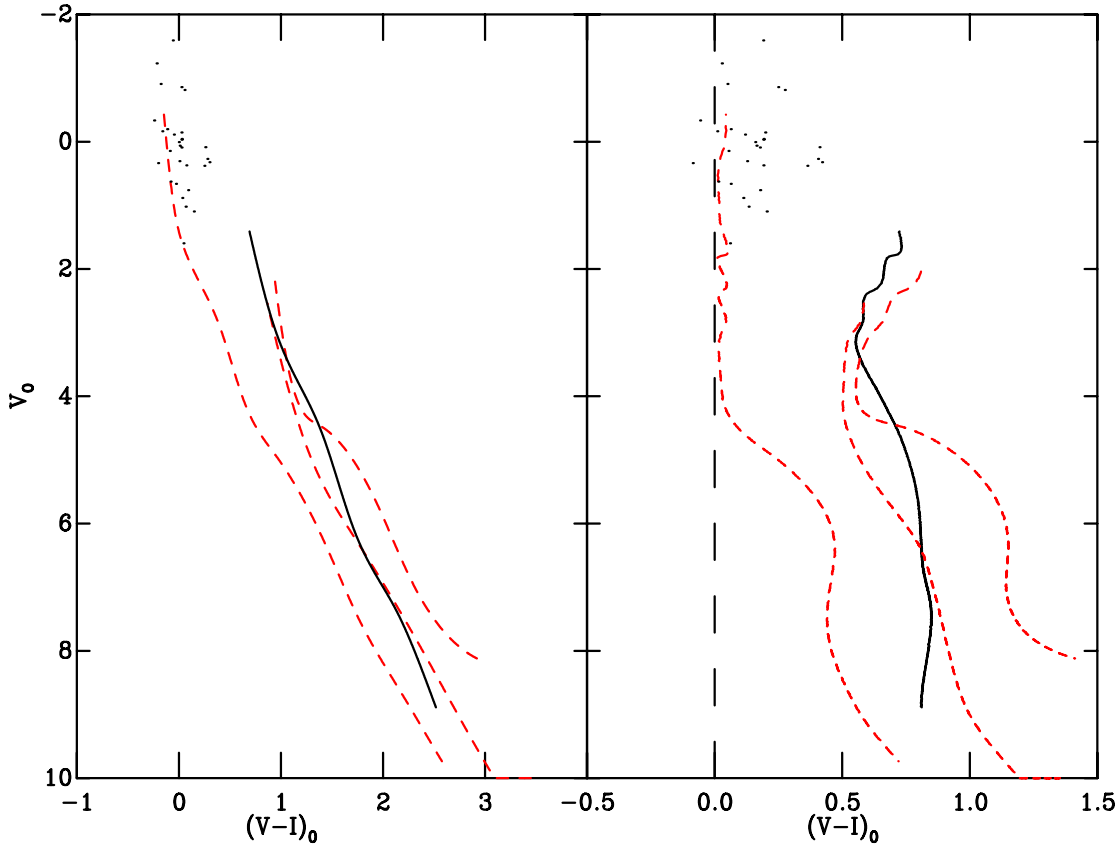

Figure 6.12: The solid line is the empirical isochrone of NGC6530, bounded by the dashed lines of IC5146 and the ONC, with NGC1960 shown as a representative older cluster. The dots show stars in the MS section of the sequence.

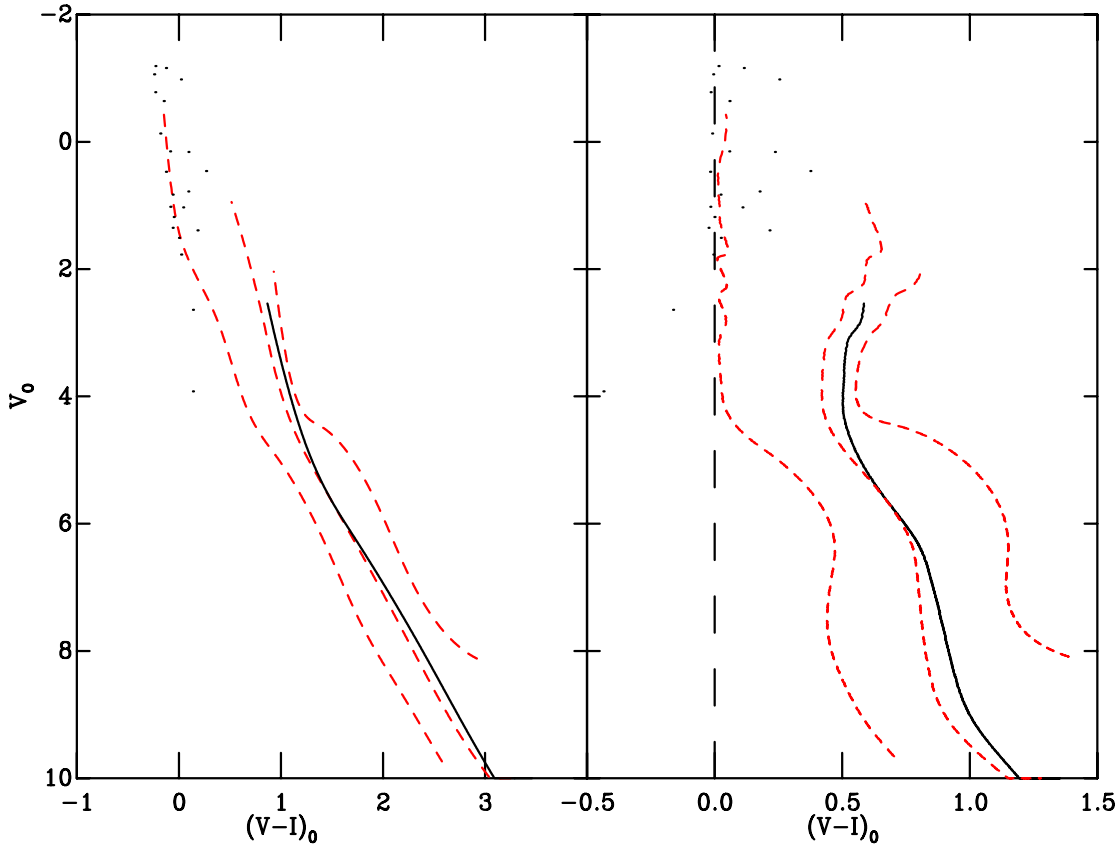

Figure 6.13: The solid line is the empirical isochrone of the ONC, bounded by the dashed lines of IC5146 and Cep OB3b, with NGC1960 showing a lower bound. The dots show stars in the MS section of the sequence.

±0.06 mag for CepOB3b and the ONC respectively). The fact that Cep OB3b can just change groups is discussed later in Section 6.3.3.

6.3.2.5 λ Ori

λ Ori is bounded by IC5146 and Cep OB3b with the representative older cluster NGC1960 in Figure 6.14. No MS photometry was available for this cluster. Figure 6.14 shows λ Ori is coincident with Cep OB3b.

6.3.2.6 Cep OB3b

Cep OB3b is shown bounded by IC5146 and NGC2264, with NGC1960 again used as a representative older cluster, in Figure 6.15. Cep OB3b and NGC2264 are coincident over most of the sequence within the distance uncertainties. In this Figure 6.15 no MS stars are present in the photometry due to saturation. Cep OB3b is discussed in Section 6.3.3, as it's large distance uncertainties allow it to move by one group.

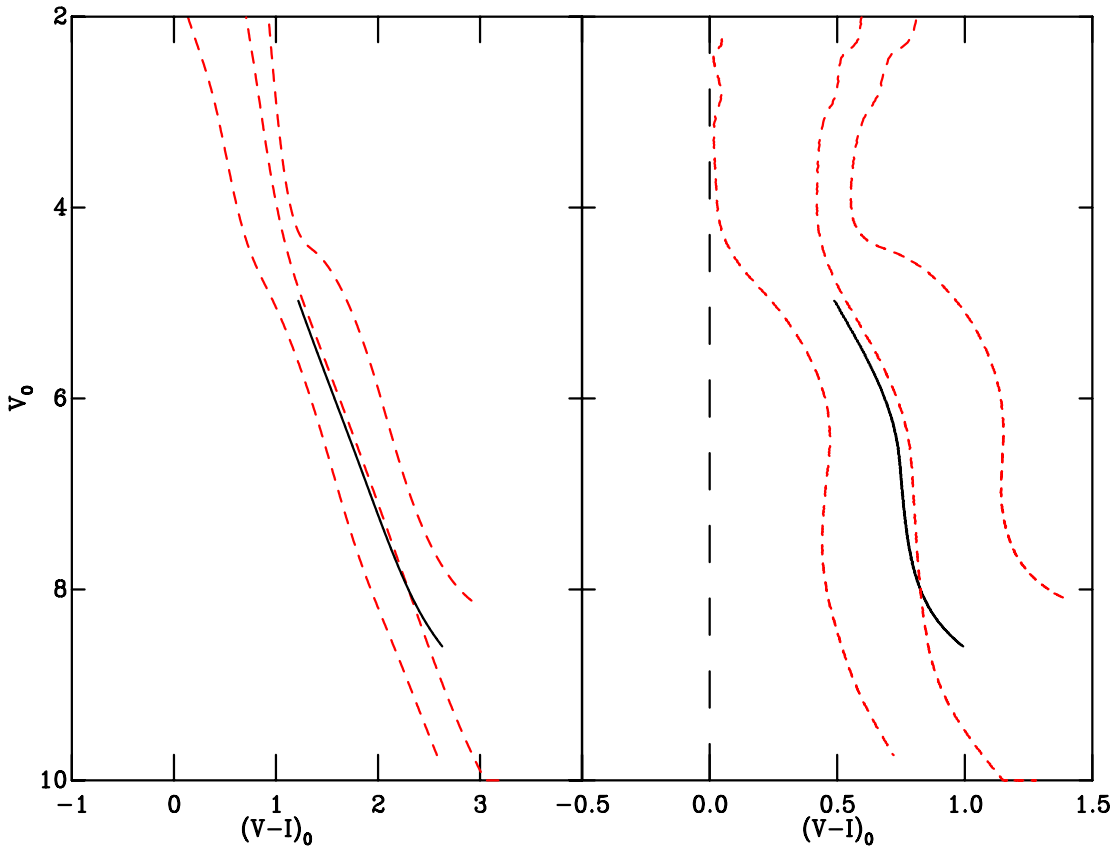

Figure 6.14: The solid line is the empirical isochrone of λ Ori, bounded by the dashed lines of IC5146 and Cep OB3b, with NGC1960 showing a representative older cluster.

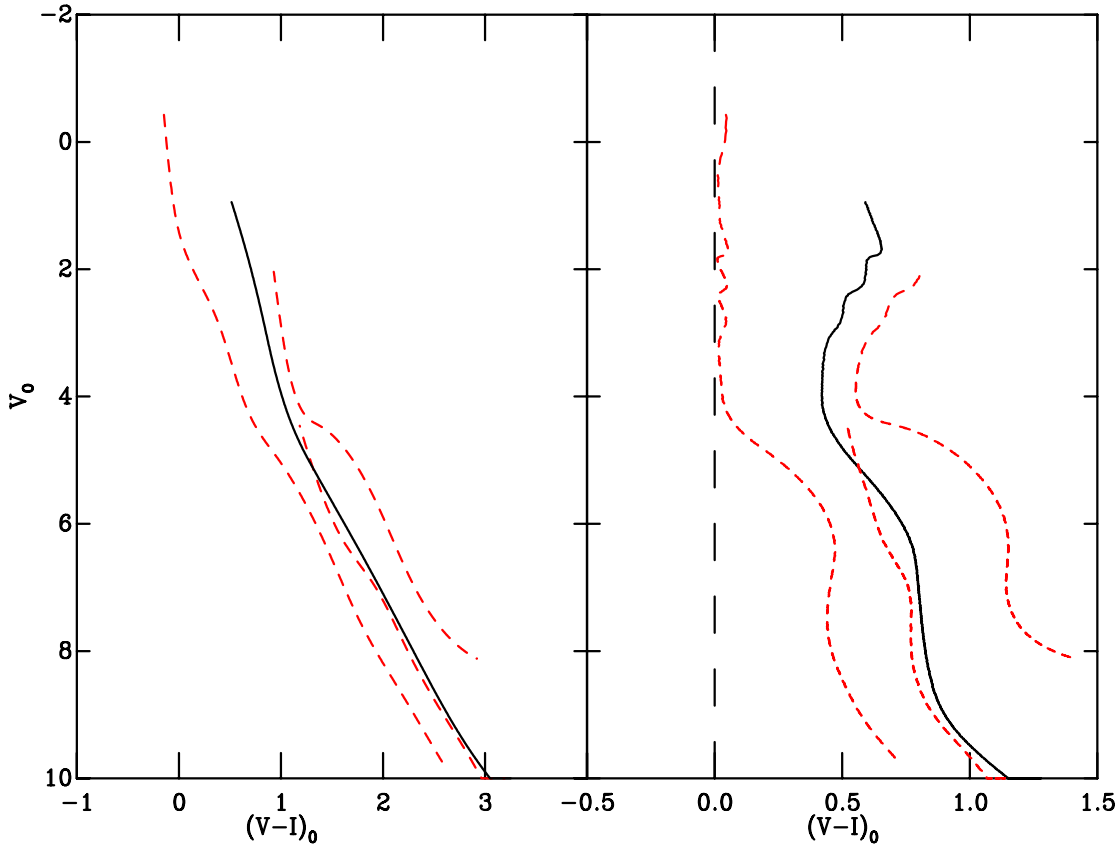

Figure 6.15: The solid line is the empirical isochrone of Cep OB3b, bounded by the dashed lines of IC5146 and NGC2264, with NGC1960 showing a representative older cluster.

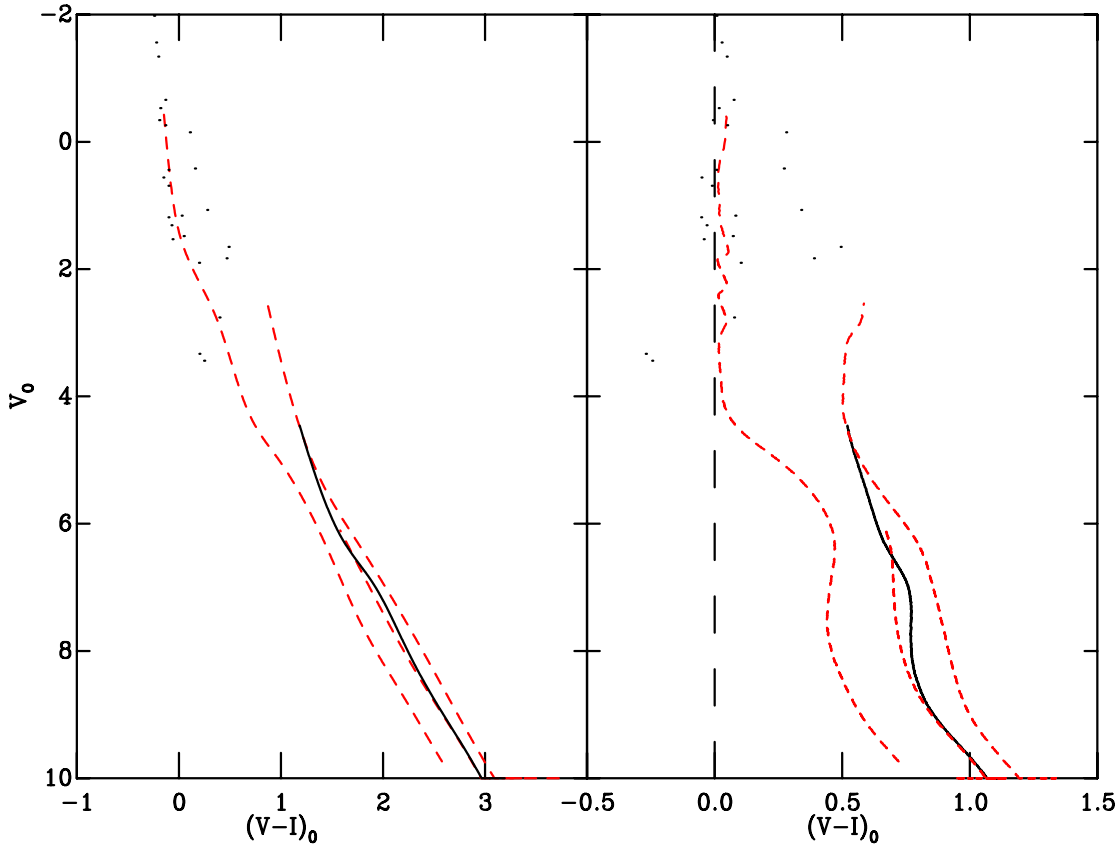

Figure 6.16: The solid line is the empirical isochrone of NGC2264, bounded by the dashed lines of the ONC and σ Ori, with NGC1960 showing a representative older cluster. The dots show stars in the MS section of the sequence.

6.3.2.7 NGC2264

NGC2264 is shown bounded by the ONC, with NGC1960 shown as a representative older cluster, in Figure 6.16. Once again the older bound provided by σ Ori in this case is coincident with NGC2264.

6.3.2.8 σ Ori

The bounds displayed with σ Ori in Figure 6.17 are provided by the ONC and NGC2362, with NGC1960 as a representative older cluster. As with Cep OB3b no MS stars are present in the photometry due to saturation. Figure 6.17 shows σ Ori just younger than NGC2362.

6.3.2.9 NGC2362

NGC2362 is shown in Figure 6.18 bounded by NGC2264 and IC348, with NGC1960 as a representative older cluster. IC348 appears coincident with NGC2362. Once again no MS stars were present in the adopted photometric catalogue.

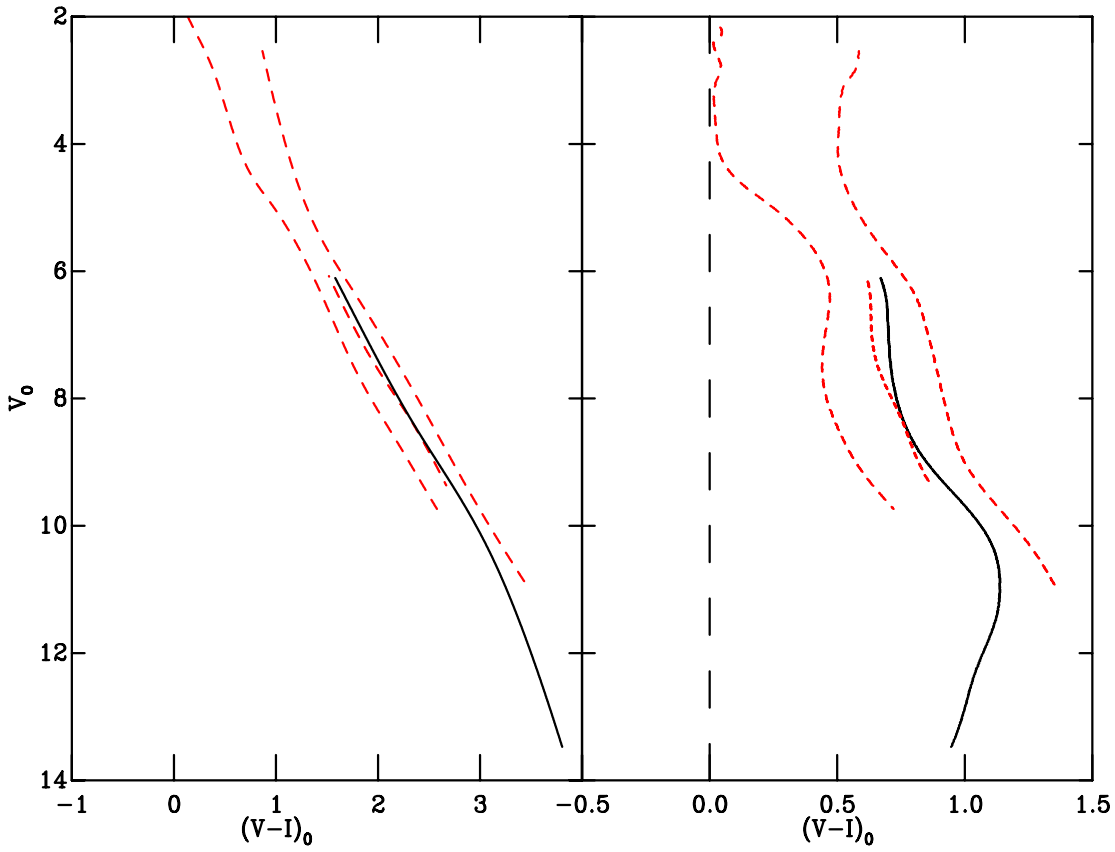

Figure 6.17: The solid line is the empirical isochrone of σ Ori, bounded by the dashed lines of the ONC and NGC2362, with NGC1960 showing a representative older cluster.

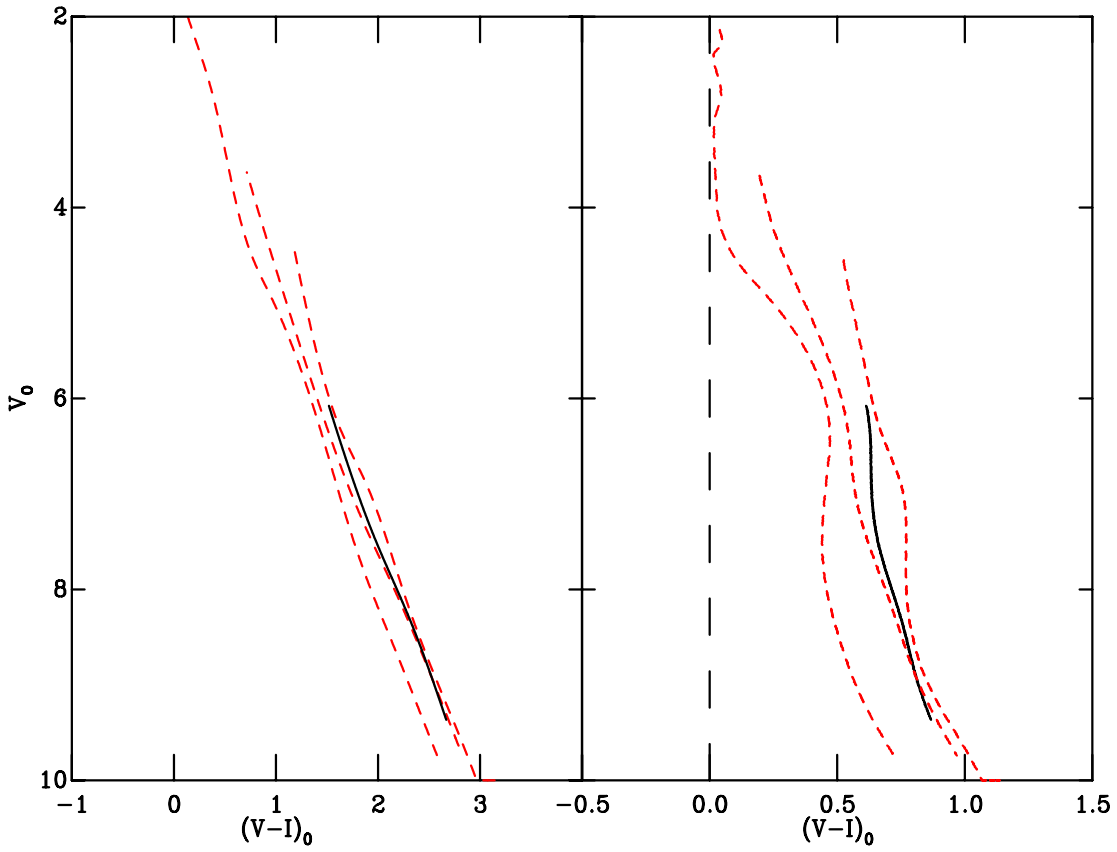

Figure 6.18: The solid line is the empirical isochrone of NGC2362, bounded by the dashed lines of NGC2264 and IC348, with NGC1960 showing a representative older cluster.

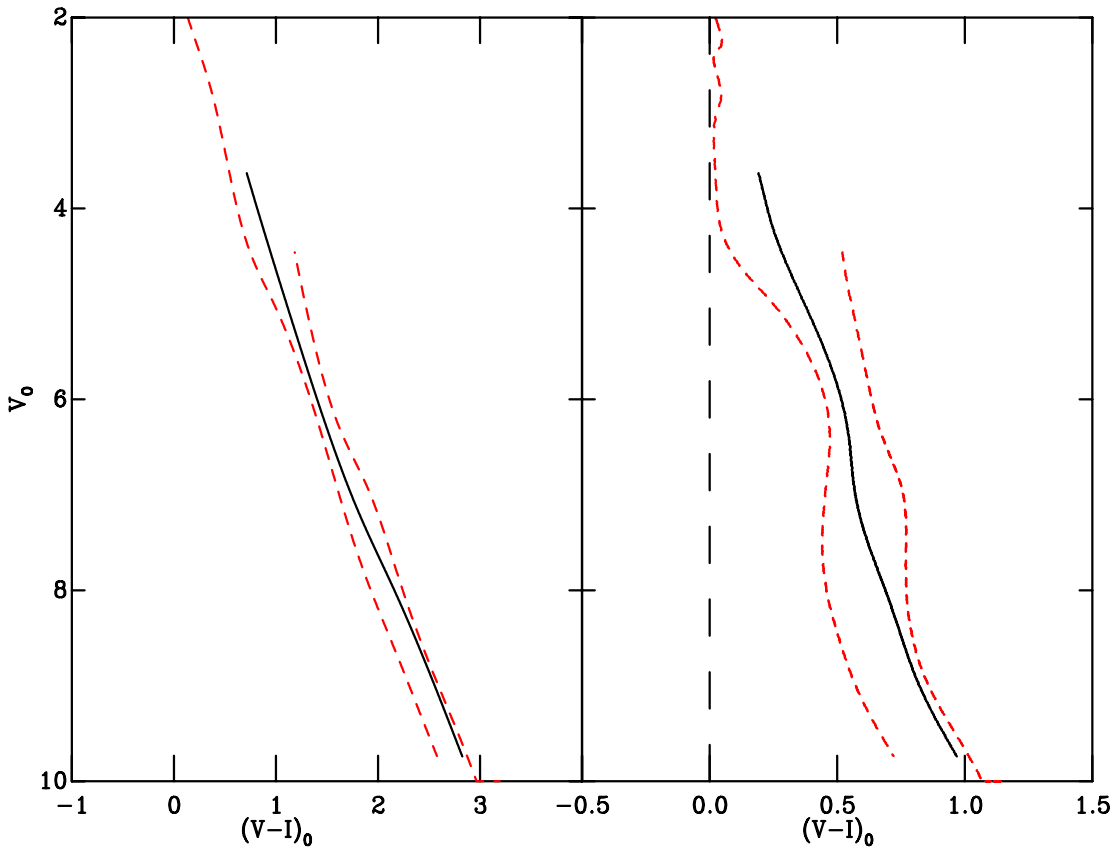

Figure 6.19: The solid line is the empirical isochrone of IC348, bounded by the dashed lines of NGC2264 and NGC1960.

6.3.2.10 IC348

Figure 6.19 shows IC348 bounded by the ONC and NGC1960. Again no MS photometry was available. NGC1960 is clearly much older than IC348.

6.3.2.11 NGC7160 and h and χ Persei

For the older clusters differences in age order are harder to define due to the bunching of isochrones with age. In addition the R-C gap is smaller and the transition across it therefore smoother for the empirical isochrones. Figure 6.20 shows the empirical isochrones of NGC7160 (solid line) bounded by h and χ Per with the ONC (both dashed lines) as a representative young cluster. These clusters are well separated with h and χ Per clearly older than NGC7160.

6.3.2.12 NGC1960 and NGC2547

The two oldest clusters in this sample are NGC1960 and NGC2547. These are shown along with the ONC in Figure 6.21.

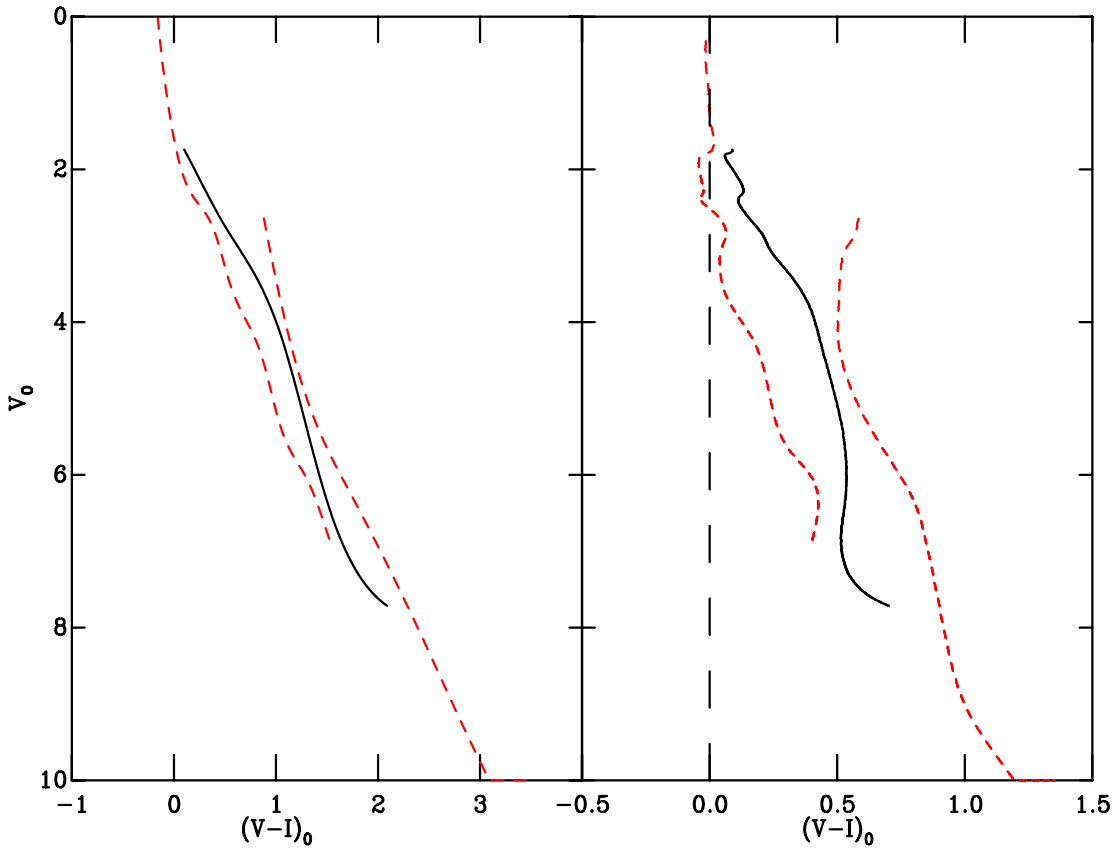

Figure 6.20: The solid line is the empirical isochrone of NGC7160, bounded by the dashed lines of the ONC and h and χ Per.

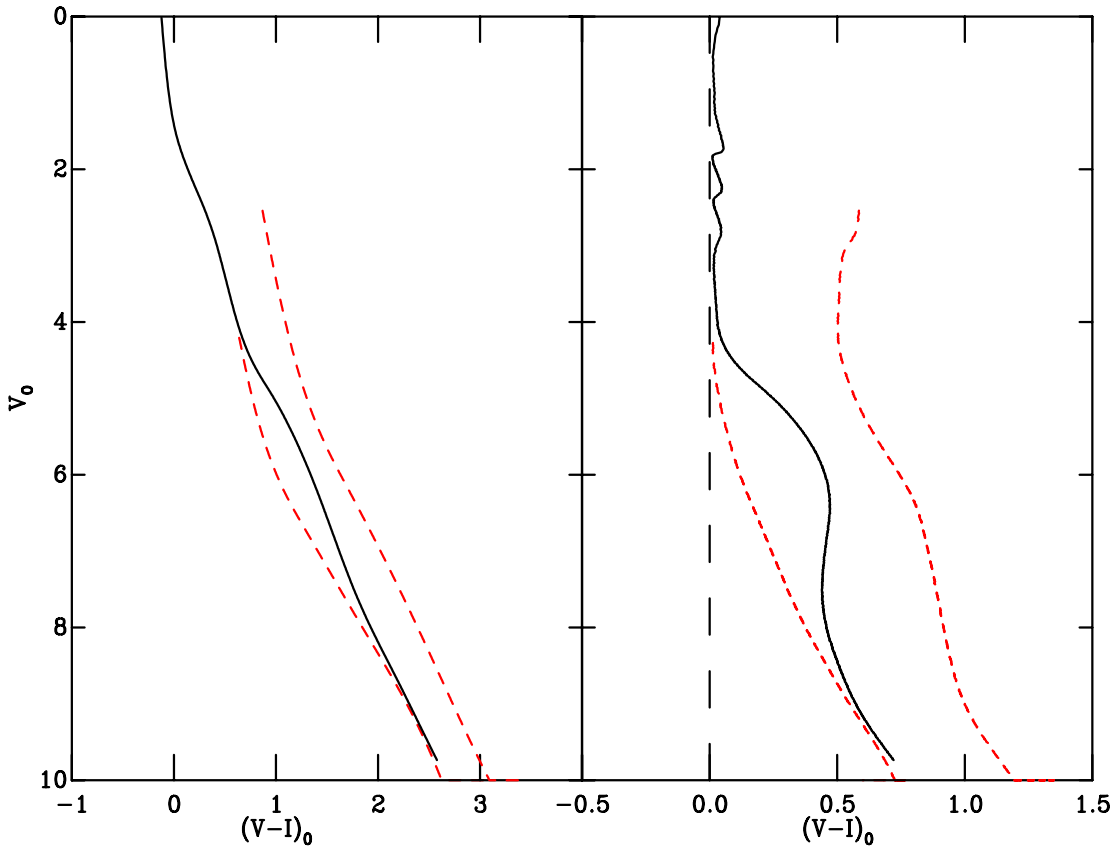

Figure 6.21: The solid line is the empirical isochrone of NGC1960, bounded by the dashed lines of the ONC and NGC2547.

6.3.3 Age groups

From the previous sections it is clear that some empirical isochrones are well separated whilst others appear coincident. In order to separate the SFRs into distinguishable groups the effect of the uncertainties of the derived distance to each SFR must be examined. Uncertainties in extinction are less important than those in distance, as in a V vs $V-I$ CMD the extinction vector lies approximately parallel to the pre-MS. The age groupings can be arranged from the age ladders in the previous sections and the sequence with the largest distance uncertainties from each group used to examine possible differences in age grouping. The distance uncertainties are taken from Chapter 4, in particular Table 4.11. In the cases where new distances could not be derived and literature distances have been adopted without quoted uncertainties, a generous uncertainty budget of ±0.2 mag is adopted. The empirical isochrones, after application of the best fit distances, group as follows (in ascending order of age):

1. NGC2244 and IC5146.
2. NGC6530 and the ONC.
3. λ Ori, Cep OB3b, NGC2264 and σ Ori.
4. NGC2362 and IC348.
5. NGC7160.
6. h and χ Per.
7. NGC1960.
8. NGC2547.

The SFRs with the largest uncertainties in distance modulus are IC5146 with $\pm \approx 0.2$ mags, the ONC $^{+0.07}_{-0.05}$ mags, Cep OB3b with ±0.20 mags and IC348 with $^{+0.14}_{-0.16}$ mags. The distance modulus uncertainties for Cep OB3b and IC5146, are almost a factor two larger than the next largest distance uncertainty (see Table 4.11). Therefore, these two SFRs, Cep OB3b and IC5146, can be used to test how robust the assigned groups are. Figures 6.22 and 6.23 show the effect on the age groups after consideration of the distance uncertainties of Cep OB3b and IC5146. Figures 6.22 and 6.23 show that even using the largest combined distance uncertainty budget from the two worst case SFRs, only Cep OB3b changes by just one group. Therefore, it is clear that for the worst distance uncertainties the assigned groups are robust.

6.3.4 Comparison with literature ages

Now the age groupings of the SFRs have been shown to be robust, a nominal age can be assigned to each group. It would be desirable to calibrate the age ladder using the distance independent age indicating properties of the R-C gap (discussed in Section 6.2) and this possibility is discussed in Chapter 7. For the moment however well established literature ages are used to assign nominal ages, with the younger groups separated by only one Myr.

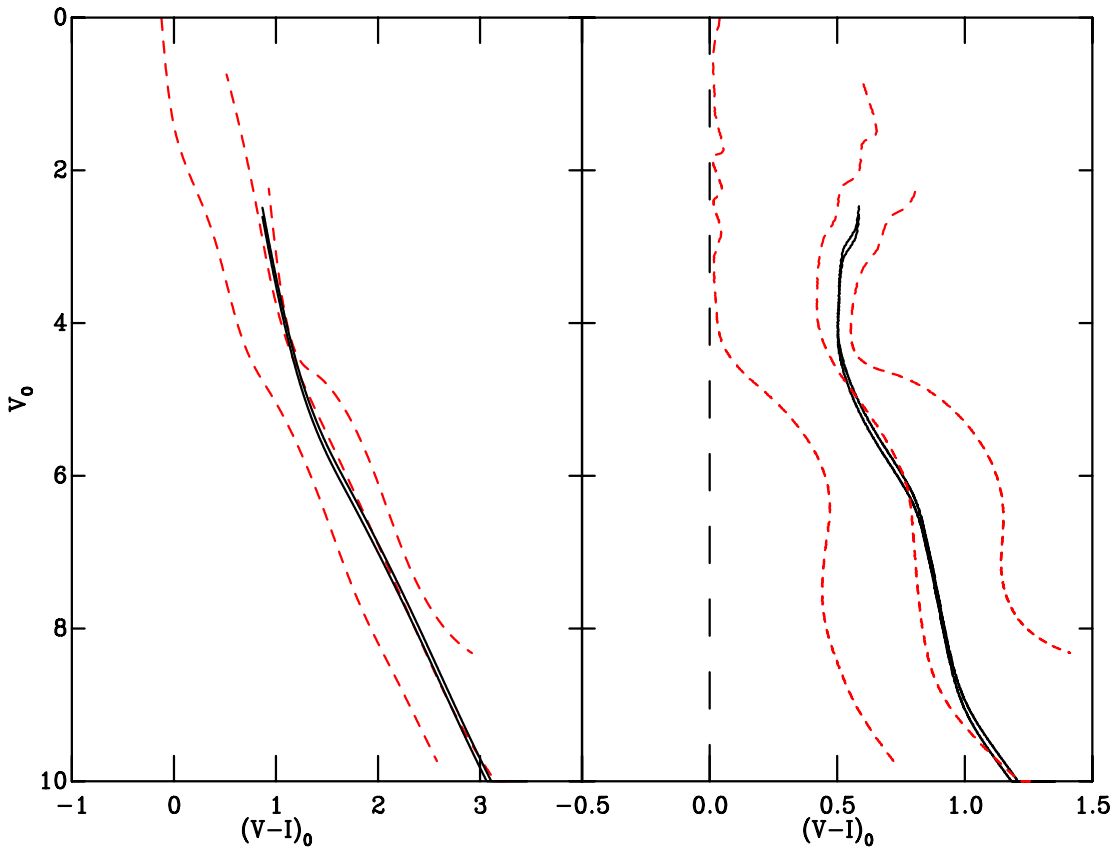

Figure 6.22: The solid lines are the empirical isochrone of the ONC at the largest and smallest distance modulus. The two bounding dashed lines are that of IC5146 at it's closest distance and Cep OB3b at it's farthest distance. The lowest dashed line shows the NGC1960 as a representative older cluster. Even using the SFRs with the most uncertain distances, which are twice that of any other, only Cep OB3b just changes by one group.

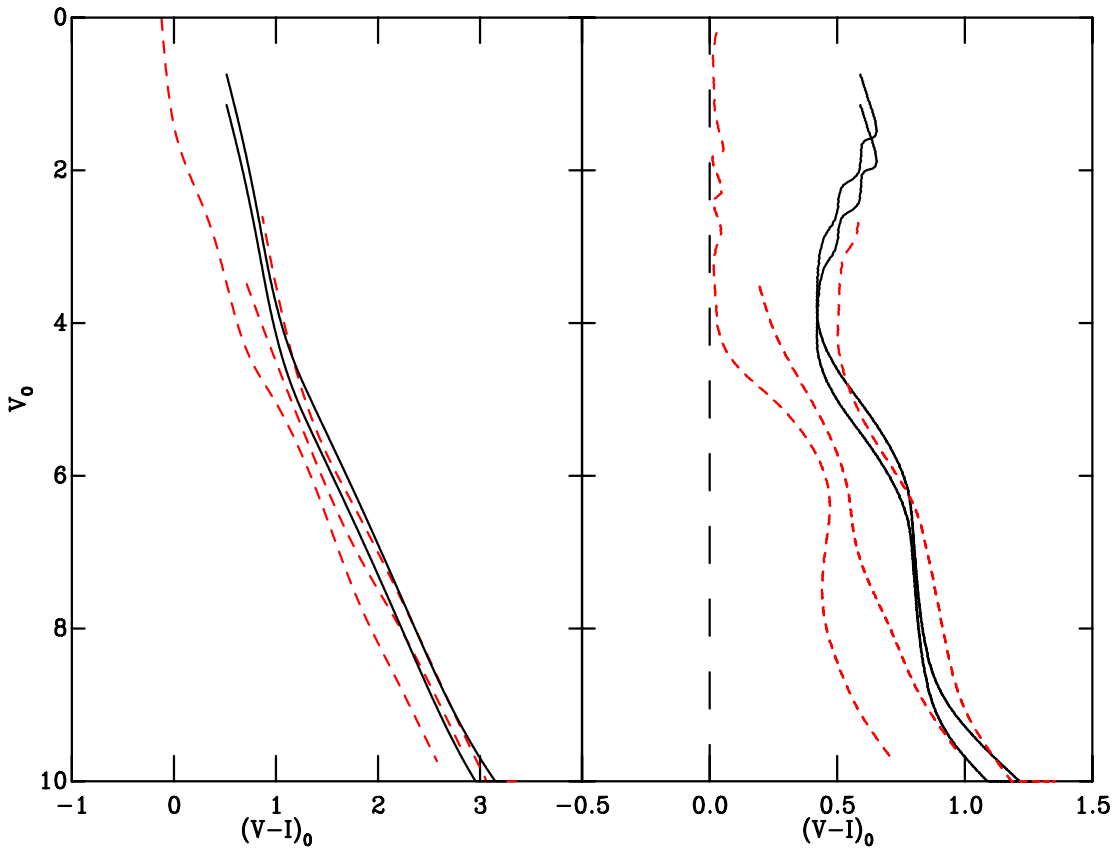

Figure 6.23: The solid lines are the empirical isochrone of Cep OB3 at the largest and smallest distance modulus. The two bounding dashed lines are that of the ONC at its closest distance and IC348 at its farthest distance. The lowest dashed line shows the NGC1960 as a representative older cluster. Again even using the SFRs with the most uncertain distances, which are twice that of any other, only Cep OB3b changes by just one group.

The ages of NGC2264 and h and χ Per are sufficient to assign nominal ages. The age of NGC2264 is adopted as ≈ 3 Myrs (Sung et al., 1997; Park et al., 2000; Lamm et al., 2004; Dahm & Simon, 2005) and ≈ 13 Myrs is adopted for h and χ Per (Keller et al., 2001; Capilla & Fabregat, 2002; Slesnick et al., 2002). The resulting nominal ages are then: NGC2244 and IC5146 ≈ 1 Myrs; NGC6530 and the ONC ≈ 2 Myrs; λ Ori, Cep OB3b, NGC2264 and σ Ori ≈ 3 Myrs; NGC2362 and IC348 $\approx 4-5$ Myrs (as there is no older bound); NGC7160 ≈ 10 Myrs; h and χ Per ≈ 13 Myrs; NGC1960 ≈ 20 Myrs and NGC2547 ≈ 40 Myrs. It is interesting to compare these nominal ages with age estimates from the literature. Many of the age differences are a direct result of the new distances derived in Chapter 4 e.g. the ONC.

6.3.4.1 Nominal age of ≈ 1 Myr

6.3.4.1.1 NGC2244 The nominal age derived here is somewhat younger than the majority of the literature derivations. Turner (1976) finds a distance modulus of 11.01 ± 0.09 mags and an age of a few million years from the MS turn-off. The same method is used by many authors, deriving or adopting ages and distance moduli of; 4 Myrs and 10.76 mags (Ogura & Ishida, 1981); 1.4 and 8.8 Myrs and 11.11 mags (Perez et al., 1989); $1.45-3.63$ Myrs using 11.11 mags (Pérez, 1991); $1-3$ Myrs and 11.37 ± 0.1 z(Massey et al., 1995) and 1.9 Myrs and 11.1 mags (Park & Sung, 2002). Most of these derivations are slightly older than the possible age range allowed in this thesis (1 ± 1 Myrs). This could be caused by several factors. Firstly turn-off ages are only based on a few stars at most (see Section 3.6.2.1), whereas the age order derived here is based on many stars. Also, as this region has large and very variable extinction, many of these studies adopted the Q-method to derive absolute colours and magnitudes of stars. As discussed in Section 4.6.3 of Chapter 4 this method has several associated problems. Finally and perhaps most crucially the distance modulus used in most of these studies is much larger than that found in Chapter 4 ($10.77^{+0.04}_{-0.11}$ mags). This new distance, as discussed in Section 4.9.1.4, is supported by the result of Hensberge et al. (2000) derived using eclipsing binaries; it must be noted however that Hensberge et al. (2000) derive an age of 2.3 ± 0.2 Myrs.

6.3.4.1.2 IC5146 The nominal age for this cluster is in line with previous derivations. The median age found by Herbig & Dahm (2002) is $\simeq 1$ Myr, agreeing with our result.

6.3.4.2 Nominal age of ≈ 2 Myrs

6.3.4.2.1 The ONC Almost all previous studies of this cluster adopted the distance of Genzel et al. (1981), which is much more distant than that derived in Chapter 4 . This fall in distance modulus (≈ 0.4 mag) can account for the difference of the nominal age of 2 ± 1 Myrs with previous lower ages such as 0.8 Myrs derived in Hillenbrand (1997). The new distance is discussed in detail in Section 4.9.1.1.

6.3.4.2.2 NGC6530 Prisinzano et al. (2005) use the isochrones of Siess et al. (2000) fitted to pre-MS stars to obtain a median age of 2.3 Myrs. Sung et al. (2000) find an age of 1.5 Myrs from fitting isochrones to an Hα selected pre-MS after conversion to an H-R diagram. Damiani et al.

(2004), using X-ray selection and the photometry of Sung et al. (2000) find an age of 0.5-1.5 Myrs. Therefore, the nominal age of 2 ± 1 Myrs is largely consistent with literature derivations.

6.3.4.3 Nominal age of ≈ 3 Myrs

6.3.4.3.1 λ Ori The nominal age derived here of 3 ± 1 Myrs is certainly consistent with the MS turn-off age of 4 Myrs derived from UBV photometry by Murdin & Penston (1977) but not with the age of 6-7 Myrs derived by Dolan & Mathieu (2001) using narrow band photometry of high mass stars. The age derived here is consistent with that of Balona & Laney (1996) who derive a turn-off age of 5 ± 1 Myrs.

6.3.4.3.2 Cep OB3b The best previous age estimate for this subgroup is Jordi et al. (1996) at 5.5 Myrs. The older estimate would have made Cep OB3b the oldest group to contain molecular material. Therefore the lower nominal age of 3 ± 1 Myrs is more likely. In addition the photometry shown in Figure 5.4 reveals evidence for an R-C gap at the head of the pre-MS in a position similar to that of NGC2264 at an age of $\simeq 3$ Myrs, also suggesting a similar age for the two groups.

6.3.4.3.3 NGC2264 This cluster has been chosen as a fiducial and therefore it's nominal relative age necessarily agrees with the literature results.

6.3.4.3.4 σ Ori The nominal age of 3 ± 1 Myrs is in agreement with the age of 2.5 ± 0.3 Myrs of Sherry et al. (2000). This is suprising given the discrepancy in distance modulus of almost 0.3 mags between that adopted in Sherry et al. (2000), (≈ 8.22 mags), and that derived in Chapter 4. The distance modulus of $7.94^{+0.16}_{-0.10}$ mags derived in Chapter 4 agrees with the distance of Caballero (2007) (as discussed in Section 4.9.1.2), which is unsurprising as the same data are used.

6.3.4.4 Nominal age of $\approx 4-5$ Myrs

6.3.4.4.1 IC348 The nominal age of $4-5$ Myrs contrasts with the literature age of 2-3 Myrs (e.g. Haisch et al., 2001). To obtain an age of 3 Myrs or less would require a shift of $\simeq 0.5$ mags in the distance modulus, yet the uncertainties in the distance to IC348 are significantly smaller than this, $-0.16/+0.14$ mag.

6.3.4.4.2 NGC2362 The nominal age for NGC2362 of $4-5$ Myrs is not consistent with the ages derived by Dahm (2005) of $\simeq$1.8 Myrs using the isochrones of D'Antona & Mazzitelli (1997). This new age is however consistent with an age of 3.5-5 Myrs from Dahm (2005) derived using the isochrones of Baraffe et al. (1998). However, the shift in distance to achieve an age of less than 1.8 Myrs would be $\simeq 0.4$ mags; larger than the typical distance modulus uncertainty.

6.3.4.5 Older SFRs

For the older SFRs the nominal ages are more difficult to assign. This is due to the bunching of the iosochrones with age meaning that their separation in magnitude is smaller. Practically this means that the bounding isochrones cannot provide useful uncertainties on their ages. However,

the exact ages of these older SFRs are of less consequence than their younger counterparts in this study. Therefore, for these older clusters literature ages are adopted.

6.3.4.5.1 NGC7160 NGC7160 has an age estimate of $\simeq$ 10 Myrs from isochrone fitting from Sicilia-Aguilar et al. (2005), this age is adopted.

6.3.4.5.2 h and χ Persei These clusters are used as fiducial clusters to calibrate the age scale for the age ladder. Therefore, the literature age of $\simeq$ 13 Myrs is adopted.

6.3.4.5.3 NGC1960 Sanner et al. (2000) find an age of $\approx 16-25$ Myrs from isochrone fitting. Using the MS section of the sequence Sanner et al. (2000) adopt an age of 16 Myrs. Due to the large uncertainties for this a cluster a representative age of 20 Myrs is adopted.

6.3.4.5.4 NGC2547 This is the oldest cluster studied in this thesis. NGC2547 has age estimates varying from 30-45 Myrs from pre-MS isochrone fitting in Naylor et al. (2002) and the Lithium Depletion Boundary in Jeffries & Oliveira (2005). Naylor & Jeffries (2006) provide a more recent and more precise derivation of the age of NGC2547 deriving an age of $38.5^{+3.5}_{-6.5}$ Myrs by fitting pre-MS isochrones using the τ^2 fitting technique. Here a representative age of 40 Myrs is adopted.

6.3.5 Summary

In this Section the empirical isochrones generated in Chapter 5 have been adjusted to intrinsic colour and absolute magnitude space using the parameters from Chapter 4. Using these empirical isochrones the sequences have been separated into age groups and nominal ages assigned to each group. These nominal ages have been assigned using the literature ages of two sequences, NGC2264 and the combined h and χ Per. These resulting nominal ages compare favourably to literature ages and any discrepancies have been discussed. Thus, the resulting ages for each SFR to be adopted for further study are:

- 1 Myr, NGC2244 and IC5146.
- 2 Myrs, NGC6530 and the ONC.
- 3 Myrs, λ Ori, Cep OB3b, NGC2264 and σ Ori.
- $4-5$ Myrs, NGC2362 and IC348.
- 10 Myrs, NGC7160.
- 13 Myrs, h and χ Per.
- 20 Myrs, NGC1960.
- 40 Myrs, NGC2547.

6.4 Secular Evolution

In the previous section a self-consistent set of age orders and nominal ages have been assigned to a range of SFRs, these have been calibrated to an absolute age scale using some fiducial clusters. In this Section the implications of these nominal ages on the current theories of stellar evolution after the addition of ancillary data are discussed.

6.4.1 Rotational period distributions

As discussed in Chapter 2 an important area of stellar evolution is that of gyrochronology or the evolution of the rotation rates of, in particular, pre-MS stars.

The consequences of the revised ages of IC348, NGC2264, NGC2362 and the ONC are particularly pertinent to recent studies in this area. Large-sample rotation studies now exist for a subset of young clusters and from these a conventional view of the rotational evolution of stars between 1 and 5 Myrs is developing, which is discussed in Chapter 2. Following the discussion in Chapter 2 and studies such as Littlefair et al. (2005), the evolution (in rotational period distribution) is most apparent for those stars with $M > 0.25M_{\odot}$, using the isochrones of D'Antona & Mazzitelli (1997) (which is approximately equivalent to $M = 0.4M_{\odot}$ using the isochrones of Siess et al., 2000). Stars below this mass range do not show the expected evolution [1] and as therefore the discussion here is limited to this mass range. The rotational period distribution of the ONC is strongly bi-modal as shown in Figure 6.24 taken from Figure 10 in Littlefair et al. (2005). This distribution is believed to evolve into a uni-modal distribution such as that of NGC2264 and NGC2362. The period distribution for NGC2264 is shown in Figure 6.25 taken from Figure 10 in Littlefair et al. (2005). IC348 has a distribution of rotation rates similar to that of the ONC, as shown in Figure 6.26 taken from Figure 10 of Littlefair et al. (2005), and yet it is found to be older than NGC2264. This clearly raises a concern for the universality of any evolutionary model. This indicates that some further effect could regulate the evolution of rotation rates in pre-MS stars. As discussed in Chapter 2 one possible mechanism is disc-locking, a magnetically driven star-disc interaction which can regulate the angular momentum of the central star. IC348 appearing out of sequence suggests that if disc-locking is important its effect is dependent on environment.

6.4.2 Disc dissipation

If one assumes that the rotation periods of pre-MS stars can be regulated by their discs over different timescales. Then, the lifetimes of discs in different SFRs should be different, and indeed a similar sequence should show IC348 out of sequence.

Haisch et al. (2001) plot the fraction of JHKL excess sources, which as discussed in Chapters 2 and 3 can be used to infer a disc fraction, as a function of age for different clusters or groups. This plot reveals a clear decrease in the inferred disc fraction with time. However, given the new

[1] There is no clear reason as to why the periods of rotation of low-mass stars do not evole in a similar way to their intermediate- and high- mass counterparts. Some confusion is caused by the specific mass at which this transistion occurs, which is different for different isochrones. It is possible that the shift in evolutionary behaviour is due to a change in the topology of the magnetic field as is observed across the R-C gap (see Saunders et al, in prep). This could be the cause of the imperfect disc locking suggested for these stars (see Dicussion in Chapter 2 Section 2.5.1.2.2.

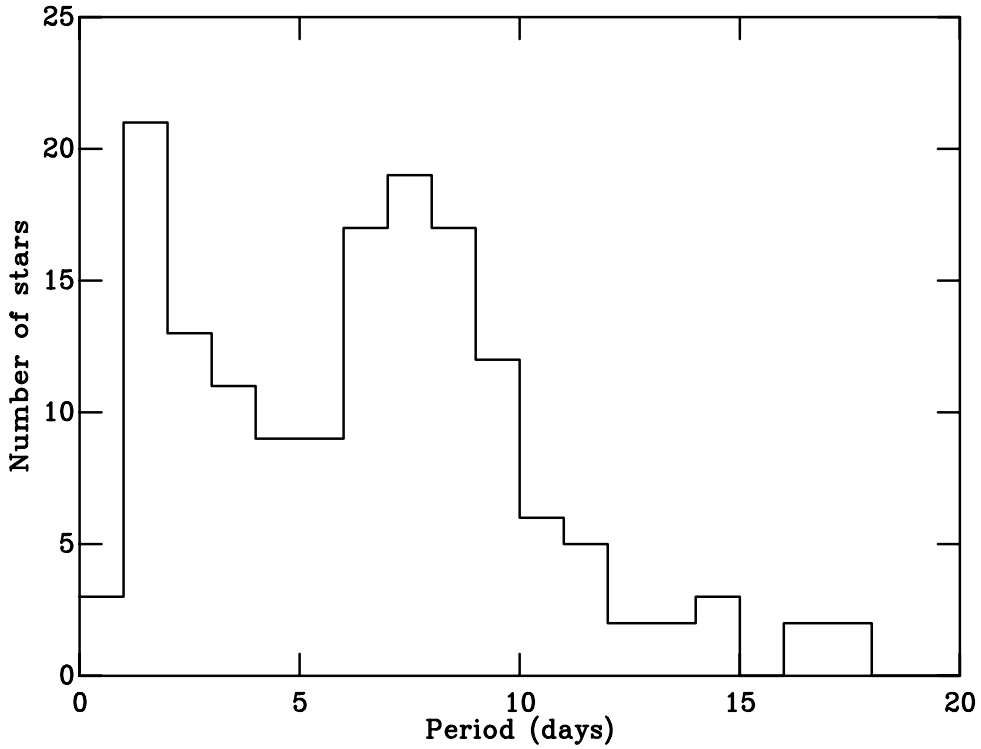

Figure 6.24: Distribution of rotation periods for stars with $M > 0.25 M_{\odot}$ in the ONC. The distribution is clearly bi-modal. This figure has been adpated from Figure 10 in Littlefair et al. (2005).

nominal ages two clusters, IC348 and NGC2264, should be relocated within this plot leading to a change in the finer structure of the trend at younger ages. The disc fractions for the ONC, IC348, NGC2264 and NGC2362 are $\simeq$ 80%, $\simeq$ 65%, $\simeq$ 52% and $\simeq$ 12% respectively from Haisch et al. (2001). The age order of these four clusters found in this work (youngest to oldest) is the ONC, NGC2264, NGC2362 and IC348. Therefore they do not show a secular decline in disc fraction.

For some of the SFRs studied more recent data are available with which to measure the fraction of stars with discs. Table 6.1 shows the SFR, the nominal age assigned to it, the fraction of stars with IR excess and the literature sources. Using the updated disc fractions and nominal ages from Table 6.1 one can examine the evolution of these discs, as in Haisch et al. (2001). Figure 6.28 shows the nominal ages for the SFRs from Table 6.1 and the inferred fraction of stars with discs. Figure 6.29 is the same plot displayed with a log(nominal age) axis. The disc fractions inferred from the data in Table 6.1 however will come from different mass ranges, dependent on the magnitude range (and therefore distance) of a given SFR. Additionally, the excess criteria used are different, with studies such as Hernández et al. (2007) using the Spitzer Space Telescope IRAC and MIPS camera channels, whereas disc fractions in Haisch et al. (2001) were calculated using *JHKL* excesses. Finally, *L* band excess surveys are usually centred around the central and youngest regions of a cluster, meaning the disc fraction would usually be biased towards higher values. This bias is generally applicable to most of these clusters however and could also be negated as the central regions of these young clusters usually contain higher ionising flux.

Therefore, given the heterogeneous nature of these data, strong conclusions cannot be

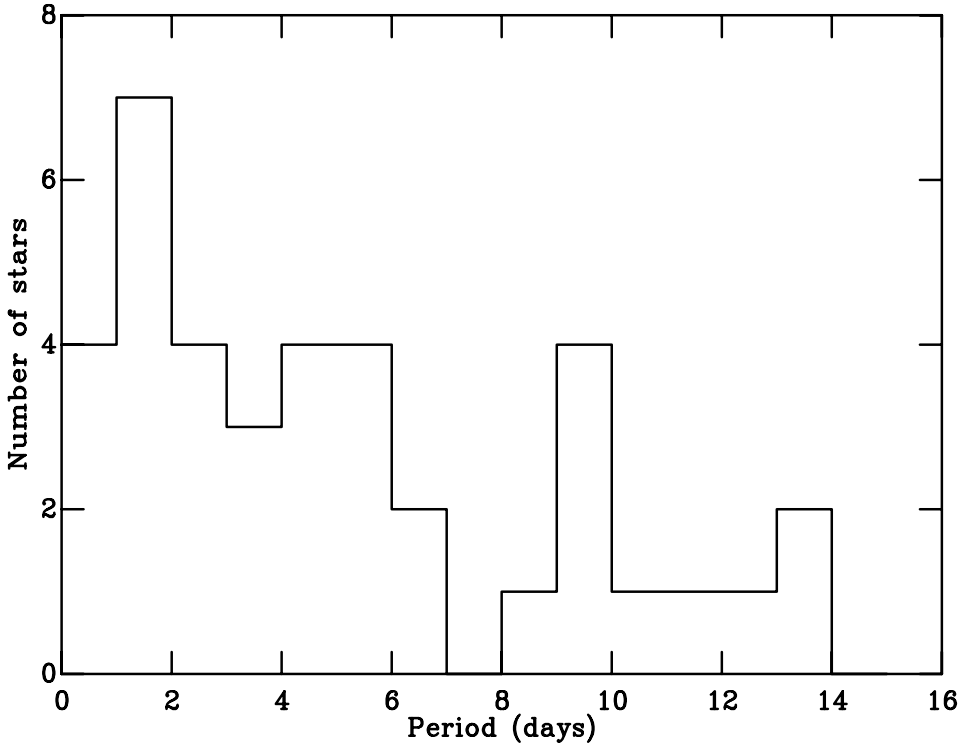

Figure 6.25: Distribution of rotation periods for stars with $M > 0.25 M_{\odot}$ in NGC2264. The distribution is not bi-modal and appears different from the distribution found for the ONC. This figure has been adpated from Figure 10 in Littlefair et al. (2005).

SFR	Nominal age	Fraction of stars with IR excess
NGC6530	2	$44\%^{(7)}$
the ONC	2	$80 \pm 5\%^{(1)}$
λ Ori	3	$\approx 25\%, \approx 14\%, \approx 31\%^{(6)}$
NGC2264	3	$52 \pm 10\%^{(1)}$
σ Ori	3	$31.1 \pm 3.8\%$, $26.6 \pm 2.8\%$ and $33.9 \pm 3.1\%^{(2)}$
NGC2362	4-5	$12 \pm 4\%^{(1)}, 7 \pm 2\%^{(3)}$
IC348	4-5	$65 \pm 8\%^{(1)}$
NGC7160	10	$\approx 20\%^{(4)}$
h and χ Per	13	$2-3\%^{(8)}$
NGC1960	20	$3 \pm 3\%^{(1)}$
NGC2547	38	$\approx 7\%^{(5)}$

Table 6.1: The new nominal ages and the fraction of stars with IR excesses. The notes are as follows. (1) Haisch et al. (2001). (2) Hernández et al. (2007). First value for TTS stars (approximate mass range $1-0.1 M_{\odot}$). Second and third values for entire sample, first thick discs and secondly thick and evolved discs. (3) Dahm & Hillenbrand (2007). (4) Sicilia-Aguilar et al. (2005). (5) Young et al. (2004). (6) Barrado y Navascués et al. (2007). First value derived from the IRAC CCD, with the second and third from spectral-energy distribution (SED) fitting (thick discs then thin and thick discs combined) all in the approximate mass range $0.1-1.0 M_{\odot}$. (7) Prisinzano et al. (2007). (8) Currie et al. (2007) for h and χ Per stars fainter than J=13.5, stars brighter than this have 0% disc fraction. It is important to note that each of these studies is over a different mass range (due to different distances and magnitude ranges) and excess candidates were selected in a heterogeneous fashion.

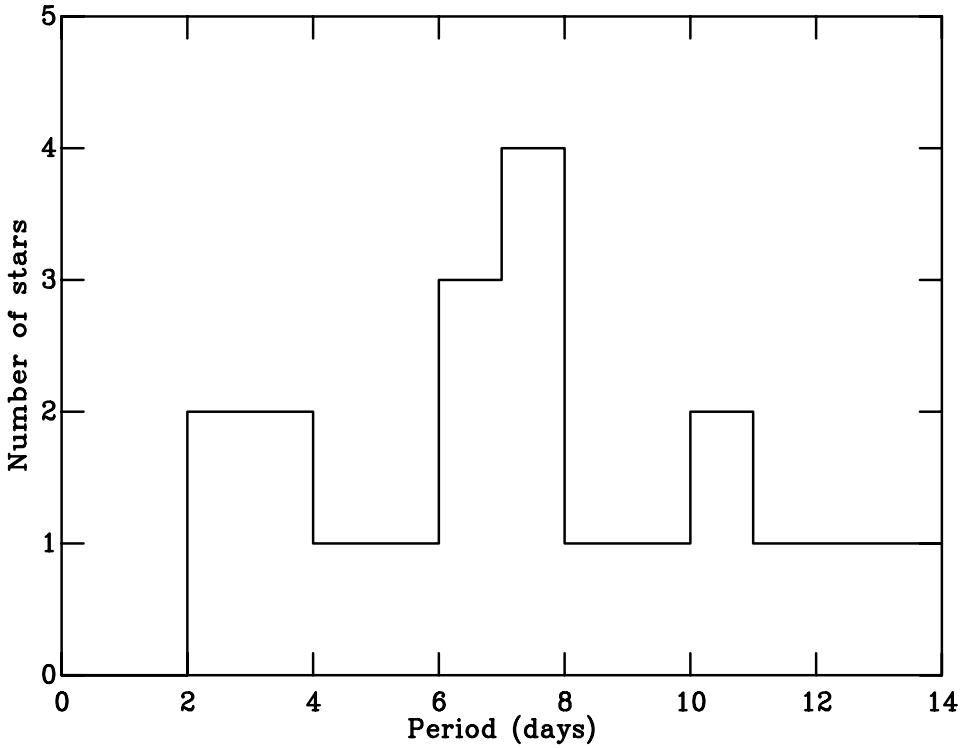

Figure 6.26: Distribution of rotation periods for stars with $M > 0.25 M_{\odot}$ in IC348. The distribution is more like that shown in Figure 6.24 than that in Figure 6.25. This figure has been adpated from Figure 10 in Littlefair et al. (2005)

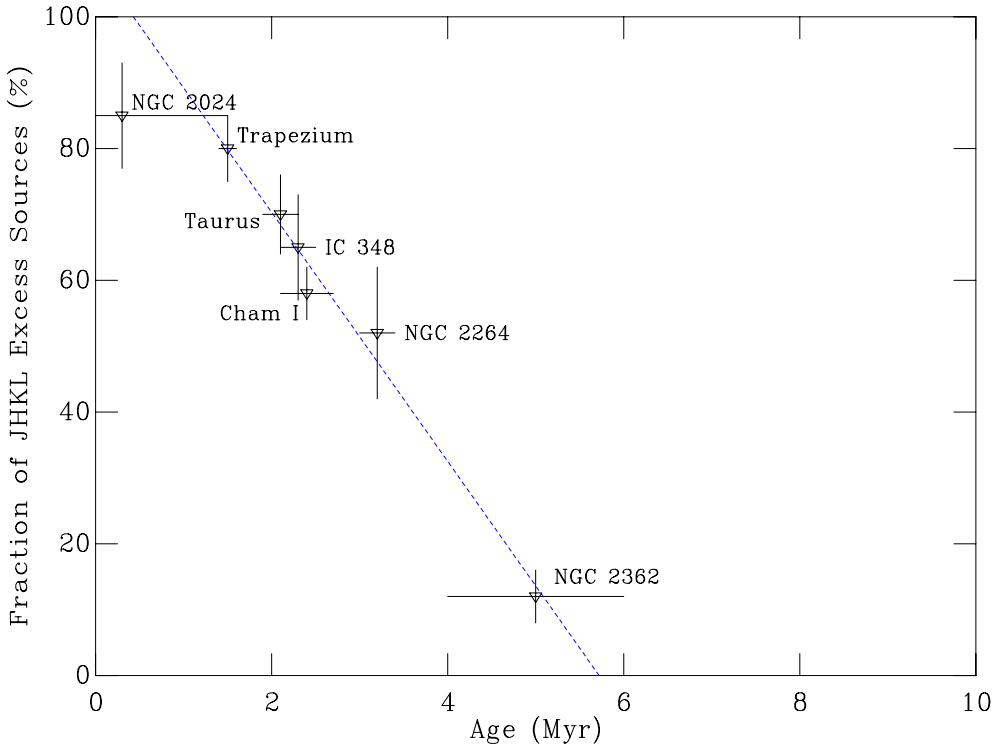

Figure 6.27: Cluster ages against the fraction of JHKL excess sources from Haisch et al. (2001), used a disc indicator. The straight line is a simple linear regression fit.

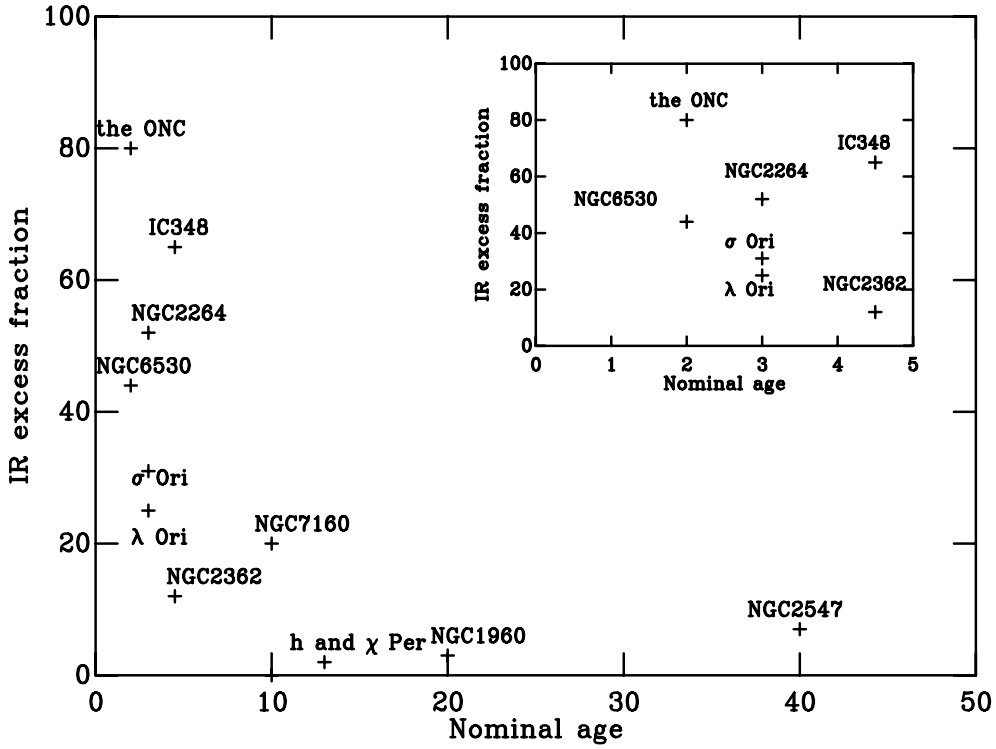

Figure 6.28: Figure showing the nominal age of each SFR with the IR excess from various literature sources. The inset panel shows the region 0-5 Myrs enlarged.

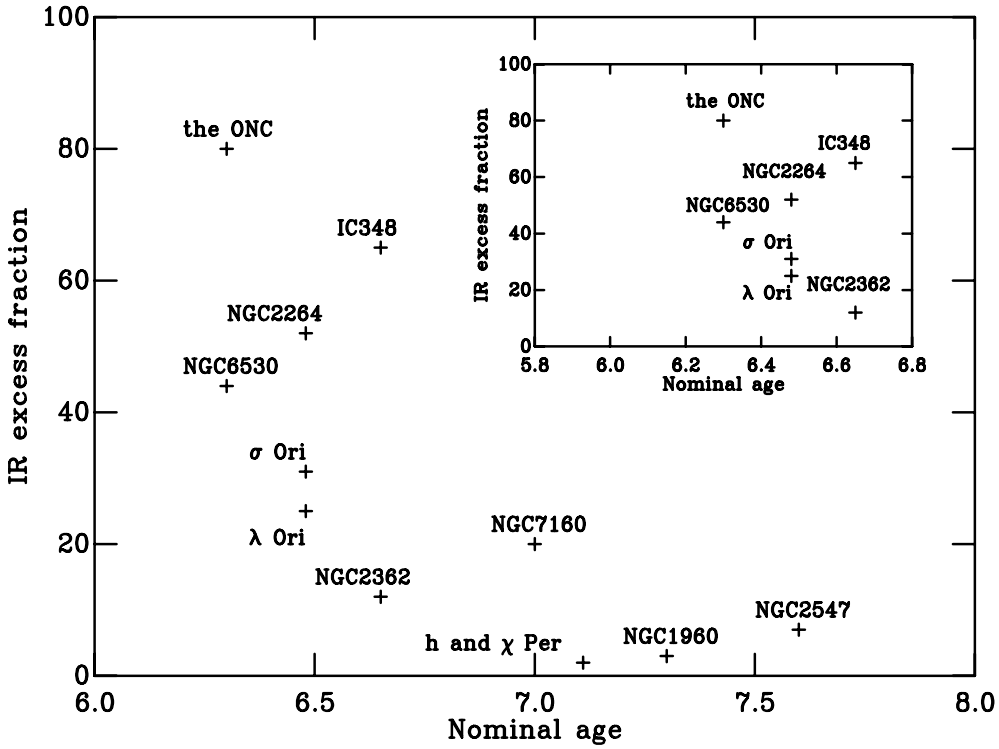

Figure 6.29: Figure showing the log(nominal age) of each SFR with the IR excess from various literature sources. The inset panel shows the region 0-5 Myrs enlarged.

drawn regarding the disc fraction as a function of age. However, the result is not completely consistent with a uniform decay, revealing possible evidence of environmental effects. As a further example, the inferred disc fractions of three SFRs in the same age group can be examined (nominal age of 3 Myrs); NGC2264, λ Orionis and σ Orionis, with distances of dm = 9.37, 8.01 and 7.94 respectively. The disc fractions adopted are (in the same order) $52 \pm 10\%$ (JHKL, Haisch et al., 2001, for masses greater than $0.85 M_{\odot}$), $\approx 25\%$ (from IRAC data, Barrado y Navascués et al., 2007, all discs in spectral range of M0-M6.5 or approximate mass range of $0.1 - 0.8 M_{\odot}$ using pre-MS isochrones), and $31.1 \pm 3.8\%$ (from IRAC data, Hernández et al., 2007, all stars in the approximate mass range $0.1 - 1.0 M_{\odot}$). In the case of these three SFRs NGC2264 has an inconsistent disc fraction, it is much higher than that of the other two SFRs. These disc fractions are taken from differing mass ranges and the SFRs are at different distances which could lead to sensitivity problems in the L band, as suggested as a possible problem for NGC2362 by Lyo et al. (2003). However, in this case the further distance to NGC2264 would result in fewer L band detections, and the lower mass limit being higher is likely to decrease the detected disc fraction. Therefore, it is likely that a consistent experiment would increase the discrepancy between NGC2264 and the two SFRs with lower disc fractions. However, even ignoring the particular case at a nominal age of 3 Myrs it is clear that the these data do not necessarily imply a smooth decline in disc fraction with age, suggesting other, presumably environmental factors, may affect disc lifetimes.

6.4.3 Local environment

Interestingly, IC348 is clearly out of sequence in both rotation rate and disc evolution. If disc evolution drives the rotational evolution, say through disc locking, this is perhaps unsurprising. The key here may be the local environment. There are no O-stars associated with IC348. NGC2362 however has six O-stars stars designated as cluster members, the ONC has 16 and NGC2264 13 (Maíz-Apellániz et al., 2004). This supports the idea that a larger fraction of the pre-MS stars in IC348 have retained discs due to the absence of winds and/or ionising radiation from massive stars. These age orders may, therefore, be amongst the first indications of the importance of environment on disc and rotation rate evolution (see also Stolte et al., 2004).

6.5 Summary

In this chapter age orders have been derived for a set of SFRs over a range of ages (1-40 Myrs) from photometric data and nominal ages assigned. In Section 6.1 the photometric data itself has been discussed qualitatively. A critical change in the nature of spreads within a CMD at $\simeq$5 Myrs has been suggested. Above $\simeq$5 Myrs the sequence members are generally not associated with molecular material and have wholly explicable photometric spreads. Below $\simeq$5 Myrs the sequence members are often associated with molecular material and show inexplicably large photometric spreads. Furthermore, in Section 6.2 analysis of the photometric data revealed a feature in the CMD termed the R-C gap. In most CMDs this feature appears as a gap between the pre-MS and MS members, or as a dearth of members at the head of the pre-MS in some younger sequences. The evolution of the gap from 1 Myr through to the intermediate age (in the context of these data) clusters of h and χ Per has been traced. The physics behind the appearance of a gap in the *V*, *V-I* sequences and the evolution of the gap with age has been explored. It is encouraging that the size of the gap, where it is visible, follows the same age ordering as found using the empirical isochrones. The possible use of the overlapping region of the R-C gap to derive spreads of isochronal age in a CMD i.e. the maximum mass stars still on the convective pre-MS and the minimum mass stars which has reached the MS, has been discussed. However, if star formation is slow and isochronal ages of individual stars are reliable this would provide a direct measurement of the age spreads present in SFRs. If star formation is rapid the R-C gap overlap region reveals the underlying spread in accretion histories within a SFR. This is important as for rapid star formation, if an accretion history is unknown, isochronal ages derived from a position in a CMD do not represent the true age of a star. Indeed it is therefore likely that if a rapid star formation model is accurate median or mean ages drawn from a population are also invalid. A more useful approach may be to compare SFRs using age order arguments or perhaps to use the age of the youngest stars which have the shortest accretion history.

Then in Section 6.3 the empirical isochrones from Chapter 5 have been compared on an absolute scale using the parameters from Chapter 4. This allowed the construction of an age ladder and the assignment of nominal ages for a defined set of indistinguishable groups. These nominal ages have been compared to literature ages. Finally, the implications of these new age orders on rotational evolution of pre-MS stars and disc dissipation timescales are discussed in Section

6.4. Further evidence for non-uniform decay of discs in SFRs, dependent on local environmental effects, has been found, although the comparisons must be re-examined using a consistent disc fraction indicator and mass range.

Chapter 7

Conclusions and future work

7.1 Conclusions

As discussed in Chapter 2 timescales of stellar formation are required to differentiate between the two main paradigms of star formation. The two models of slow-star-formation (SSF) and rapid-star-formation (RSF) are crucially distinguished by their formation timescales of $t_{\rm form} \approx 5-10$ Myrs and $t_{\rm form} < 3$ Myrs respectively. Timescales are also required to separate or lend favour to subsequent stellar evolutionary models. A current theory of the regulation of a star's rotation rate through a magnetic disc-locking mechanism relies crucially on the age order of different SFRs. These age orders can then be used to chart the rotational evolution and disc presence as a function of age. Ages for the individual SFRs are required to derive approximate timescales for the star-disc interaction and disc survival timescales. Subsequently, the disc survival timescales can be used to constrain planet formation models. The ages of SFRs and, more importantly, their age orders can be found from analysis of SFR populations in a CMD. The techniques for deriving ages (and age orders) using CMDs rely implicitly on the distances and extinctions adopted for a given SFR, as discussed in Chapter 3.

A new, statistically robust method of deriving distances (and mean extinctions), and corresponding uncertainties, to SFRs using CMDs is employed in Chapter 4. This resulted in the derivation of a set of homogeneous distances to several SFRs of a superior precision than those existing in the literature. In addition, a widely used method of deriving individual extinctions (the Q-method Johnson & Morgan, 1953) has been revised and the effect of its implicit assumptions formalised.

The metallicity of SFRs was found to be a crucial parameter when deriving distances. Current assumptions of solar metallicty for star formation studies are undermined by evidence from eclipsing binary studies (Southworth et al., 2004,a). This discrepancy is exacerbated by the recent study of Santos et al. (2008), who find solar metallicity for six SFRs (following the derivation of solar metallicities for three SFRs in James et al., 2006). This discrepancy must be explained or resolved through further study to ensure robust subsequent distances and age order derivations.

Further to the derived distances a method of modelling the pre-MS of SFRs was required. A new technique has been introduced in Chapter 5, which after membership selection resulted in empirically derived isochrones for a range of SFRs. These empirical isochrones were then used

in conjunction with the distances (and extinctions) derived in Chapter 4 to derive age orders and ages (after calibration using fiducial sequences) in Chapter 6. The combination of this age ladder and ancillary data, such as rotation rate distributions and disc fractions, was then used to uncover possible environmental effects.

The derivations of formation time of stars, from age spreads in SFRs, cannot currently be used to decisively reject either star-formation model. As discussed in Chapter 6, the spreads within a CMD often used to support or reject either model may be caused by varying accretion histories (Siess et al., 1999; Tout et al., 1999), and so do not represent true age spreads. In addition, this means that current ages derived for single stars or SFRs using isochrones cannot be relied upon until the effect of accretion on stellar evolution is better understood. This further supports the use of empirical isochrones and age orders. If one accepts that some form of star-disc interaction can regulate stellar rotation (for which strong evidence can now be found, see Cieza & Baliber, 2007), then comparison of rotation rate distributions and disc fractions using the age ladder confirm timescales of ≈ 5 Myrs for disc dissipation. However, strong evidence was found for local environment effects on this timescale. Specifically, IC348, which contains no O stars is out of the perceived evolutionary sequence of both rotation rate distribution and disc fraction. Therefore, further investigation of the impact of massive neighbouring stars on star-disc systems is required to fully constrain planet formation timescales as a function of environment.

Perhaps most importantly during the study of pre-MS populations a potentially vital feature (within a CMD) was discovered. This feature, a clear separation between the fully convective pre-MS and the MS stars with radiative cores, I term the R-C gap. The R-C gap size, which can be measured in colour, was found to be a function of age and to have robust underlying physical causes. The characteristics of the R-C gap mean it is an excellent tool for deriving distance independent ages and therefore reliable age orders for SFRs. Moreover, the R-C gap overlap, the overlap in magnitude of the fully convective pre-MS and MS could provide an exceptional diagnostic for star formation theories. The R-C gap overlap suggests that stars of equal mass within the studied SFRs have evolved at different rates or for different durations. Thus the R-C gap overlap demands a **spread** in **isochronal** ages of stars in a given SFR. The interpretation of these isochronal age spreads is vital to differentiate between the two current paradigms of star formation. If one adopts a SSF model the spreads across the R-C gap must be construed as real and evidence of a formation time. However, if one adopts a RSF model, one can invoke the theorised effects of past accretion upon stellar evolution, meaning that these isochronal ages no longer provide the real ages of the stars.

To summarise the work in this thesis has:

- Applied a new technique to derive statistically robust distances (and mean extinctions) with uncertainties. This has resulted in new precise distances (and extinctions) to several SFRs.
- Updated and formalised a technique for deriving individual extinctions, the revised Q-method.
- Highlighted the effect of errors in composition assumption on the derived distance to and therefore age of a given SFR.

- Created and applied a technique for modeling the pre-MS, deriving **empirical isochrones** for several SFRs.
- Created an age ordered ladder for the studied SFRs.
- Used the age ladder to confirm approximate disc dissipation timescales and uncover possible evidence of local environment effects upon the star-disc system.
- Discovered the R-C gap, explained the underlying physics, and described its possible use as a distance independent age indicator.
- Discussed the implications of the R-C gap overlap which shows a spread in **isochronal** ages of stars in the studied SFRs.

Most, if not all of these achievements can and should be built upon to ensure the maximum scientific potential is extracted.

7.2 Future Work

The future work required after the work in this thesis can be separated into two main categories. Firstly, the techniques introduced can be applied to a greater and more self-consistently calibrated dataset. Secondly, the successful extension of these techniques relies on additional studies to be undertaken. This includes further projects which are suggested by the implications of the results in this thesis.

7.2.1 Extending introduced techniques

It is clear that the techniques for derivation of distances (and extinctions) from Chapter 4 are robust. These techniques, in conjunction with those used in the derivation of empirical isochrones, should be applied to a larger and more homogeneous dataset. It is crucial that a further study is undertaken using a precisely calibrated photometric system for a range of SFRs. Data have been acquired through a proposal written by the author and Tim Naylor to derive such a set of empirical isochrones. These data are currently being reduced by Tim Naylor and Cameron Bell and could provide a benchmark set of empirical isochrones for comparison to theory. In addition, these techniques could also be applied to the O star survey of Ben Burningham and Tim Naylor and further surveys. For example the IPHAS and VISTA surveys represent an excellent opportunity to develop and automate these techniques. When combined with further homogeneously derived ancillary data such as a self-consistent set of disc fractions or rotation rate distributions, these techniques will provide more robust constraints on stellar evolution and both stellar and planet formation theories. This would also allow a more robust study of the effects of local environment, when combined with models of, for instance, the mean O star *UV* flux in a given SFR.

7.2.2 Further studies

7.2.2.1 Metallicity

As discussed in Section 7.1, to enable the use of the age ladder and the underlying techniques, robust compositions must be derived for a range of SFRs. The assumption of solar metallicity, often used, as suggested by the studies of James et al. (2006) and Santos et al. (2008), must be investigated given the evidence of non-solar metallicities found using eclipsing binaries in some SFRs (Southworth et al., 2004,a). Errors associated with uncertainties in composition have previously been assumed negligible; as highlighted in this thesis this is no longer the case. In collaboration with Sofia Randich, Francesco Palla and Tim Naylor I am aiming to investigate the composition of SFRs such as the ONC.

7.2.2.2 R-C gap

The discovery of the R-C gap is potentially the most important result in this thesis. The R-C gap could provide a powerful diagnostic for evolutionary models and provide extremely robust constraints for theories. Firstly, the R-C gap provides a distance independent age indicator. The change in the size (in colour) of the R-C gap as a function of age must however be calibrated. A dataset has already been taken using the WYFFOS multi-fibre spectrograph on the WHT with the aim of characterising the R-C gap. I am currently reducing these data. This work is ongoing and nearing completion. Once completed this will provide both an initial calibration and a proof of concept for a further and much larger survey proposal.

I have also been involved in a study of periodic variability, both as a tracer for the R-C gap, and as indicative of changes in the magnetic field topology of stars across the R-C gap. This study revealed a sharp decrease in the number of periodically variable stars across the R-C gap, which we interpret as a destruction of large scale surface cool spots and therefore a change in the magnetic field structure. This highlights the potential of such an important phase change (i.e. from fully convective to a radiative core as found across the R-C gap) as an incredibly model-sensitive feature. Work on this project has finished and a paper will be submitted within the next two months (Saunders et al, in prep).

Finally, the R-C gap overlap, as mentioned in Section 7.1, provides a means of deriving precise isochronal age spreads within SFRs. These spreads, of either age (SSF) or accretion history (RSF), could then be 'normalised out' and used to strengthen conclusions drawn using the age ordered ladder. In order to favour either interpretation of these spreads, more, and more quantitative studies are required on the effect of both current and past accretion on the evolution of a star.

7.2.2.3 Initial mass functions

Finally, the τ^2 fitting technique can be used to test the pre-MS evolutionary models more precisely, allowing for their continued improvement. More importantly perhaps, this method, upon adoption of a given theoretical model, could provide a statistically derived best fit IMF. IMFs have had little mention in this thesis as their derivation is beyond the scope of this work. Nevertheless,

these values are important to studies of star formation and star formation rates. The goal is to discern whether local-mass-functions (LMFs) are equivalent to the global IMF. If they are indeed equivalent this shows that star formation is not dependent on location and is a robust and universal physical process. A precise theoretical basis for the IMF has not yet been developed but despite its empirical nature it appears universal within current uncertainty limits. The current state of the universality of the IMF is discussed in Kennicutt (1998). The masses of pre-MS stars required to constrain IMFs however are difficult to derive and highly model dependent. If one model is adopted the τ^2 technique could allow a statistically robust derivation of the best fitting IMF by using this as a free parameter. Conversely, the assumption of a universal IMF could provide a further lever with which to compare pre-MS models.

Bibliography

Adams F. C., Hollenbach D., Laughlin G., Gorti U., 2004, ApJ, 611, 360

Adams F. C., Shu F. H., 2007, ArXiv e-prints, 708

Aigrain S., Hodgkin S., Irwin J., Hebb L., Irwin M., Favata F., Moraux E., Pont F., 2007, MNRAS, 375, 29

Allain S., Bouvier J., Prosser C., Marschall L. A., Laaksonen B. D., 1996, A&A, 305, 498

Allen R. J., Atherton P. D., Tilanus R. P. J., 1986, Nature, 319, 296

Andre P., Montmerle T., 1994, ApJ, 420, 837

Andre P., Ward-Thompson D., Barsony M., 2000, Protostars and Planets IV, pp 59–+

Appenzeller I., Mundt R., 1989, A&A Rev., 1, 291

Assousa G. E., Herbst W., Turner K. C., 1977, ApJL, 218, L13

Bacciotti F., Ray T. P., Mundt R., Eislöffel J., Solf J., 2002, ApJ, 576, 222

Ballesteros-Paredes J., 2006, MNRAS, 372, 443

Ballesteros-Paredes J., Hartmann L., 2007, Revista Mexicana de Astronomia y Astrofisica, 43, 123

Ballesteros-Paredes J., Hartmann L., Vázquez-Semadeni E., 1999, ApJ, 527, 285

Balog Z., Muzerolle J., Rieke G. H., Su K. Y. L., Young E. T., Megeath S. T., 2007, ApJ, 660, 1532

Balona L. A., Laney C. D., 1996, MNRAS, 281, 1341

Baraffe I., Chabrier G., Allard F., Hauschildt P., 2001a, in Montmerle T., André P., eds, From Darkness to Light: Origin and Evolution of Young Stellar Clusters Vol. 243 of Astronomical Society of the Pacific Conference Series, Pre-Main Sequence Models for Low-Mass Stars and Brown Dwarfs. pp 571–+

Baraffe I., Chabrier G., Allard F., Hauschildt P., 2001b, in Zinnecker H., Mathieu R., eds, The Formation of Binary Stars Vol. 200 of IAU Symposium, Pre-Main Sequence Models for Low-Mass Stars and Brown Dwarfs. pp 483–+

Baraffe I., Chabrier G., Allard F., Hauschildt P. H., 1998, A&A, 337, 403

Barnes S., 1998, Journal of the American Association of Variable Star Observers (JAAVSO), 26, 162

Barnes S., Sofia S., 1996, ApJ, 462, 746

Barnes S. A., 2003, ApJ, 586, 464

Barnes S. A., Sofia S., Prosser C. F., Stauffer J. R., 1999, ApJ, 516, 263

Barrado y Navascués D., Stauffer J. R., Morales-Calderón M., Bayo A., Fazzio G., Megeath T., Allen L., Hartmann L. W., Calvet N., 2007, ApJ, 664, 481

Basri G., Marcy G. W., Valenti J. A., 1992, ApJ, 390, 622

Basri G., Martin E. L., Bertout C., 1991, A&A, 252, 625

Basu S., Mouschovias T. C., 1994, ApJ, 432, 720

Béjar V. J. S., Zapatero Osorio M. R., Rebolo R., 1999, ApJ, 521, 671

Benson P. J., Myers P. C., 1989, ApJS, 71, 89

Berghöfer T. W., Christian D. J., 2002, A&A, 384, 890

Bergin E. A., Ciardi D. R., Lada C. J., Alves J., Lada E. A., 2001, ApJ, 557, 209

Bertout C., Basri G., Bouvier J., 1988, ApJ, 330, 350

Bessell M. S., 1979, PASP, 91, 589

Bessell M. S., 1990, PASP, 102, 1181

Bessell M. S., 2000, PASP, 112, 961

Bessell M. S., 2005, ARA&A, 43, 293

Bessell M. S., Castelli F., Plez B., 1998, A&A, 333, 231

Binney J., Tremaine S., 1987, Galactic dynamics. Princeton, NJ, Princeton University Press, 1987, 747 p.

Blaauw A., 1991, in Lada C. J., Kylafis N. D., eds, NATO ASIC Proc. 342: The Physics of Star Formation and Early Stellar Evolution OB Associations and the Fossil Record of Star Formation. pp 125–+

Blaauw A., Hiltner W. A., Johnson H. L., 1959, ApJ, 130, 69

Bodenheimer P., 1965a, PASP, 77, 124

Bodenheimer P., 1965b, ApJ, 142, 451

Bodenheimer P., 1995, ARA&A, 33, 199

Bonatto C., Bica E., Girardi L., 2004, A&A, 415, 571

Bonsack W. K., 1961, ApJ, 133, 340

Bourke T. L., Myers P. C., Robinson G., Hyland A. R., 2001, ApJ, 554, 916

Bouvier J., Covino E., Kovo O., Martin E. L., Matthews J. M., Terranegra L., Beck S. C., 1995, A&A, 299, 89

Bouvier J., Forestini M., Allain S., 1997, A&A, 326, 1023

Brown A. G. A., de Geus E. J., de Zeeuw P. T., 1994, A&A, 289, 101

Burke C. J., Pinsonneault M. H., Sills A., 2004, ApJ, 604, 272

Burningham B., Naylor T., Jeffries R. D., Devey C. R., 2003, MNRAS, 346, 1143

Burningham B., Naylor T., Littlefair S. P., Jeffries R. D., 2005a, MNRAS, 363, 1389

Burningham B., Naylor T., Littlefair S. P., Jeffries R. D., 2005b, MNRAS, 356, 1583

Buser R., Kurucz R. L., 1978, A&A, 70, 555

Caballero J. A., 2007, A&A, 466, 917

Cabrit S., Edwards S., Strom S. E., Strom K. M., 1990, ApJ, 354, 687

Camenzind M., 1990, in Klare G., ed., Reviews in Modern Astronomy Vol. 3 of Reviews in Modern Astronomy, Magnetized Disk-Winds and the Origin of Bipolar Outflows.. pp 234–265

Capilla G., Fabregat J., 2002, A&A, 394, 479

Cardelli J. A., Clayton G. C., Mathis J. S., 1989, ApJ, 345, 245

Castelli F., Gratton R. G., Kurucz R. L., 1997, A&A, 318, 841

Castelli F., Kurucz R. L., 2004, ArXiv Astrophysics e-prints

Cepa J., Beckman J. E., 1990, ApJ, 349, 497

Chabrier G., Baraffe I., 1997, A&A, 327, 1039

Chabrier G., Küker M., 2006, A&A, 446, 1027

Chandrasekhar S., 1967, An introduction to the study of stellar structure. New York: Dover, 1967

Cieza L., Baliber N., 2007, ArXiv e-prints, 707

Claria J. J., 1982a, A&AS, 47, 323

Claria J. J., 1982b, A&AS, 47, 323

Coffey D., Bacciotti F., Ray T. P., Eislöffel J., Woitas J., 2007, ApJ, 663, 350

Cohen R. E., Herbst W., Williams E. C., 2004, AJ, 127, 1602

Collier Cameron A., Jianke L., 1994, MNRAS, 269, 1099

Collins G. W., 1989, The fundamentals of stellar astrophysics. New York, W. H. Freeman and Co., 1989, 512 p.

Covey K. R., Greene T. P., Doppmann G. W., Lada C. J., 2005, AJ, 129, 2765

Covino E., Alcala J. M., Allain S., Bouvier J., Terranegra L., Krautter J., 1997, A&A, 328, 187

Crutcher R. M., 1999, ApJ, 520, 706

Cuffey J., 1940, ApJ, 92, 303

Currie T., Balog Z., Kenyon S. J., Rieke G., Prato L., Young E. T., Muzerolle J., Clemens D. P., Buie M., Sarcia D., Grabu A., Tollestrup E. V., Taylor B., Dunham E., Mace G., 2007, ApJ, 659, 599

Dahm S. E., 2005, AJ, 130, 1805

Dahm S. E., Hillenbrand L. A., 2007, AJ, 133, 2072

Dahm S. E., Simon T., 2005, AJ, 129, 829

Damiani F., Flaccomio E., Micela G., Sciortino S., Harnden F. R., Murray S. S., 2004, ApJ, 608, 781

Damiani F., Micela G., Sciortino S., Huélamo N., Moitinho A., Harnden Jr. F. R., Murray S. S., 2006, A&A, 460, 133

D'Antona F., Mazzitelli I., 1997, Memorie della Societa Astronomica Italiana, 68, 807

de Zeeuw P. T., Hoogerwerf R., de Bruijne J. H. J., Brown A. G. A., Blaauw A., 1999, AJ, 117, 354

Dean J. F., Warren P. R., Cousins A. W. J., 1978, MNRAS, 183, 569

Delgado A. J., Alfaro E. J., Yun J. L., 2007, ArXiv Astrophysics e-prints

Diplas A., Savage B. D., 1994, ApJS, 93, 211

Dobashi K., Yonekura Y., Mizuno A., Fukui Y., 1992, AJ, 104, 1525

Dobbs C., Price D., Bonnell I., 2007, ArXiv e-prints, 706

Dobbs C. L., Bonnell I. A., 2007, MNRAS, 376, 1747

Dolan C. J., Mathieu R. D., 1999, in NOAO Proposal ID #1999A-0057 A Lithium Survey for Young Stars in the (lambda) Orionis Star Forming Region. pp 57–+

Dolan C. J., Mathieu R. D., 2001, AJ, 121, 2124

Ducourant C., Rapaport M., Camargo J. I. B., Soubiran C., Teixeira R., Fresneau A., Colin J., 2006, Exploiting Large Surveys for Galactic Astronomy, 26th meeting of the IAU, Joint Discussion 13, 22-23 August 2006, Prague, Czech Republic, JD13, #33, 13

Durney B. R., De Young D. S., Roxburgh I. W., 1993, Sol. Phys., 145, 207

Echevarría J., Michel R., 2007, Revista Mexicana de Astronomia y Astrofisica, 43, 291

Eddington A. S., 1924, MNRAS, 84, 308

Edwards S., Strom S. E., Hartigan P., Strom K. M., Hillenbrand L. A., Herbst W., Attridge J., Merrill K. M., Probst R., Gatley I., 1993, AJ, 106, 372

Eggen O. J., 1950a, ApJ, 111, 65

Eggen O. J., 1950b, ApJ, 111, 81

Eggen O. J., 1951, ApJ, 113, 657

Elmegreen B. G., 1991, ApJ, 378, 139

Elmegreen B. G., 2000, ApJ, 530, 277

Elmegreen B. G., 2007, ArXiv e-prints, 707

Endal A. S., Sofia S., 1981, ApJ, 243, 625

Falgarone E., Puget J.-L., Perault M., 1992, A&A, 257, 715

Feigelson E. D., 1983, Revista Mexicana de Astronomia y Astrofisica, vol. 7, 7, 240

Feigelson E. D., Gaffney III J. A., Garmire G., Hillenbrand L. A., Townsley L., 2003, ApJ, 584, 911

Feigelson E. D., Montmerle T., 1985, in Hjellming R. M., Gibson D. M., eds, Radio Stars Vol. 116 of Astrophysics and Space Science Library, An extremely variable radio star in the Rho Ophiuchi cloud. pp 335–338

Feigelson E. D., Montmerle T., 1999, ARA&A, 37, 363

Flaccomio E., Damiani F., Micela G., Sciortino S., Harnden F. R., Murray S. S., Wolk S. J., 2003, ApJ, 582, 398

Flaccomio E., Micela G., Sciortino S., 2006, A&A, 455, 903

Flaccomio E., Micela G., Sciortino S., Favata F., Corbally C., Tomaney A., 1999, A&A, 345, 521

Flower P. J., 1996, ApJ, 469, 355

Garay G., Lizano S., 1999, PASP, 111, 1049

Garcia Lopez R. J., Rebolo R., Martin E. L., 1994, A&A, 282, 518

Garrison R. F., 1967, PASP, 79, 433

Garrison R. F., 1970, AJ, 75, 1001

Genzel R., Reid M. J., Moran J. M., Downes D., 1981, ApJ, 244, 884

Georgelin Y. M., Georgelin Y. P., 1976, A&A, 49, 57

Getman K. V., Feigelson E. D., Townsley L., Broos P., Garmire G., Tsujimoto M., 2006, ApJS, 163, 306

Giampapa M. S., Rosner R., Kashyap V., Fleming T. A., Schmitt J. H. M. M., Bookbinder J. A., 1996, ApJ, 463, 707

Girardi L., Bertelli G., Bressan A., Chiosi C., Groenewegen M. A. T., Marigo P., Salasnich B., Weiss A., 2002, A&A, 391, 195

Glass I. S., 1973, MNRAS, 164, 155

Goodman A. A., Benson P. J., Fuller G. A., Myers P. C., 1993, ApJ, 406, 528

Grevesse N., 1968, Sol. Phys., 5, 159

Grevesse N., Sauval A. J., 1998, Space Science Reviews, 85, 161

Grossman A. S., Hays D., Graboske Jr. H. C., 1974, A&A, 30, 95

Guenther E. W., Ball M., 1999, A&A, 347, 508

Gullbring E., Hartmann L., Briceno C., Calvet N., Muzerolle J., 1998, in Donahue R. A., Bookbinder J. A., eds, ASP Conf. Ser. 154: Cool Stars, Stellar Systems, and the Sun Color Anomalies of Weak Lined T Tauri stars. pp 1709–+

Haisch Jr. K. E., Lada E. A., Lada C. J., 2001, ApJL, 553, L153

Halley E., 1717, Philosophical Transactions Series I, 30, 736

Harper Jr. C. L., 1996, ApJ, 466, 1026

Hartmann L., 1998, Accretion Processes in Star Formation. Accretion processes in star formation / Lee Hartmann. Cambridge, UK ; New York : Cambridge University Press, 1998. (Cambridge astrophysics series ; 32) ISBN 0521435072.

Hartmann L., 2001, Accretion Processes in Star Formation. Accretion Processes in Star Formation, by Lee Hartmann, pp. 237. ISBN 0521785200. Cambridge, UK: Cambridge University Press, January 2001.

Hartmann L., 2002, ApJ, 578, 914

Hartmann L., Ballesteros-Paredes J., Bergin E. A., 2001, ApJ, 562, 852

Hayashi C., 1966, ARA&A, 4, 171

Hayashi C., Nishida M., Sugimoto D., 1962, Progress of Theoretical Physics, 27, 1233

Hayashi M., 1965, PASJ, 17, 177

Heithausen A., Brüns C., Kerp J., Weiss A., 2001, in Pilbratt G. L., Cernicharo J., Heras A. M., Prusti T., Harris R., eds, The Promise of the Herschel Space Observatory Vol. 460 of ESA Special Publication, The Structure of Cirrus Clouds at Different Galactic Altitudes. pp 431–+

Hensberge H., Pavlovski K., Verschueren W., 2000, A&A, 358, 553

Henyey L. G., Lelevier R., Levée R. D., 1955, PASP, 67, 154

Herbig G. H., 1960, ApJS, 4, 337

Herbig G. H., 1962, Advances in Astronomy and Astrophysics, 1, 47

Herbig G. H., 1965, ApJ, 141, 588

Herbig G. H., 1998, ApJ, 497, 736

Herbig G. H., Dahm S. E., 2002, AJ, 123, 304

Herbst W., Bailer-Jones C. A. L., Mundt R., Meisenheimer K., Wackermann R., 2002, A&A, 396, 513

Herbst W., Eislöffel J., Mundt R., Scholz A., 2007, in Reipurth B., Jewitt D., Keil K., eds, Protostars and Planets V The Rotation of Young Low-Mass Stars and Brown Dwarfs. pp 297–311

Herbst W., Herbst D. K., Grossman E. J., Weinstein D., 1994, AJ, 108, 1906

Herbst W., Mundt R., 2005, ApJ, 633, 967

Hernández J., Briceño C., Calvet N., Hartmann L., Muzerolle J., Quintero A., 2006, ApJ, 652, 472

Hernández J., Hartmann L., Megeath T., Gutermuth R., Muzerolle J., Calvet N., Vivas A. K., Briceño C., Allen L., Stauffer J., Young E., Fazio G., 2007, ApJ, 662, 1067

Hertzsprung E., 1911, Publikationen des Astrophysikalischen Observatoriums zu Potsdam, 63

Hillenbrand L. A., 1997, AJ, 113, 1733

Hollenbach D., Adams F. C., 2004, in Johnstone D., Adams F. C., Lin D. N. C., Neufeeld D. A., Ostriker E. C., eds, Star Formation in the Interstellar Medium: In Honor of David Hollenbach Vol. 323 of Astronomical Society of the Pacific Conference Series, The Disruption of Planet-Forming Disks. pp 3–+

Hollenbach D., Gorti U., 2005, in Protostars and Planets V The Photoevaporation of Protoplanetary Disks by Their Central Stars. pp 8433–+

Hollenbach D. J., Werner M. W., Salpeter E. E., 1971, ApJ, 163, 165

Irwin J., Aigrain S., Hodgkin S., Irwin M., Bouvier J., Clarke C., Hebb L., Moraux E., 2006, MNRAS, 370, 954

James D. J., Melo C., Santos N. C., Bouvier J., 2006, A&A, 446, 971

Jeans J. H., 1902, Phil. Trans. R. Soc., 199

Jeffries R. D., 1997, MNRAS, 292, 177

Jeffries R. D., 1998, in Donahue R. A., Bookbinder J. A., eds, Cool Stars, Stellar Systems, and the Sun Vol. 154 of Astronomical Society of the Pacific Conference Series, Lithium Abundances in the Low Metallicity Hyades Analogue NGC 6633. pp 940–+

Jeffries R. D., 1999a, MNRAS, 304, 821

Jeffries R. D., 1999b, MNRAS, 309, 189

Jeffries R. D., 2000, in Pallavicini R., Micela G., Sciortino S., eds, Stellar Clusters and Associations: Convection, Rotation, and Dynamos Vol. 198 of Astronomical Society of the Pacific Conference Series, Lithium depletion in open clusters. pp 245–+

Jeffries R. D., 2004, ArXiv Astrophysics e-prints

Jeffries R. D., 2007a, MNRAS, 376, 1109

Jeffries R. D., 2007b, MNRAS, pp 851–+

Jeffries R. D., James D. J., Thurston M. R., 1998, MNRAS, 300, 550

Jeffries R. D., Maxted P. F. L., Oliveira J. M., Naylor T., 2006a, MNRAS, 371, L6

Jeffries R. D., Maxted P. F. L., Oliveira J. M., Naylor T., 2006b, MNRAS, pp L62+

Jeffries R. D., Naylor T., 2001, in Montmerle T., André P., eds, From Darkness to Light: Origin and Evolution of Young Stellar Clusters Vol. 243 of Astronomical Society of the Pacific Conference Series, The Lithium Depletion Boundary as a Clock and Thermometer. pp 633–+

Jeffries R. D., Oliveira J. M., 2005, MNRAS, 358, 13

Jeffries R. D., Oliveira J. M., Naylor T., Mayne N. J., Littlefair S. P., 2007, MNRAS, 376, 580

Jeffries R. D., Tolley A. J., 1998, MNRAS, 300, 331

Jeffries R. D., Totten E. J., Stauffer J. R., Barrado Y Navascués D., Hambly N. C., 2000, in Pallavicini R., Micela G., Sciortino S., eds, Stellar Clusters and Associations: Convection, Rotation, and Dynamos Vol. 198 of Astronomical Society of the Pacific Conference Series, The lithium depletion boundary and age of NGC 2547. pp 281–+

Johnson H. L., 1966, ARA&A, 4, 193

Johnson H. L., Morgan W. W., 1951, ApJ, 114, 522

Johnson H. L., Morgan W. W., 1953, ApJ, 117, 313

Jones B. F., Fischer D. A., Stauffer J. R., 1996, AJ, 112, 1562

Jordi C., Trullols E., Galadi-Enriquez D., 1996, A&A, 312, 499

Joy A. H., 1945, ApJ, 102, 168

Joy A. H., 1949, ApJ, 110, 424

Kawaler S. D., 1988, ApJ, 333, 236

Keller S. C., Grebel E. K., Miller G. J., Yoss K. M., 2001, AJ, 122, 248

Kennicutt Jr. R. C., 1998, in Gilmore G., Howell D., eds, The Stellar Initial Mass Function (38th Herstmonceux Conference) Vol. 142 of Astronomical Society of the Pacific Conference Series, Overview: The Initial Mass Function in Galaxies. pp 1–+

Kenyon M. J., Jeffries R. D., Naylor T., Oliveira J. M., Maxted P. F. L., 2005, MNRAS, 356, 89

Kilambi G. C., 1977, MNRAS, 178, 423

Kleinmann S. G., Lysaght M. G., Pughe W. L., Schneider S. E., Skrutskie M. F., Weinberg M. D., Price S. D., Matthews K. Y., Soifer B. T., Huchra J. P., 1994, Experimental Astronomy, 3, 65

Koenigl A., 1991, ApJL, 370, L39

Kouwenhoven T., 2005, ArXiv Astrophysics e-prints

Kraus S., Balega Y. Y., Berger J.-P., Hofmann K.-H., Millan-Gabet R., Monnier J. D., Ohnaka K., Pedretti E., Preibisch T., Schertl D., Schloerb F. P., Traub W. A., Weigelt G., 2007, A&A, 466, 649

Krishnamurthi A., Terndrup D. M., Pinsonneault M. H., Sellgren K., Stauffer J. R., Schild R., Backman D. E., Beisser K. B., Dahari D. B., Dasgupta A., Hagelgans J. T., Seeds M. A., Anand R., Laaksonen B. D., Marschall L. A., Ramseyer T., 1998, ApJ, 493, 914

Lada C. J., 1987, in Peimbert M., Jugaku J., eds, Star Forming Regions Vol. 115 of IAU Symposium, Star formation - From OB associations to protostars. pp 1–17

Lamm M. H., Bailer-Jones C. A. L., Mundt R., Herbst W., Scholz A., 2004, A&A, 417, 557

Lamm M. H., Mundt R., Bailer-Jones C. A. L., Herbst W., 2005, A&A, 430, 1005

Landolt A. U., 1992, AJ, 104, 340

Larson R. B., 1981, MNRAS, 194, 809

Larson R. B., 2003, Reports of Progress in Physics, 66, 1651

Lee C. W., Myers P. C., Tafalla M., 2001, ApJS, 136, 703

Leggett S. K., 1992, ApJS, 82, 351

Lejeune T., Cuisinier F., Buser R., 1998, A&AS, 130, 65

Lejeune T., Schaerer D., 2001, A&A, 366, 538

Lindoff U., 1968, Arkiv for Astronomi, 5, 1

Littlefair S. P., Naylor T., Burningham B., Jeffries R. D., 2005, MNRAS, 358, 341

Long M., Romanova M. M., Lovelace R. V. E., 2005, ApJ, 634, 1214

Luhman K. L., 1999, ApJ, 525, 466

Luhman K. L., Lada E. A., Muench A. A., Elston R. J., 2005, ApJ, 618, 810

Luhman K. L., McLeod K. K., Goldenson N., 2005, ApJ, 623, 1141

Luhman K. L., Stauffer J. R., Muench A. A., Rieke G. H., Lada E. A., Bouvier J., Lada C. J., 2003, ApJ, 593, 1093

Lynga G., 1981, Astronomical Data Center Bulletin, 1, 90

Lyo A.-R., Lawson W. A., Mamajek E. E., Feigelson E. D., Sung E.-C., Crause L. A., 2003, MNRAS, 338, 616

Lyra W., Moitinho A., van der Bliek N., Alves J., 2006a, ArXiv Astrophysics e-prints

Lyra W., Moitinho A., van der Bliek N. S., Alves J., 2006b, A&A, 453, 101

Mac Low M.-M., Klessen R. S., 2004, Reviews of Modern Physics, 76, 125

MacGregor K. B., Brenner M., 1991, ApJ, 376, 204

Magnani L., Blitz L., Mundy L., 1985, ApJ, 295, 402

Maíz-Apellániz J., Walborn N. R., Galué H. Á., Wei L. H., 2004, ApJS, 151, 103

Marco A., Bernabeu G., 2001, A&A, 372, 477

Martin E. L., 1997, A&A, 321, 492

Martin E. L., Rebolo R., Magazzu A., 1994, ApJ, 436, 262

Massey P., Johnson K. E., Degioia-Eastwood K., 1995, ApJ, 454, 151

Mathieu R. D., 2004, in Maeder A., Eenens P., eds, Stellar Rotation Vol. 215 of IAU Symposium, The Rotation of Low-Mass Pre-Main-Sequence Stars (Invited Review). pp 113–+

Mathis J. S., 1990, ARA&A, 28, 37

Matt S., Pudritz R. E., 2005a, ApJL, 632, L135

Matt S., Pudritz R. E., 2005b, MNRAS, 356, 167

Mayne N. J., Naylor T., Littlefair S. P., Saunders E. S., Jeffries R. D., 2007, MNRAS, 375, 1220

Mazzei P., Pigatto L., 1989, A&A, 213, L1

McCaughrean M. J., O'Dell C. R., 1996, AJ, 111, 1977

McCray R., Snow Jr. T. P., 1979, ARA&A, 17, 213

Mendoza V. E. E., Gomez T., 1980, MNRAS, 190, 623

Mitchell R. I., Johnson H. L., 1957, ApJ, 125, 414

Moitinho A., Alves J., Huélamo N., Lada C. J., 2001, ApJL, 563, L73

Monck W. H. S., 1892, PASP, 4, 98

Moreno-Corral M. A., Chavarria K. C., de Lara E., Wagner S., 1993, A&A, 273, 619

Morgan W. W., Keenan P. C., Kellman E., 1943, An atlas of stellar spectra, with an outline of spectral classification. Chicago, Ill., The University of Chicago press [1943]

Muminov M., 1996, VizieR Online Data Catalog, 5027, 0

Mundt R., 1984, ApJ, 280, 749

Murdin P., Penston M. V., 1977, MNRAS, 181, 657

Muzerolle J., Calvet N., Hartmann L., 1998, ApJ, 492, 743

Nakano T., 1998, ApJ, 494, 587

Naylor T., 1998, MNRAS, 296, 339

Naylor T., Fabian A. C., 1999, MNRAS, 302, 714

Naylor T., Jeffries R. D., 2006, MNRAS, 373, 1251

Naylor T., Totten E. J., Jeffries R. D., Pozzo M., Devey C. R., Thompson S. A., 2002, MNRAS, 335, 291

Ogura K., Ishida K., 1981, PASJ, 33, 149

Ogura K., Sugitani K., Pickles A., 2002, AJ, 123, 2597

Oliveira J. M., Jeffries R. D., van Loon J. T., Rushton M. T., 2006, MNRAS, 369, 272

Oyama T., Miyoshi M., Deguchi S., Imai H., Shen Z., 2007, ArXiv e-prints, 710

Palla F., Galli D., 1997, ApJL, 476, L35+

Palla F., Randich S., Flaccomio E., Pallavicini R., 2005, ApJL, 626, L49

Palla F., Randich S., Pavlenko Y. V., Flaccomio E., Pallavicini R., 2007, ApJL, 659, L41

Palla F., Stahler S. W., 1999, ApJ, 525, 772

Park B.-G., Sung H., 2002, AJ, 123, 892

Park B.-G., Sung H., Bessell M. S., Kang Y. H., 2000, AJ, 120, 894

Patten B. M., Simon T., 1996, ApJS, 106, 489

Payne C. H., 1925, Proceedings of the National Academy of Science, 11, 192

Pérez M. R., 1991, Revista Mexicana de Astronomia y Astrofisica, 22, 99

Perez M. R., Joner M. D., The P. S., Westerlund B. E., 1989, PASP, 101, 195

Perez M. R., The P. S., Westerlund B. E., 1987, PASP, 99, 1050

Pinsonneault M. H., Deliyannis C. P., Demarque P., 1992, ApJS, 78, 179

Pinsonneault M. H., Terndrup D. M., Hanson R. B., Stauffer J. R., 2003, ApJ, 598, 588

Pinsonneault M. H., Terndrup D. M., Hanson R. B., Stauffer J. R., 2004, ApJ, 600, 946

Polosukhina N. S., Shavrina A. V., 2007, Astrophysics, 50, 381

Pozzo M., 2001, PhD thesis, PhD Thesis, Keele (Staffordshire, U.K.), 2001

Pozzo M., Naylor T., Jeffries R. D., Drew J. E., 2003, MNRAS, 341, 805

Preibisch T., Brown A. G. A., Bridges T., Guenther E., Zinnecker H., 2002, AJ, 124, 404

Preibisch T., Feigelson E. D., 2005, ApJS, 160, 390

Preibisch T., Zinnecker H., 2002, AJ, 123, 1613

Pringle J. E., Allen R. J., Lubow S. H., 2001, MNRAS, 327, 663

Prisinzano L., Damiani F., Micela G., Pillitteri I., 2007, A&A, 462, 123

Prisinzano L., Damiani F., Micela G., Sciortino S., 2005, A&A, 430, 941

Prosser C. F., 1992, AJ, 103, 488

Prosser C. F., 1994, AJ, 107, 1422

Prosser C. F., Schild R. E., Stauffer J. R., Jones B. F., 1993, PASP, 105, 269

Prosser C. F., Stauffer J. R., Caillault J.-P., Balachandran S., Stern R. A., Randich S., 1995, AJ, 110, 1229

Radick R. R., Skiff B. A., Lockwood G. W., 1990, ApJ, 353, 524

Radick R. R., Thompson D. T., Lockwood G. W., Duncan D. K., Baggett W. E., 1987, ApJ, 321, 459

Randich S., 2006, Mixing on the Main Sequence: Lithium and Beryllium in Old Open Clusters. Chemical Abundances and Mixing in Stars in the Milky Way and its Satellites, ESO ASTROPHYSICS SYMPOSIA. ISBN 978-3-540-34135-2. Springer-Verlag, 2006, p. 173, pp 173–+

Randich S., Aharpour N., Pallavicini R., Prosser C. F., Stauffer J. R., 1997, A&A, 323, 86

Rebull L. M., 2001, AJ, 121, 1676

Reipurth B., Chini R., Lemke R., 2004, Astronomische Nachrichten, 325, 671

Reipurth B., Pedrosa A., Lago M. T. V. T., 1996, A&AS, 120, 229

Richling S., Hollenbach D., Yorke H. W., 2006, Destruction of protoplanetary disks by photoevaporation. Planet Formation, pp 31–+

Richmond M. W., Droege T., Albertson C., Gombert G., Gutzwiller M., Johnson H., Wickersham R., Henden A., Beser N., Pittinger M., Kluga B., 1998, in Bulletin of the American Astronomical Society Vol. 30 of Bulletin of the American Astronomical Society, The Amateur Sky Survey (TASS): Two years and counting. pp 900–+

Robichon N., Arenou F., Mermilliod J.-C., Turon C., 1999, A&A, 345, 471

Ruprecht J., 1966, Bulletin of the Astronomical Institutes of Czechoslovakia, 17, 33

Russell H. N., 1910, AJ, 26, 147

Russell H. N., 1913, The Observatory, 36, 324

Russell H. N., 1929, ApJ, 70, 11

Rydgren A. E., Strom S. E., Strom K. M., 1976, ApJS, 30, 307

Sandstrom K. M., Peek J. E. G., Bower G. C., Bolatto A. D., Plambeck R. L., 2007, ArXiv e-prints, 706

Sanner J., Altmann M., Brunzendorf J., Geffert M., 2000, A&A, 357, 471

Santos N. C., Melo C., James D. J., Gameiro J. F., Bouvier J., Gomes J. I., 2008, ArXiv e-prints, 801

Sanz-Forcada J., Franciosini E., Pallavicini R., 2004, A&A, 421, 715

Savage B. D., de Boer K. S., 1981, ApJ, 243, 460

Schatzman E., 1962, Annales d'Astrophysique, 25, 18

Scholz A., Coffey J., Brandeker A., Jayawardhana R., 2007, ApJ, 662, 1254

Scholz A., Eislöffel J., 2004, A&A, 421, 259

Sherry W. H., Walter F. M., Wolk S. J., 2000, Bulletin of the American Astronomical Society, 32, 1412

Sherry W. H., Walter F. M., Wolk S. J., 2004, AJ, 128, 2316

Shu F., Najita J., Ostriker E., Wilkin F., Ruden S., Lizano S., 1994, ApJ, 429, 781

Shu F. H., 1977, ApJ, 214, 488

Shu F. H., Adams F. C., Lizano S., 1987, ARA&A, 25, 23

Sicilia-Aguilar A., Hartmann L. W., Briceño C., Muzerolle J., Calvet N., 2004, AJ, 128, 805

Sicilia-Aguilar A., Hartmann L. W., Hernández J., Briceño C., Calvet N., 2005, AJ, 130, 188

Siess L., Dufour E., Forestini M., 2000, A&A, 358, 593

Siess L., Forestini M., Bertout C., 1999, A&A, 342, 480

Sills A., Pinsonneault M. H., Terndrup D. M., 2000, ApJ, 534, 335

Simonson III S. C., van Someren Greve H. W., 1976, A&A, 49, 343

Skumanich A., 1972, ApJ, 171, 565

Slesnick C. L., Hillenbrand L. A., Carpenter J. M., 2004, ApJ, 610, 1045

Slesnick C. L., Hillenbrand L. A., Massey P., 2002, ApJ, 576, 880

Smith K., Pestalozzi M., Guedel M., Conway J., Benz A., 2003, in IAU Symposium Vol. 221 of IAU Symposium, The Magnetosphere of T Tauri South. pp 166P–+

Soderblom D. R., Jones B. F., Balachandran S., Stauffer J. R., Duncan D. K., Fedele S. B., Hudon J. D., 1993, AJ, 106, 1059

Soderblom D. R., Mayor M., 1993, ApJL, 402, L5

Soderblom D. R., Stauffer J. R., Hudon J. D., Jones B. F., 1993, ApJS, 85, 315

Southworth J., Clausen J. V., 2007, A&A, 461, 1077

Southworth J., Maxted P. F. L., Smalley B., 2004a, MNRAS, 349, 547

Southworth J., Maxted P. F. L., Smalley B., 2004b, MNRAS, 351, 1277

Southworth J., Zucker S., Maxted P. F. L., Smalley B., 2004, MNRAS, 355, 986

Stassun K. G., Mathieu R. D., Mazeh T., Vrba F. J., 1999, AJ, 117, 2941

Stauffer J., Hartmann L. W., Jones B. F., McNamara B. R., 1989, ApJ, 342, 285

Stauffer J. R., Balachandran S. C., Krishnamurthi A., Pinsonneault M., Terndrup D. M., Stern R. A., 1997, ApJ, 475, 604

Stauffer J. R., Hartmann L., Soderblom D. R., Burnham N., 1984, ApJ, 280, 202

Stauffer J. R., Hartmann L. W., 1987, ApJ, 318, 337

Stauffer J. R., Hartmann L. W., Fazio G. G., Allen L. E., Patten B. M., Lowrance P. J., Hurt R. L., Rebull L. M., Cutri R. M., Ramirez S. V., Young E. T., Rieke G. H., Gorlova N. I., Muzerolle J. C., Slesnick C. L., Skrutskie M. F., 2007, ApJS, 172, 663

Stauffer J. R., Hartmann L. W., Jones B. F., 1989, ApJ, 346, 160

Stauffer J. R., Hartmann L. W., Prosser C. F., Randich S., Balachandran S., Patten B. M., Simon T., Giampapa M., 1997, ApJ, 479, 776

Stauffer J. R., Jones B. F., Backman D., Hartmann L. W., Barrado y Navascués D., Pinsonneault M. H., Terndrup D. M., Muench A. A., 2003, AJ, 126, 833

Stauffer J. R., Prosser C. F., Giampapa M. S., Soderblom M. S., Simon T., 1993, AJ, 106, 229

Stetson P. B., 2000, PASP, 112, 925

Stolte A., Brandner W., Brandl B., Zinnecker H., Grebel E. K., 2004, AJ, 128, 765

Straizys V., Kuriliene G., 1981, Ap&SS, 80, 353

Strom S. E., 1972, PASP, 84, 745

Strom S. E., Strom K. A., Carrasco L., 1974, PASP, 86, 798

Strömgren B., 1932, Zeitschrift fur Astrophysik, 4, 118

Strömgren B., 1933, Zeitschrift fur Astrophysik, 7, 222

Sung H., Bessell M. S., Lee S., 1997, AJ, 114, 2644

Sung H., Chun M.-Y., Bessell M. S., 2000, AJ, 120, 333

Tan J. C., 2007, in Elmegreen B. G., Palous J., eds, IAU Symposium Vol. 237 of IAU Symposium, Massive star and star cluster formation. pp 258–264

Terndrup D. M., Krishnamurthi A., Pinsonneault M. H., Stauffer J. R., 1999, AJ, 118, 1814

Tout C. A., Livio M., Bonnell I. A., 1999, MNRAS, 310, 360

Turner D. G., 1976, ApJ, 210, 65

Uribe A., García-Varela J., Sabogal-Martínez B., Higuera G. M. A., Brieva E., 2002, PASP, 114, 233

van Leeuwen F., Alphenaar P., Meys J. J. M., 1987, A&AS, 67, 483

Ventura P., Zeppieri A., Mazzitelli I., D'Antona F., 1998, A&A, 331, 1011

Vitense E., 1953, Zeitschrift fur Astrophysik, 32, 135

Walker M. F., 1957, ApJ, 125, 636

Walter F. M., Brown A., Mathieu R. D., Myers P. C., Vrba F. J., 1988, AJ, 96, 297

Walter F. M., Wolk S. J., Sherry W., 1998, in Donahue R. A., Bookbinder J. A., eds, Cool Stars, Stellar Systems, and the Sun Vol. 154 of Astronomical Society of the Pacific Conference Series, The sigma Orionis Cluster. pp 1793–+

Ward-Thompson D., 2002, Science, 295, 76

Ward-Thompson D., Motte F., Andre P., 1999, MNRAS, 305, 143

Westera P., Lejeune T., Buser R., 1999, in Hubeny I., Heap S., Cornett R., eds, Spectrophotometric Dating of Stars and Galaxies Vol. 192 of Astronomical Society of the Pacific Conference Series, Metallicity calibration of theoretical stellar SEDs using UBVRIJHKL photometry of globular clusters. pp 203–+

Wichmann R., Krautter J., Covino E., Alcala J. M., Neuhaeuser R., Schmitt J. H. M. M., 1997, A&A, 320, 185

Woitas J., Bacciotti F., Ray T. P., Marconi A., Coffey D., Eislöffel J., 2005, A&A, 432, 149

Wolk S. J., Walter F. M., Freyberg M., 1996, in Pallavicini R., Dupree A. K., eds, Cool Stars, Stellar Systems, and the Sun Vol. 109 of Astronomical Society of the Pacific Conference Series, X-Ray Sources and Other PMS Stars Near alpha Orionis.. pp 445–+

Xiong D.-R., Deng L., 2005, ApJ, 622, 620

Young E. T., Lada C. J., Teixeira P., Muzerolle J., Muench A., Stauffer J., Beichman C. A., Rieke G. H., Hines D. C., Su K. Y. L., Engelbracht C. W., Gordon K. D., Misselt K., Morrison J., Stansberry J., Kelly D., 2004, ApJS, 154, 428